LAGRANGIAN COHERENT STRUCTURES IN IONOSPHERIC-THERMOSPHERIC FLOWS

BY

NINGCHAO WANG

Submitted in partial fulfillment of the
requirements for the degree of
Doctor of Philosophy in Mechanical and Aerospace Engineering
in the Graduate College of the
Illinois Institute of Technology

Approved
Advisor

Chicago, Illinois
July 2018

ACKNOWLEDGMENT

On this journey, there are many people who have helped and supported me. I humbly thank all of them.

First and foremost, I wish to express my sincere and deep appreciation to my advisor Professor Seebany Datta-Barua, for her tireless and energetic efforts over the past four years. I thank her for allowing me the opportunity to join the Space Weather lab at Illinois Institute of Technology, for encouraging my research interests, and for helping me to overcome the fears and challenges throughout my graduate career. My passion for the space sciences and the success of this work are largely the result of her mentorship.

Thanks to Professors Kevin Cassel, Jinqiao Duan, and Boris Pervan for serving on my defense committee, giving me insights, and reviewing this dissertation. Their continuous efforts made this work as solid as possible and guided me to become a better researcher.

This work was supported by National Science Foundation award AGS-1352602. I thank the project manager Dr. Ruth S. Lieberman for her enthusiasm for this project over the past 4 years.

Thanks to Armour College of Engineering and to Daniel Miladinovich, Dino Okic, Francisco Flores Vazquez, Houshine Sabbagh Zadeh, Kierra Herron, Roohollah Parvizi, Uriel Ramirez, Vaishnavi Sreenivash, Jordi Xing Zhang, and Yang Su at Space Weather Lab for their constructive academic and research support.

Thanks to Dr. Shawn Shadden for providing the publicly available FlowVC code as well as online tutorial materials. Thanks to Dr. Douglas Drob for providing the Horizontal Wind Model (HWM14) software and valuable comments on this work. Thanks to Dr. Daniel Weimer for the electric potential model source code. Thanks to Dr. Alex T. Chartier and Dr. Cathryn N. Mitchell for providing the MIDAS data.

Thanks to each of my dear friends met in Chicago, Desai Fan, Shiyang Li, Kaijie Zhang, Muduo Shi, Guohao Cai, Dr. Yawei Zhai, Xinyao Liu, Wenbo Sui, Siwei Dong, Mingjun Lei, Yilei Lin, Yuanchang Gao, Xiao Li, Dr. Jun Cao, Shan-Ju Chiang, Dr. Ming Yin, Dr. Yang Zhou, Dr. Mateos Kassa, Yuze Chen, Jingyan Wang, Haoyang Yan, Zhengyang Guo, Suohai Gu, Aibo Zhang, Xiaowei He, Dr. Peng Zhao, Hui Jia, Jialiang Wei, Xuanhong An, and Yuanhao Zhuge (the sequence of name is arranged by time we met) for the helps and joys they give me. Special thank to my roommates for making Chicago feel like home.

I would like to thank all my family from the bottom of my heart for their support and love. Special thank to my aunt Guiqing Guan for supporting and encouraging me in my scholarly pursuits.

Last, but no least, I am grateful for my parents Guili Guan and Mian Wang, who have selflessly supported, and unconditionally loved me for my whole life. They are my source of happiness, giving me endless energy to get over failure and stand up again.

TABLE OF CONTENTS

Page

CHAPTER

LIST OF TABLES

Table Page

LIST OF FIGURES

Figure Page

LIST OF SYMBOLS

Symbol	Definition
AE	Auroral Electrojet index
AL	amplitude lower
A_p	Planetary-A index
AU	amplitude upper
ALOMAR	Arctic Lidar Observatory for Middle Atmospheric Research
CCMC	Community Coordinated Modeling Center
DWM07	disturbance wind model 2007
Dst	disturbance storm time
ECEF	earth-centered earth-fixed
EMPIRE	Estimating Model Parameters from Ionospheric Reverse Engineering
EUV	extreme ultraviolet
FSLE	finite size Lyapunov exponent
FTLE	finite time Lyapunov exponent
GNSS	Global Navigation Satellite System
GPS	Global Positioning System
GTIM	Global Theoretical Ionospheric Model
HAO	High-Altitude Observatory
HWM14	horizontal wind model 2014
IGRF-12	12th generation International Geomagnetic Reference Field
IGS	International GNSS Service

I-LCS	ionospheric LCS
I-LCS-Q	ionospheric LCS during the geomagnetically quiet period
I-LCS-S	ionospheric LCS during the geomagnetically stormy period
IMF	interplanetary magnetic field
IT	Ionosphere Thermosphere
ITALCS	Ionosphere-Thermosphere Algorithm for Lagrangian Coherent Structures
K_p	Planetary-K index
LCS	Lagrangian Coherent Structure
MIDAS	Multi-Instrument Data Analysis System
MISI	MIcrowave Spectrometer at the Institute of Atmospheric Physics
NCAR	National Center for Atmospheric Research
PMC	polar mesospheric cloud
RMR	Rayleigh-Mie-Raman
SAPS	sub-auroral polarization stream
SED	storm enhanced density
SMR	Sub-Millimeter Radiometer
SSC	storm sudden commencement
SWS	Space Weather Services
TEC	total electron content
TECU	total electron content units
TIEGCM	Thermosphere Ionosphere Electrodynamics General Circulation Model

T-LCS	thermospheric LCS
T-LCS-Q	thermospheric LCS during the geomagnetically quiet period
T-LCS-S	thermospheric LCS during the geomagnetically stormy period
TOI	tongue of ionization
UV	ultraviolet
WDC	World Data Center
R_E	Earth radius
v_e	zonal velocity component
v_n	meridional velocity component
ϕ	longitude
λ	latitude
$\dot{\phi}$	angular rate of change in longitude
$\dot{\lambda}$	angular rate of change in latitude
m	mass of a particle
q	charge of a particle
$\vec{v}$	velocity
$\vec{E}$	electric field
$\vec{B}$	magnetic field
$\vec{v}_{drift}$	velocity of $\vec{E} \times \vec{B}$ drifts
τ	integration time
x	fluid particle position in a two-dimensional flow domain
x^1	fluid particle position in horizontal direction

x^2	fluid particle position in vertical direction
x_0	initial fluid particle position
$\dot{x}$	velocity of the fluid particle at x
t	time
t_0	initial time
t_f	final time
F	flow map
δ^1	infinitesimal displacement in horizontal direction of the domain
δ^2	infinitesimal displacement in vertical direction of the domain
$\mathbf{J}$	Jacobian matrix
σ	FTLE value
λ_{e-max}	maximum eigenvalue
Δt	temporal resolution of the velocity field
dt	numerical integration time resolution
f	velocity field of a flow
r	radius of a sphere
E	(superscript) earth-centered earth-fixed frame
O	origin
L	(superscript) Lagrangian frame
$\vec{r}^P$	the position of particle P from origin
h	the height of an atmospheric layer
${}^E\vec{v}^P$	the velocity of particle P in the ECEF frame

${}^{E}\vec{\omega}^{L}$	the angular velocity of the frame L with respect to the frame E
${}^{E}\vec{\omega}^{A}$	the angular velocity of the frame A with respect to the frame E
${}^{A}\vec{\omega}^{L}$	the angular velocity of the frame L with respect to the frame A
ϕ_{min}	the minimum value of longitude
ϕ_{max}	the maximum value of longitude
λ_{min}	the minimum value of latitude
λ_{max}	the maximum value of latitude
$\Delta\phi$	longitudinal distance
$\Delta\phi'$	updated longitudinal distance
$\Delta\lambda$	latitudinal distance
σ_{TH}	threshold of FTLE value
ϕ_{E}	eastern-most point of the LCS ridge
ϕ_{E}^{Q}	eastern-most point of the LCS ridge during the geomagnetically quiet period
${}^{T}\phi_{E}^{Q}$	eastern-most point of the thermospheric LCS ridge during the geomagnetically quiet period
${}^{I}\phi_{E}^{Q}$	eastern-most point of the ionospheric LCS ridge during the geomagnetically quiet period
ϕ_{E}^{S}	eastern-most point of the LCS ridge during the geomagnetically stormy period
${}^{T}\phi_{E}^{S}$	eastern-most point of the thermospheric LCS ridge during the geomagnetically stormy period
${}^{I}\phi_{E}^{S}$	eastern-most point of the ionospheric LCS ridge during the geomagnetically stormy period

ϕ_W	western-most point of the LCS ridge
ϕ_W^Q	western-most point of the LCS ridge during the geomagnetically quiet period
${}^T\phi_W^Q$	western-most point of the thermospheric LCS ridge during the geomagnetically quiet period
${}^I\phi_W^Q$	western-most point of the ionospheric LCS ridge during the geomagnetically quiet period
ϕ_W^S	western-most point of the LCS ridge during the geomagnetically stormy period
${}^T\phi_W^S$	western-most point of the thermospheric LCS ridge during the geomagnetically stormy period
${}^I\phi_W^S$	western-most point of the ionospheric LCS ridge during the geomagnetically stormy period
ϕ_C	midpoint of the LCS ridge
ϕ_C^Q	midpoint of the LCS ridge during the geomagnetically quiet period
ϕ_C^S	midpoint of the LCS ridge during the geomagnetically stormy period
${}^T\phi_C$	midpoint of the thermospheric LCS ridge
${}^T\phi_C^Q$	midpoint of the thermospheric LCS ridge during the geomagnetically quiet period
${}^T\phi_C^S$	midpoint of the thermospheric LCS ridge during the geomagnetically stormy period
${}^I\phi_C$	midpoint of the ionospheric LCS ridge
${}^I\phi_C^Q$	midpoint of the ionospheric LCS ridge during the geomagnetically quiet period
${}^I\phi_C^S$	midpoint of the ionospheric LCS ridge during the geomagnetically stormy period

$\Delta\phi_C$	angle between the midpoint of the thermospheric LCS and the ionospheric LCS ridges
$\Delta\phi_C^Q$	angle between the midpoint of the thermospheric LCS and the ionospheric LCS ridges during the geomagnetically quiet period
$\Delta\phi_C^S$	angle between the midpoint of the thermospheric LCS and the ionospheric LCS ridges during the geomagnetically stormy period
ν_{O^+}	O^+ neutral collision frequency
T_i	temperature of ions
T_n	temperature of neutral particles

ABSTRACT

The ionosphere and thermosphere are coupled through the charged and neutral particles' interactions that re-distribute energy and momentum. The interactions have been analyzed through modeling, measurements, and data assimilation. However, transport is still not well understood because of multisystem coupling and nonlinearities in the interactions. After a finite time, two neighboring fluid elements in the ionosphere and thermosphere (IT) region can be very far apart in different areas of flow, challenging our ability to forecast the IT state. Recently, Lagrangian Coherent Structure (LCS) analysis, a novel numerical technique in fluid dynamical analysis predicting transport and interaction processes, has been used to give insight into time evolving dynamics in the IT system. LCSs are frame-invariant structures independent of the observer describing the maximum separation (or convergence) regions in the flow and are located at the points whose finite time Lyapunov exponent (FTLE) is locally maximum.

In this work, a 2-D algorithm, Ionosphere-Thermosphere Algorithm for Lagrangian Coherent Structures (ITALCS), is developed and used for computing the forward-time FTLE scalar fields in the non-Euclidean spherical domain, e.g. modeled IT flows. Thermospheric LCSs (T-LCSs) are found and illustrated in the neutral winds flows modeled by horizontal wind model 2014 (HWM14). These LCSs are more prominent at higher altitudes and latitudes, respond to the geomagnetic activity, and act as predictive transport barriers in thermosphere. To explore the LCSs in ionospheric plasma drifts, Weimer 2005 polar electric potential model and the 12th generation International Geomagnetic Reference Field (IGRF-12) are used to generate the $\vec{E} \times \vec{B}$ drifts. The ionospheric LCSs (I-LCS) are found in the high-latitude ionosphere appearing as a "U" shape oriented to open on the nightside, and they respond to geomagnetic activity by shifting equatorward. By comparing the shape of

LCSs in the thermosphere and ionosphere during both a geomagnetically quiet period and an active period, the dynamical interaction of neutral and charged particles in IT region is analyzed. A coupled IT model, Thermosphere Ionosphere Electrodynamics General Circulation Model (TIEGCM) is used to self-consistently simulate both neutral wind convection and plasma convection. With TIEGCM, both T-LCSs and I-LCSs respond to geomagnetic activity with the T-LCS and I-LCS aligning more closely as geomagnetic activity increases.

CHAPTER 1

INTRODUCTION

On 8 July 2011, the last space shuttle deposited 350 t of water vapor off the east coast of the U.S. at 100-115 km altitude during its launch. The water vapor plume was tracked over the next few days in the thermosphere, the layer of Earth's neutral atmosphere above 85 km that is dominated by neutral gas dynamics and diurnal heating. Figure 1.1 shows the space shuttle plume observations. The water vapor appeared at Kühlungsborn's location, marked as 'Δ', but not at Arctic Lidar Observatory for Middle Atmospheric Research (ALOMAR), marked as '$*$', within two days. The water vapor eventually appeared as high latitude clouds, a result considered surprising given how far south it had been deposited [62].

The possibility of such large latitudinal transport was not anticipated by atmospheric models. Diffusion [46] and two-dimensional turbulence [34] were presented as possible mechanisms for the high rate of meridional transport. Nevertheless, it is important to be able to anticipate where launch byproducts (or other material) may or may not end up in the upper atmosphere, especially since such dramatic meridional water vapor transport was not an isolated occurrence [57, 63].

1.1 Geospace system

Geospace, also as known as the solar-terrestrial environment shown in Figure 1.2, refers to the upper part of the Earth's atmosphere (i.e. thermosphere, ionosphere), magnetosphere, the outer part of the geomagnetic field, and solar wind flowing past the Earth. [26] This region, starting some 50–70 km above the Earth's surface and extending to distances measured in tens of Earth radii (R_E), is a closely-coupled, interactive dynamical system, which is near enough to be analyzed from the ground

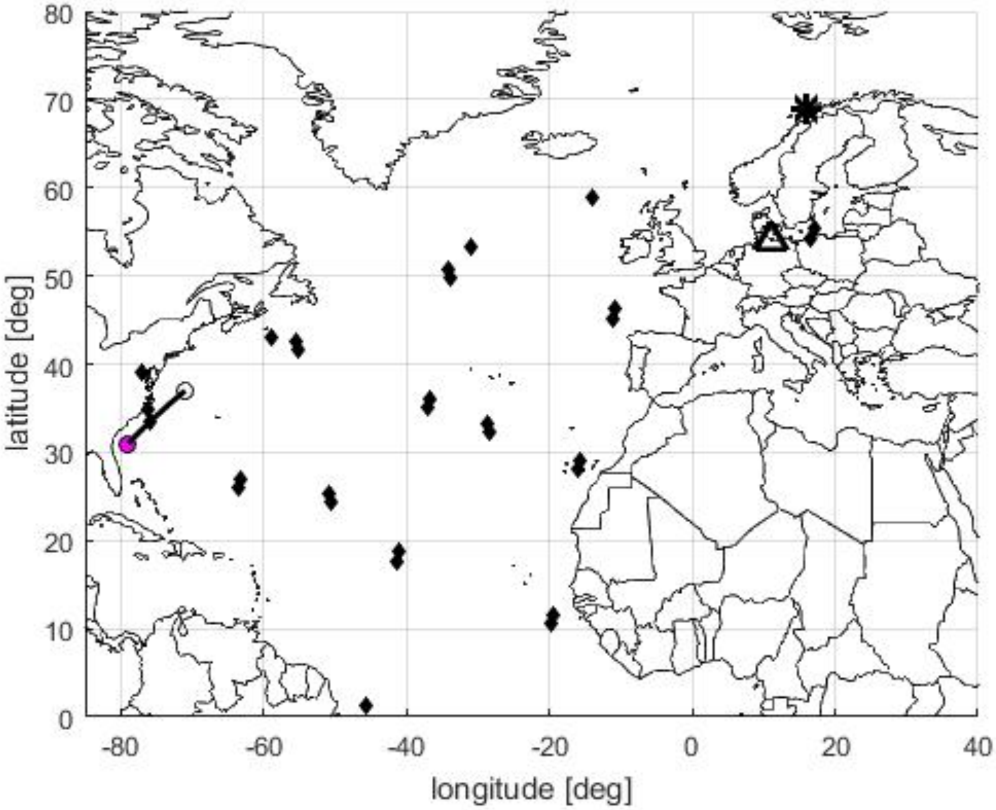

Figure 1.1. The space shuttle plume observations on 8-10 July 2011 at 100 km. The trajectory of the space shuttle during the deposition interval is marked as a black curved line. The deposition interval is shown as magenta circle (at the start) and white (end). Water vapor observations made by the satellite-based Sub-Millimeter Radiometer (SMR) within 48 hours of the shuttle plume release [62] are black diamonds. The location of ground-based observatories are shown at Kühlungsborn, marked 'Δ', and Arctic Lidar Observatory for Middle Atmospheric Research (ALOMAR), marked '$*$'.

and to affect human's daily lives but remote enough not to be experienced every day. This section introduces the primary components of the solar-terrestrial system, e.g. the magnetosphere, ionosphere, and thermosphere, and the coupling system, ionosphere-thermosphere (IT) system.

1.1.1 Magnetosphere. The magnetosphere is the region surrounding Earth containing Earth's magnetic field. The magnetosphere acts as a semi-permeable buffer that shields Earth from the solar wind. The solar wind stretches the magnetic dipole

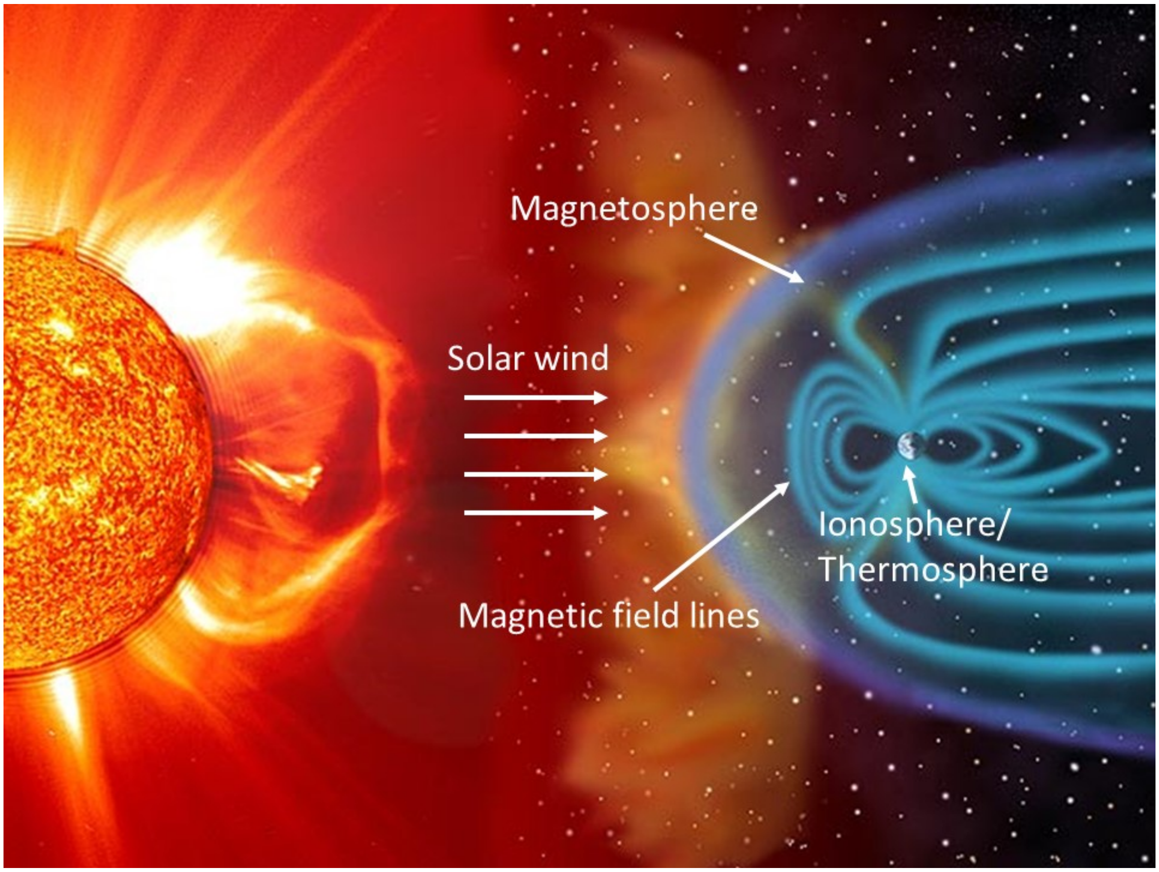

Figure 1.2. The geospace environment (Modified from the original image by NASA).

many Earth radii ($\sim$100 R_E) on the nightside. The surface at which Earth's magnetic field pressure and the solar wind plasma magnetic pressures are balanced determines the magnetopause. The magnetopause occurs approximately 10 Earth radii (R_E) at the upstream (sunward) location, but extends many tens to hundreds of R_E in the downstream side, with a tail-like shape formed by the stretched geomagnetic field lines. As the solar wind plasma reaches the magnetosphere, a bow shock is formed in front of the magnetopause. Across the bow shock, the supersonic solar wind is slowed to subsonic speeds, and as the flow is compressed and heated, a plasma region formed between the bow shock and magnetopause is the magnetosheath. Each magnetospheric field line has an Earthward footpoint located in the high-latitude ionosphere. Variations in the solar wind plasma density and velocity, and the interplanetary magnetic field (IMF) embedded in it, strongly modulate magnetospheric behavior.

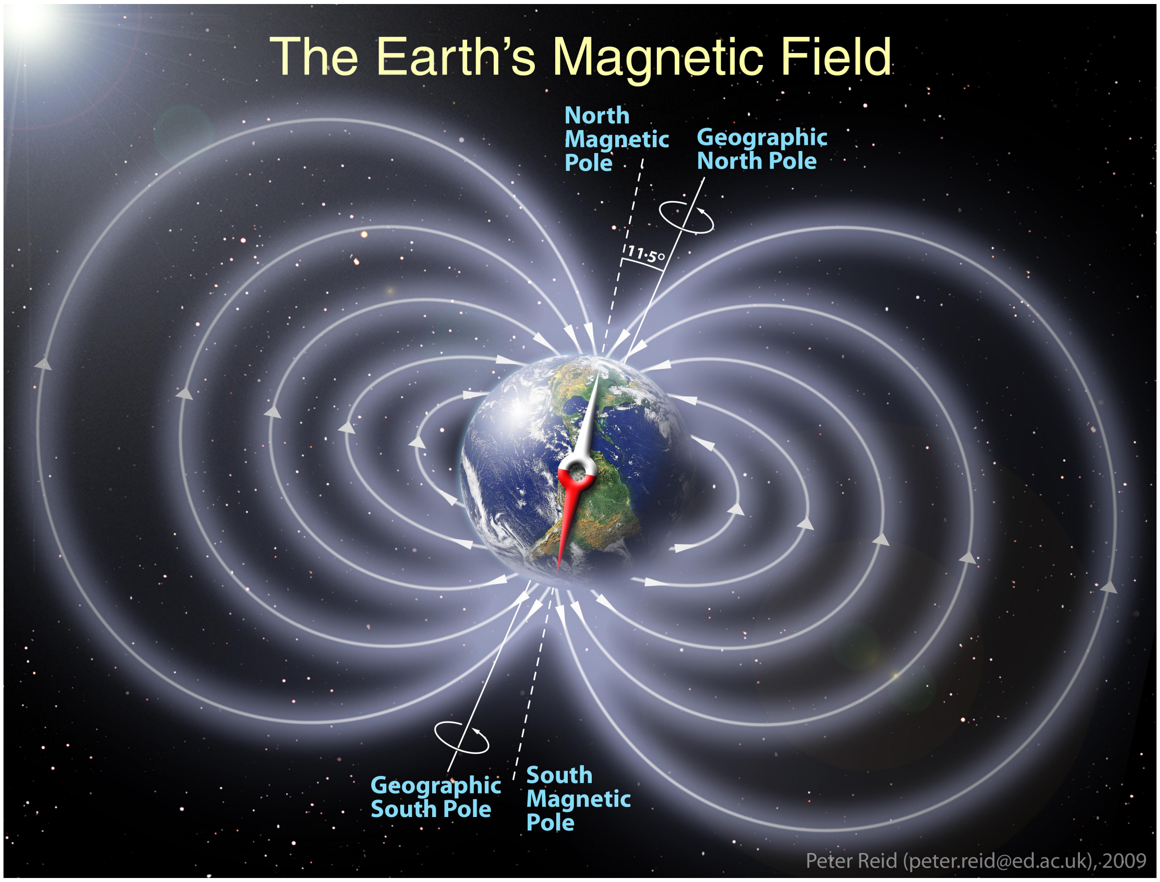

Figure 1.3. The earth's magnetic field. (Credit: Peter Reid)

Earth's interior magnetic field, generated by electric currents, and the presence of charges in the upper atmosphere and radiation belts produce an overall magnetic field from the surface of Earth to several Earth radii away (see Figure 1.3). The Earth's near-steady magnetic field is primarily a dipole, tilted about 10° with respect to Earth's rotational axis. Note that the point referred to as the "north magnetic pole" is actually the south pole of a magnet, such that the field lines are pointing toward it [67].

1.1.2 Ionosphere. The ionosphere is the partially ionized region of the Earth's upper atmosphere that extends from about 60 km to 1000 km (from the top of the lower atmosphere to the bottom of the magnetosphere). Ionospheric plasma is formed by photoionization of neutral atoms and molecules by absorbing solar extreme ultraviolet (EUV) and ultraviolet (UV) radiation [67]. Due to low gas densities, the recombination of the ions and electrons proceeds slowly in the ionosphere, resulting in high concentrations of plasma even throughout the night.

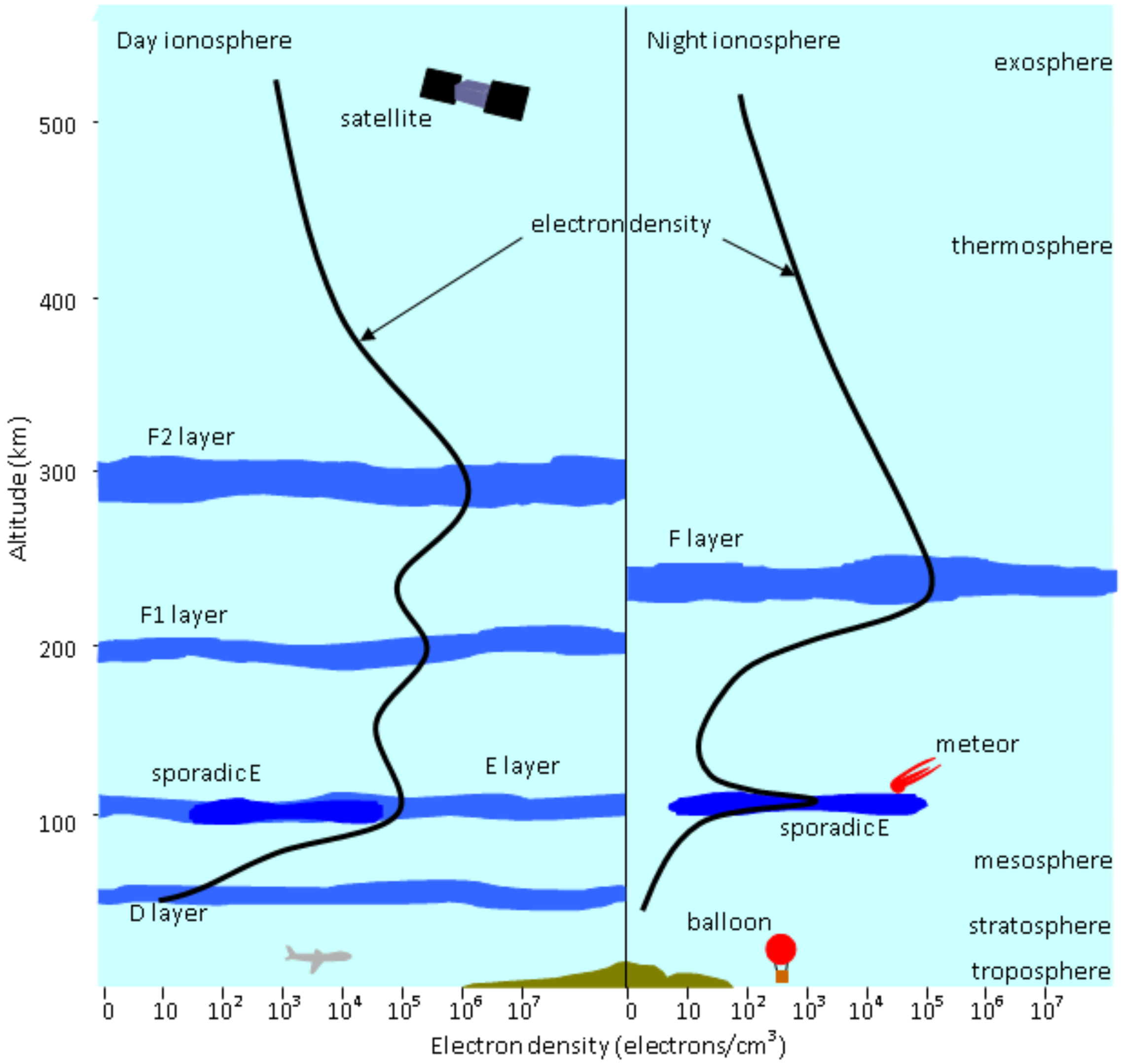

Figure 1.4. Structure of the ionosphere with black lines indicating electron density as a function of height on the vertical axis. Credit: Space Weather Services (SWS)

The ionosphere can be divided into low-, mid-, and high-geomagnetic latitude zones. The behavior of the ionosphere in these zones differs primarily due to the orientation of the magnetic field lines. The vertical structure of the ionosphere is characterized by variations in density that reach local maximum at each of three main layers called the D, E, and F regions, as shown in Figure 1.4.

The D region ionosphere (50–95 km), with density varying from 1 cm^{-3} at 50 km, to about 10^4 cm^{-3} at 95 km, primarily exists on the dayside and disappears completely at night due to recombination. The E region plasma (95–150 km) has a peak density of 10^5 cm^{-3}. Compared to the neutral density of 10^{11} cm^{-3}, the E region plasma is weakly ionized. The F region can be divided into two layers during the day time, with F_1 ranging from 150 km to 250 km and F_2 starting from 250 km. During nighttime, the D and F_1 layers disappear completely at night, and the nighttime E becomes weak. However, the F_2 layer persists throughout the night [30, 67].

1.1.3 Thermosphere.

The ionospheric plasma exists from the ionization of neutral particles of the upper atmosphere, which is known as the thermosphere. The thermosphere extends from approximately 80 km to over 500 km, so the ionosphere is embedded in the thermosphere. The variation in radiation energy from the sun influences both the height of the top of this layer and the temperature within it, making the top of the thermosphere shift between 500 km to 1000 km [67]. The thermosphere is popularly regarded as the edge of space due to the low density of air, although scientifically it is considered part of the Earth's atmosphere. The main neutral species in this layer are O_2, N_2, and NO; this layer is almost cloudless and free of water vapor. Low Earth orbit satellites and the International Space Station orbit within the thermosphere and are subject to a small but nonzero thermospheric drag force.

As shown in Figure 1.5, particle densities are low, of order 10^{10} cm^{-3}, enough so that the dominant species N_2, O_2, and O are not completely mixed [67]. The

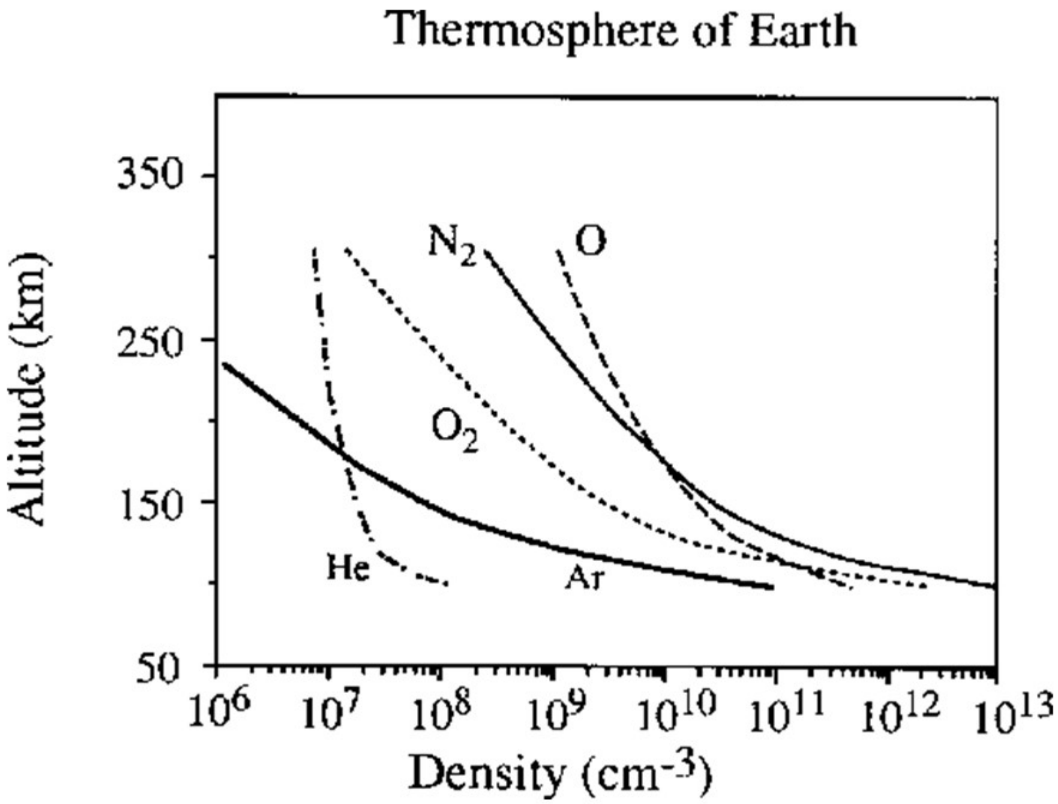

Figure 1.5. Thermospheric neutral densities for various molecular and atomic species. Image credit:[12]

thermosphere is also characterized by high kinetic temperatures on the order of 1000 K. Neutral winds are driven by heating due to solar EUV and UV radiation, which also is ionizing. For example, at high latitascione2010tudes neutral transport is affected by ion drag forces and heating in the pole area [35].

In the thermosphere, the neutral densities decrease exponentially with altitude. At 80–100 km, higher density results in the neutral particles being well-mixed. Between 100–500 km, thermosphere is dominated by diffusion. In this region, the interaction of charged and neutral particles is more important, coupling the ionosphere and thermosphere together. Above 500 km, the ionosphere-thermosphere interactions are minor due to low particle densities and fewer collisions.

1.1.4 System coupling. The thermosphere, dominated by neutral wind processes, and ionosphere, dominated by plasma and electromagnetic field behavior, are coupled together to form the ionosphere-thermosphere (IT) system (see Figure 1.6). The IT system is affected by the magnetosphere above, which provides electromagnetic and energetic particle connections from the solar wind into the IT system, and the mesosphere below, which transfers wave energy. In the IT system, charged and neutral particles interact to re-distribute energy and momentum. The Dynamics Explorer satellite made polar wind measurements that showed a momentum transfer effect of ion convection superimposed on a background wind field [36]. Polar cap patches are transport evidence of IT interaction as well [58].

1.2 Geomagnetic activity

The geospace environment is affected by solar activity. The geomagnetic storm, a temporary disturbance of Earth's magnetosphere, is caused by a solar wind shock wave. During the storm, the Earth's magnetosphere is compressed by the increasing solar wind pressure [67]. As shown in Figure 1.7, the solar wind interacts with the Earth's magnetic field and transfers increased energy in the form of radiation and particles into the magnetosphere. The magnetosphere shields most solar wind from Earth, but at times solar wind particles and energy can be funneled into Earth's magnetosphere, creating current systems. These currents generate magnetic fields that are superposed on the quiet time magnetic fields. They are measured as variations in the magnetic field at the surface. The level of geomagnetic activity may be quantified by a number of metrics measuring the degree of variation in the Earth's surface magnetic field. The geomagnetic storm may be defined by geomagnetic indices such as disturbance storm time (Dst) index, Planetary-K (K_p) index , Planetary-A (A_p) index, and Auroral Electrojet index (AE index) [67].

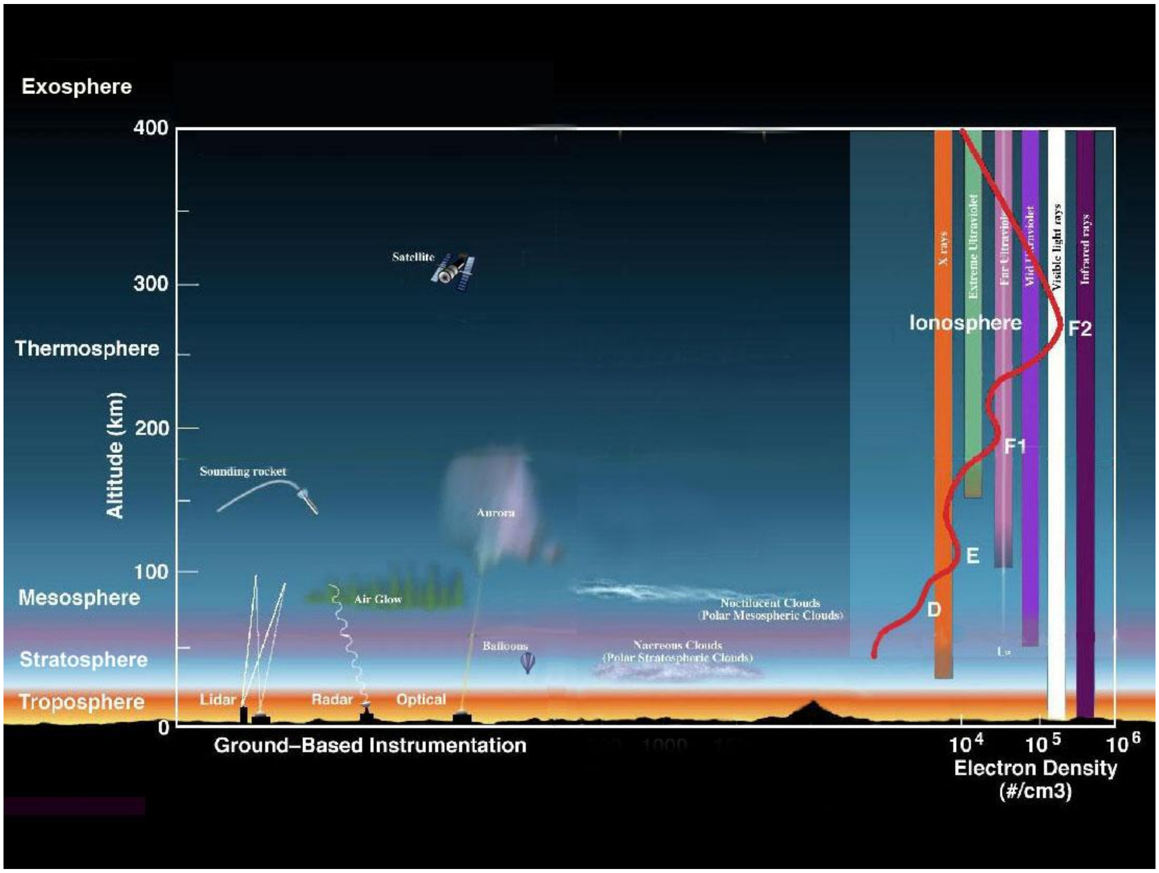

Figure 1.6. The earth's atmospheric layers (Credit: NASA). The neutral thermosphere and plasma ionosphere lie in the same altitude range above about 85 km.

The Dst index, based on measurements from low latitude magnetometer stations is an hourly index that estimates the globally averaged change of the horizontal component of the Earth's magnetic field at the magnetic equator [67, 26]. A Dst index between -20 and +20 nT describes the geomagnetically quiet period. Figure 1.8 shows the Dst index for March 2015. As shown in the figure, there is a geomagnetic storm during 17 to 19 March 2015. A geomagnetic storm has three phases: initial, main, and recovery. During the initial phase, the Dst increases by 20 to 50 nT rapidly. This increase is referred to as a storm sudden commencement (SSC). The main phase is characterized by Dst decreasing to some minimum value. The subsequent changing of Dst from its minimum value to its quiet time value is defined as the recovery phase. The hourly Dst index is computed in near real-time and can be retrieved from the

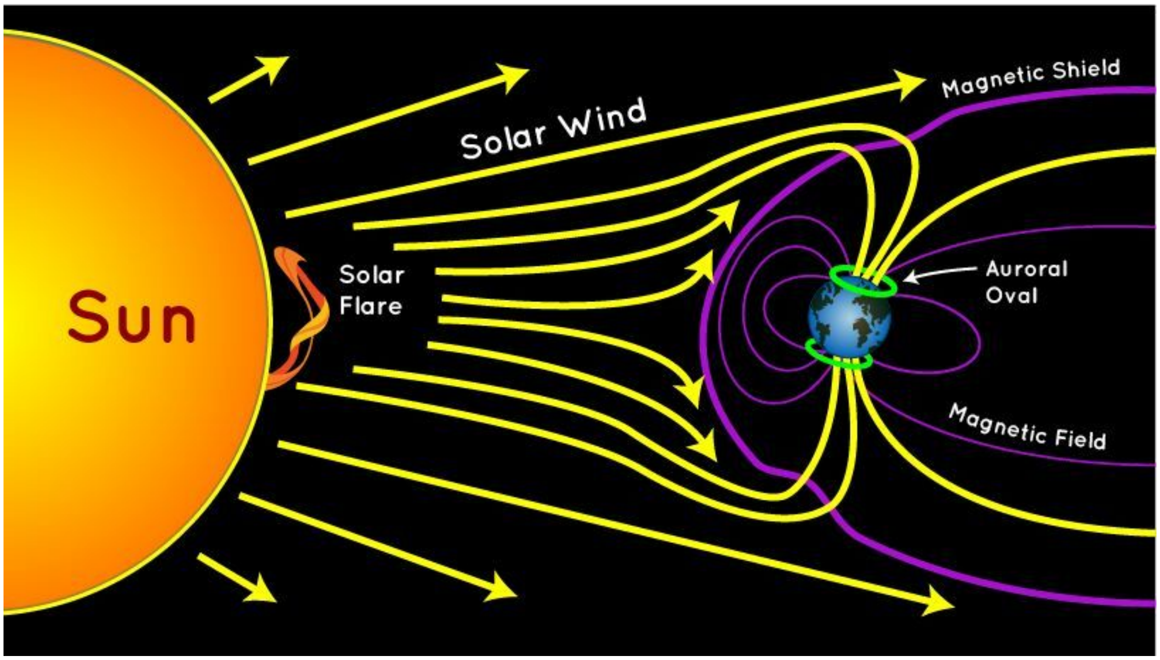

Figure 1.7. Solar wind magnetic field interacts the Earth's magnetic field (Credit: NASA).

World Data Center (WDC) for Geomagnetism, Kyoto Dst index service [79].

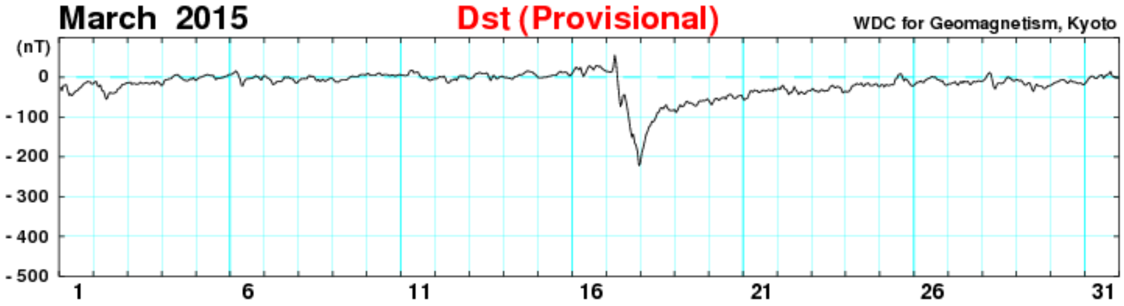

Figure 1.8. Dst plot for March 2015 [79].

The K_p index, introduced by Bartels [4], is a tri-hourly global quasi-logarithmic geomagnetic storm index based on a weighted average of the most disturbed horizontal component of the magnetic field quantified by K-index at several mid- to high- latitude stations worldwide. The K_p index ranges from 0 (minimal activity) to 9 (extreme geomagnetic storm). A K_p index of 5 is the threshold of a geomagnetic storm. The

A_p index, converting the non-linear K_p value back into linear scale, provides a daily average level for geomagnetic activity.

The Auroral Electrojet (AE) index provides a global, quantitative measure of auroral zone magnetic activity produced by enhanced ionospheric currents flowing below and within the auroral oval. The AE index is computed by taking the difference of the AU (amplitude upper) and AL (amplitude lower) which are the indices of the upper and lower envelope of auroral-zone magnetic observations [32].

1.3 Lagrangian Coherent Structure and its application

Coherent structures are features of a time-evolving flow that persist in space and time. They may appear at many scales, and indicate transport and energy transfer processes. A formal definition of coherence in Earth's fluid environment can be challenging [71] particularly for turbulent or time-varying fluid flows, such as that of the upper atmosphere.

One set of approaches to identifying coherent structures relies on analysis of the fluid from the Lagrangian frame, which flows with the fluid, rather than the Eulerian fixed-point frame. Instantaneous Eulerian field properties to define vorticity, e.g., the Okubo-Weiss criterion [52, 78], have historically been more commonly used.

In the Lagrangian frame, coherent structures describe regions of maximal separation (or convergence) for neighboring fluid elements in the flow [24]. In contrast to structures based on an Eulerian definition, Lagrangian Coherent Structures (LCSs) are objective: their existence is independent of the observer [23], making them appropriate to study in Earth's non-inertial frame [73, 72]. LCSs are useful because they demarcate and can allow us to predict where contaminants in a fluid may or may not spread [53]. Prominent geophysical uses of LCS analysis have been undertaken to understand ocean flows [31] and hurricane entrainment [17]. For example, in oceanography scientists use the LCS to predict whether an oil spill will circulate into a nearby bay, making shore habitats toxic, or dispel into the open ocean [10]. In essence the LCS is an intrinsic surface in the flow, separating trajectories that flow into the bay from those that flow into the ocean.

In the upper atmosphere coherent structuring may be due to both charged and/or neutral particle population motion. The ionosphere is subject to electrodynamic forcing. In the ionosphere-thermosphere (IT) system charged and neutral particles interact to re-distribute energy and momentum. Neutral transport is affected by high-latitude ion drag forces and heating in the polar cap [35]. The Dynamics Explorer satellite made polar wind measurements that showed a momentum transfer effect of ion convection superimposed on a background wind field [36]. Polar cap patches are transport evidence of IT interaction as well [58].

1.4 Motivation

While thermospheric neutral parcel transport has been traced before [35], and LCSs have specifically been sought in 100-km scale modeling of the mid-latitude ionosphere [66], a systematic investigation of ionospheric and thermospheric Lagrangian coherent structuring has not been performed.

LCS analysis of the ionosphere-thermosphere presents a novel way to elucidate the effects that IT interactions such as Joule heating, which is caused by the collision of neutral particles and charged particles, impose on material transport. Additionally, LCSs can enable a better understanding of structuring in aperiodic, possibly turbulent, flows. Analyzing LCSs will enable us to ask and answer new kinds of questions about the IT system despite its complexity. LCS analysis allows us to trace materials deposited in the upper atmosphere, as illustrated in Figure 1.1, delimiting the regions where they will travel. LCS analysis will open a wide range of practical questions and applications.

Analysis of ionospheric plasma transport structuring at high latitudes, especially during geomagnetic storms, can provide a better understanding of material and energy transfer in the ionosphere and improve the predictability of ionospheric irregularities' motion. In the high-latitude upper atmosphere the polar cap patch, a 100s kilometer-scale ionospheric plasma irregularity poleward of the auroral oval, is an enhanced plasma density island surrounded by lower density plasma [13]. A polar cap patch is often associated with ionospheric plasma density irregularities varying from 100 m to several kilometers scale size that adversely affect Global Navigation Satellite System(GNSS) service [50] by causing scintillation, a rapid fluctuation in signal amplitude and phase [14, 82, 81]. The mechanism for scintillation is electromagnetic wave scattering due to variations in density [60]. Polar cap patch scintillations are believed to arise due to a number of possible instability mechanisms [6, 50, 3]. While there is no consensus on how exactly patches lead to scintillation, Moen et al. (2013) [50] points out the importance of tracking patches and the flow channels and shears in which they drift, which can drive instabilities.

For this reason, this dissertation asks: 1) are there governing structures in the upper atmosphere and do they bound the transport; 2) could the structures help us to have a better understanding of the upper atmospheric dynamics and improve the predictability of it?

1.5 Contributions

This dissertation involves four main contributions, each of which is described throughout the following chapters. Prior methods in modeling upper atmospheric flows as well as the formal definition of LCSs are reviewed in Chapter 2. Then the contributions of this work in investigating LCSs in IT flows can be outlined as follows:

HOW are LCSs identified at global scale? As discussed in Chapter 3, an algorithm, Ionosphere-Thermosphere Algorithm for Lagrangian Coherent Structures (ITALCS) is developed to explore the LCSs in the IT system. In this contribution, ITALCS is validated by testing with a canonical flow, the time-varying 2-D double gyre. Then equations are derived for applying ITALCS to a closed 2-D spherical domain.

WHERE are the LCSs in the thermospheric flows, and HOW can they bound material transport? In Chapter 4, for the first time, thermospheric LCSs are predicted to exist based on global simulations with an empirical model. The LCSs are more prominent at higher altitudes and latitudes, and they respond to geomagnetic activity. A thermospheric LCS is found to be the poleward barrier of space shuttle water vapor plume transport.

WHERE are the LCSs in the ionospheric flows, and HOW can they bound material transport? Chapter 5 shows the anticipated global high latitude ionospheric LCSs based on 2-D flows computed by modeled electric field and magnetic field. The ionospheric LCSs appear at high latitudes and respond to geomagnetic activity. The LCSs give insight into necessary conditions for the formation and transport of the polar cap patch.

WHAT are the dynamical interactions of LCSs in the IT system? Comparisons of thermospheric LCSs and ionospheric LCSs are addressed in Chapter 6. A preliminary comparison between the thermospheric LCSs and ionospheric LCSs based on independent empirical models of the thermosphere and the plasma drifts shows the response to geomagnetic activity of the ionospheric LCSs and its similarities to and differences from the thermospheric LCSs. A coupled IT model is applied to self-consistently simulate both neutral wind convection and plasma convection. By comparing the LCS patterns, the material and energy transport processes in the coupled thermosphere and ionosphere are analyzed.

CHAPTER 2

TECHNICAL BACKGROUND

2.1 Models of Earth's upper atmosphere

2.1.1 Horizontal Wind Model 2014 (HWM14). As shown in Figure 1.6, ground-based lidar and radar are used to make measurements of the lower thermosphere. Those measurements are limited to a local area and the lower thermosphere. Fabry-Perot instruments measuring airglow emissions from the thermosphere are also available in certain areas, and can make measurements around 250 km [45]. Even so, the study of the global thermosphere is difficult with sparsely distributed measurements, because a complete global neutral wind field is required. Therefore, in order to study the neutral wind flow at a global scale in this work, the flow field is simulated by a thermospheric model. In this work, Horizontal Wind Model 2014 (HWM14) is used to simulate the 2-D global neutral wind field by providing local ground speeds of the winds at each desired location.

HWM14 is an empirical model based on satellite- and ground-based measurements of winds [16]. HWM14 is parameterized by day of year, solar local time, latitude, longitude, and altitude, and can compute the zonal (eastward) and meridional (northward) velocity components of horizontal neutral winds from the ground to about 500 km. HWM14 can represent variation due to geomagnetic activity via the disturbance wind model 2007 (DWM07) [19] built into it. DWM07 uses geomagnetic activity indices (K_p index derived from user-provided A_p index) as input to compute winds during geomagnetically stormy periods. The output from HWM14 is ground speed v_e and v_n (in m/s) at a geographic longitude and latitude (ϕ, λ) for a given altitude and time. This velocity (v_e, v_n) is expressed in east-north coordinates local

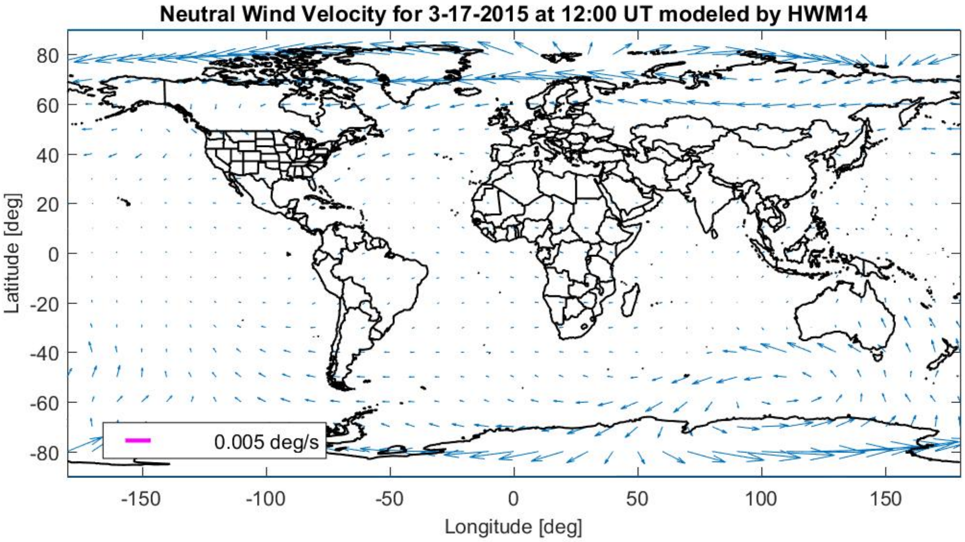

Figure 2.1. 2-D global neutral wind field at t_0 = 12:00 UT, on 17 March 2015 at 250 km altitude modeled by HWM14.

to each point. Figure 2.1 is an example of the 2-D global neutral wind flow field at 250 km at 12:00 UT on 17 March 2015, as simulated by HWM14.

2.1.2 Ionospheric convection. The ionosphere is a charged particle layer embedded in the thermosphere created by the partial ionization of neutral atoms and molecules by solar UV radiation, and is subject to electrodynamic forcing. The motion of a single charged particle is governed by the Lorentz force equation:

$$m\frac{d\vec{v}}{dt} = q(\vec{E} + \vec{v} \times \vec{B}) \tag{2.1}$$

where m is the particle mass, $\vec{v}$ is its velocity, q is the charge of the particle, and $\vec{E}$ and $\vec{B}$ are local electric and magnetic fields, respectively.

In the presence of only a magnetic field, a charged particle will gyrate about a field line. When both electric $\vec{E}$ and magnetic $\vec{B}$ fields are present, the particle motion is a superposition of gyrating motion in the plane perpendicular to the magnetic field and a drift of the center of gyration, or guiding center, in the direction parallel to $\vec{B}$. The drifting velocity of the guiding center is described as:

$$\vec{v}_{drift} = \frac{\vec{E} \times \vec{B}}{B^2} \tag{2.2}$$

$\vec{v}_{drift}$ is the average perpendicular velocity, which is independent of q and m.

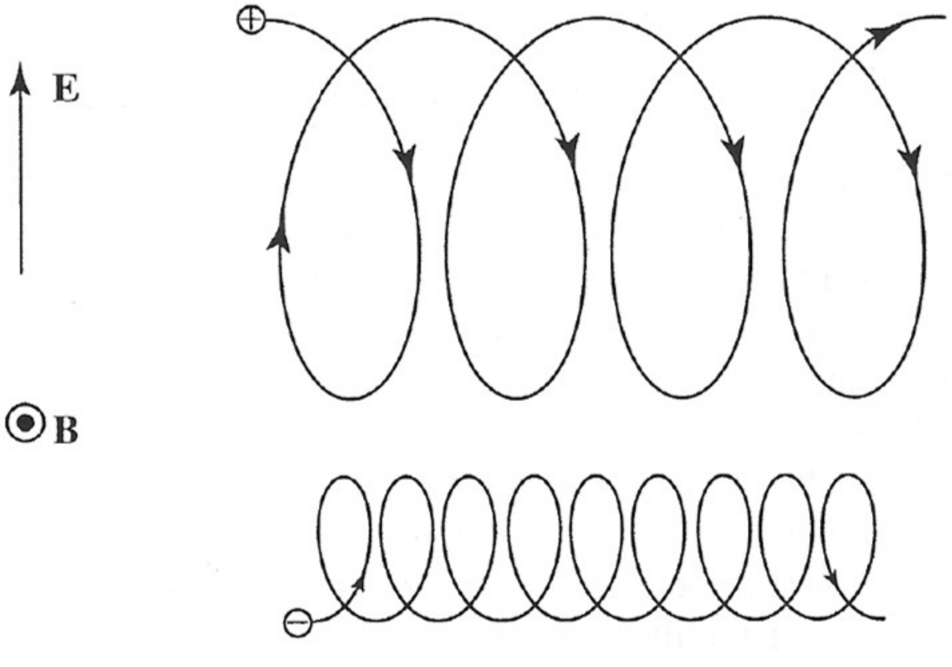

Figure 2.2. Charged particle drift motion. Reprinted from [5]

Figure 2.2 shows that, while the sense of the gyration is opposite for an ion and electron, both ion and electron drift in the same direction, so the drift motion of charged particles does not generate current under collisionless conditions. The ionosphere exhibits this drift due to the presence of electric and magnetic fields, known as $\vec{E} \times \vec{B}$ drift.

As with the thermosphere a complete drift field of ionospheric charged parti-

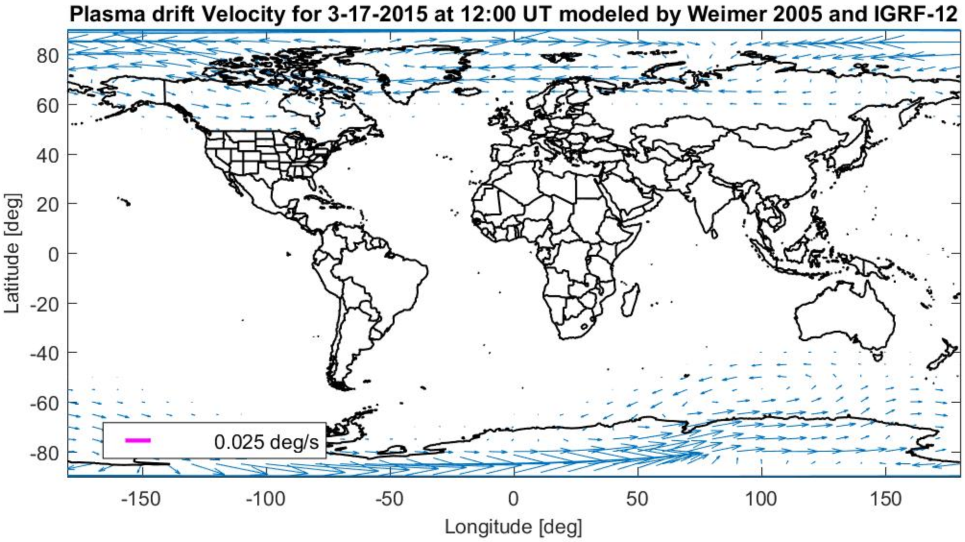

Figure 2.3. 2-D global charged particle drift field at t_0 = 12:00 UT, on 17 March 2015 at 250 km modeled by Weimer 2005 and IGRF-12.

cles, sometimes also referred to as convection, is hard to measure given the spatial sparsity of sensors (e.g., radar, satellite-based in situ instruments). In order to study the plasma convection at global scale, the global electric and magnetic field needs to be simulated by models. The twelfth generation International Geomagnetic Reference Field (IGRF-12) is a multi-pole expansion model of Earth's interior magnetic field [68]. At high geomagnetic latitudes, an electric field is present in the polar regions [67]. The Weimer 2005 electric potential model is used for generating the high latitude potential field [76]. With the electric scalar potential $\mathbf{V}$, the electric field can be computed as:

$$\vec{E} = -\nabla \mathbf{V} \tag{2.3}$$

For generating ionospheric $\vec{E} \times \vec{B}$ convection fields, the drift at each grid point in a single layer of the ionosphere is computed by using the outputs of Weimer 2005 for $\vec{E}$ and IGRF-12 for $\vec{B}$. At high latitudes, the magnetic field is oriented primarily vertically, so the drift is primarily horizontal. The zonal and meridional components of the ionospheric drift velocity with respect to the ground are (v_e, v_n) in m/s at a geographic location (ϕ, λ) for a given altitude and time.

Since the Weimer model is a fit to high latitude electrostatic potential, it has an equatorward boundary at which the potential goes to 0. All locations equatorward of this boundary will have no electric field. The 2-D global plasma $\vec{E} \times \vec{B}$ drift flow field at 12:00 UT on 17 March 2015 is shown in Figure 2.3 as generated by Weimer 2005 and IGRF-12.

2.1.3 Thermosphere Ionosphere Electrodynamics General Circulation Model (TIEGCM).

TIEGCM is a three-dimensional (3-D) global physical model, developed at the National Center for Atmospheric Research (NCAR) High-Altitude Observatory (HAO). TIEGCM simulates the nonlinear energetically, dynamically, electrodynamically, and chemically coupled ionosphere-thermosphere (IT) system from about 97 km to about 500 to 700 km depending on solar activity [40].

In the IT system, the fully coupled, nonlinear, hydrodynamic, thermodynamic, and continuity equations of the neutral gas, the ion and electron energy and momentum equations, the ion continuity equation, and neutral wind dynamo, are solved self-consistently in TIEGCM via fourth order finite differencing method. For example, the neutral winds are solved from the momentum equations in the zonal (east-west) and meridional (north-south) directions.

TIEGCM is an open-source community model, with two types of grid resolutions in the spherical geographic domain, 2.5° × 2.5° and 5° × 5°. TIEGCM can output 3-D solutions (i.e. 3-D neutral wind flows, 3-D plasma drifts, potential both in geomagnetic and geographic coordinates, and temperatures of neutral and charged particles). The inputs required by TIEGCM are solar inputs (solar irradiance, ionization rates, dissociation rates, and heating rates) and magnetospheric inputs (geomagnetic activity index K_p or interplanetary magnetic field (IMF), solar wind or specified cross-cap potential, and hemispheric power). TIEGCM is also available at the NASA Community Coordinated Modeling Center (CCMC) for runs-on-request [40].

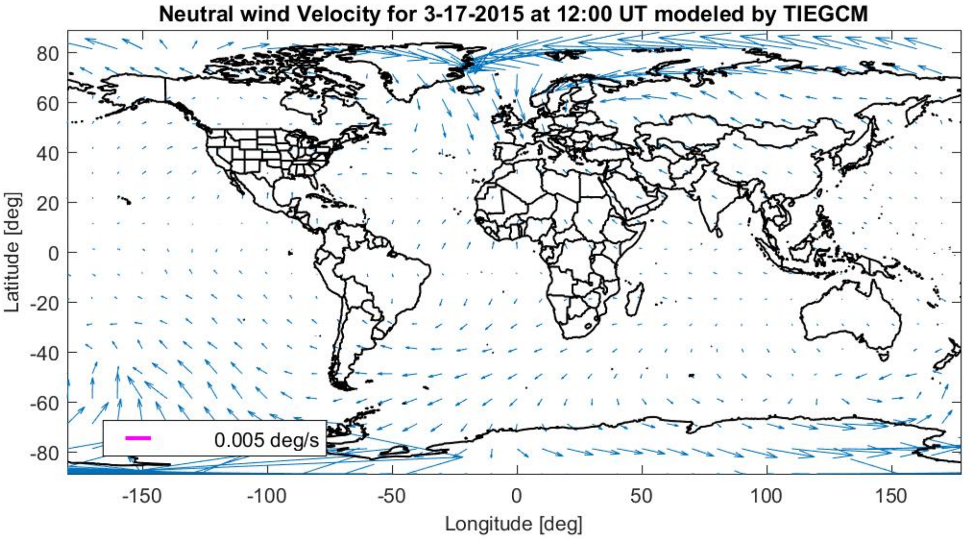

Figure 2.4. 2-D global neutral wind field at t_0 = 12:00 UT, on 17 March 2015 at 250 km modeled by TIEGCM.

Figure 2.4 is an example of the 2-D global neutral wind flow field at 250 km at 12:00 UT on 17 March 2015, as simulated by TIEGCM. The 2-D global plasma $\vec{E} \times \vec{B}$ drift flow field modeled by TIEGCM at 12:00 UT on 17 March 2015 is shown

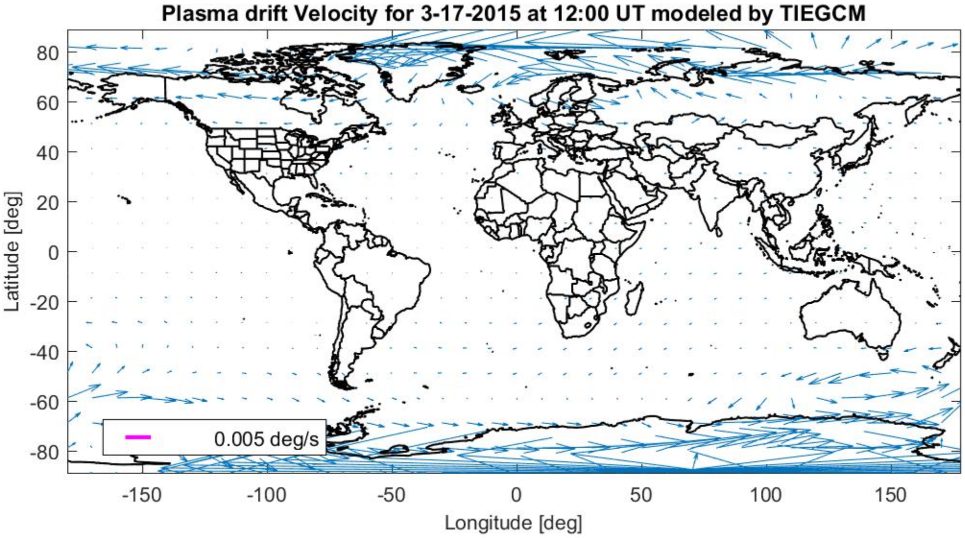

Figure 2.5. 2-D global charged particle drift field at $t_0 = 12{:}00$ UT, on 17 March 2015 at 250 km modeled by TIEGCM.

in Figure 2.5.

2.2 Finite time Lyapunov exponent and LCS numerical solver

The finite-time Lyapunov exponent (FTLE) and finite-size Lyapunov exponent (FSLE) are two common diagnostics for defining trajectory separation in dynamical systems. The FSLE, measuring the separation time for a given initial separation distance, is indirectly linked to the flows during the time interval τ. However, the FSLE field is sensitive to the flow data's temporal resolution, causing inaccuracy in the FSLE analysis [33]. Compared to the FSLE field, the FTLE field, a scalar field measuring the degree of stretching of a fluid element at a certain location after a given interval of time, relative to its initial extent [73], avoids the jump-discontinuities and ill-posedness everywhere continuous for a certain time interval τ [33]. The ridge in 2-D (or surface in a three-dimensional flow) of maximal FTLE values then represents a barrier in material transport [55]. The basic equations for the FTLE [24, 22] are summarized here for a two-dimensional flow domain. Advection of the fluid particle at each point $x = (x^1, x^2)$ at time t can be described as:

$$\dot{x} \;=\; v(x,t), \;\; x \in U, t \in [t_0, t_f] \tag{2.4}$$

where $U \subset \mathbb{R}^2$ is the domain. A flow map F at time t_f maps particles at all initial positions x_0 at t_0 to their current positions $x(t_f; x_0, t_0)$ at final time t_f after a finite period of time $\tau = t_f - t_0$:

$$\begin{aligned} F_{t_0}^{t_f}(x_0) &= x(t_f; x_0, t_0)\,,\, t \in [t_0, t_f] && (2.5) \\ &= x_0 + \int_{t_0}^{t_f} v(x,t)dt && (2.6) \end{aligned}$$

where $x_0 = x(t_0; x_0, t_0)$, and the velocity v is integrated to propagate fluid elements forward in time.

The flow map traces a fluid particle from initial position x_0 to a final position after time τ. By keeping track of each particle's initial and final positions, the amount of stretching that has occurred is quantified by computing the Jacobian $\mathbf{J}$ of the flow map. As shown in Figure 2.6, for each particle in a two-dimensional flow domain this is a 2×2 matrix:

$$\mathbf{J} \equiv \nabla F_{t_0}^{t_f}(x_0) \;=\; \begin{bmatrix} \frac{x^1(t_f;t_0,x_0^1+\delta^1)-x^1(t_f;t_0,x_0^1-\delta^1)}{|2\delta^1|} & \frac{x^1(t_f;t_0,x_0^1+\delta^1)-x^1(t_f;t_0,x_0^1-\delta^1)}{|2\delta^2|} \\ \\ \frac{x^2(t_f;t_0,x_0^2+\delta^2)-x^2(t_f;t_0,x_0^2-\delta^2)}{|2\delta^1|} & \frac{x^2(t_f;t_0,x_0^2+\delta^2)-x^2(t_f;t_0,x_0^2-\delta^2)}{|2\delta^2|} \end{bmatrix} \tag{2.7}$$

where δ^1, δ^2 are infinitesimal displacements in each respective direction of the domain. Then the finite time Lyapunov exponent (FTLE) σ is the normalized maximum eigen-

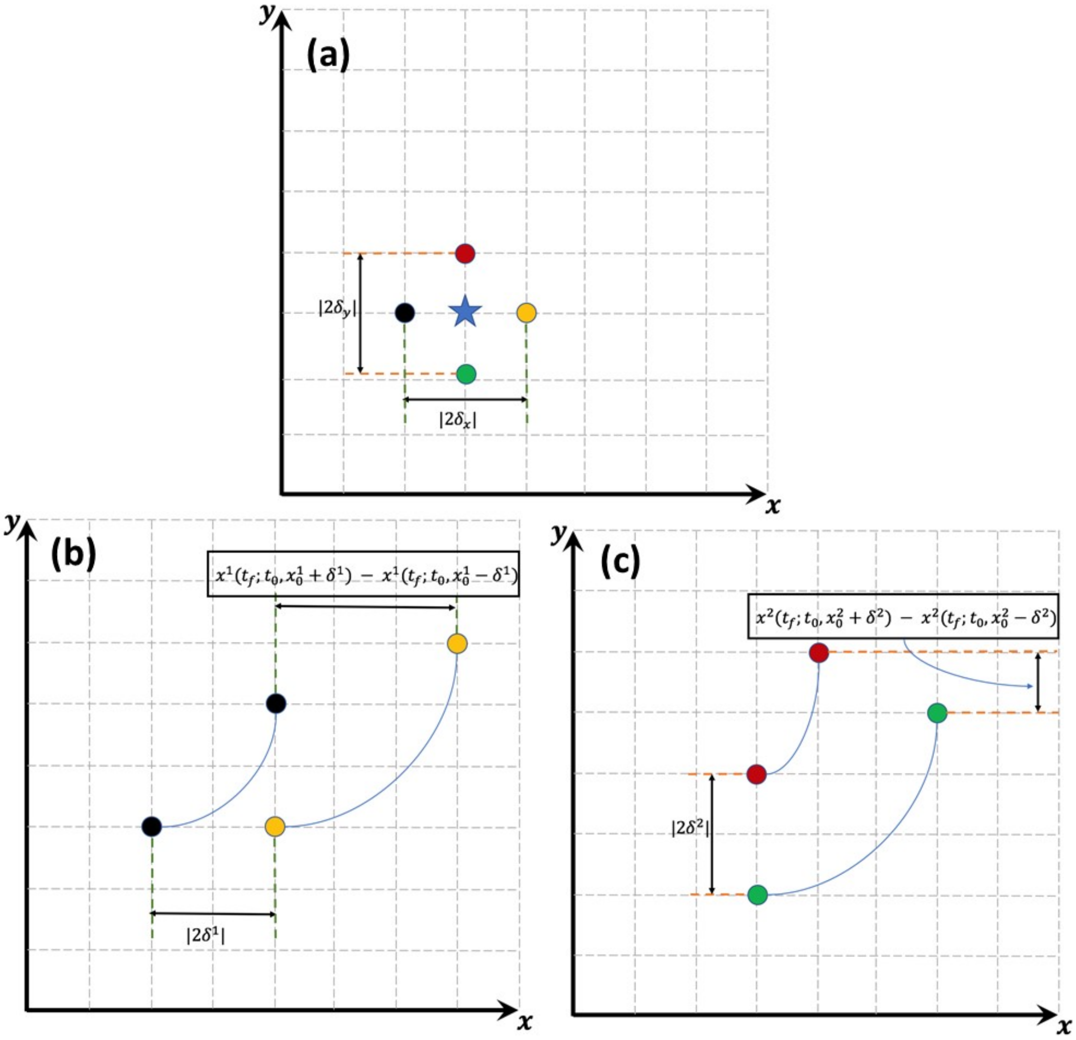

Figure 2.6. An example for computing the FTLE value for a gridpoint in a 2-D domain. (a) The initial position of the gridpoint is shown as a blue star. Two horizontal adjacent points are shown in black and yellow with an initial separation of $|2\delta^1|$, and two vertical adjacent points (green and red) have a separation of $|2\delta^2|$. (b) The initial and final positions of the horizontal points. (c) The initial and final separations of the two vertical points.

value λ_{e-max} as follows:

$$\sigma\left(\mathbf{J}\right) = \frac{1}{|\tau|}\log\left(\sqrt{\lambda_{e-max}\left(\mathbf{J}^T\mathbf{J}\right)}\right) \tag{2.8}$$

An FTLE is computed for every initial particle x_0 in the domain, and the LCS is the ridge of local FTLE maxima, a maximally repelling material surface. To find LCSs of maximum attraction, the integration in Eq. (2.6) is carried out backwards in time.

There are a number of publicly available software tools for computing LCSs: MANGEN [39], Newman [69], and FlowVC [56]. None of them are developed specifically to handle a spherical domain.

CHAPTER 3

IONOSPHERE-THERMOSPHERE ALGORITHM FOR LAGRANGIAN COHERENT STRUCTURES

Existing LCS computation tools perform well when applied to a Euclidean domain. However, the ionosphere and thermosphere are spherical domains which form a non-Euclidean surface. None of the currently available LCS solvers were obviously adaptable to a non-Euclidean domain. In addition, for a spatially finite domain, the lack of velocity data beyond the boundary causes spurious LCS ridges at the boundary [65]. To address these issues, Ionosphere-Thermosphere Algorithm for Lagrangian Coherent Structures (ITALCS) is developed to be used for a spherical domain.

3.1 ITALCS

3.1.1 Description of the algorithm. Based on the equations for the finite-time Lyapunov exponent (FTLE) computation, I developed the Ionosphere-Thermosphere Algorithm for Lagrangian Coherent Structures (ITALCS) to investigate upper atmospheric LCSs. ITALCS uses input 2-D velocity data to compute the FTLE scalar fields as well as tracer trajectories.

The spatial domain for which ITALCS computes FTLE values and tracer trajectories must be discretized into a regular mesh of generalized coordinates, specified by bounds on x^1, x^2 and resolutions δ^1, δ^2 for each. The temporal domain $[t_0, t_f]$ defines the time interval within which ITALCS may compute the integration shown in Eq. (2.6). Within that time interval, velocity fields must be provided over the grid at n epochs spaced in time by Δt such that $\tau = n\Delta t$.

For the forward-time FTLE computation, after reading in the input velocities for the gridded domain and timespan specified, ITALCS computes the FTLE values for every initial gridpoint in the domain. I use the particles' positions at a chosen start time t_0 to find the particles' ending positions by numerically integrating over duration τ. The velocity data are provided at time intervals Δt, which is subdivided into m smaller intervals dt with $\Delta t = mdt$. In this way the flow map in Eq. (2.6) is discretized as:

$$\begin{aligned} x(t_f; x_0, t_0) &\approx x_0 + \sum_{i=0}^{n-1} v_i(x_i, t_i)\Delta t && (3.1) \\ &\approx x_0 + \sum_{i=0}^{n-1} \sum_{j=0}^{m-1} v_i(x_{ij}, t_{ij})dt && (3.2) \end{aligned}$$

The purpose of the subdivision $\Delta t = mdt$ is to decouple the integration interval from the velocity field data cadence. If velocity field data are provided by measurement, the Δt resolution may be limited by the measurement process. In the case of a model, as in this work, having $\Delta t > dt$ decreases the runtime of the model significantly. In some cases, a model may have a finite time resolution. The velocity field $f(t) = v(x, t)$ of the flow at time $t \in [t_i, t_{i+1}]$ within each time interval Δt will be linearly interpolated between the velocity fields $f(t_i) = v(x, t_i)$ and $f(t_{i+1}) = v(x, t_{i+1})$ at the start and end of the time interval as shown in Eq. (3.3).

$$f(t) = \frac{t_{i+1} - t}{\Delta t} f(t_i) + \frac{t - t_i}{\Delta t} f(t_{i+1}) \tag{3.3}$$

After each numerical integration step dt, since the particle at $x(t_{ij}; x_0, t_0)$ will not in general fall at exactly another gridpoint, the velocity data are bilinearly interpolated to its location. Figure 3.1 shows one cell of a 2-D mesh. A particle $P(x, y)$ is not in general located at the gridpoint. Instead it is located in the cell of $A_{11}(x_1, y_1), A_{21}(x_2, y_1), A_{22}(x_2, y_2), A_{12}(x_1, y_2)$. The values of $A_{11}, A_{21}, A_{22}, A_{12}$ are known as $f(A_{11}), f(A_{21}), f(A_{22}), f(A_{12})$. By bilinearly interpolating, I can obtain a value for $f(P)$ at point $P(x, y)$. The equation is described as follows:

$$f(P) = \begin{bmatrix} \frac{x_2-x}{x_2-x_1}, \frac{x-x_1}{x_2-x_1} \end{bmatrix} \begin{bmatrix} f(A_{11}) f(A_{12}) \\ \\ f(A_{21}) f(A_{22}) \end{bmatrix} \begin{bmatrix} \frac{y_2-y}{y_2-y_1} \\ \\ \frac{y-y_1}{y_2-y_1} \end{bmatrix} \tag{3.4}$$

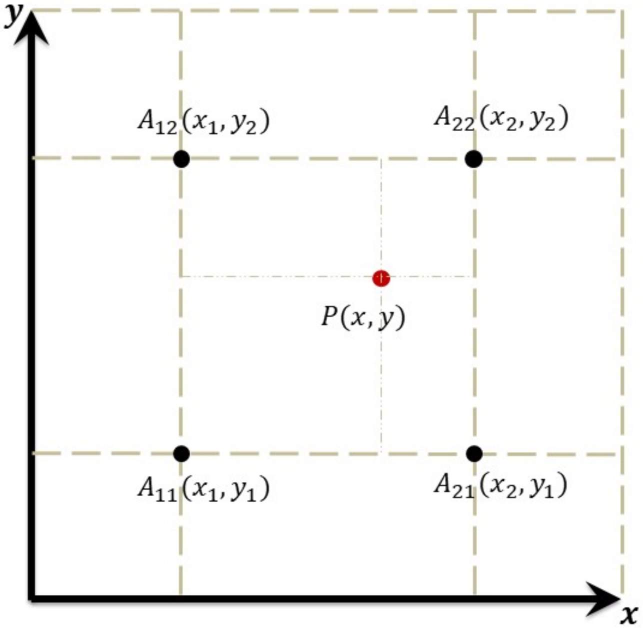

Figure 3.1. One cell of the 2-D mesh with the gridpoints labeled as A_{11}, A_{21}, A_{22}, A_{12}, particle P is located in the cell.

The flow map computation starts at t_0 and stops at t_f after integration time τ. The Jacobian matrix is composed by substituting a particle's starting position $x(t_0; x_0, t_0)$ and ending position $x(t_f; x_0, t_0)$ into Eq. (2.7). The output FTLE scalar field from Eq. (2.8) for a given t_0 is a matrix of the same dimension as the meshed grid domain. For tracer trajectory calculations, the intermediate locations $x(t_0 + i\Delta t; x_0, t_0)$ and final position $x(t_f; x_0, t_0)$ of a tracer particle are output.

3.1.2 Algorithm verification. To demonstrate that ITALCS is accurate, I validate its results with a canonical flow, the time-varying 2-D double gyre, given in the literature [55]. The basic equations for the simplified 2-D double-gyre flow described by the stream function are summarized here:

$$\psi(x, y, t) = A\sin(\pi f(x, t))\sin(\pi y) \tag{3.5}$$

where

$$f(x, t) = a(t)x^2 + b(t)x \tag{3.6}$$

$$a(t) = \epsilon\sin(\omega t) \tag{3.7}$$

$$b(t) = 1 - 2\epsilon\sin(\omega t) \tag{3.8}$$

The flow is over a [0,2]×[0,1] domain. The parameters in equations 3.7 and 3.8 are chosen to produce a simple time-dependent flow with fixed boundaries.

The velocity field is given by

$$u = -\frac{\partial\psi}{\partial y} = -\pi A\sin(\pi f(x))\cos(\pi y) \tag{3.9}$$

$$v = \frac{\partial\psi}{\partial x} = \pi A\cos(\pi f(x))\sin(\pi y)\frac{df}{dx} \tag{3.10}$$

Figure 3.2(a) is the flow field for the double-gyre at $t_0 = 0$, 0.5, and 1 s, (b) at $t_0 = 0.25$ s, and (c) $t_0 = 0.75$ s for $\epsilon = 0.1$. For $\epsilon = 0$, the flow is time-independent and has the same pattern as Figure 3.2(a). However, for $\epsilon \neq 0$ the flow is time-dependent and the double gyre consists of two counter-rotating vortices that alternately expand and contract with time in the $x-$direction.

Figure 3.3(a) shows the forward-time FTLE values from 0 (blue) to 5 s^{-1} (yellow) over the double-gyre domain when integrated forward in time from $t_0 = 0$ s

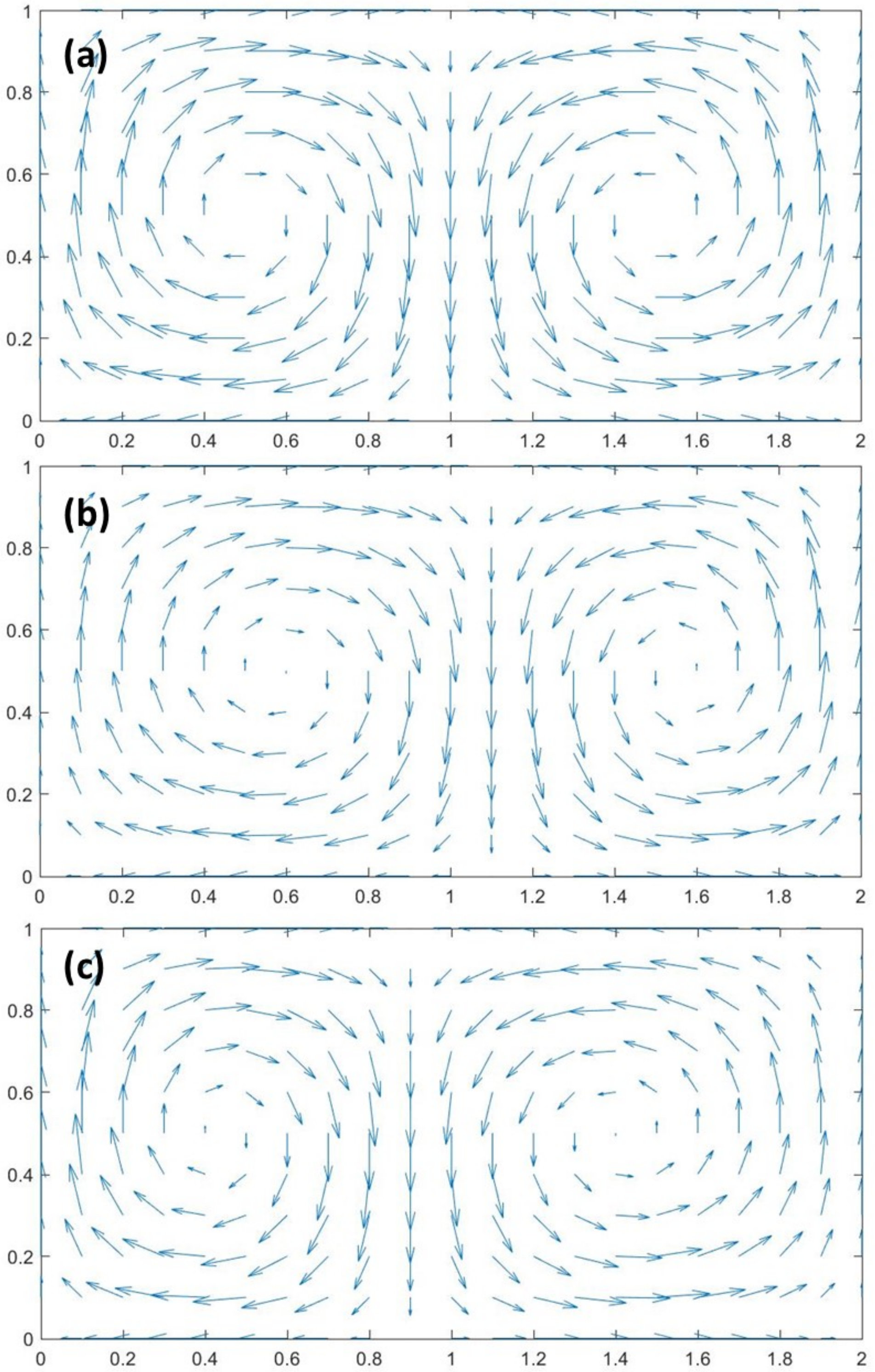

Figure 3.2. The time-varying double-gyre flow fields at (a) $t_0 = 0$, 0.5, and 1 s, (b) $t_0 = 0.25$ s, and (c) $t_0 = 0.75$ s for $A = 1$, $\omega = 2\pi$, and $\epsilon = 0.1$

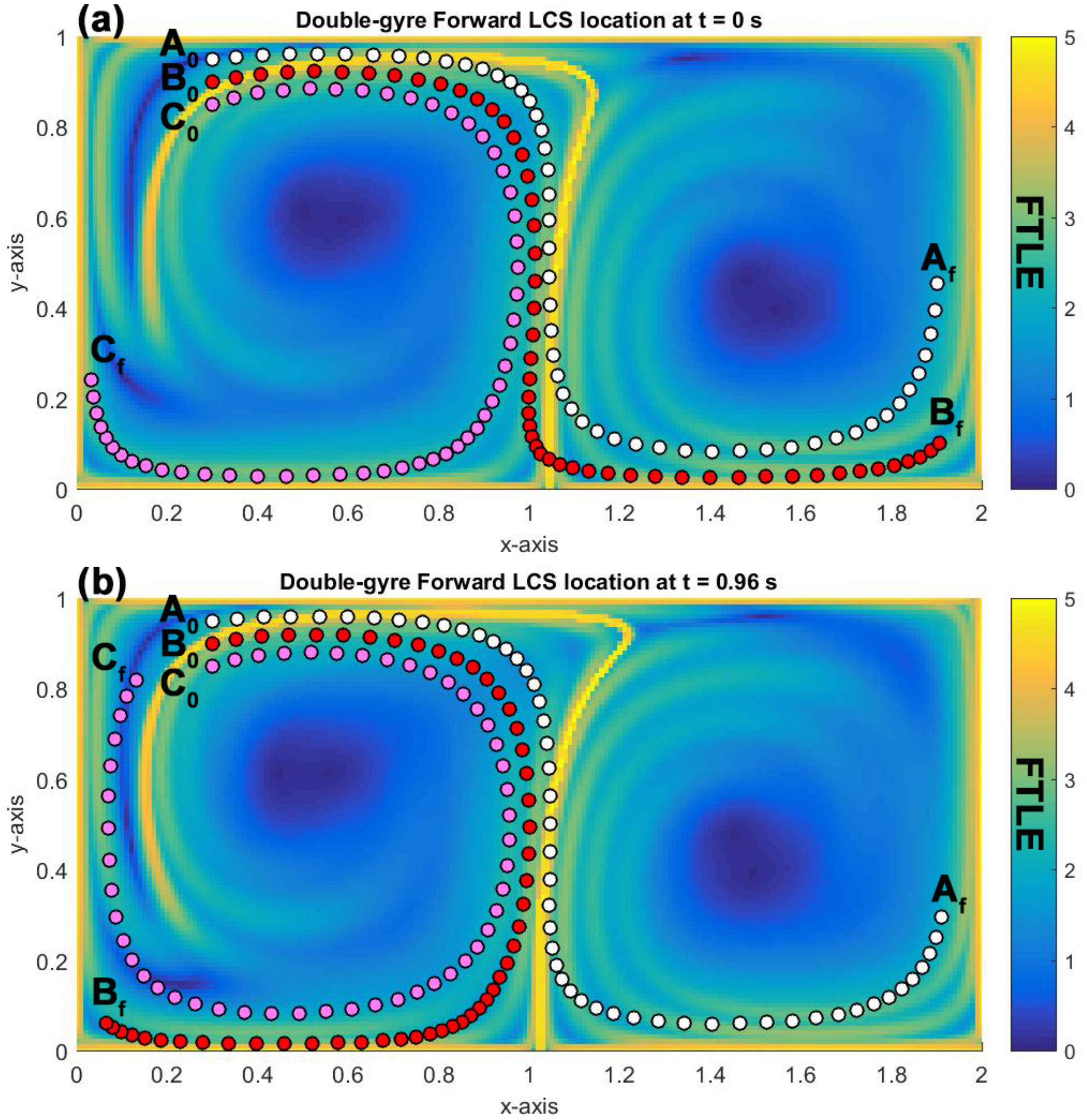

Figure 3.3. FTLE maps for time-varying double-gyre field at (a) $t_0 = 0$ s, (b) $t_0 = 0.96$ s with integration time $\tau = 1$ s. The color scale in each map represents the FTLE value ranging from 0 to 5 s^{-1}. The three tracers' initial positions are labeled as A_0 and A_f (white), B_0 and B_f (red), and C_0 and C_f (magenta).

with $\tau = 1$ s. The FTLE values quantify the degree of separation, and the LCS is composed of the locally maximum FTLE values (i.e., the bright yellow curve). The LCS surface indicates the strongest separation of the flow (the most stretching of the fluid element) in the local area. The LCS can be seen running up the center of the domain and curving left toward the top. This is a snapshot of the LCS at time t_0.

In a time-varying flow field, the LCS itself advects over time. The FTLE maps of double-gyre flow for different initial times over the interval $t_0 = [0\text{ s}, 0.98\text{ s}]$ with an integration time $\tau = 1$ s are shown in Appendix A.

Figure 3.3(a) also shows the location of three tracer particles in the double-gyre and their movement over time. There are three equally spaced tracer particles on the plot initially at A_0, B_0, and C_0. Tracers A_0 and B_0 are on the same side of the LCS, while tracers B_0 and C_0 are on opposite sides of the structure. Subsequent locations of the particles are shown for later epochs $t_0 + i\Delta t$ during the integration time. The end locations of particles A and B are A_f and B_f, both to right half of the domain, while particle C_f ends up in the left half domain. The particles B_0, C_0 initially straddling the LCS have a larger separation distance $\overline{B_f C_f}$ between their end locations, and thus show a stronger stretching than tracers A and B which began on the same side of the LCS.

In addition, the LCS for a different start time and time interval has different initial conditions so is not the same LCS [24]. Figure 3.3(b) shows the LCS of the double gyre for initial time $t_0 = 0.96$ s, $\tau = 1$ s. The shape of the structure can be seen running up the center of the domain and curving right toward the top. Because the flow map yields a different LCS for $t_0 = 0.96$ s than for $t_0 = 0$ s, the particles starting at identical initial locations A_0, B_0, and C_0 to Figure 3.3(a), but at a different moment in time, undergo different stretching. Here the particles starting at A_0 and B_0 end up further apart than B_0 and C_0 do.

In Figure 3.3(a) and Figure 3.3(b), each FTLE map is a snapshot of the LCSs at an instant t_0 while the tracers are plotted at regular intervals within $t = [t_0, t_0 + \tau]$. For this reason tracer trajectories appear to cross the LCS ridges.

The location and shape of the LCSs and the FTLE values in Figure 3.3 are

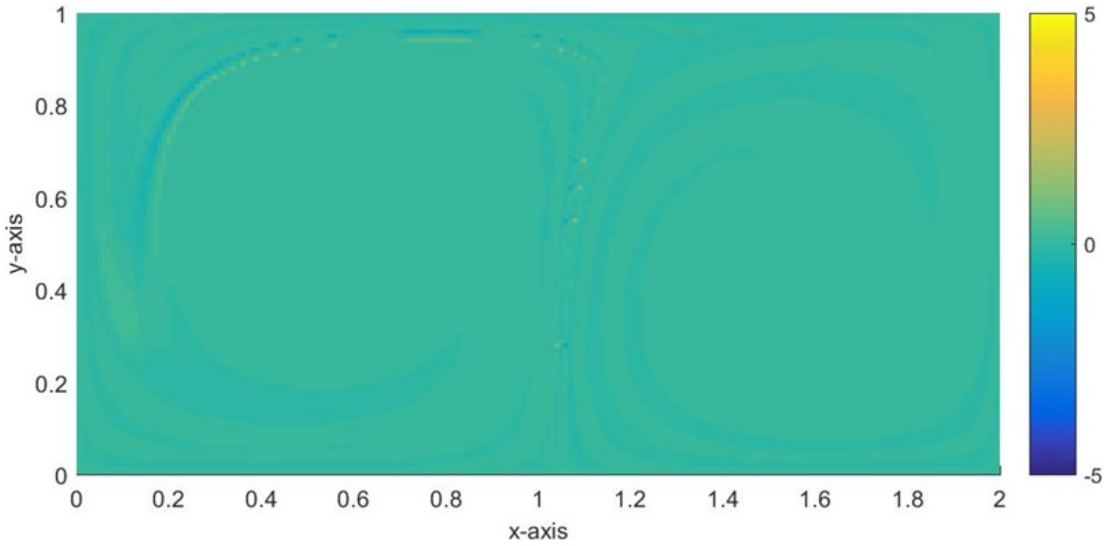

Figure 3.4. The differential map of FTLE values for the time-varying double-gyre flow field computed by ITALCS vs. FlowVC, for an initial time of $t_0 = 0$ s and an integration time of $\tau = 1$ s.

virtually identical to those shown in [55]. A plot differencing the ITALCS FTLE map and FlowVC map is shown in Figure 3.4. The non-zero points in the FTLE map are due to the interpolation method. FlowVC uses the Runge-Kutta 4th order interpolation method while ITALCS uses bi-linear interpolation.

A flowmap and therefore its Jacobian is a function of initial time and also of integration time. By increasing the integration time τ, the FTLE map may change by making the LCS more sharply defined. Figure 3.5 shows the FTLE map of the double-gyre flow with $t_0 = 0$ s and the integration time $\tau = 2$ s. The color scale is [0, 2.5]. As shown in Eq. 2.8, the FTLE value is normalized by τ, so the FTLE values for $\tau = 2$ s are smaller than the FTLE values with $\tau = 1$ s, shown in Figure 3.3. In this figure, the LCSs are running up the center of the FTLE map from bottom to the top and curving leftward on the top. There are also some substructures appearing as locally maximum LCS ridges in the center of each cell. As the integration time increases, the FTLE map becomes more structured and more LCSs appear.

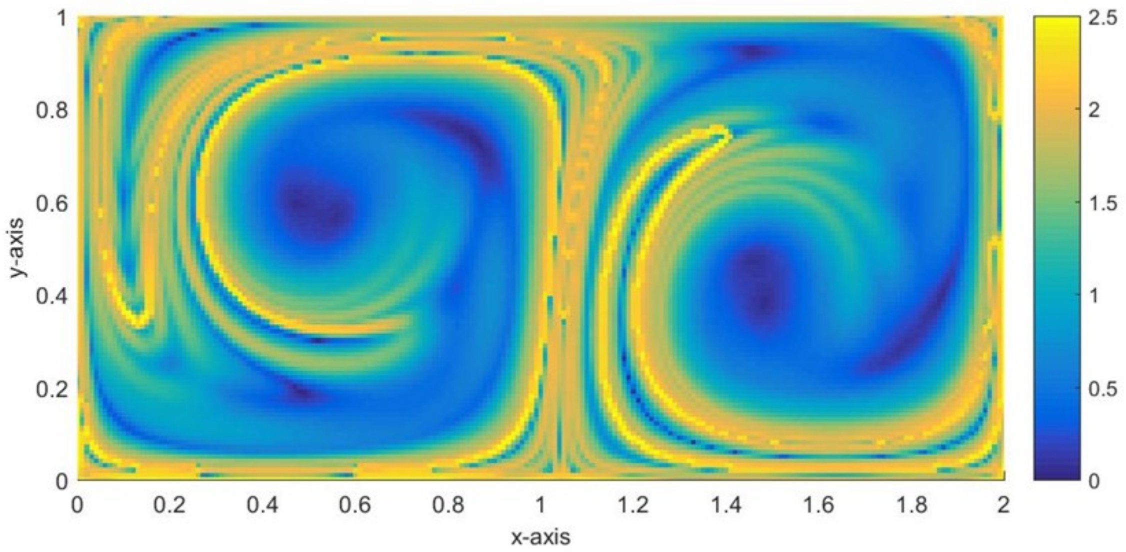

Figure 3.5. FTLE map for time-varying double-gyre field at $t_0 = 0$ s with the integration time $\tau = 2$ s. The color scale in each map represents the FTLE value ranging from 0 to 2.5 s^{-1}.

3.2 Application to the Earth's atmosphere

To identify the LCS in a spherical domain such as the ionosphere, I search globally to ensure a closed domain. For a given altitude, I mesh the domain for the generalized coordinates $x^1 = \phi$, $x^2 = \lambda$ where ϕ and λ are geographic longitude and latitude, respectively. In this case, the density of the gridpoints is higher at higher latitudes.

3.2.1 Velocity transformation. For most of the ionospheric-thermospheric (IT) models, the velocity of each gridpoint will be described as a linear velocity, but the LCS grid is parameterized by angles $(x^1 = \phi, x^2 = \lambda)$. For these reasons, the velocity is transformed to angular rates $\dot{\phi}$, $\dot{\lambda}$ as described below.

Figure 3.6 shows a diagram of the relevant frames and coordinate systems on a sphere of radius r. The earth-centered earth-fixed (ECEF) frame E has coordinates $\hat{e}_1, \hat{e}_2, \hat{e}_3$ and origin O. A Lagrangian frame L is at point P and moves with a particle that is at point P at time t. The L frame's coordinates $\hat{l}_1, \hat{l}_2, \hat{l}_3$ are locally up-east-

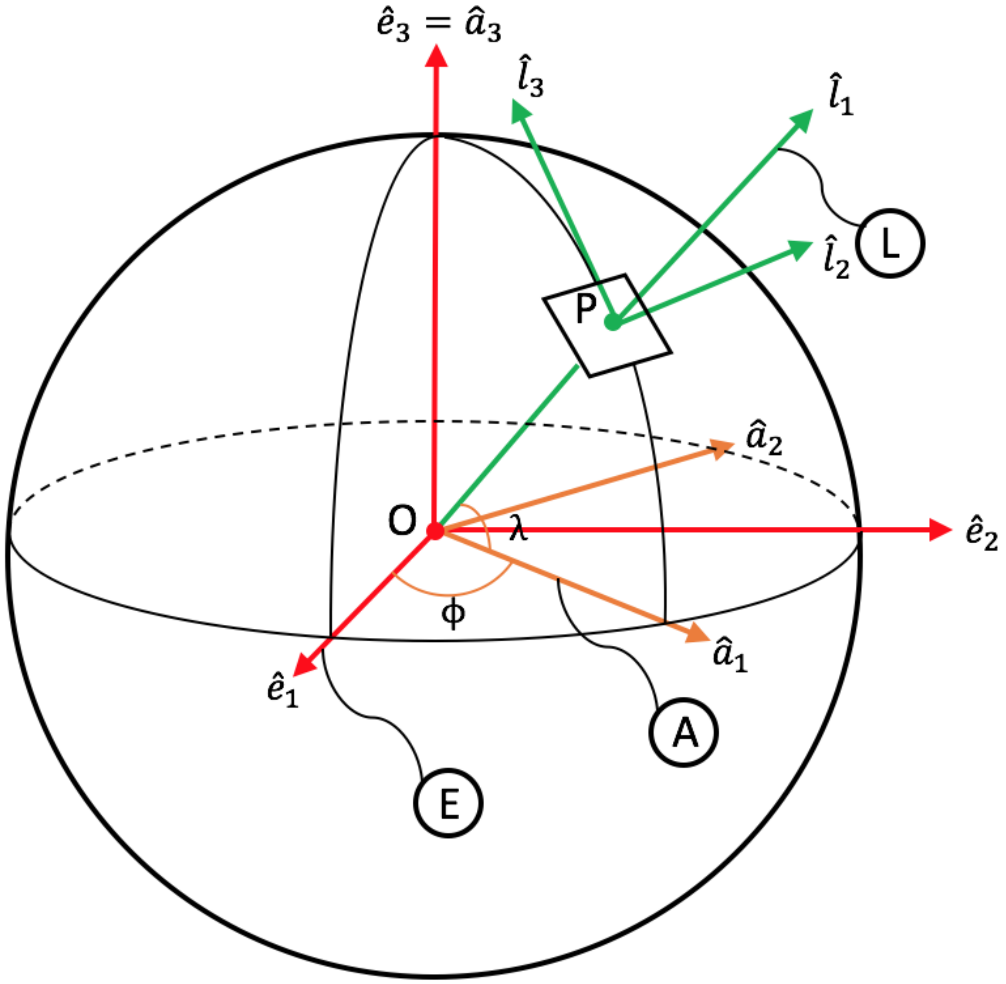

Figure 3.6. Relation of earth-centered earth-fixed (ECEF) frame and Lagrangian frame

north, respectively. The angles $\phi = \phi_0 + \Delta\phi$, $\lambda = \lambda_0 + \Delta\lambda$ are the longitude and latitude of a particle at point P with $\Delta\phi_0 = \Delta\lambda_0 = 0$ at time t_0 and ϕ_0 and λ_0 are constant. The position of particle P from O is:

$$\vec{r}^P = r\hat{l}_1 \tag{3.11}$$

where $r = R_E + h$, a summation of the mean radius of Earth (R_E) and the height h of a certain atmospheric layer is constant. Kinematically, the velocity of particle P

in the ECEF frame is the time derivative of $\vec{r}^P$:

$$\begin{aligned} {}^E\vec{v}^P &= \frac{{}^E d\vec{r}^P}{dt} && (3.12) \\ &= \frac{{}^L d\vec{r}^P}{dt} + {}^E\vec{\omega}^L \times \vec{r}^P && (3.13) \end{aligned}$$

where the pre-superscript indicates the observer's frame. The time derivative of $\vec{r}^P$ as seen in the L frame differs from that seen in the E frame due to the angular velocity ${}^E\vec{\omega}^L$ that observer E sees the L frame having. Because the position $\vec{r}^P$ is constant in the L frame, $\frac{{}^L d\vec{r}^P}{dt} = 0$, so the first term in Eq. (3.13) vanishes, leaving:

$$ {}^E\vec{v}^P = {}^E\vec{\omega}^L \times \vec{r}^P \tag{3.14}$$

There are two rotations between the E and L frames. The first rotation is from the E frame to an intermediate frame A about the $\hat{e}_3$ axis with the rate $\dot{\phi}$. The second rotation is from frame A to frame L about the $-\hat{l}_2$ axis with the rate $\dot{\lambda}$, which gives:

$$\begin{aligned} {}^E\vec{\omega}^L &= {}^E\vec{\omega}^A + {}^A\vec{\omega}^L && (3.15) \\ &= \dot{\phi}\hat{a}_3 - \dot{\lambda}\hat{l}_2 && (3.16) \\ &= \dot{\phi}\left(\cos\lambda\hat{l}_3 + \sin\lambda\hat{l}_1\right) - \dot{\lambda}\hat{l}_2 && (3.17) \end{aligned}$$

Substitute Eqs. (3.17) and (3.11) into Eq. (3.14)

$$ {}^E\vec{v}^P = \dot{\phi}r\cos\lambda\hat{l}_2 + \dot{\lambda}r\hat{l}_3 \tag{3.18}$$

The horizontal velocity of the particle at point P as seen in the ECEF frame is provided as

$$ {}^E\vec{v}^P = v_e\hat{l}_2 + v_n\hat{l}_3 \tag{3.19}$$

where v_e and v_n are the eastward and northward components, respectively. Comparing Eq. (3.18) with Eq. (3.19) then I have

$$\begin{aligned} \dot{\phi} &= \frac{v_e}{r\cos\lambda} && (3.20) \\ \dot{\lambda} &= \frac{v_n}{r} && (3.21) \end{aligned}$$

Eqs. (3.20) and (3.21) form the velocity field that are time-integrated in ITALCS to search for LCSs globally.

3.2.2 Enforcing a closed domain.

Since the spherical domain mesh is over longitude and latitude, the closed non-Euclidean domain is periodic in both longitude and latitude. This periodicity requires additional logic in ITALCS to keep particles within a longitudinal domain of $(\phi_{min}, \phi_{max}) = (-180°, 180°)$ and latitude domain of $(\lambda_{min}, \lambda_{max}) = (-90°, 90°)$. To convert the longitude and latitude of gridpoints flowing "beyond" the boundaries to their locations within the domain, the coordinates need to be wrapped around back into the domain. Figure 3.7 shows three map projections of the global domain meshed by longitude ϕ and latitude λ.

Figure 3.7(a) illustrates the boundary problem caused by the longitude limit on an azimuthal orthographic projection of the world with $\phi = \pm 180°$ as the central meridian. When a particle $P_{(lon)i}$ travels westward across the longitude line $\phi = -180°$, it should arrive at $P_{(lon)i+1}$. However, given the regularly gridded configuration space (ϕ, λ), the particle $P_{(lon)i}$, located at time t_i, traveling westward across the west boundary $\phi = -180°$, will exit the domain stopping at $P'_{(lon)i+1}$ as shown in Figure 3.7(c). In order to ensure the domain remains closed, the missing point must be brought back to its equivalent location within the domain to $P_{(lon)i+1}$. As shown in Figure 3.7(c), when the particle $P_{(lon)i}$ runs out of the left-most boundary, it will return from the right-most boundary, and vice versa. Based on this, $\vec{r}^{P_{lon}} = (\phi_{P_{lon}}, \lambda_{P_{lon}})$ can be updated as:

$$\lambda_{P_{lon}} = \lambda'_{P_{lon}} \tag{3.22}$$

$$\phi_{P_{lon}} = ((\phi'_{P_{lon}} - \phi_{min}) \mod (\phi_{max} - \phi_{min})) + \phi_{min} \tag{3.23}$$

where $\phi_{max} = 180°, \phi_{min} = -180°$. This logic works for windings of more than 360°. After updating the coordinate, particle P will remain within the longitudinal domain.

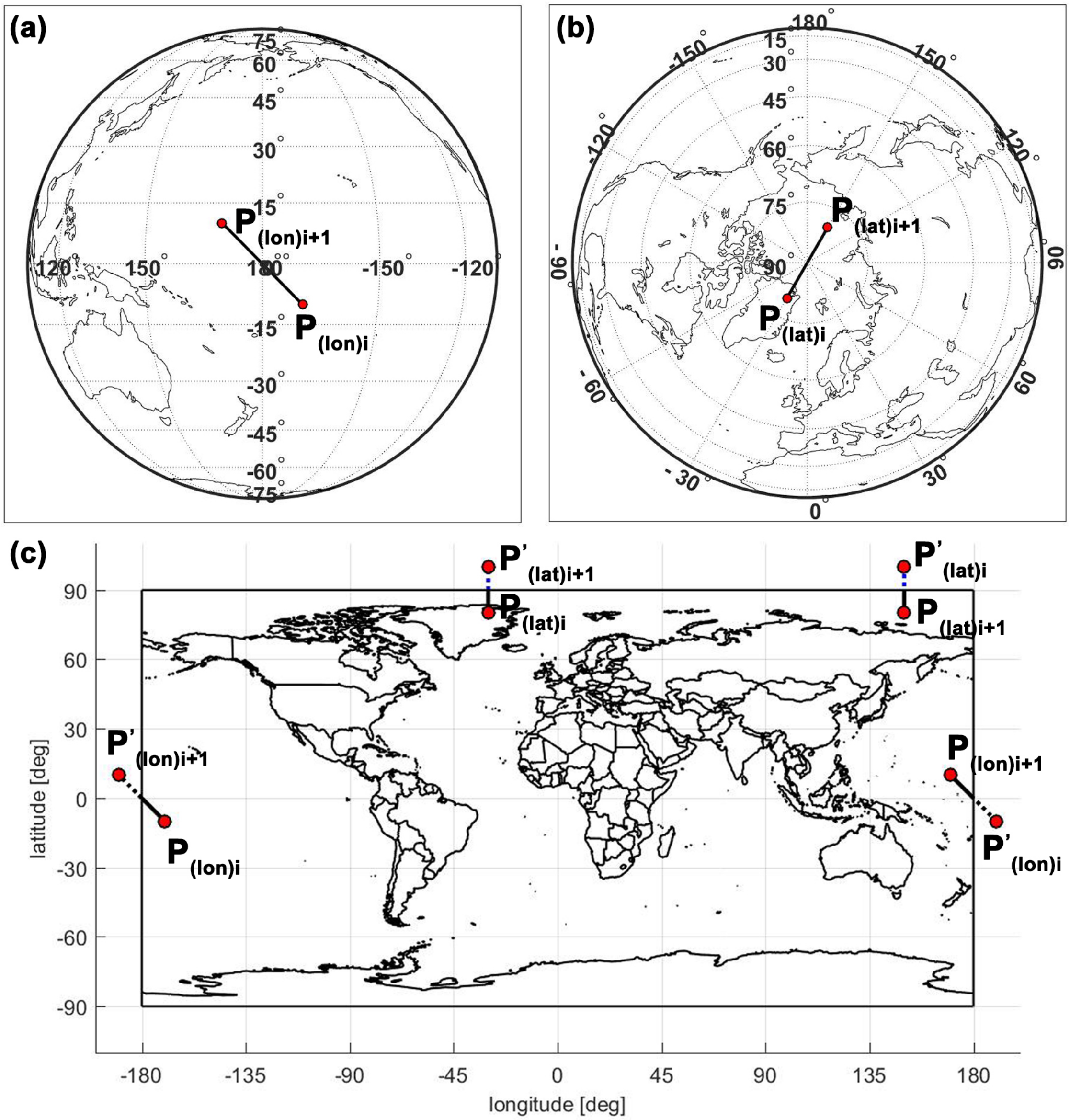

Figure 3.7. (a) Longitude boundary-crossing illustration: general perspective projection viewed of the world with $\phi = \pm 180^\circ$ as the central meridian. (b) Latitude boundary-crossing illustration: general perspective projection viewed of the world from north pole. (c) Geographic projection, which corresponds to a regular spacing of the generalized coordinates ϕ, λ.

Figures 3.7(b) and 3.7(c) show the boundary problem caused by the latitude limit. Figure 3.7(b) shows a general perspective projection view of the north pole. As shown in Figure 3.7(b), when the particle $P_{(lat)i}$ travels across the north pole, it must end at $P_{(lat)i+1}$ and remain in the domain. However, the single north pole point corresponds to the entire top boundary of the domain as shown in Figure 3.7(c). For particle $P_{(lat)i}$ to travel across the north pole it must go due north to cross the $\lambda = 90°$ boundary. In order to keep the domain closed, the position of $\vec{r}^{P}_{lat} = (\phi_{P_{lat}}, \lambda_{P_{lat}})$ needs to be updated as:

$$a = \left\lfloor \frac{\lambda'_{P_{lat}} - \lambda_{min}}{\lambda_{max} - \lambda_{min}} \right\rfloor \tag{3.24}$$

$$\lambda_{P_{lat}} = 180(a \mod 2) + (-1)^a(\lambda'_{p_{lat}} \mod 360) \tag{3.25}$$

$$\phi_{P_{lat}} = \phi'_{P_{lat}} - \operatorname{sgn} \phi'_{P_{lat}}(180)(a \mod 2) \tag{3.26}$$

where $\lambda_{max} = 90°, \lambda_{min} = -90°$, and the symbol $\lfloor \rfloor$ represents the floor operation. These expressions are generalizations of the $|\lambda| < 180°$ case, for which λ is changed to the supplementary angle, and ϕ is shifted by 180°. Both latitude and longitude domain crossings are generalized because velocities near the poles can become near-singular and could produce ϕ, λ more than one winding beyond the domain. These boundary crossings are checked and updated at each step dt of integration.

3.2.3 Enforcing the shorter distance. After meshing the spherical domain over a longitude span of $(\phi_{min}, \phi_{max}) = (-180°, 180°)$ and latitudes of $(\lambda_{min}, \lambda_{max}) = (-90°, 90°)$, in a closed domain, the maximal longitudinal distance for two points is 180° which requires additional logic in ITALCS.

For a pair of arbitrary points $A(\phi_A, \lambda_A)$ and $B(\phi_B, \lambda_B)$, the longitudinal distance between A and B is

$$\Delta\phi' = |\phi_A - \phi_B| \tag{3.27}$$

When $\Delta\phi'$ is larger than 180°, ITALCS will automatically update the longitudinal distance as

$$\Delta\phi = 360° - \Delta\phi' \tag{3.28}$$

In this case, there is no such restriction on the latitudinal distance.

3.3 Summary

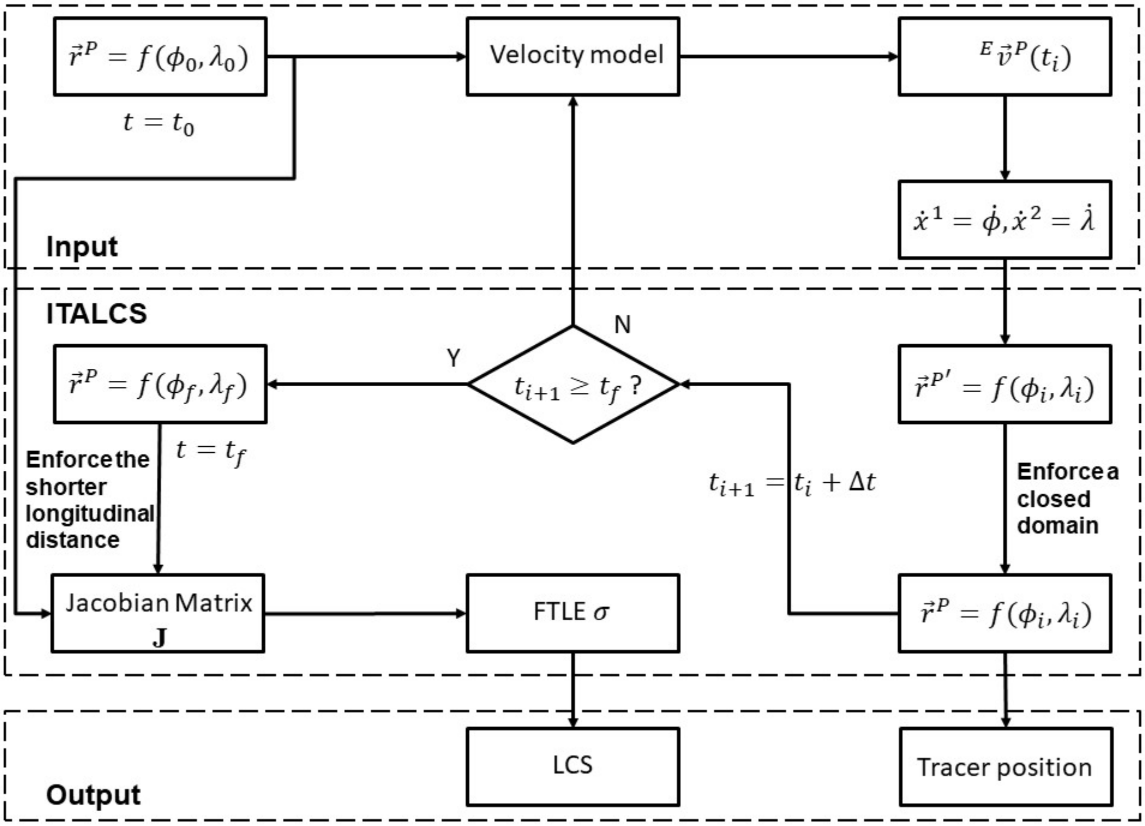

Figure 3.8. Process for tracing the position of particle P on Earth's atmosphere over time and computing the finite-time Lyapunov exponent (FTLE) to identify the Lagrangian coherent structures (LCSs) in the flow.

Figure 3.8 is the workflow for using ITALCS to compute the final position $\vec{r}^P$ at time t_f and associated FTLE σ of a particle P in a flow initialized at a gridpoint (ϕ_0, λ_0). A particle P's velocity ${}^E\vec{v}^P$ in an Earth-fixed frame (indicated by the pre-superscript "E"), is output from a velocity model for a given $\vec{r}^P$. This velocity (v_e, v_n) is expressed in east-north coordinates local to each point, and transformed to angular rates $\dot{\phi}, \dot{\lambda}$ as described in Section 3.2.1. ITALCS updates the coordinates of the particle according to Eq. (3.2) to be (ϕ_i, λ_i) at time $t_{i+1} = t_i + \Delta t$, wrapping the longitude and latitude back into the domain $\phi = [-180°, 180°], \lambda = [-90°, 90°]$

if needed, as described in Section 3.2.2. At the next epoch, the velocity field is generated at the gridpoints with the velocity model and bilinearly interpolated to the particle's current location (ϕ_i, λ_i). Tracing the particle until time t_f gives the final position (ϕ_f, λ_f) of particle P, after which the FTLE can be computed with Eq. (2.8). Repeating this process for every initial gridpoint in the domain I generate the FTLEs for the whole domain as output as well as output individual tracer locations if desired.

CHAPTER 4

THERMOSPHERIC LCSS

4.1 Overview

In this chapter, I test: 1) whether modeled thermospheric winds yield LCSs globally, 2) whether the LCSs vary with altitude, 3) whether the LCSs respond to geomagnetic activity, and 4) whether the structures bound material transport. In this work, the thermosphere is regarded as a two-dimensional flow field, in which vertical velocities are negligible. For the lower thermosphere, Kelley et al. [34] hypothesize this could be possible through the existence of magnetized Rossby waves (meanders in flow due to the Coriolis effect). Even with significant upwelling or downwelling, e.g., during a storm, the time scale for the vertical transport is expected to be longer than the time scale for the horizontal transport, so for the two-day integration conducted in this work I may reasonably assume horizontal transport only.

The Horizontal Wind Model 2014 (HWM14) is used to generate the local ground speed of the winds at each gridpoint. Although the uncertainties for any individual storm may be higher since HWM14 is an empirical fit, it is sufficient to test whether LCSs exist and change with activity. The output from HWM14 is ground speed v_e and v_n (in m/s) at a geographic longitude and latitude (ϕ, λ) for a given altitude and time. This velocity (v_e, v_n) is expressed in east-north coordinates local to each point, and transformed to angular rates $\dot{\phi}, \dot{\lambda}$ as described in Section 3.2.1. This velocity field is used as the input of ITALCS to do the FTLE computation and locate the thermospheric LCSs.

4.2 Simulation Configuration

To do these tests, I simulate the thermospheric winds at altitudes of 150, 250, and 350 km and provide them as inputs to ITALCS to compute the FTLE scalar fields. Since the domain over which I search for thermospheric LCSs is global in extent, the domain is parameterized by longitude and latitude, and a particle assumed at each grid point at time t_0. I generate wind fields at the gridpoints every $\Delta t = 3600$ s, with $dt = 20$ s. For the first three studies, I use the K_p index [4] to select a geomagnetically quiet day and storm day.

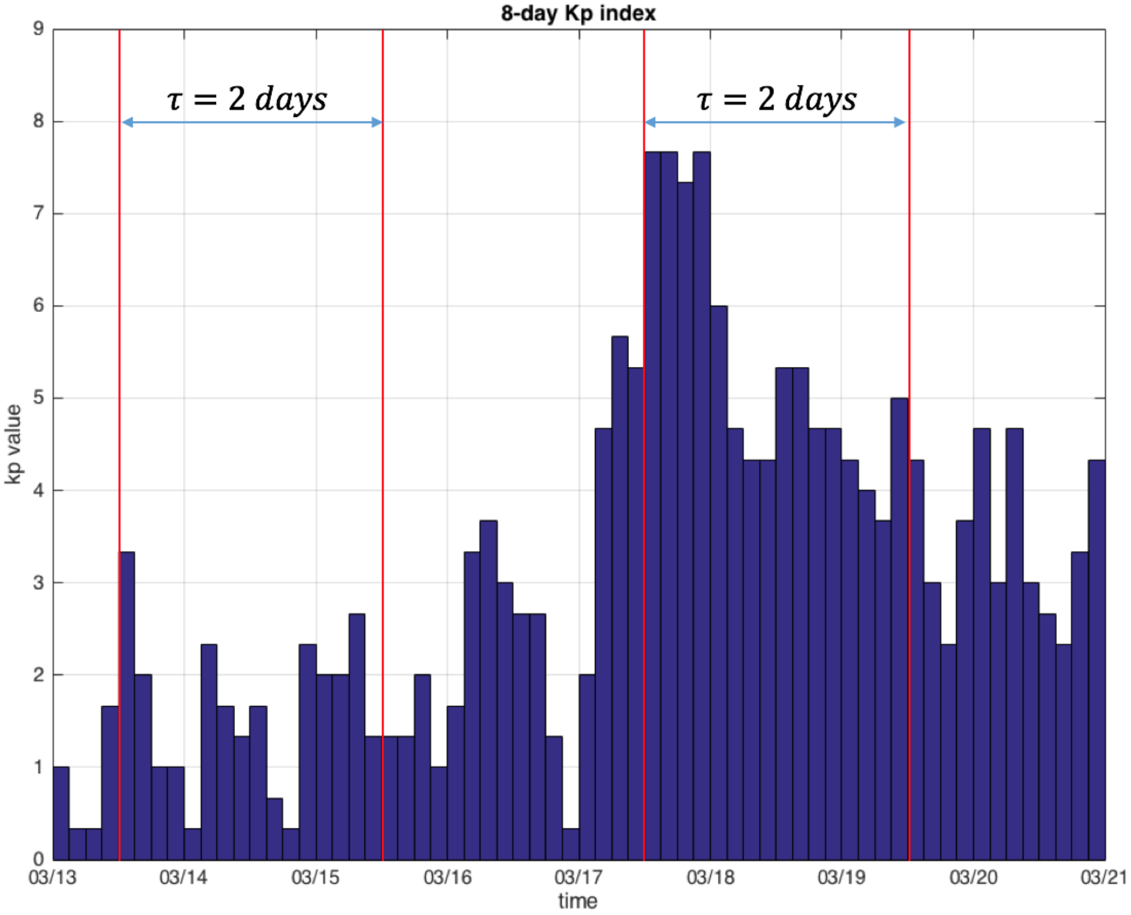

Figure 4.1. K_p index values from 13 to 20 March 2015. Two-day intervals for which LCSs are found are marked at 13 March at 12:00 UT (geomagnetically quiet) and 17 March at 12:00 UT (active).

Figure 4.1 plots the K_p index for 13-20 March 2015. To investigate whether LCSs respond to geomagnetic activity, I select t_0 =12:00 UT on 13 March 2015 for the quiet time LCS analysis and t_0 =12:00 UT on 17 March 2015 for the active period. The figure also shows that the storm effects last for at least two days, so the integration time $\tau = 2$ days. Choosing intervals within a week of each other ensures similar season and solar cycle conditions.

This chapter is organized as follows: an initial study of 13 March 2015 at 150 km shows the modeled winds fields yield the thermospheric LCSs discussed in Section 4.3. A comparison of the FTLE values at different altitudes, h = 150, 250, 350 km during the geomagnetically quiet period, shows how the structuring differs between the lower and upper thermosphere, shown in Section 4.4. A comparison of the simulated results between a geomagnetically quiet day and a geomagnetically stormy day demonstrates the sensitivity of the structures to the geomagnetic activity, discussed in Section 4.5. A simulation of the flow field during the space shuttle launch on 8 July 2011, which had geomagnetically quiet conditions with $K_p \leq 4$, and its associated LCSs are compared to documented observations [62] shown in Figure 1.1 to illustrate how LCSs act as barriers to material transport, discussed in Section 4.6, and are followed by a summary in Section 4.7.

4.3 Global thermospheric LCSs during geomagnetic quiet period

Figure 4.2 is a world map of FTLE values for the geomagnetically quiet period at 150 km height. The contour lines of the continent are marked with thin white lines. In this map, each pixel represents the FTLE value, and the color bar shows that the FTLE value ranges from 0 (blue) to 3×10^{-5} s^{-1} (yellow). In Figure 4.2, a bright yellow ridge is a maximally repelling LCS, i.e., a barrier in material transport. The maximum FTLE is $\sigma \sim 3 \times 10^{-5}$ s^{-1}. This value is much smaller than that of the double-gyre tested earlier, but this is simply due to the normalization. The relative value of the FTLE matters compared to other regions in the domain more than its absolute value. The FTLE map shows that the LCSs appear in the northern middle

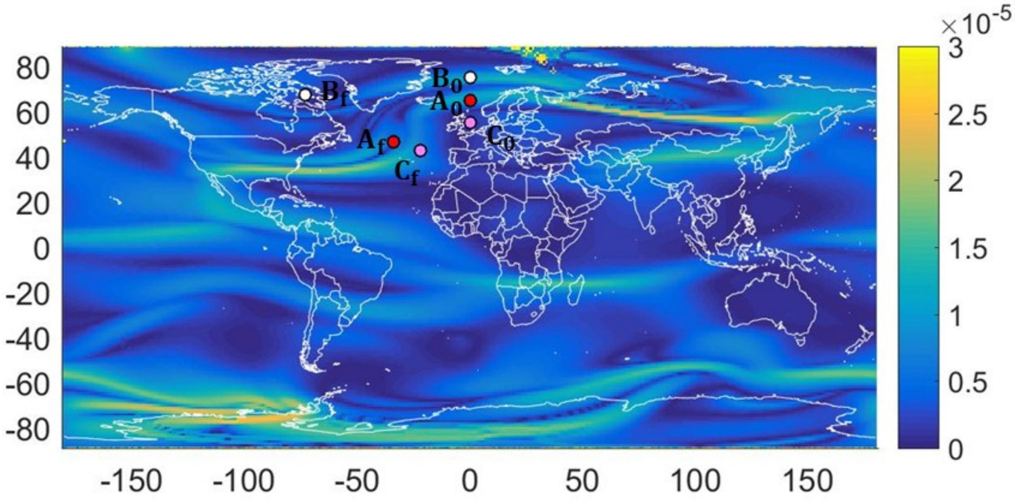

Figure 4.2. Global FTLE map for neutral winds at 150 km with $t_0 = 13$ March 2015 at 12:00 UT and $\tau = 2$ days. The color scale represents the FTLE value ranging from 0 to $3 \times 10^{-5}\ s^{-1}$.

to high latitudes and in the southern hemisphere high latitudes. There are three tracers initially equally spaced in latitude on the local noon longitude: A_0 in red at 65° N, B_0 in white at 75° N, and C_0 in magenta at 55° N . These locations are chosen to illustrate the effect of LCSs lying between the particles. Their final positions are A_f, B_f, and C_f. The tracers' initial and final positions are labeled in Figure 4.2, and their intermediate locations are labeled in Figure 4.3, which is a map viewed from north pole. Figure 4.3 shows the trajectories of the tracers, with thick a red line for A, thick black line for B, and thick magenta line for C. The continents are outlined by the thin black lines. The tracer positions in Figure 4.3 indicate that, over two days, particle A has a change in position of $(\Delta\phi, \Delta\lambda) = (40°W, 15°S)$ and C has

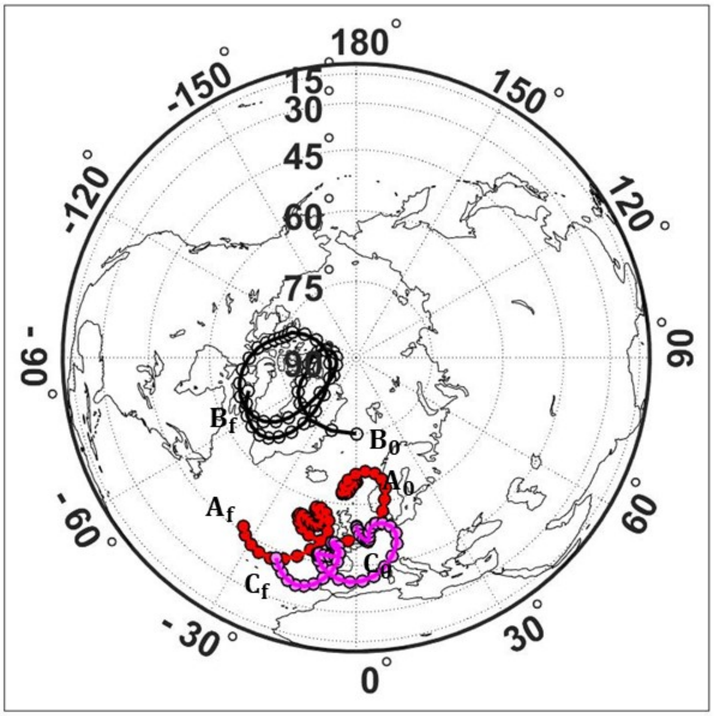

Figure 4.3. North pole view of tracer locations from t_0 to $t_0 + \tau$ for neutral winds at 150 km with $t_0 = $ 13 March 2015 at 12:00 UT and $\tau = 2$ days.

$(\Delta\phi, \Delta\lambda) = (30°W, 5°S)$. In contrast, particle B shifts by $(\Delta\phi, \Delta\lambda) = (70°W, 10°S)$ from its initial position. There is a local maximum FTLE structure between A and B (Figure 4.2, light blue) indicating a weakly repelling LCS. With equal separations at the initial positions of the three tracers, the final distance $\overline{A_f C_f}$ is smaller than $\overline{A_f B_f}$, which corresponds to the FTLE values between them. Since 150 km is a lower layer of thermosphere, there are higher densities, more collisions, and generally lower speeds which lead to less distance traveled and lower FTLEs than higher altitudes, as I will show next.

4.4 Global thermospheric LCSs at different altitudes

Figure 4.4 is a world map of FTLE values for the geomagnetically quiet period

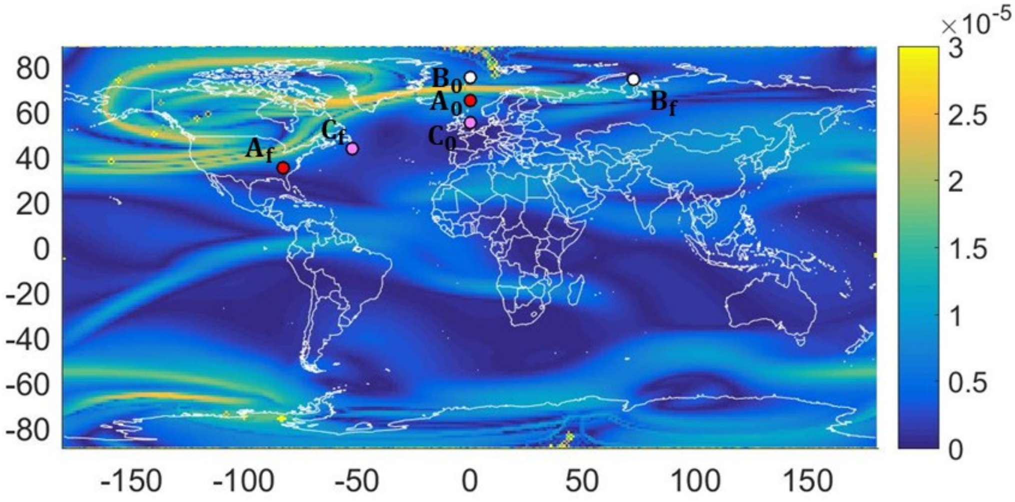

Figure 4.4. Global FTLE map for neutral winds at 250 km with $t_0 = 13$ March 2015 at 12:00 UT and $\tau = 2$ days. The color scale represents the FTLE value ranging from 0 to $3 \times 10^{-5}\ s^{-1}$.

at 250 km height. Each pixel color represents the FTLE values, and the color scale is same as that in Figure 4.2 ranging from 0 (blue) to $3 \times 10^{-5}\ s^{-1}$ (yellow). There are three tracers initially equally spaced in latitude on the local noon longitude: A_0 in red at 65° N, B_0 in white at 75° N, and C_0 in magenta at 55° N . These locations are identical to the tracers in Figure 4.2, and are chosen to illustrate the effect of LCSs lying between the particles. Their final positions are A_f, B_f, and C_f.

At the higher altitude of 250 km, more strongly repelling LCSs (bright yellow) appear in the middle to high latitudes in both hemispheres. The LCSs are located in the local morning sector. An LCS running approximately east-west at 70° N separates B_0 from A_0 and C_0. Despite equal initial separation distances, the final distance $\overline{A_f B_f}$

is larger than $\overline{A_f C_f}$. The trajectories of particles A, B, and C indicate a repulsive tendency between A_0 and B_0 (in contrast to the A_0 and C_0 pair), which is precisely what the LCS ridge between particles A_0 and B_0 identifies.

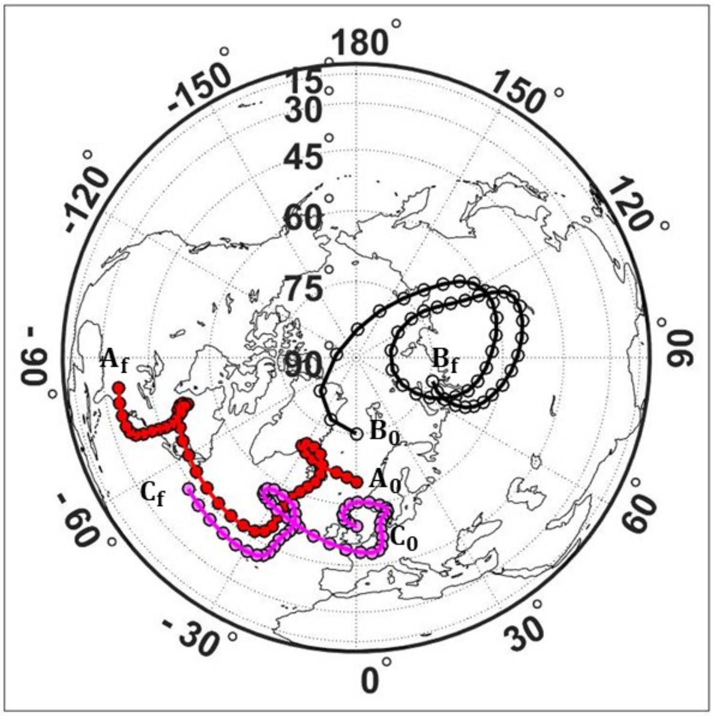

Figure 4.5. North pole view of tracer locations from t_0 to $t_0 + \tau$ for neutral winds at 250 km with $t_0 = 13$ March 2015 at 12:00 UT and $\tau = 2$ days.

Figure 4.5 is a map viewed from geographic north pole showing the trajectories of the tracers, with thick a red line for A, thick black line for B, and thick magenta line for C. The continents are outlined by the thin black lines. The tracer's initial and final positions are labeled, and their intermediate locations are shown by dots with the corresponding color.

The tracer positions in Figure 4.5 indicate that, over two days, particle A has a change in position of $(\Delta\phi, \Delta\lambda) = (85°W, 30°S)$ and C has $(\Delta\phi, \Delta\lambda) = (55°W, 10°S)$.

In contrast, particle B shifts by $(\Delta\phi, \Delta\lambda) = (65°E, 4°N)$ from its initial position. There is a local maximum FTLE structure between A and B (bright yellow) indicating a strongly repelling LCS. With equal separations at the initial positions of the three tracers, the final distance $\overline{A_f C_f}$ is smaller than $\overline{A_f B_f}$, which corresponds to the FTLE values between them.

The trajectories shown in Figure 4.5 illustrate that during the two days, particle A and particle C have similar motion and move southwestward while particle B has a different motion and moves eastward. This phenomenon also reveals that there is an invisible governing structure lying between particle A and particle B to bound the particles' transport which is the repelling LCS.

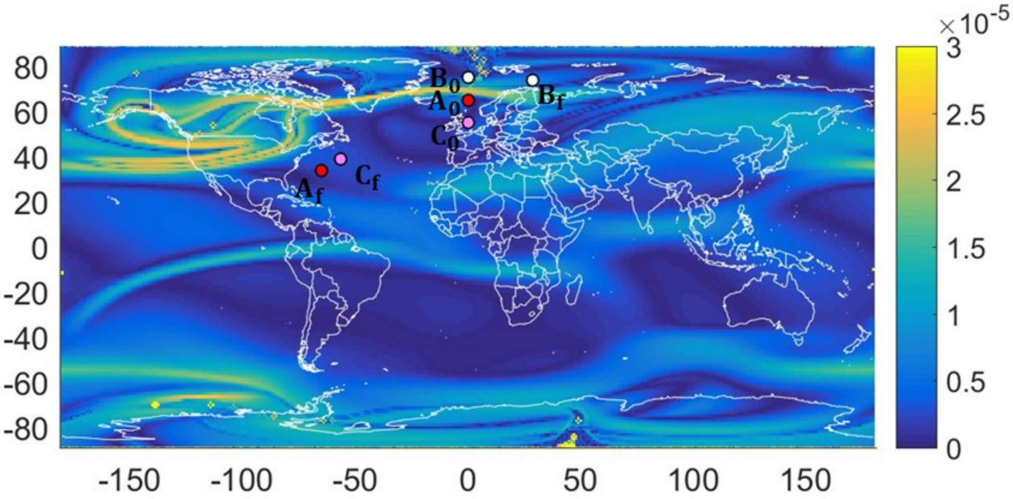

Figure 4.6. Global FTLE map for neutral winds at 350 km with $t_0 = 13$ March 2015 at 12:00 UT and $\tau = 2$ days. The color scale represents the FTLE value ranging from 0 to 3×10^{-5} s^{-1}.

Figure 4.6 is the FTLE map for the quiet period at 350 km height. LCS ridges are again located at middle to high latitudes in the local morning sector. The LCSs at 350 km appear similar to those at 250 km except the curve of the ridge at 250 km that runs east-west at 80° N has shifted equatorward to about 60° N. The tracers' initial positions are identical to those in Figure 4.2 and Figure 4.4. There is also an LCS running approximately east-west at 70° N that separates B_0 from A_0 and C_0. Despite equal initial separation distances, the final distance $\overline{A_f B_f}$ is larger than $\overline{A_f C_f}$. The trajectories of particles A, B, and C indicate a repulsive tendency between A_0 and B_0 (in contrast to the A_0 and C_0 pair), which is precisely what the LCS ridge between particles A_0 and B_0 identifies.

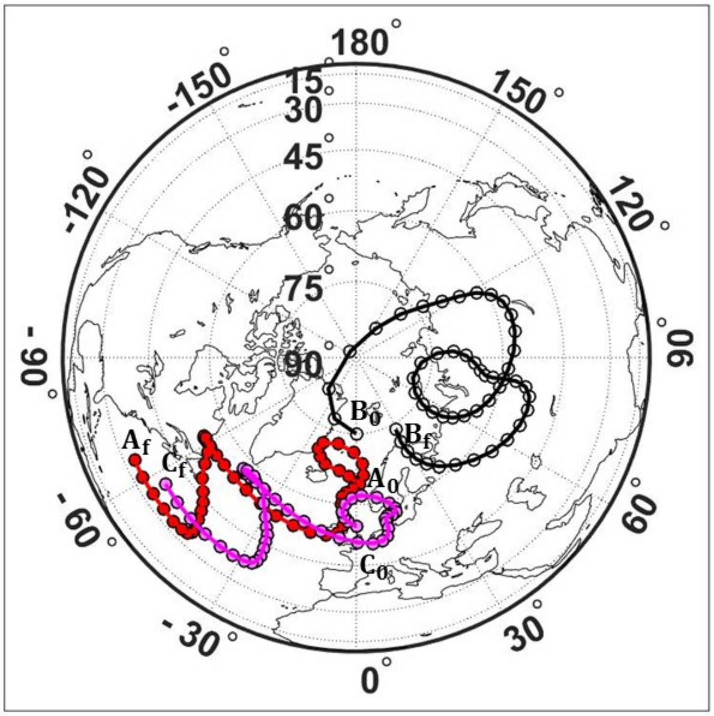

Figure 4.7. North pole view of tracer locations from t_0 to $t_0 + \tau$ for neutral winds at 350 km with t_0 = 13 March 2015 at 12:00 UT and $\tau = 2$ days.

Figure 4.7 shows the tracers' intermediate locations and trajectories. The tracer positions indicate that over two days particle A has a change in position of $(\Delta\phi, \Delta\lambda) = (65°W, 30°S)$ and C has $(\Delta\phi, \Delta\lambda) = (58°W, 20°S)$. In contrast, particle B shifts by $(\Delta\phi, \Delta\lambda) = (30°E, 2°S)$ from its initial position. There is a local maximum FTLE structure between A and B (bright yellow) indicating a strongly repelling LCS. With equal separations at the initial positions of the three tracers, the final distance $\overline{A_f C_f}$ is smaller than $\overline{A_f B_f}$, which corresponds to the FTLE values between them.

Since 250 km and 350 km are higher layer of thermosphere, there are lower densities, fewer collisions, and generally higher speeds which lead to greater distance traveled and thus higher FTLEs than at lower altitudes. Therefore, there are more strongly repelling LCSs (bright yellow) in the middle to high latitudes in both hemispheres at higher altitudes.

4.5 The influence of geomagnetic activity on thermospheric LCSs

I use $h = 250$ km to study the influence of geomagnetic activity on LCSs by comparing to the geomagnetically quiet day at 250 km. This altitude is one at which satellite-based measurements to which HWM14 was fit were made [16].

Figure 4.8 is the LCS map at 250 km for 17 March 2015 at 12:00 UT, the geomagnetically active day. The bright yellow LCSs appear at the middle to high latitudes for both hemispheres. Compared to the quiet day at this altitude (Figure 4.4), the LCSs have more complex topology and extend into local afternoon. In fact, in the northern hemisphere the LCSs appear to form two distinct cells of concentric ridge loops. In Figure 4.9, A_0 and C_0 are initially on the same side of the LCS, while A_0 and B_0 are straddling the LCS. Even though the three tracers have equal initial separations, the final distance $\overline{A_f B_f}$ is greater than $\overline{A_f C_f}$. The trajectories

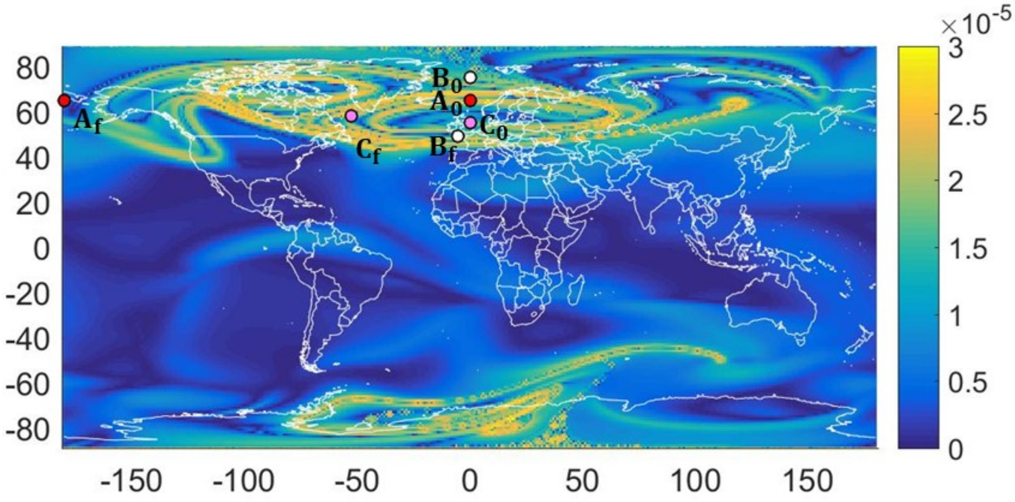

Figure 4.8. Global FTLE map for neutral winds at 250 km with $t_0 = 17$ March 2015 at 12:00 UT and $\tau = 2$ days. The color scale represents the FTLE value ranging from 0 to $3 \times 10^{-5}\ s^{-1}$.

of particles A, B, and C again indicate a repulsive tendency between A_0 and B_0 compared to A_0 and C_0.

The results in Figure 4.2,4.4,4.6, and 4.8 show that LCSs exist in two-dimensional model horizontal flows in the thermosphere. The results for the different altitudes on the quiet day show that the global LCSs are more prominent at $h = 250, 350$ km than in the lower thermosphere. LCS ridges are more prominent at higher latitudes of $40° - 80°$ in the thermosphere; evidence of LCSs at other choices of t_0 support this (shown in Appendix B). The altitudinal variation in the LCSs in Figures 4.2–4.9 is in agreement with studies by Wang et al. [74], in which vertical shears in horizontal winds are not smoothed out by viscosity at high latitudes, as is often assumed.

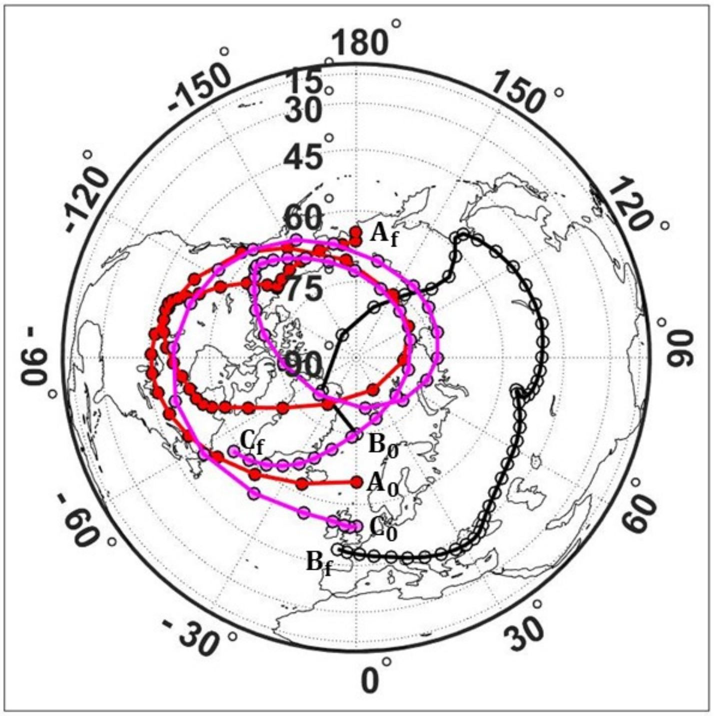

Figure 4.9. North pole view of tracer locations from t_0 to $t_0 + \tau$ for neutral winds at 250 km with t_0 = 17 March 2015 at 12:00 UT and $\tau = 2$ days.

Comparison between the LCSs of the geomagnetically quiet day and active day shows that the LCS ridges in the thermosphere appear to respond to the geomagnetic storm. The neutral wind flow in the northern hemisphere changes significantly during the storm, with the LCSs growing equatorward, sunward, and more complex compared to the quiet day.

4.6 Predictive transport barriers

For the last study, I simulate the thermospheric conditions during the 8 July 2011 space shuttle launch at 100 km, the altitude at which 350 metric tons of water vapor were deposited. This event is chosen because its observations are documented in particular detail, enabling a straightforward comparison of observations to the

LCSs. After identifying the LCS ridge at time t_0 =15:35 UT, the points of the ridge are propagated forward in time for 48 hours. The LCS location is compared to observations of water vapor in the thermosphere reported by Stevens [62]. The geomagnetic conditions for the shuttle plume were quiet, with $K_p \leq 4$ the whole time.

To examine how this LCS barrier mechanism affects transport in the lower thermosphere, I revisit the final space shuttle launch. The shuttle launched from Florida (about 28.5° N) during local morning on 8 July 2011. At 15:35 UT the shuttle deposited 350 t of water vapor at 100-115 km altitude. The approximate shuttle ground track during the period of water vapor deposition is marked with a black line east of Florida in Figure 4.10. Subsequent detections of the water vapor in the thermosphere by the Sub-Millimeter Radiometer (SMR) on the Odin satellite [43] and by ground-based instruments at 54° N and 69° N were reported by Stevens [62].

Figure 4.10 shows the FTLE map and LCS on a color scale from 0 to 1.5 $\times 10^{-5}$ s^{-1} predicted to have existed in the thermosphere for the 8 July 2011 space shuttle plume using HWM14 and ITALCS with initial time t_0 = 15:35 UT on 8 July 2011 and τ = 2 days. In addition, the start and end points of the vapor deposition period are initialized with magenta and white tracer particles, respectively, in the HWM14 flow field simulation. The water vapor is initialized with the background wind velocity. Propagating forward hourly over the two days, the tracers show primarily eastward transport, crossing the Atlantic. These tracer particles do not exhibit the degree of meridional transport apparent in the SMR observations, but they are not expected to do so. HWM14 does not parameterize diffusion or turbulence, posited as possible mechanisms, but rather represents empirically based mean conditions for a given location, time of day, and season.

The black line of crosses highlights the locations of maximum FTLE values

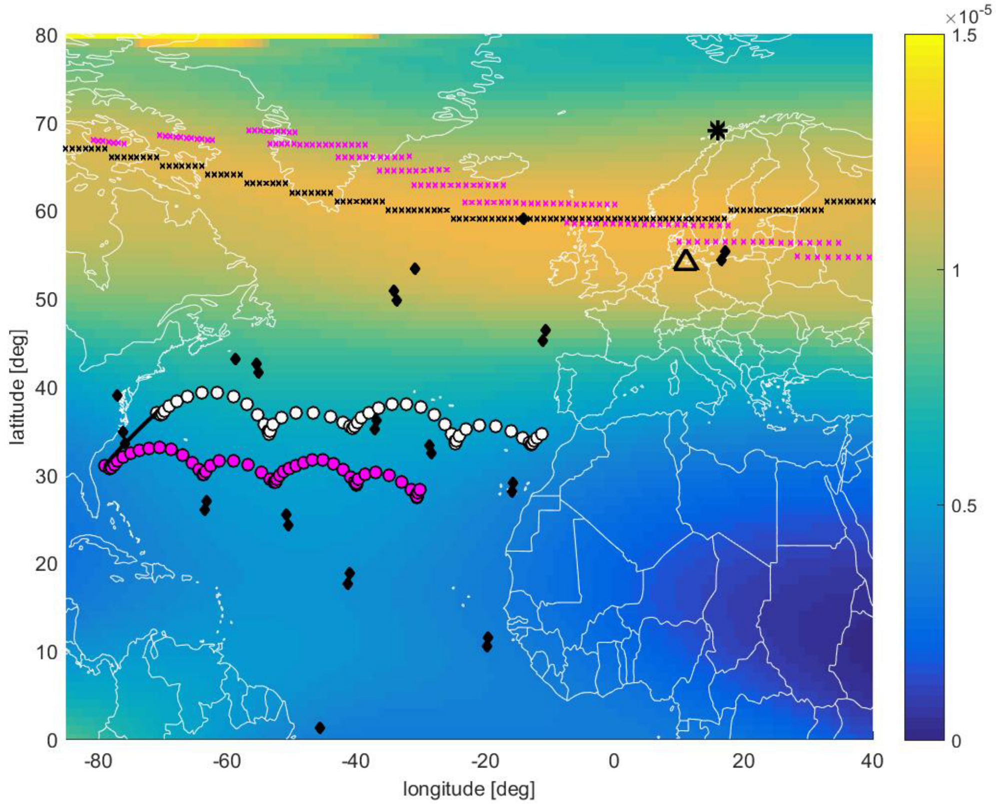

Figure 4.10. FTLE map for space shuttle water vapor plume simulation at 100 km for $t_0 = 8$ July 2011 at 15:35 UT and $\tau = 2$ days. The color scale represents the FTLE value ranging from 0 to 1.5×10^{-5} s^{-1}. The location of the LCS ridge at time t_0 (black crosses) and its corresponding final location at time t_f (magenta crosses) are highlighted. Water vapor observations made by SMR within 2 days of the shuttle plume release [62] are black diamonds. The location of Kühlungsborn is marked 'Δ' and ALOMAR is marked '$*$'. Transport of tracers at the start (magenta circles) and end (white) of the deposition interval is shown.

at each longitude, i.e., the location of the LCS at t_0. The magenta crosses are the corresponding final location of the LCS after propagating its location forward for $\tau =$ 2 days. The result shows that essentially all the observations of water vapor made by SMR in the first 48 hours are located equatorward of the LCS ridge. The LCS is acting as a material wall to bound water vapor transport over time.

The SMR observations are not the only data that Stevens [62] provided as observational evidence of the shuttle plume. The MIcrowave Spectrometer at the

Institute (MISI) of Atmospheric Physics at Kühlungsborn (marked 'Δ' in the figure) is the ground-based upper atmosphere water vapor measurement instrument. It is equatorward of the 2-day LCS at 100 km altitude, so LCS analysis does not preclude water vapor reaching that location.

The Arctic Lidar Observatory for Middle Atmospheric Research (ALOMAR) ground observatory (marked '$*$' in the figure) has both the cWASPAM1 [25] instrument and a Rayleigh-Mie-Raman (RMR) lidar. The cWASPAM1 instrument senses water vapor above 85 km. RMR lidar detects polar mesospheric clouds (PMCs) at 80-85 km.

ALOMAR is poleward of the 2-day LCS at 100 km altitude, and observations of elevated water vapor and PMCs were made there. However, the cWASPAM1 observations at ALOMAR were made more than 2 days after deposition. Even if the observations had been made within the $\tau = 2$ days time interval, the comparison to our LCS found for 100 km altitude would be inconclusive since cWASPAM1 does not resolve the altitude at which it senses water vapor, and LCSs vary with height as seen in Figures 4.2, 4.4, and 4.6. The RMR lidar observations were made within the first 48 hours, but sensed at lower altitudes of ~85 km. Again, the LCS for the 2-D flow at 100 km is not expected to bound transport at 85 km, since there are vertical shears in the horizontal flow. While HWM14 could be used to compute LCSs at 85 km, without a way to anticipate the time at which the vapor initially reaches that altitude and then forward propagate, choosing the appropriate t_0 from which to forward propagate is not possible.

In comparing the LCS to observational data, note that I can only compare to detected events. It is possible that water exists at high latitudes but is undetectable due to a phase change from vapor to ice or the sparsity of sensors. To mitigate against this, I have attempted to compare to an event well-documented by observational evidence, including satellite water vapor observations that extend to high latitudes.

The analyses shown in Figure 4.2-4.9 and 4.10 have implications for other events. In 2003, water vapor exhaust and iron that ablated during a space shuttle launch reached the lower thermosphere. Two to three days later noctilucent clouds appeared and the iron was detected over the Antarctic [64]. From Figure 4.2-4.9, the lack of LCSs at low latitudes means that such transport is not precluded by any LCS barriers. While detections in the Antarctic may have been unusual, with LCS analysis they might not be considered unexpected.

4.7 Summary

LCS ridges for neutral winds in the thermosphere are predicted to exist based on global simulations with an empirical model. For the cases studied, LCSs are more strongly repelling at 250 and 350 km than 150 km, and are at 40°-80° latitudes in the morning sector. During geomagnetic activity the LCSs have more complex structuring and may extend into local afternoon. The strong separation tendency between tracer particles located on different sides of the LCSs illustrate that the LCS location does indicate strong stretching. The LCS is demonstrated to act as a barrier to transport of material in the thermosphere.

The prominence of the LCSs at high latitudes and heights in the thermosphere, and their apparent response to geomagnetic activity, are most likely signatures of energy input and possible interactions with the ionosphere. While the evidence of IT interaction is not new or surprising, the use of LCSs is new. In the space shuttle plume study shown, the LCS served as a barrier ridge poleward of the water vapor observations made in the thermosphere over the 48 hours after launch. In the future, it might be usable as a proxy indicator of charge-neutral collision rate or nitrogen oxides (NO_x) or oxygen transport.

CHAPTER 5

IONOSPHERIC LCSS

5.1 Overview

In the high-latitude upper atmosphere poleward of the auroral oval, the polar cap patch is a few 100-km-scale ionospheric enhancement surrounded by lower-density plasma [13]. Lagrangian coherent structures (LCSs) are barriers to transport in nonlinear time-varying flow fields, found by computing the local maximum finite time Lyapunov exponent (FTLE). I propose that LCSs are barriers governing polar cap patch formation and convection.

To do these studies, I analyze synoptic scale ionospheric LCSs, specifically asking: are there governing structures in the high-latitude ionosphere? Do the structures guide and predict possible patch formation or transport sites? I compute and visualize the LCSs in high-latitude ionospheric convection by computing the FTLE field with the Ionosphere-Thermosphere Algorithm for Lagrangian Coherent Structures (ITALCS), and test (1) whether the LCSs exist at high latitude of the modeled plasma drifts, (2) whether the high latitude ionospheric LCSs respond to geomagnetic activity, and (3) what the LCS indicates about the polar cap patch source plasma region.

5.2 Simulation Configuration

For this analysis, the flow of interest is the plasma drift convection as a flow field at high latitudes in both hemispheres. While in general plasma drift is a superposition of electric Pedersen drift, gravitational Pedersen drift, pure gravitational drift, and parallel mean flow [3, 60], in the high latitude region above 50° geomagnetic latitude, the plasma drift is dominated by $\vec{E} \times \vec{B}$ drift due to the absence of vertical shears [37, 1]. The $\vec{E} \times \vec{B}$ drift is governed by the local electric and magnetic fields:

$$\vec{v}_{E\times B} = \frac{-\vec{\nabla} V \times \vec{B}}{B^2} \tag{5.1}$$

where V is an electrostatic potential function and $\vec{B}$ is the magnetic field. At high latitudes, this $\vec{E} \times \vec{B}$ drift is primarily horizontal and is understood to describe magnetic flux tube transport. For simplification, I treat the high-latitude plasma drift as the $\vec{E} \times \vec{B}$ drift. Such an assumption has also been used in several ionospheric models, such as the Global Theoretical Ionospheric Model (GTIM) which has been used to model polar patches of enhanced F-region plasma density [59, 15] and boundary blobs [2].

I compute the high latitude plasma drifts for a single atmosphere layer with the electric potential simulated with Weimer 2005 [77] and magnetic field modeled by the twelfth-generation International Geomagnetic Reference Field (IGRF-12) [68], and provide them as the input to ITALCS to get the FTLE scalar fields. For this study, I model the plasma drift at 350 km height, which lies in the F_2 region. The Weimer 2005 polar electric potential model is used for generating the global potential V, and IGRF-12 is used for simulating the global magnetic field $\vec{B}$. Then the $\vec{E} \times \vec{B}$ drift field at each grid point P in a single layer of the ionosphere is computed by applying the outputs of those two models to Eq. 5.1, and taking the horizontal zonal and meridional components to obtain (v_e, v_n).

$$^{E}\vec{v}^{P} = (\underbrace{\vec{v}_{E\times B} \cdot \hat{l}_2}_{v_e})\hat{l}_2 + (\underbrace{\vec{v}_{E\times B} \cdot \hat{l}_3}_{v_n})\hat{l}_3 = v_i(x_i, t_i) \tag{5.2}$$

where the coordinates are as shown in Figure 3.6. The velocity $^{E}\vec{v}^{P}$ is ground speed v_e and v_n (in m/s) at a geodetic location (ϕ, λ) for a given altitude and time. While the $\vec{E} \times \vec{B}$ drift by definition lies in the 2-D plane normal to the local $\vec{B}$ field at every point, at high latitudes at which the $\vec{B}$ field is nearly vertical, the $\vec{E} \times \vec{B}$ drift is primarily horizontal. Therefore, treating the 2-D convection as horizontal flow in this work $\vec{v}_{E\times B} \approx {}^{E}\vec{v}^{P}$ is a reasonable approximation for high latitudes. The velocity is transformed to angular rates $\dot{\phi}$, $\dot{\lambda}$, and used as the input to ITALCS.

Since Weimer 2005 is a high-latitude model I search for 2-D ionospheric LCSs in the high latitude zone. However, I simulate the flow field at global scale, with all velocities equatorward of the Weimer potential boundary defined as $\vec{v}_{E\times B} = 0$, to avoid discontinuity at the middle-to-high latitude boundary. This study thus makes no claims about LCSs at low latitudes. The 2-D global domain is parameterized with longitude and latitude as the generalized coordinates with a 1° resolution in each direction. In the domain, each gridpoint is assumed to contain a particle at time t_0. The plasma drifts for these particles are computed every $\Delta t = 5$ min, with $dt = 30$ s. Due to the fact that plasma drift velocities are large (∼1000 m/s) at high latitudes, I choose $\tau = 3$ hours as the integration time.

For the first and second studies, I use the AE index to select a geomagnetically quiet period and a geomagnetically stormy period. AE index is defined by the separation between AU and AL, which are the indices of the upper and lower envelope of auroral-zone magnetic observation [32]. Figure 5.1(a) plots the AE index for 15-18 March 2015. For the first study, in which I examine whether LCSs exist in the convection field, I choose four periods with initial time t_0 as 00:00 UT, 06:00 UT, 12:00 UT, and 18:00 UT on 16 March 2015 (see Figure 5.1(b)) For the second study, to explore the influence of geomagnetic activity on the ionospheric LCSs, I select $t_0 =$ 12:00 UT on 16 March 2015 as the initial time of the geomagnetically quiet period and $t_0 =$ 12:00 UT on 17 March 2015 for the geomagnetically active period. The AE indices for these two days are shown in Figure 5.1(b) and Figure 5.1(c), respectively. Choosing the two periods within two days ensures similar solar tilt angle and solar

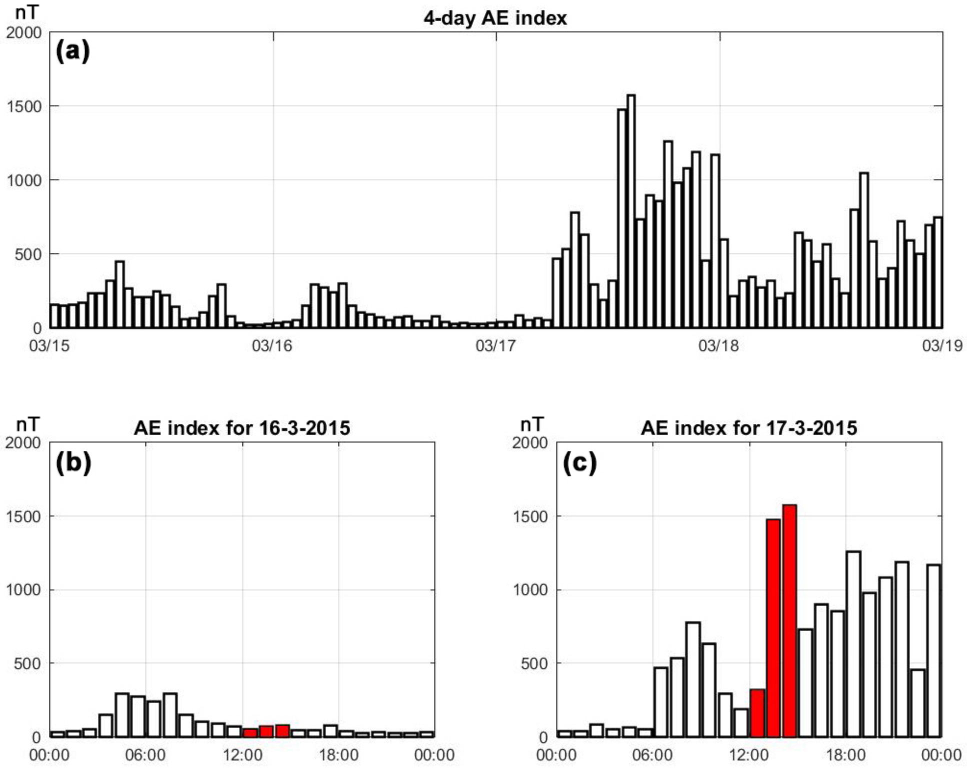

Figure 5.1. (a) AE index from 15–18 March 2015; (b) AE index for geomagnetic quiet period on 16 March 2015; (c) AE index for geomagnetic period on 17 March 2015. The periods labeled in red in (b) and (c) are used to study the influence of geomagnetic activity.

cycle conditions. IMF measurements during the storm can be found in [38].

I also set up three tracers at high latitudes for both the geomagnetically quiet period at t_0 = 12:00 UT on 16 March 2015 and storm period at t_0 = 12:00 UT on 17 March 2015. The three tracers are initially equally spaced in latitude on the local noon longitude, with A_0 at 76°N, B_0 at 72°N, and C_0 at 68°N for the quiet period and A_0 at 66°N, B_0 at 62°N, and C_0 at 58°N for the active period. Their corresponding final positions are A_f, B_f, and C_f. The tracer locations are chosen to demonstrate the effect of LCSs lying between the particles. I also compare LCSs to electric potential contours.

For the last study, I identify a polar cap patch at 16:40 UT on 17 March 2015 based on observational data. I simulate the ionospheric conditions on 17 March 2015 at 450 km before and after, tracing the polar cap patch at 16:40 UT forward in time 100 min to study its transport, backward in time 60 min to study its formation, and identifying the associated dominant LCS horseshoe shape during those times based on the modeled drifts.

This chapter is organized as follows: an initial study of 16 March 2015 at 350 km shows the modeled $\vec{E} \times \vec{B}$ convection fields yield the ionospheric LCSs discussed in Section 5.3. A comparison of the simulated results between a geomagnetically quiet period and a geomagnetically storm period demonstrates the sensitivity of the structures to the geomagnetic activity, discussed in Section 5.4. The analysis of an observed polar cap patch indicates that a necessary condition for its formation and transport is that storm-enhanced density exist poleward of the LCS, shown in Section 5.5. Discussions are made in Section 5.6 followed by the summary in Section 5.7

5.3 High latitude 2-D ionospheric LCSs during geomagnetic quiet period

For the first study, in which I examine whether LCSs exist in the convection field, I choose 4 periods with initial times t_0 of 00:00 UT, 06:00 UT, 12:00 UT, and 18:00 UT on 16 March 2015. Figure 5.2 shows world map of FTLE values at 350 km viewed from the geographic north pole on 16 March 2015 at t_0 = 00:00 UT. In the map, pixel colors represent the FTLE values from 0 to $5\times10^{-4}\ s^{-1}$. The blank area at low latitudes is due to the vanishing of the Weimer potential to 0. On this map, a bright yellow ridge is a repelling LCS. In the figure, the FTLE maxima are much smaller than that of the double-gyre example shown in Figure 3.3, because of the normalization by integration time τ in Eq. 2.8. Since LCSs are located at local FTLE maxima, the absolute value of the FTLE is not significant.

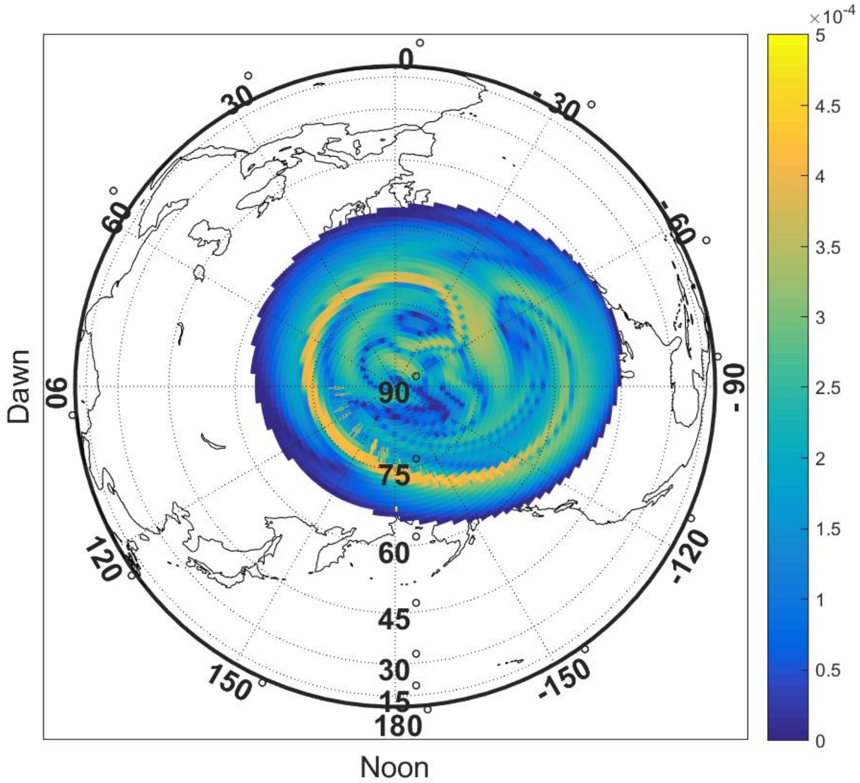

Figure 5.2. FTLE map for plasma drifts at 350 km viewed from the geographic north pole on 16 March 2015 at t_0 = 00:00 UT with an integration time $\tau = 3$ hours. Local noon is fixed at the bottom of the plot. The color scale represents for the FTLE values varying from 0 to 5×10^{-4} s^{-1}; yellow ridges are the LCSs.

Figure 5.2 shows that at t_0 = 00:00 UT, the LCSs are run east-west in the day sector and curve poleward in the night sector. The LCSs are located at higher latitude in the dawn sector with the LCS ridges lying in between $70°N$ and $77°N$ than those in the dusk sector with the LCS ridges lying in between $55°N$ and $60°N$, and the locally maximum FTLE values in the dawn sector are larger than those locally maximum FTLE values in the dusk sector.

Figure 5.3 shows world map of FTLE values at 350 km viewed from the geographic north pole on 16 March 2015 at t_0 = 06:00 UT, with local noon fixed at the bottom of the plot. The figure shows that at t_0 = 06:00 UT, the LCSs also run east-

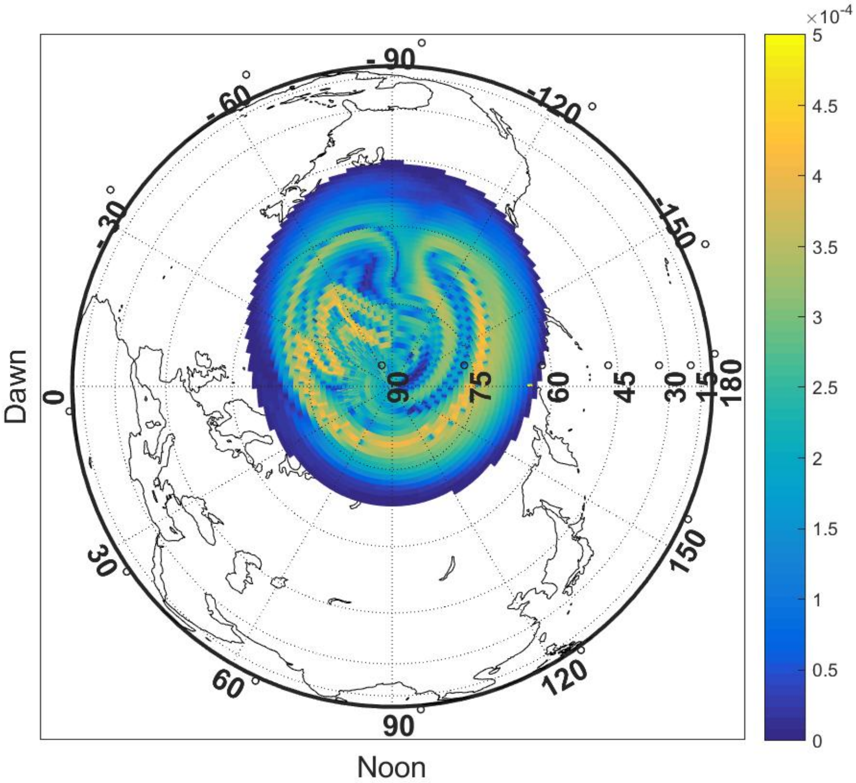

Figure 5.3. FTLE map for plasma drifts at 350 km viewed from the geographic north pole on 16 March 2015 at t_0 = 06:00 UT with an integration time $\tau = 3$ hours. Local noon is fixed at the bottom of the plot. The color scale represents for the FTLE values varying from 0 to $5 \times 10^{-4}\ s^{-1}$; yellow ridges are the LCSs.

west in the day sector and curve poleward in the night sector. In the noon sector, the most equatorward locally maximum LCS ridges lie between 75°N and 80°N, while in the midnight sector, the locally maximum LCS ridges reach as low as 60°N. In both morning and afternoon sectors, the equator-most locally maximum LCS ridges lie between 70°N and 80°N.

Compared to Figure 5.2, which showed the FTLE map at t_0 = 00:00 UT, there are more LCSs in the pole area at t_0 = 06:00 UT. From Figure 5.1(b), the AE index values during 06:00 UT to 09:00 UT are larger than the AE index values during 00:00 UT to 03:00 UT, which indicates that the geomagnetic condition is more active during 06:00 UT to 09:00 UT.

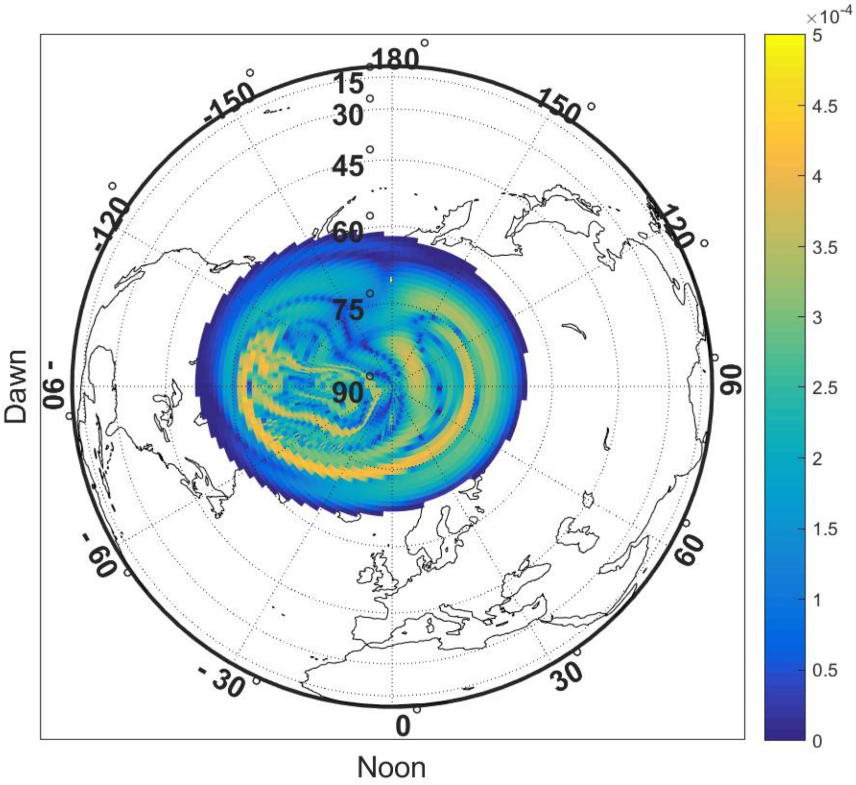

Figure 5.4. FTLE map for plasma drifts at 350 km viewed from the geographic north pole on 16 March 2015 at t_0 = 12:00 UT with an integration time $\tau = 3$ hours. Local noon is fixed at the bottom of the plot. The color scale represents for the FTLE values varying from 0 to 5×10^{-4} s^{-1}; yellow ridges are the LCSs.

Figure 5.4 shows world map of FTLE values at 350 km viewed from the geographic north pole on 16 March 2015 at t_0 = 12:00 UT, with local noon fixed at the bottom of the figure. In this map, the equator-most LCSs run east-west in the day sector. There are more secondary LCSs in high latitude. In the morning sector, the locally maximum LCS ridges reach as low as 60°N, while in the dusk sector, the locally maximum LCS ridges are located between 70°N and 75°N. The LCSs in the local noon sector appear between 70°N and 80°N.

Figure 5.5 shows world map of FTLE values at 350 km viewed from the ge-

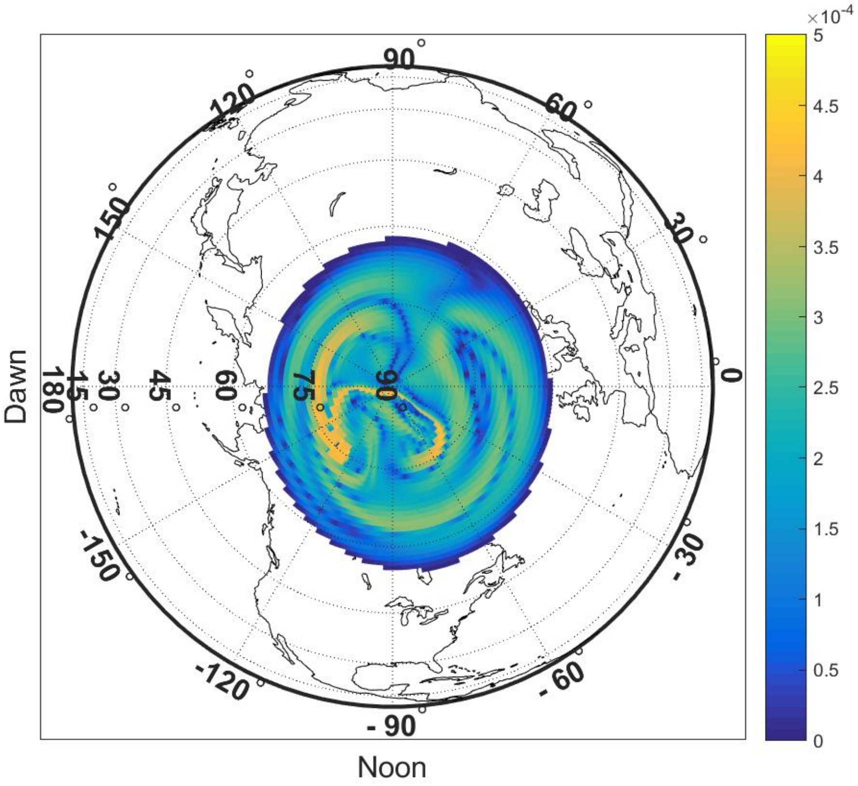

Figure 5.5. FTLE map for plasma drifts at 350 km viewed from the geographic north pole on 16 March 2015 at t_0 = 18:00 UT with an integration time τ = 3 hours. Local noon is fixed at the bottom of the plot. The color scale the FTLE values varying from 0 to 5×10^{-4} s^{-1}; yellow ridges are the LCSs.

ographic north pole for 16 March 2015 at t_0 = 18:00 UT, with local noon fixed at the bottom of the figure. The locally maximum equatorward LCS ridges are again running east-west in the day sector and curving poleward in the night sector. There is also an LCS ridge running from dawn to dusk, crossing the pole, and curving equatorward in the day side. The locally maximum LCS ridges appear at lower latitudes in the dusk sector than those in the dawn sector.

Figures 5.2 - 5.5 show that the ionospheric LCSs exist in the modeled plasma convection fields, and are more prominent at high latitudes in the pole area. The most repelling ridges are predominantly horseshoe-like ridges appear in the day sector oriented with the “U” opening on the local nightside.

5.4 The influence of geomagnetic activity on ionospheric LCSs

For the second study, in which I analyze the effect of geomagnetic activity, I set up 3 tracers at high latitude for both the geomagnetically quiet period at $t_0 =$ 12:00 UT, 16 March 2015, and storm period at $t_0 =$ 12:00 UT, 17 March 2015. The three tracers are initially equally spaced in latitude on the local noon longitude, with A_0 at $76°N$, B_0 at $72°N$, and C_0 at $68°N$ for the quiet period and A_0 at $66°N$, B_0 at $62°N$, and C_0 at $58°N$ for the active period. Their corresponding final positions are A_f, B_f, and C_f. The tracer locations are chosen to demonstrate the effect of LCSs lying between the particles.

Figure 5.6 shows the FTLE map over the north pole for the geomagnetically quiet period at $t_0 =$ 12:00 UT, 16 March 2015. In the map, pixel colors represent the FTLE values from 0 to $5{\times}10^{-4}$ s^{-1}. The blank area at low latitudes is due to the vanishing of the Weimer potential to 0. On this map, a bright yellow ridge is a repelling LCS. In Figure 5.6, tracers are initialized in the northern hemisphere, A_0 at $76°N$ in white, B_0 at $72°N$ in red, and C_0 at $68°N$ in magenta, and the trajectories of the three tracers are shown in the figure with the final positions labeled A_f, B_f, and C_f.

The motion of the tracers shown in Figure 5.6 indicates that over 3 hours, particle A has a change in position $(\Delta\phi, \Delta\lambda) = (123.7°E, 2°N)$. In contrast, B has $(\Delta\phi, \Delta\lambda) = (39.6°W, 3.5°S)$, and particle C shifts by $(\Delta\phi, \Delta\lambda) = (0.6°W, 0°N)$ from its initial position. There is a local maximum FTLE structure between A_0 and B_0 indicating a repelling LCS. With equal separations at the initial positions of the three tracers, the final distance $\overline{A_fB_f}$ is larger than $\overline{B_fC_f}$, which corresponds to the FTLE values between them.

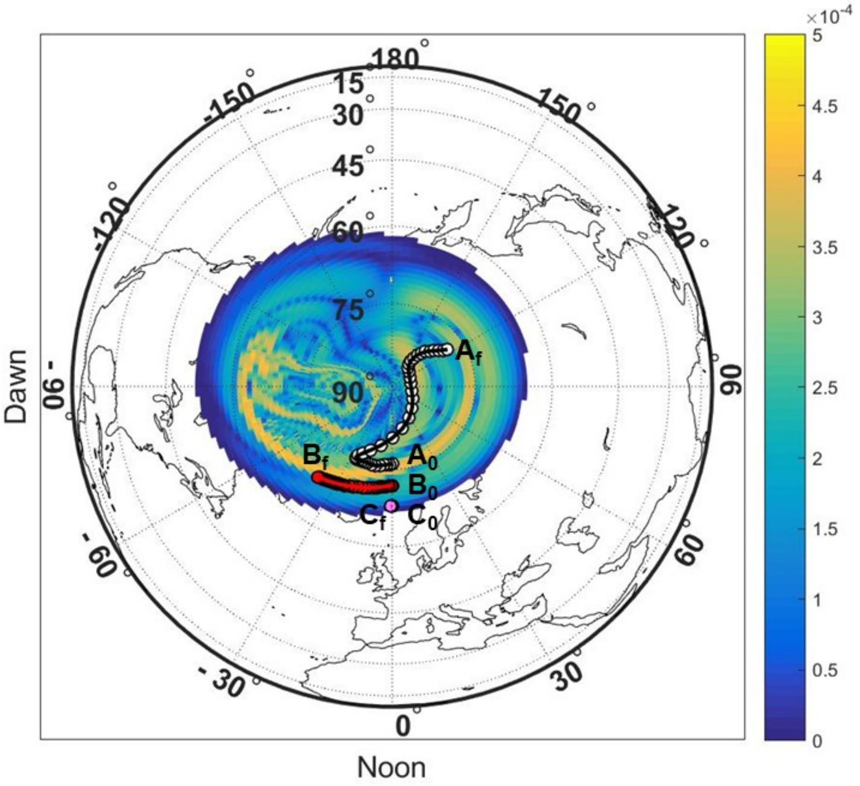

Figure 5.6. FTLE map of plasma drifts at 350 km over the northern hemisphere during the geomagnetically quiet period at t_0 = 12:00 UT, 16 March 2015, $\tau = 3$ hours. Local noon is fixed at the bottom of the plot. The color scale represents the FTLE values ranging from 0 to 5×10^{-4} s^{-1}. The tracers' initial and final positions are labeled as A_0 and A_f (white), B_0 and B_f (red), and C_0 and C_f (magenta).

Figure 5.7 shows the FTLE map over the south pole for the geomagnetically quiet period with t_0 = 12:00 UT, on 16 March 2015. Local noon is fixed at the bottom of the plot. In the map, pixel colors represent the FTLE values from 0 to 5×10^{-4} s^{-1}. The blank area at low latitudes is due to the vanishing of the Weimer potential to 0. On this map, a bright yellow ridge is a repelling LCS.

In southern hemisphere, the LCSs run east-west in the day sector and curve poleward in the night sector. In the dawn sector, the locally maximum FTLE values are larger and appear at higher latitude than the locally maximum FTLE values in

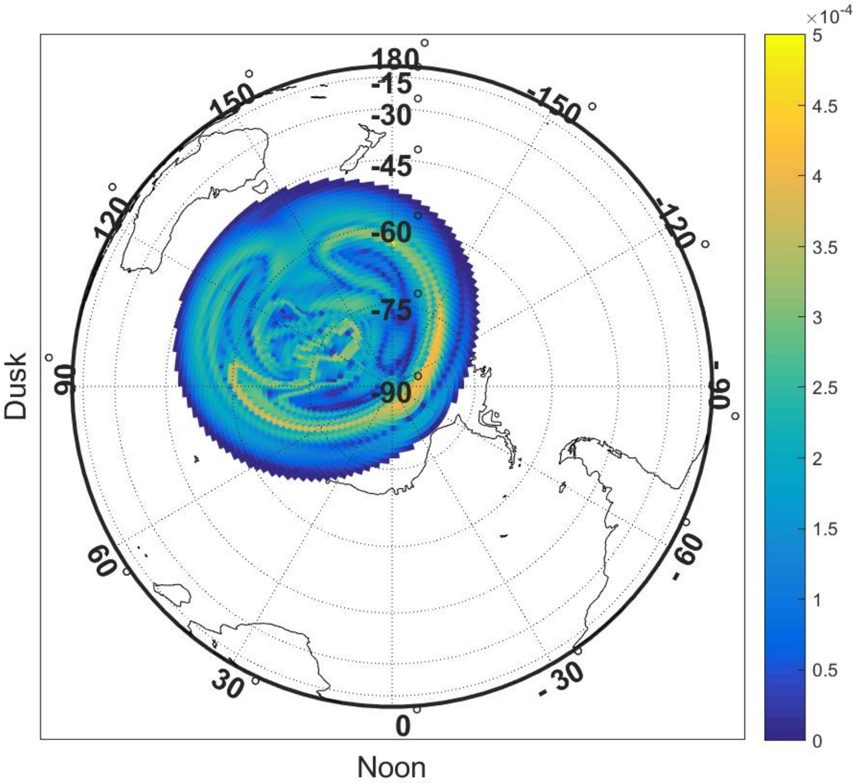

Figure 5.7. FTLE map of plasma drifts at 350 km over the southern hemisphere during the geomagnetically quiet period at t_0 = 12:00 UT, 16 March 2015, $\tau = 3$ hours. The color scale represents the FTLE values ranging from 0 to $5 \times 10^{-4}\ s^{-1}$

the dusk sector. The most equatorward LCS ridges in the dawn sector are located between 80°S and 90°S, while in the dusk sector, the most equatorward LCS ridges lie between 45°S and 60°S.

Figure 5.8 shows the FTLE map over the north pole for geomagnetic active period at t_0 = 12:00 UT, 17 March 2015. In the map, each pixel color represents the FTLE value varying from 0 to $5{\times}10^{-4}\ s^{-1}$. The blank area at lower latitudes is due to the vanishing of the Weimer potential to 0. On this map, a bright yellow ridge is a repelling LCS. Compared to the result of geomagnetically quiet period in northern hemisphere shown in Figure 5.6, the LCSs are more complex and appear at lower latitudes. The LCSs run east-west in the local day sector at 60°N and curve

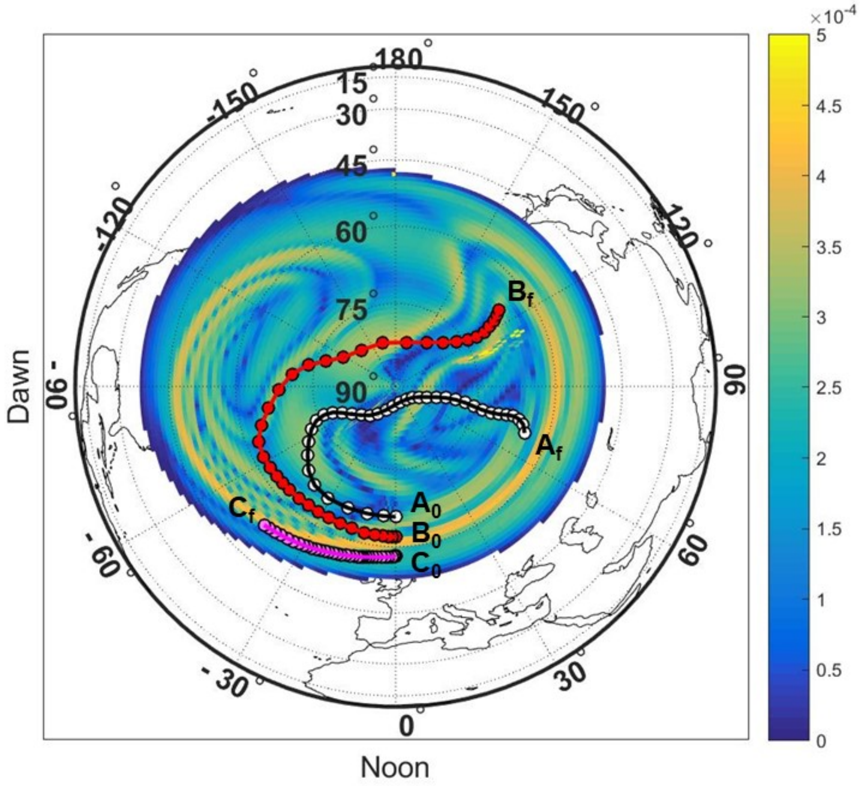

Figure 5.8. FTLE map of plasma drifts at 350 km over the northern hemisphere during the geomagnetically active period at $t_0 =$ 12:00 UT, 17 March 2015, $\tau = 3$ hours. The color scale represents the FTLE values ranging from 0 to $5 \times 10^{-4}\ s^{-1}$. The tracers' initial and final positions are labeled as A_0 and A_f (white), B_0 and B_f (red), and C_0 and C_f (magenta).

poleward at the local night sector.

In Figure 5.8, tracers are initialized in the northern hemisphere, A_0 at $66°N$ in white, B_0 at $62°N$ in red, and C_0 at $58°N$ in magenta, and the trajectories of the three tracers are shown in the figure with the final positions labeled A_f, B_f, and C_f.

During 3 hours, tracer A shown in Figure 5.8 has a change in position $(\Delta\phi, \Delta\lambda)$ $= (70.2°E, 1.5°S)$, and B has $(\Delta\phi, \Delta\lambda) = (126.4°E, 4.3°N)$. In contrast, particle C shifts by $(\Delta\phi, \Delta\lambda) = (43.5°W, 4.6°S)$ from its initial position. The larger separation tendency between B and C than B and A corresponds to the LCS ridge between B_0

and C_0. Figure 5.8 shows that LCSs run east-west in the local day sector at 60°N and curve poleward at the local night sector.

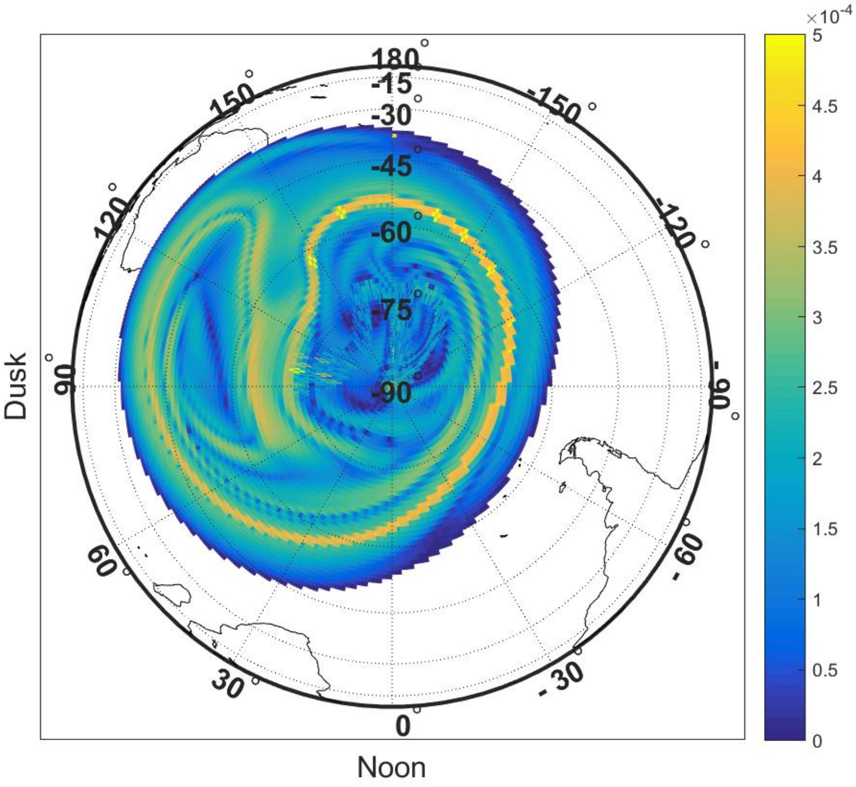

Figure 5.9. FTLE maps of plasma drifts at 350 km over the southern hemisphere during the geomagnetically active period with t_0 = 12:00 UT, 17 March 2015, τ = 3 hours. The color scale represents the FTLE values ranging from 0 to 5×10^{-4} s^{-1}.

Figure 5.9 shows the FTLE map over the south pole for the geomagnetically active period at t_0 = 12:00 UT, 17 March 2015. Local noon is fixed at the bottom of the plot. In the map, color scale represents the FTLE values from 0 to $5{\times}10^{-4}$ s^{-1}. The blank area at lower latitudes is due to the vanishing of the Weimer potential to 0. A bright yellow ridge is a repelling LCS.

In southern hemisphere, the LCSs are more complicated compared with the quiet period, oriented east-west in the dayside and curving poleward in the nightside.

In the dawn sector, the locally maximum FTLE values are larger and appear at higher latitude than the locally maximum FTLE values in the dusk sector. The most equatorward LCS ridges in the dawn sector are located between $60°S$ and $70°S$, while in the dusk sector, the most equatorward LCS ridges lie between $30°S$ and $45°S$.

A comparison of Figures 5.8 and 5.9 with Figures 5.6 and 5.7 shows that the LCSs respond to geomagnetic activity. During the geomagnetically active period, in both hemispheres, the LCSs have more complex topology and extend to lower latitude. However, the LCSs do not appear to have perfect conjugacy between northern and southern high latitudes. FTLE maps for the plasma drifts for both the northern and southern high latitudes during the geomagnetically quiet and active periods at 350 km for different initial times over the interval t_0 = [0:00 UT, 23:00 UT] and the integration time $\tau = 3$ hours are shown in Appendix C.

The LCS structures are reminiscent of the two-cell potential and convection pattern modeled by Weimer 2005. For this reason I compare the LCS locations to electric potential contours. Figure 5.10 and Figure 5.11 contain the north pole view plots of LCS ridges superimposed over electric potential contours simulated by Weimer 2005 for a geomagnetically quiet period (see Figure 5.10) and geomagnetically active period (see Figure 5.11), respectively. In Figures 5.10 and 5.11, the red contour lines are the electric potential boundary which is the equator-most point of vanishing potential during the interval $t = [t_0, t_f]$. The yellow ridges are the repelling LCSs identified as $\sigma \geq 2.5 \times 10^{-4}\ s^{-1}$. Comparing Figures 5.10 and 5.11, it is clear the electric potential boundary for the geomagnetically active period is lower in latitude than the boundary for the geomagnetically quiet period, so the LCSs for the geomagnetically active period appear more equatorward than the LCSs for the geomagnetically quiet period. The color contour lines are the electric potential modeled by Weimer 2005 at time t_0. For both storm and quiet periods, the most equatorward

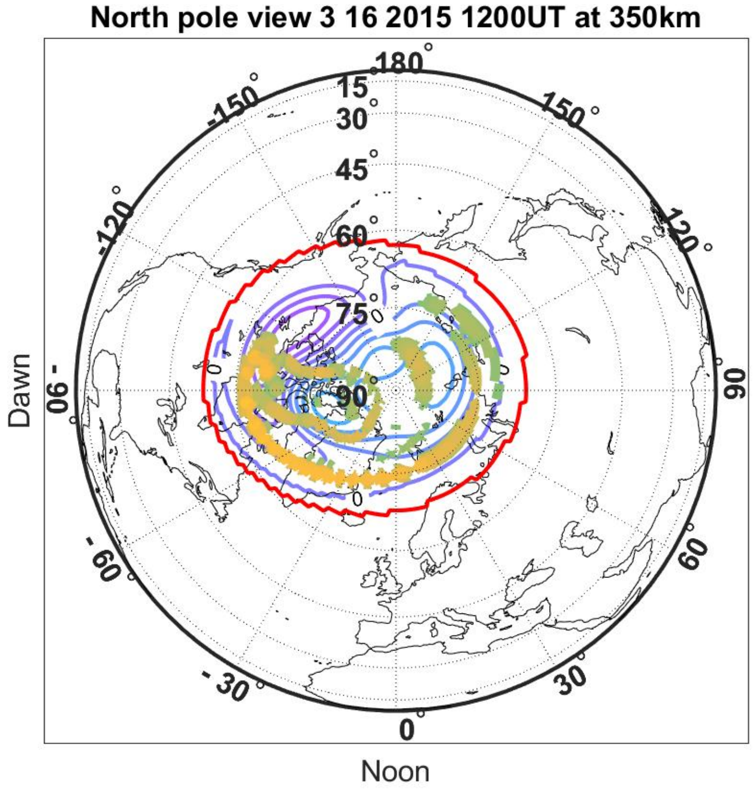

Figure 5.10. LCS ridges (yellow) for $\sigma \geq 2.5 \times 10^{-4}\ s^{-1}$ on the electric potential contours viewed from the geographic north pole for a geomagnetically quiet period at t_0 = 12:00 UT, 16 March 2015. The red contour line is the high latitude electric potential boundary during the time interval $t = [t_0, t_f]$.

LCS ridges in the day sector are parallel to the electric potential boundary.

5.5 Analysis of polar cap patch transport and formation

5.5.1 Polar Cap Patch. The polar cap patch, a 100s kilometer-scale ionospheric plasma irregularity poleward of the auroral oval, is often associated with ionospheric plasma density irregularities varying from 100 m to several kilometers scale size that adversely affect Global Navigation Satellite System(GNSS) service [50] by causing scintillation, a rapid fluctuation in signal amplitude and phase [14, 82, 81].

Tracking the patch is an important way to understand the source of scintil-

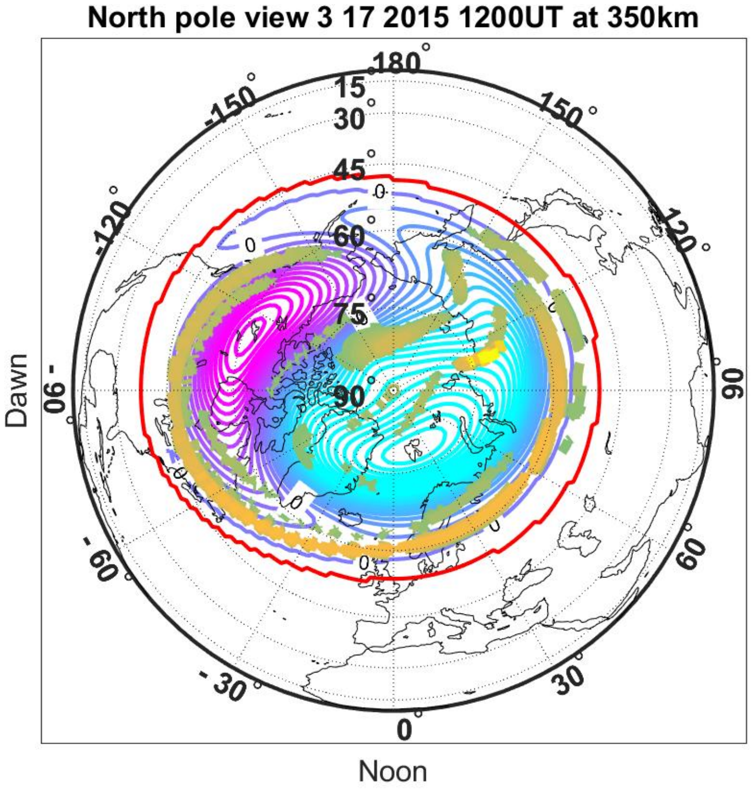

Figure 5.11. LCS ridges (yellow) for $\sigma \geq 2.5 \times 10^{-4}\ s^{-1}$ on the electric potential contours viewed from the geographic north pole for a geomagnetically active period at $t_0 = $ 12:00 UT, 17 March 2015 at 350 km. The red contour line is the high latitude electric potential boundary during the time interval $t = [t_0, t_f]$.

lation. For this reason, sensing patches and their movement has become an important application of ionospheric tomographic and assimilative algorithms [7]. By using plasma density and path-integrated total electron content (TEC) measurements, ionospheric imaging can produce electron density in two, three, and four dimensions including temporal variation, as reviewed by Bust and Mitchell (2008) [8].

Polar cap patch movement is coupled to the magnetosphere. In the high latitudes, magnetospheric field lines transition from the closed lines that return to Earth in the opposite hemisphere, to open lines that extend into interplanetary space and may interconnect with the interplanetary magnetic field (IMF) [30]. The polar cap describes the ionospheric region of open field lines that are swept back away from the sun. The cusps are the regions on the dayside in both hemispheres in which the magnetic field lines extend to the dayside magnetopause, the boundary between the IMF and magnetosphere.

Due to solar wind motion, magnetospheric flux tubes typically circulate from noon to midnight across the polar cap, with return circulation around the dawn and dusk sides. Superposed with a co-rotation electric field, this circulation maps down along the field lines into the ionosphere to form what is typically a two-cell electric potential pattern [30]. This cross-polar-cap electric field combined with the magnetic field largely governs plasma motion at high latitudes. During geomagnetic storms, magnetic reconnection is a framework for understanding the erosion of the dayside magnetopause. Enhanced erosion of the flux on the dayside leads to an accumulation on the nightside [9]. Observation and theory both show that geomagnetic storms are enhanced when the IMF points southward ($B_z < 0$); magnetic reconnection is especially effective in this condition.

After initiating on the dayside cusp region, patches are transported across the center of the polar cap region toward night side [51, 49] and may circulate back on the dawn and dusk sides. Of the unresolved questions regarding polar cap patches, in this work I focus on asking: what is the source of the plasma? Formation mechanisms of polar cap patches were studied by Weber et al. (1984) [75]; Lockwood and Carlson (1992) [41]; Lockwood et al. (2005) [42]; MacDougall and Jayachandran (2007) [44]; and Zhang et al. (2011) [80] and classified as Type L for low density patches ionized by particle precipitation and Type H for high density ones formed by segmenting the tongue of ionization (TOI) [82]. In this work I focus on the H type patches. A backward tracing of a polar cap patch studied by Bust and Crowley (2007) [7] indicates that the patch did not originate from the mid-latitude part of the TOI.

TOIs themselves are observed to form from mid-latitude storm enhanced density (SED), which has been defined as a latitudinally narrow, spatially continuous region of enhanced plasma density extending from geomagnetic mid-latitude [20]. A sub-auroral polarization stream (SAPS) has been theorized as an electric field mechanism in the dusk sector for erosion of SED into a TOI [21].

Zhang et al. (2013) [82] refers to patches as caused by an equatorward shift of the open-closed field line boundary "entraining" ionized plasma into the polar cap. Moen et al. (2015) [49] notes that regional forecasts of scintillation conditions require an understanding of how plasma is "entrained" into the polar cap convection flow, as well as its exit. Hosokawa et al. (2009) [29] and Hosokawa, Tsugawa, et al. (2010) [28] describe Global Positioning System (GPS) TEC-based observations originally reported by Foster et al. (2005) [21] of a TOI "entrained" into the noontime cusp and into the nightside along a streamline.

Hosokawa, St-Maurice, et al. (2010) [27] notes that "time varying plasma flow is an important factor for producing patches." However, in a time-varying flow, streamlines differ from pathlines, the actual trajectories of individual fluid elements. For this reason, a TOI structure does not always align with instantaneous electric isopotentials, which are effectively streamlines (e.g., Foster et al. (2005) [21]; Zhang, Zhang, Lockwood, et al. (2013) [81]; Zou et al. (2014) [83]).

Yet analyzing coherent structures can help in forecasting the transport of plasma patches, mitigating their impacts on transionospheric signals. Many approaches for identifying flow coherence have relied on Eulerian definitions of structures such as vorticity, but these definitions are not observer-independent [23], so inappropriate to study in Earth's non-inertial frame at global scale [73, 72].

However, to treat patches requires a larger scale flow domain, in which the plasma fluid is regarded as a single species. This section analyzes the synoptic scale ionospheric LCSs. I use data-driven observations of a polar cap patch that are confirmed with an independent data set, and examine this polar cap patch's relationship with the modeled ionospheric LCSs over time.

5.5.2 Polar Cap Patch Simulation Configuration.

In this study, I identify a polar cap patch at 16:40 UT on 17 March 2015 based on observational data. I simulate the ionospheric conditions on 17 March 2015 at 450 km before and after, tracing the polar cap patch at 16:40 UT forward in time 100 min to study its transport, backward in time 60 min to study its formation, and identifying the associated dominant LCS horseshoe shape during those times based on the modeled drifts.

The patch is observed in total electron content (TEC) maps of the ionosphere generated using Multi-Instrument Data Analysis System (MIDAS). MIDAS performs three-dimensional, time-dependent electron density inversions constrained by vertical basis functions based on Chapman profiles and horizontal Tikhonov regularization [48, 61, 11]. About 100 high-latitude dual-frequency GPS reference stations from the International GNSS Service (IGS) network are used in the inversion, which are performed at 10-minute resolution from 00:00 to 24:00 UT for 17 March 2015.

To show that the MIDAS results are reconstructing patches of enhanced plasma, Figure 5.12 shows the MIDAS estimates of polar cap patches with north pole TEC maps at (a) 17:30 UT and (b) 18:00 UT. These are compared with in situ measurements of Swarm satellite densities at about 450 km altitude over time, as the satellites pass through the vicinity of the patches at those times. In these plots, a point on the satellite ground track on the map corresponds to the instant on the density time series subplot directly below it. The correspondence of high and low densities with high and low TEC regions spatially gives strong evidence that the TEC estimated by MIDAS in fact corresponds to polar cap patch plasma.

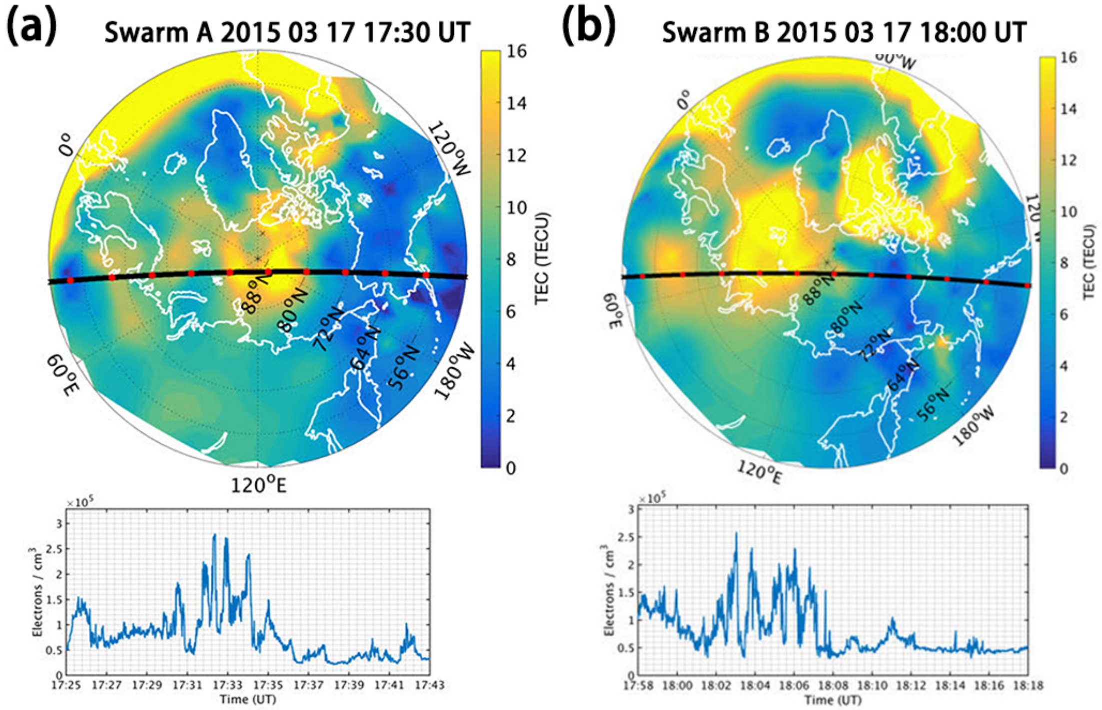

Figure 5.12. (Top) MIDAS reconstructed vertical TEC maps over the north geographic pole at (a) 17:30 UT and (b) 18:00 UT. The Swarm satellite track is marked in black, and Swarm travels from left to right across the plot. Regular time intervals are marked with red dots. (Bottom) Swarm satellite in situ densities measured over time for the satellite track shown.

5.5.3 Polar Cap Patch Simulation Results. In order to explore the formation and propagation of the polar cap patch, I apply the LCS analysis technique to the flows at 16:40 UT, 17 March 2015, at which time a polar cap patch is visually identified during this storm by using MIDAS. Figure 5.13 contains total electron content (TEC) maps viewed from the geographic north pole with local noon fixed at the bottom of the map. Figure 5.13(a) shows the TEC map of 16:40 UT. A patch visually identified to be located at approximately (72° N, 75° W) is labeled with a black star. The purple contours are LCS ridges ($\sigma \geq 2.5 \times 10^{-4}\ s^{-1}$) at t_0= 16:40 UT, 17 March 2015 with τ = 3 hours. Using the Weimer 2005 and IGRF-12 models for convective drift, I trace this patch forward at 20 minute intervals over the next 100 minutes in Figures 5.13(b)-5.13(f), with the current position of the tracer circled in black, and intermediate locations in red dots at 10-minute intervals. These plots span the times at which the MIDAS reconstruction of plasma was independently corroborated by Swarm in situ densities in Figure 5.12. The Weimer 2005 and IGRF-12 models are providing estimates of drift consistent with TEC observations. This consistency is notable in light of the fact that the tracer is assumed to be at 450 km altitude, whereas TEC is a vertically integrated plasma density. This means that the LCSs shown are likely representative of the material transport barriers during this event. These plots show the modeled LCSs form channels through which the patches propagate.

In Figures 5.14(a)–5.14(d), the patch is traced backward in time from 16:40 UT at 20 minute intervals over the previous hour. The TEC maps in Figures 5.14(a)–5.14(d) indicate that the observed patch originated from a tongue of ionization (TOI) extending poleward from a storm enhanced density (SED) at about 60° W longitude. This observation is to be expected as patches are understood to come from TOIs in the literature.

Figure 5.14(a) shows that the center of the patch observed from the MIDAS image is poleward of the LCS ridge at t_0 = 16:40 UT. The TOI throughout the time interval shown (both prior and subsequent to 16:40 UT) also appears to be poleward of the horseshoe LCS for each respective t_0. However, the vast bulk of the SED is *equatorward* of the LCS. Figures 5.14(a)–5.14(d) show that the part of the SED poleward of the LCS ridge is the TOI, and that therefore it has the potential to become a polar cap patch in the future. In other words, the horseshoe LCS appears to demarcate a necessary condition for the formation of a polar cap patch by the criterion that SED plasma exist poleward of it. When SED plasma is poleward of the LCS, it can be entrained into a polar cap patch.

5.6 Discussion

Since convective transport structures in the high-latitude ionosphere map out to the dayside magnetosphere, an important implication of this work is that the LCS ridge in the high latitude ionosphere should map out along field lines to the dayside magnetopause. The existence of a horseshoe ridge in the ionosphere would demarcate the most highly separating magnetic field lines, which are carried along by the plasma. The horseshoe likely describes those flux tubes which are undergoing the most stretching over the time interval considered. Interestingly, the LCS opening on the nightside shows that there is no significant analogous magnetotail coherent structure, of maximal repulsion. A backward time FTLE calculation would define LCSs of maximal convergence, which are likelier to be on the nightside ionosphere with corresponding locations in the magnetotail.

It may or may not be a coincidence that the LCS I show is similar in shape, though different in orientation, to the horseshoe aurora observed during an IMF southward event during which part of the auroral oval was missing [70]. In this work I focused on flow transport of plasma. The relationship between the auroral oval, substorms, and LCSs are beyond the scope of this particular study.

Note that in this work, I have examined synoptic scale model convection drifts. This scale of flow field does not include smaller scale turbulent flow velocities, so this work does not address the LCSs that might be produced at regional (100 km or even smaller) scales due to various instability mechanisms. However, to the extent that the TOI and patches are confined to within the channel demarcated by the LCSs and instabilities form on the structure boundaries, the LCSs may provide an approximate location at which instabilities are likelier to form. Such an implication should be examined in the future. The plasma convection in this study is simplified as the high-latitude horizontal $\vec{E} \times \vec{B}$ drift by ignoring other contributions to drift. However, to examine LCSs globally, a study would need to be conducted with modeled plasma drifts including electric Pedersen drift, gravitational Pedersen drift, pure gravitational drift, and parallel mean flow [3, 60]. This would likely lead to a three-dimensional flow field, requiring 3-D LCS analysis, which ITALCS does not currently treat.

5.7 Summary

LCS ridges for plasma drifts in the ionosphere are predicted to exist based on flows simulated with Weimer 2005 and IGRF-12. For the cases studied, the strongly repelling ridges are predominantly horseshoe-like structures centered in the day sector and curving back on themselves to form the opening of a "U" on the nightside. During a geomagnetic storm, LCSs have more complicated topologies and appear at lower latitudes. The strong separation between simulated tracers located on different sides of the LCS ridge illustrates that the LCS location indicates strong stretching. LCS analysis indicates that a necessary condition for the formation and transport of the polar cap patch in ionospheric plasma drifts is that storm enhanced density plasma exist poleward of the LCS in order to be entrained into the polar cap patch.

Since the Weimer 2005 model has an equatorward boundary at which the potential goes to 0, all locations equatorward of this point will have 0 drift velocity. This particular study thus makes no claims about ionospheric LCSs at low latitudes. A simulation including both low- and high-latitude electrodynamics would likely require a full 3-D drift field integration in ITALCS. In addition using data assimilation drifts from methods such as Estimating Model Parameters from Ionospheric Reverse Engineering (EMPIRE) [47] could provide data-driven plasma drifts that could be used as the inputs to ITALCS in the future.

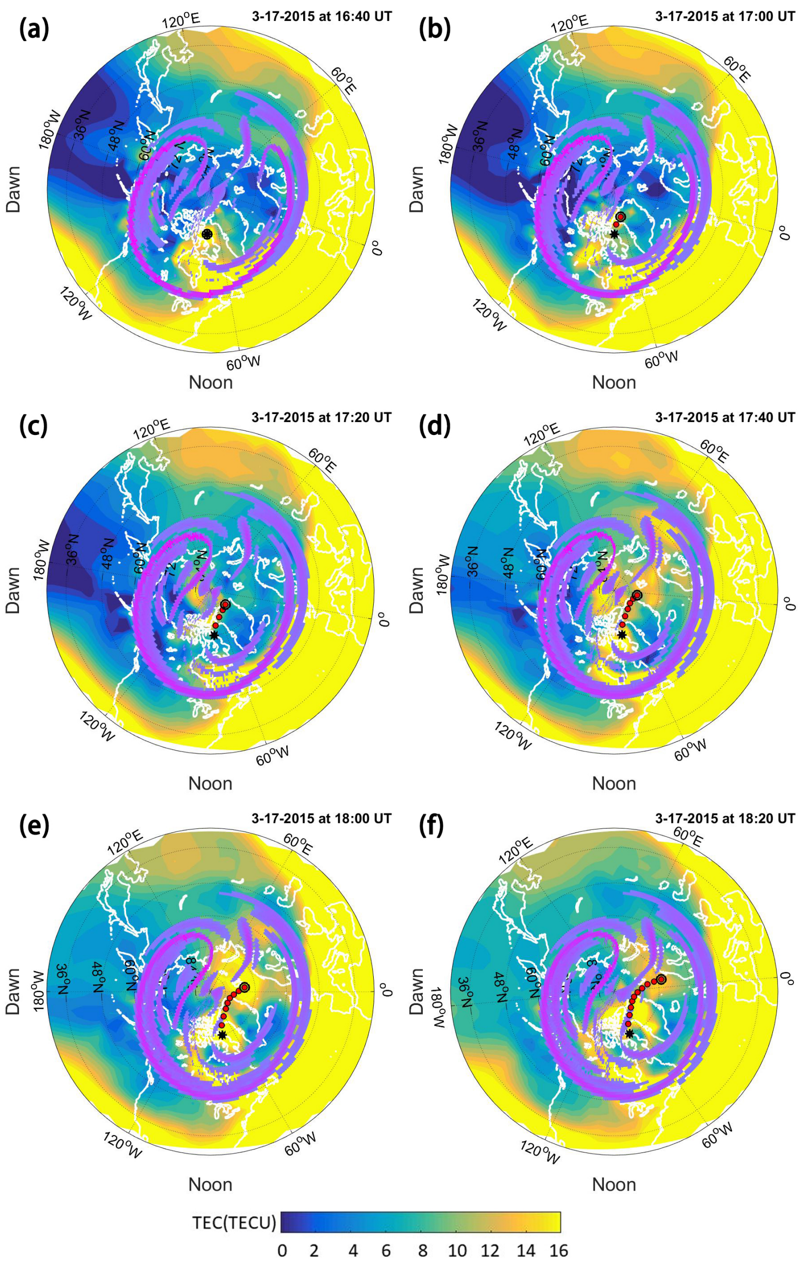

Figure 5.13. North pole view of TEC maps from MIDAS on 17 March 2015, from 0 to 16 TEC units (TECU), stepping forward in time at 20 minute intervals. Local noon is at the bottom of each figure. The purple ridges identify the LCSs of $\sigma \geq 2.5 \times 10^{-4}\ s^{-1}$ for a given t_0, with $\tau = 3$ hours. A black star represents the initial position (72° N, 75° W) of a polar cap patch identified at 16:40 UT. Modeled tracer locations for the patch are identified with red circles at 10 minute intervals. The tracer circled is the position at the current time in each figure. Modeled tracer locations for the patch are identified with red circles at 10 minute intervals. (a) 16:40 UT (b) 17:00 UT (c) 17:20 UT (d) 17:40 UT (e) 18:00 UT (f) 18:20 UT.

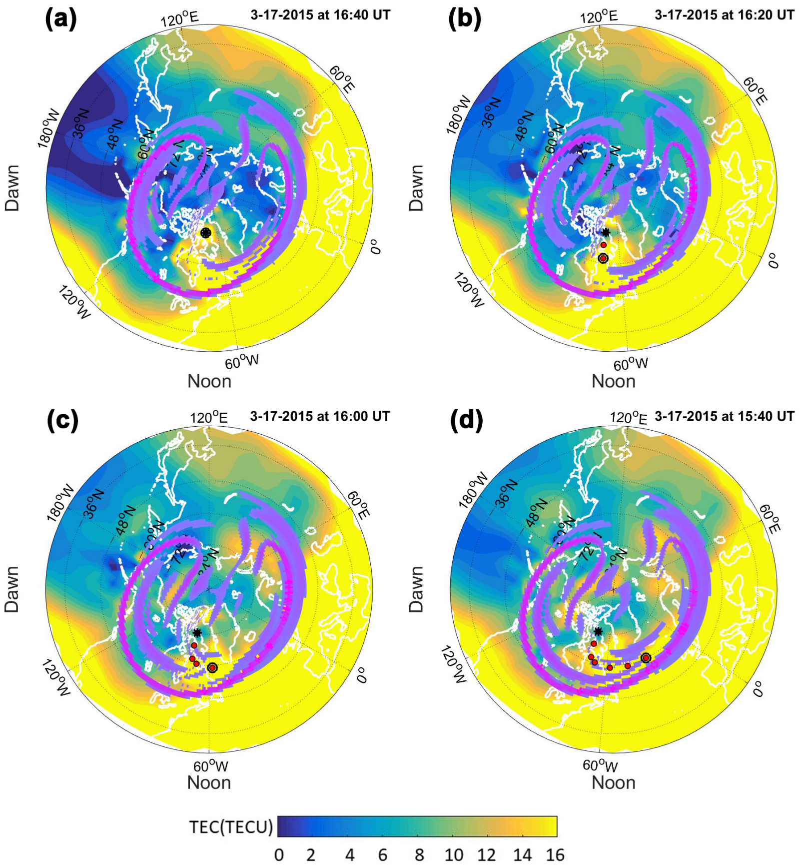

Figure 5.14. North pole view of TEC maps from MIDAS on 17 March 2015, from 0 to 16 TEC units (TECU), stepping backwards in time at 20 minute intervals. Local noon is at the bottom of each figure. The purple ridges identify the LCSs of $\sigma \geq 2.5 \times 10^{-4}\ s^{-1}$ for a given t_0, with $\tau = 3$ hours. A black star represents the initial position (72° N, 75° W) of a polar cap patch identified at 16:40 UT. Modeled tracer locations for the patch are identified with red circles at 10 minute intervals. The tracer circled is the position at the current time in each figure. (a) $t_0 = $ 16:40 UT (b) $t_0 = $ 16:20 UT (c) $t_0 = $ 16:00 UT (d) $t_0 = $ 15:40 UT.

CHAPTER 6

DYNAMICAL INTERACTION IN THE IONOSPHERE-THERMOSPHERE SYSTEM

The ionosphere and thermosphere are coupled through the charged and neutral particles' interactions that re-distribute energy and momentum. The interactions have been analyzed through modeling, measurements, and data assimilation. However, transport is still not well enough understood because of multisystem coupling and nonlinearities in the interactions. After a finite time, two neighboring fluid elements in the IT region can be very far apart in different areas of flow, challenging our ability to forecast the IT state.

A comparison of structures in thermospheric flows and ionospheric flows can provide evidence of the interactions between the charged and neutral particles. Also LCS analysis of the IT system can provide a better understanding of the upper atmosphere and improve the ability to forecast the IT system state. The response to geomagnetic activity of the ionospheric LCSs in Chapter 5 and of the thermospheric LCSs discussed in [73] and shown in Chapter 4, indicates the energy exchange and transport in the ionosphere-thermosphere system is visible in the formation of LCSs.

This chapter is organized as follows: A preliminary comparison of LCSs in the thermospheric flows and ionospheric flows modeled by two independent empirical models is discussed in Section 6.1. In Section 6.2, a physics-based model is applied to model the thermospheric and ionospheric flows. Both thermospheric LCSs and ionospheric LCSs are found in both the independent and self-consistent modeled flows and respond to geomagnetic conditions. The comparison of the governing structures (LCSs) in neutral winds flows and plasma drifts is also discussed in this section. The discussion is in Section 6.3 followed by concluding remarks in Section 6.4.

6.1 Preliminary comparison between the thermospheric LCSs and the ionospheric LCSs using independent models

Chapters 4 and 5 showed that the LCSs in both thermospheric flows and ionospheric flows modeled by empirical models respond to geomagnetic activity. For the initial study of the dynamical interaction in IT system, I compare the structures based on the independent empirical models used in those chapters: HWM14 for the thermosphere, and Weimer 2005 and IGRF-12 for the ionosphere.

6.1.1 Simulation Configuration. In this study, the global domain is parameterized by longitude and latitude, and a particle assumed at each grid point at time t_0. The grid spacing is 1 degree. Both the thermospheric winds modeled by HWM14 and $\vec{E} \times \vec{B}$ plasma drifts computed by Weimer 2005 and IGRF-12 outputs are simulated at 350 km height. Those velocity fields are computed every 5 minutes. Due to the larger drift velocity of ions, the integration time τ is selected as 3 hours for both plasma and neutrals. In order to show the effect of geomagnetic activity on LCSs, I use the AE index shown in Figure 5.1 to select the geomagnetic quiet period and active period. According to the AE index, $t_0 =$ 12:00 UT, on 16 March 2015 is set as the initial time of the geomagnetically quiet period, and $t_0 =$ 12:00 UT, on 17 March 2015 is selected as the initial time of the geomagnetically active period.

In this work, I map the FTLE fields for neutral wind flows and plasma drifts on polar maps viewed from the geographic north pole, and compare the shapes of the equator-most locally maximum FTLE ridges in those maps. To extract the most equatorward or locally prominent LCSs, during the geomagnetically quiet period, I choose a latitude belt between $60°N$ and $75°N$ and pick the maximum FTLE value at each longitude. FTLE values larger than $1 \times 10^{-4}\ s^{-1}$ (for the thermospheric FTLE field) and $2.7 \times 10^{-4}\ s^{-1}$ (for the ionospheric FTLE field) are regarded as the LCS ridges. The thresholds of FTLE value for thermospheric FTLE maps and ionospheric FTLE maps are different because ionospheric FTLE values are generally larger than thermospheric FTLE values.

As discussed in Chapters 4 and 5, both the thermospheric LCSs and the ionospheric LCSs expand equatorward during geomagnetic storm. To identify the LCSs, I choose a more equatorward belt region between $45°N$ and $65°N$ and select the maximum FTLE value at each longitude. FTLE values larger than 2×10^{-4} s^{-1} (for the thermospheric FTLE field) and 3.3×10^{-4} s^{-1} (for the ionospheric FTLE field) are treated as the LCS ridges. The parameters for this analysis are summarized in the following table:

Table 6.1. Parameters of the LCS identification method for the HWM14 and Weimer 2005 comparison.

LCS	latitude bands	σ_{TH} (s^{-1})
T-LCS-Q	$60°N$–$75°N$	1.0×10^{-4}
I-LCS-Q	$60°N$–$75°N$	2.7×10^{-4}
T-LCS-S	$45°N$–$65°N$	2.0×10^{-4}
I-LCS-S	$45°N$–$65°N$	3.3×10^{-4}

In this table, the first column lists the names of the thermospheric LCSs (T-LCS) and ionospheric LCSs (I-LCS) during both the geomagnetically quiet (-Q) and active (-S) periods. The latitude band used in the automated LCS identification process for each scenario is listed in the second column. The thresholds of FTLE values (σ_{TH}) are listed in the last column.

After obtaining the equator-most LCS ridge, the western-most point (ϕ_W) and eastern-most point (ϕ_E) of the LCS ridge can be defined. The midpoint of each LCS is computed by substituting the values of ϕ_W and ϕ_E into Eq. 6.1.

$$\phi_C = \frac{\phi_W + \phi_E}{2} \tag{6.1}$$

I compare the longitudinal angular difference between the midpoints of the thermospheric and ionospheric LCSs by making a difference between the midpoint of the thermospheric LCS (${}^T\phi_C$) and the midpoint of the ionospheric LCS (${}^I\phi_C$) as described in Eq. 6.2

$$\Delta\phi_C = {}^I\phi_C - {}^T\phi_C \tag{6.2}$$

6.1.2 Comparison of the thermospheric LCSs and the ionospheric LCSs during the geomagnetically quiet period.

Figure 6.1 shows a world map of FTLE values for neutral wind flows modeled by HWM14 at 350 km viewed from the geographic north pole for 16 March 2015 at t_0 = 12:00 UT, and τ = 3 hours. Local noon is fixed at the bottom of the plot. In this map, each pixel color represents the FTLE value and the color scale ranges from 0 (blue) to $5 \times 10^{-4}\ s^{-1}$ (yellow).

Due to the low neutral wind velocity and short integration time interval, there are few structures appearing at high latitudes in the map. There is a repelling LCS ridge that appears at $77°N$ in the local dusk sector. Equatorward of the yellow ridge, there is a locally maximum horseshoe like LCS ridge (light blue) that runs east-west at around $65°N$ from day sector to night sector. This light blue ridge may be interpreted as the equator-most LCS ridge, marked with red dots connected by a red line. This ridge appears to be similar to the ionospheric LCSs identified in Chapter 5, in that it is horseshoe-like.

As shown in Figure 6.1, the western-most point of this "U"-shaped structure is at $\phi_W^Q = -16°$, and the eastern-most point of it is at $\phi_E^Q = 176°$. So the horseshoe-like thermospheric LCSs is centered at longitude $\phi_C^Q = 80°$.

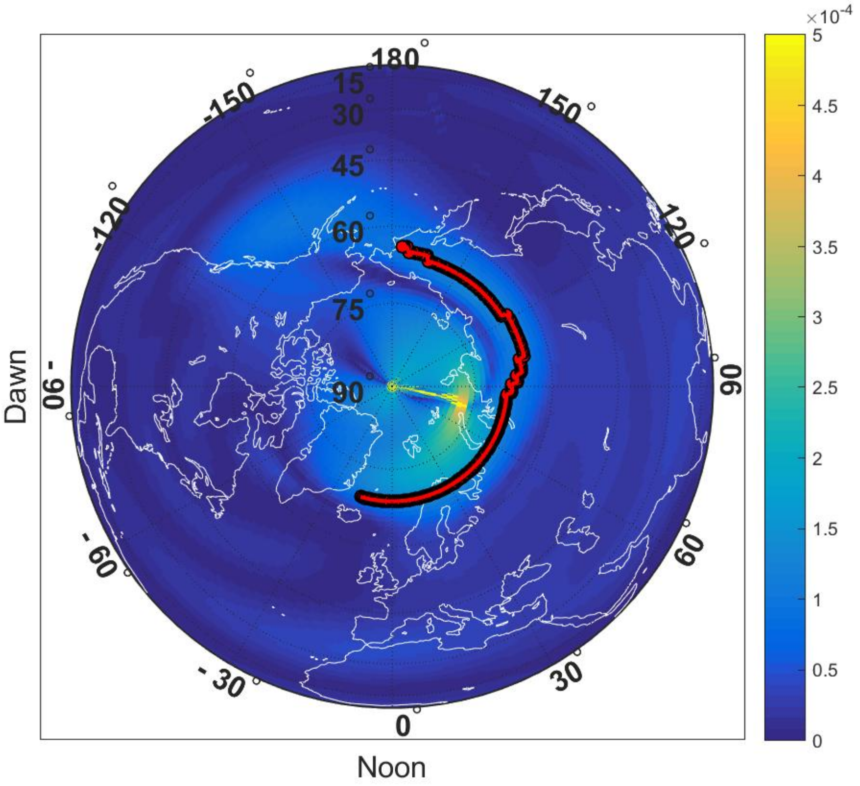

Figure 6.1. FTLE map for neutral winds at 350 km viewed from the geographic north pole on 16 March 2015 at t_0 = 12:00 UT and an integration time τ = 3 hours. Local noon is fixed at the bottom of the plot. The color scale represents the FTLE values varying from 0 to 5×10^{-4} s^{-1}; yellow ridges are the LCSs. The equator-most LCS ridge is marked with red dots connected by a red line.

Figure 6.2 is the north pole view of the FTLE map for plasma drifts modeled by Weimer 2005 and IGRF-12, at 350 km with the initial time at t_0 = 12:00 UT on 16 March 2015 and an integration interval of 3 hours. Local noon is fixed at the bottom of the plot. Each pixel color represents the FTLE value ranging from 0 to 5×10^{-4} s^{-1} and the yellow ridge is a repelling LCS. The blank area at lower latitudes is due to the vanishing of the Weimer potential to 0 V. There is a horseshoe-like LCS ridge that runs east-west in the day sector. The equator-most LCS ridge is marked with red dots connected by a red line.

As shown in Figure 6.2, the equator-most ionospheric LCS appears horseshoe-

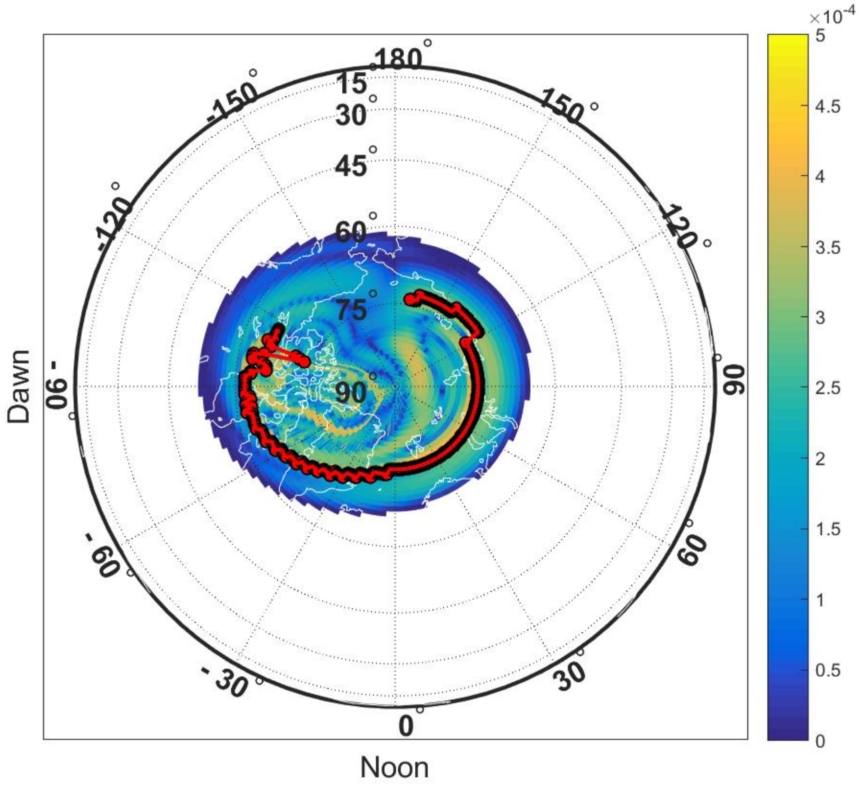

Figure 6.2. FTLE map for plasma drifts at 350 km viewed from the geographic north pole on 16 March 2015 at t_0 = 12:00 UT and an integration time $\tau = 3$ hours. Local noon is fixed at the bottom of the plot. The color scale represents the FTLE values varying from 0 to $5 \times 10^{-4}\ s^{-1}$. The equator-most LCS ridge is marked with red dots connected by a red line.

like, with the "U"-shaped structure opening at local night side. The western-most point of the horseshoe-like LCS is at $\phi_W^Q = -116°$ and the eastern-most point of it is at $\phi_E^Q = 170°$, making the "U"-shaped ionospheric LCS centered at a longitude of $\phi_C^Q = 27°$.

Compared to the FTLE map shown in Figure 6.1, there are more structures in the FTLE map of the modeled plasma drifts as shown in Figure 6.2, because the $\vec{E} \times \vec{B}$ drift velocity is larger than the neutral wind velocity at high latitudes.

Table 6.2 shows the parameters of the thermospheric LCSs and the ionospheric

Table 6.2. Parameters of the equator-most thermospheric LCS and ionospheric LCS in the northern hemisphere for the geomagnetically quiet period on 16 March 2015. The IT flows are simulated by separate empirical models.

LCS	ϕ_W^Q	ϕ_E^Q	ϕ_C^Q
T-LCS-Q	-16°	176°	80°
I-LCS-Q	-116°	170°	27°

LCSs during the geomagnetically quiet period. The types of LCSs during the quiet period are listed in the first column. The western-most point ϕ_W^Q and eastern-most point ϕ_E^Q of each LCS are listed in the second and third columns respectively. The last column shows the midpoint ϕ_C^Q of each LCS.

Since both the thermospheric LCS (T-LCS) and the ionospheric LCS (I-LCS) are horseshoe-like, to compare the shape of the T-LCS and the I-LCS, I use the angle between the center of those two "U"-shaped LCSs to quantify structure's difference in shape.

The angle between the midpoints of the T-LCS and the I-LCS is computed by substituting the midpoints of the T-LCS and the I-LCS listed in the last column of Table 6.2 into Eq. 6.2. The longitudinal difference angle between the midpoints of the T-LCS and the I-LCS during the geomagnetically quiet period is $\Delta\phi_C^Q = -53°$, which indicates that the I-LCS midpoint has a 53° westward shift with respect to the midpoint of the T-LCS. In other words, the T-LCS is 53° duskward of the I-LCS during the geomagnetically quiet condition investigated here.

6.1.3 Comparison of the thermospheric LCSs and the ionospheric LCSs during the geomagnetically active period.

Figure 6.3 shows the northern hemisphere FTLE map for neutral wind fields during the geomagnetically active period at t_0 = 12:00 UT on 17 March 2015 at 350 km. Local noon is fixed at the bottom of the plot. In this map the FTLE values are shown in pixel color ranging from 0 to $5 \times 10^{-4} s^{-1}$ and a yellow ridge is the repelling LCS. Compared to the FTLE map during the geomagnetically quiet period in Figure 6.1, there are more structures appearing at middle to high latitudes, extending equatorward. During the storm, the neutral winds have larger speeds than those during quiet period, so the neutral wind flows have more motion and fluid elements can repel further from each other in the flow.

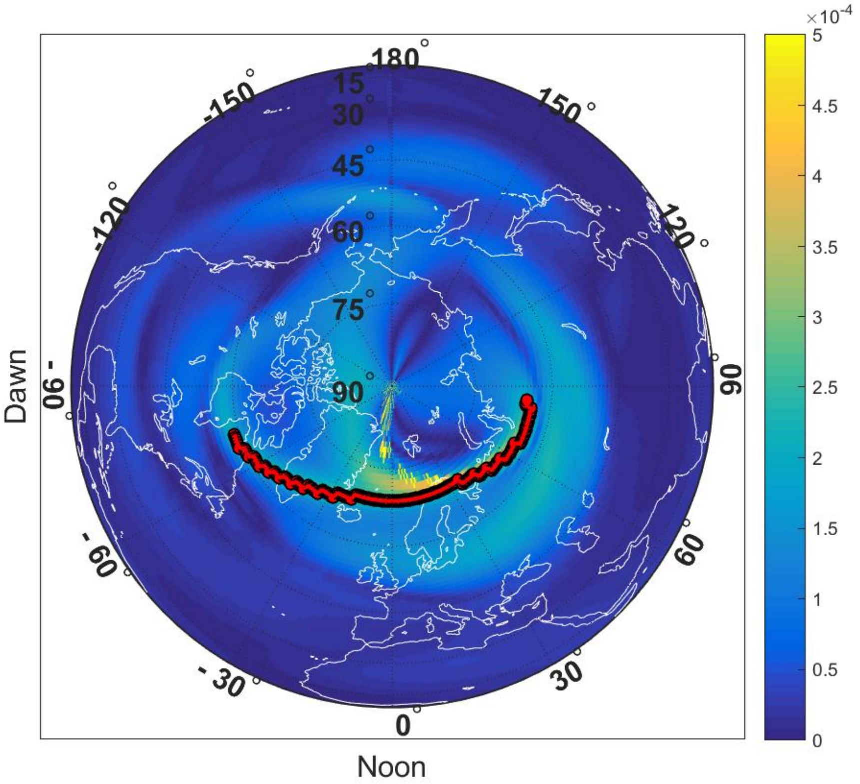

Figure 6.3. FTLE map for neutral winds at 350 km viewed from the geographic north pole on 17 March 2015 at $t_0 = 12{:}00$ UT and an integration time $\tau = 3$ hours. Local noon is fixed at the bottom of the plot. The color scale represents the FTLE values varying from 0 to $5 \times 10^{-4}\ s^{-1}$. The prominent LCS ridge is marked with red dots connected by a red line.

As shown in Figure 6.3, there is a yellow ridge that runs east-west at around $75°N$ in the dayside. There are also some secondary ridges (shown in light blue) appearing at lower latitude; however, in this work I focus on the prominent LCS ridge shown in yellow located at $75°N$. The LCS ridge is marked with red dots connected by a red line shown in Figure 6.3. The horseshoe-like LCS runs east-west from $\phi_W^S = -73°$ to $\phi_E^S = 84°$. The LCS is centered at ${}^T\phi_C^S = 5.5°$. Compared to the thermospheric LCS during the geomagnetically quiet period shown in Figure 6.1, the thermospheric LCS shifts sunward to local noon.

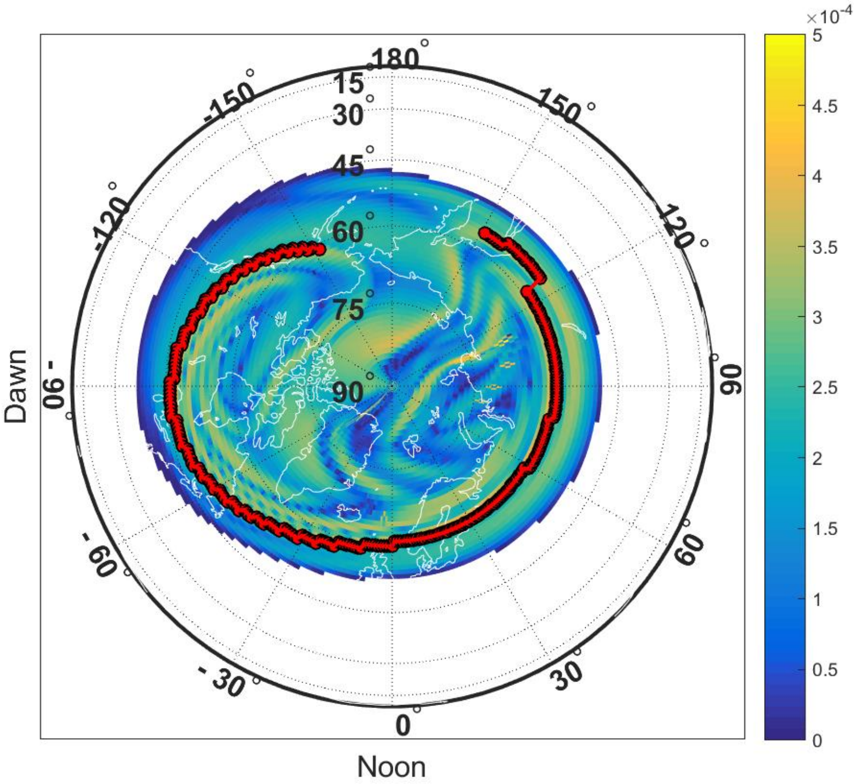

Figure 6.4. FTLE map for plasma drifts at 350 km viewed from the geographic north pole on 17 March 2015 at t_0 = 12:00 UT and an integration time τ = 3 hours. Local noon is fixed at the bottom of the plot. The color scale represents the FTLE values varying from 0 to $5 \times 10^{-4}\ s^{-1}$. The prominent LCS ridge is marked with red dots connected by a red line.

Figure 6.4 is the north pole view of the FTLE map of plasma drift during the geomagnetically stormy period at 350 km with the initial time at t_0 = 12:00 UT on 17 March 2015. In this map, LCSs appear at lower latitudes in the northern hemisphere.

There is a horseshoe-like repelling LCS that runs east-west in the day sector and curves poleward in the nightside. During the geomagnetically active period, the topology of LCSs becomes more complicated compared to the LCS patterns during the quiet period shown in Figure 6.2.

Compared to the thermospheric LCSs during the geomagnetically active period shown in Figure 6.3, there are more structures in the plasma drifts, due to the fast speed of the plasma drift. The equator-most prominent LCS ridge, marked with red dots connected by a red line within the latitude band of $45°N$ to $60°N$, runs east-west from $\phi_W^S = -152°$ to $\phi_E^S = 149°$. This LCS is centered at ${}^I\phi_C^S = -1.5°$. With respect to the "U"-shaped ionospheric LCS during the geomagnetically quiet period shown in Figure 6.2, the horseshoe-like ionospheric LCS during the geomagnetically active period moves sunward as the midpoint rotates westward, in other words, ${}^I\phi_C^S - {}^I\phi_C^Q = -28.5°$.

Table 6.3. Parameters of the equator-most thermospheric LCS and ionospheric LCS in the northern hemisphere for the geomagnetically active period on 17 March 2015. The IT flows are simulated by separate empirical models.

LCS	ϕ_W^S	ϕ_E^S	ϕ_C^S
T-LCS-S	-73°	84°	5.5°
I-LCS-S	-152°	149°	-1.5°

Table 6.3 shows the parameters of the thermospheric LCSs and the ionospheric LCSs, with the LCS types listed in the first column, the western-most and eastern-most points (ϕ_W and ϕ_E) listed in the second and third columns respectively, and the midpoint (ϕ_C) listed in last column.

Since both the thermospheric LCS (T-LCS) and the ionospheric LCS (I-LCS) are horseshoe-like, to compare the shape of the T-LCS and the I-LCS, I use the angle between the midpoints of those two “U”-shaped LCSs to quantify the difference.

The angle between the midpoints of the T-LCS and the I-LCS is computed by substituting the midpoints of the T-LCS and the I-LCS listed in the last column of Table 6.3 into Eq. 6.2. The longitudinal difference angle between the midpoints of the T-LCS and the I-LCS during the geomagnetically active period is $\Delta\phi_C^S = -7^\circ$, which indicates that the I-LCS has 7° westward shift with respect to the T-LCS. In other words, the T-LCS is only 7° duskward of the I-LCS during the geomagnetically active condition shown here. This is in contrast to the difference between the IT LCS midpoints during the quiet period, of 21.5°. The reduction in the difference during storm-times indicates increased IT coupling, which seems to bring the I-LCS and T-LCS into closer alignment during the geomagnetically active period.

In the following section, I use a self-consistent explicitly coupled physics-based model to simulate the IT flows and apply the LCS technique to confirm whether the LCS alignment in the IT flows also increases when using an explicitly coupled IT model.

6.2 Comparison of the thermospheric LCS and the ionospheric LCS based on TIEGCM

In Section 6.1, I compared the thermospheric LCSs and the ionospheric LCSs based on the flows modeled by two independent empirical models, HWM14 for neutral winds and Weimer 2005 and IGRF-12 for plasma drifts. The results show that even the LCSs yielded from the flows simulated by individual models can reveal the dynamical interaction between the thermospheric flows and ionospheric flows.

In this study, I use a self-consistent physical model , the Thermosphere Ionosphere Electrodynamics General Circulation Model (TIEGCM), to model the thermospheric winds and ionospheric drifts. By comparing the structures yielded from these flows, I analyze the dynamical interaction in the IT system.

6.2.1 Simulation Configuration. To do this, I parameterize the 2-D global atmosphere by longitude and latitude with the grid space of 2.5°, and assign a particle to each gridpoint at time t_0. This grid resolution is the finest resolution at which TIEGCM currently operates. This work is conducted at the height of 350 km, identical to the setup in Section 6.1. TIEGCM is used to generate the velocity fields for both neutral winds and plasma drifts. Each flow field is computed every 5 minutes and used as inputs to ITALCS to compute the FTLE scalar field. The temporal setup in this work is same as that in Section 6.1. According to the AE-index shown in Figure 5.1, introduced in Chapter 5, the quiet period is from 12:00 UT to 15:00 UT on 16 March 2015, and the active period is from 12:00 UT to 15:00 UT on 17 March 2015. I compare the thermospheric LCS and ionospheric LCS during both the geomagnetically quiet period and storm period.

In this work, I map the FTLE fields for neutral winds flows and plasma drifts on polar maps viewed from the geographic north pole, and compare the shapes of the locally maximum FTLE ridges in those maps. To extract the equator-most or prominent LCSs, during the geomagnetically quiet period, I choose a latitude zone between $43.75°N$ and $76.25°N$ and select the position of the maximum FTLE value at each longitude. FTLE values larger than $1.1 \times 10^{-4}\ s^{-1}$ (for the thermospheric FTLE field) and $2 \times 10^{-4}\ s^{-1}$ (for the ionospheric FTLE field) are regarded as the LCS ridges. The thresholds of FTLE value for the thermospheric FTLE maps and ionospheric FTLE maps are different, because the ionospheric FTLE values are generally larger than the thermospheric FTLE values. As discussed in Chapters 4 and 5, both the thermospheric LCSs and the ionospheric LCSs expand equatorward during a geomagnetic storm. To get the most equatorward LCSs, however in this work, I also choose a latitude zone between $43.75°N$ and $76.25°N$ and pick the position of the maximum FTLE value at each longitude. FTLE values larger than 1.4×10^{-4} s^{-1} (for the thermospheric FTLE field) and 2×10^{-4} s^{-1} (for the ionospheric FTLE field) are treated as the LCS ridges. The parameters for this work are summarized in Table 6.4.

Table 6.4. Parameters of the identification method for the analysis with the IT flows modeled by TIEGCM.

LCS	latitude bands	σ_{TH} s^{-1}
T-LCS-Q	$43.75° N$–$76.25° N$	1.1×10^{-4}
I-LCS-Q	$43.75° N$–$76.25° N$	2.0×10^{-4}
T-LCS-S	$43.75° N$–$76.25° N$	1.4×10^{-4}
I-LCS-S	$43.75° N$–$76.25° N$	2.0×10^{-4}

In this table, the first column lists the names of the thermospheric LCSs (T-LCS) and ionospheric LCSs (I-LCS) during both the geomagnetically quiet (-Q) and active (-S) periods. The latitude band for each scenario is listed in the second column. The thresholds of FTLE values (σ_{TH}) are listed in the last column.

After obtaining the equator-most LCS ridge, the western-most point (ϕ_W) and eastern-most point (ϕ_E) of the LCS ridge can be defined. The midpoint of each LCS is computed by substituting the values of ϕ_W and ϕ_E into Eq. 6.1. I compare the longitudinal angular difference between the midpoints of the thermospheric and ionospheric LCSs by computing the difference between the midpoint of the thermospheric LCS (${}^{T}\phi_C$) and the midpoint of the ionospheric LCS (${}^{I}\phi_C$) as described in Eq. 6.2.

6.2.2 Comparison of the thermospheric LCSs and the ionospheric LCSs during the geomagnetically quiet period.

Figure 6.5 shows the world map of FTLE values for neutral winds modeled by TIEGCM at 350 km viewed from the geographic north pole on 16 March 2015 at t_0 = 12:00 UT, and $\tau = 3$ hours. Local noon is fixed at the bottom of the plot. In this map, each pixel color represents the FTLE value, and the color scale ranges from 0 (blue) to $5 \times 10^{-4} s^{-1}$ (yellow). A yellow ridge is a repelling LCS.

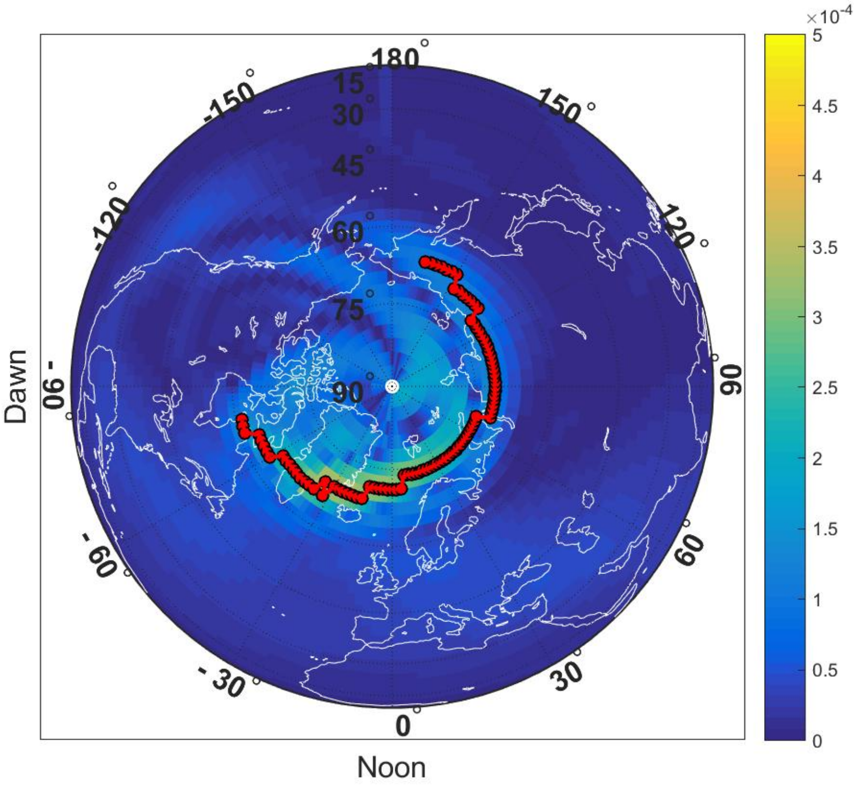

Figure 6.5. FTLE map for neutral winds at 350 km on 16 March 2015 at t_0 = 12:00 UT with an integration time $\tau = 3$ hours, for neutral wind fields modeled by TIEGCM viewed from the geographic north pole. Local noon is fixed at the bottom of the plot. The color scale represents the FTLE values varying from 0 to $5 \times 10^{-4}\ s^{-1}$; yellow ridges are the LCSs. The prominent LCS ridge is marked with red dots connected by a red line.

In Figure 6.5, the thermospheric LCSs yielded from the neutral wind flows modeled by TIEGCM appear at high latitudes in the northern hemisphere during the geomagnetically quiet period. There is a repelling LCS ridge that runs east-west between $60°N$ and $75°N$ from day sector to night sector, marked with red dots connected by a red line. The LCS appears horseshoe-like with the “U”-shaped structure opening on the local night side.

As shown in Figure 6.5, the western-most point of this “U”-shaped structure is at ${}^{T}\phi_{W}^{Q} = -77.5°$, and the eastern-most point of it is at ${}^{T}\phi_{E}^{Q} = 165°$. The thermospheric LCS’s midpoint is at ${}^{T}\phi_{C}^{Q} = 43.75°$.

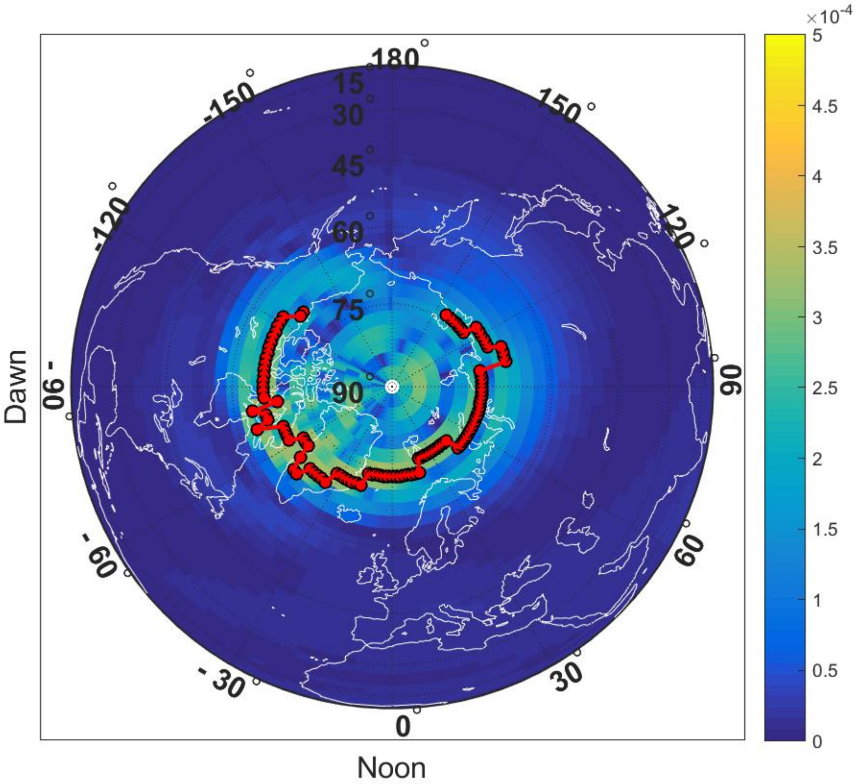

Figure 6.6. FTLE map for plasma drifts at 350 km viewed from the geographic north pole on 16 March 2015 at $t_0 = $ 12:00 UT and an integration time $\tau = 3$ hours. Local noon is fixed at the bottom of the plot. The color scale represents the FTLE values varying from 0 to $5 \times 10^{-4}\ s^{-1}$; yellow ridges are the LCSs. The equator-most LCS ridge is marked with red dots connected by a red line.

Figure 6.6 is the north pole view of the FTLE map for plasma drifts modeled by TIEGCM, at 350 km with the initial time at $t_0 = $ 12:00 UT on 16 March 2015 and an integration time of $\tau = 3$ hours. Local noon is fixed at the bottom of the plot. Each pixel color represents the FTLE value ranging from 0 to $5 \times 10^{-4}\ s^{-1}$, and the yellow ridge is a repelling LCS. The strong repelling ridges are more prominent at high latitudes. There is a horseshoe-like LCS ridge that runs east-west in the day sector and curves poleward in the night side. The equator-most LCS ridge is marked with red dots connected by a red line.

As shown in Figure 6.6, the equator-most ionospheric LCSs again appear horseshoe-like, with the "U"-shaped structure opening on the local nightside. The LCS extends from ${}^{I}\phi_W^Q = -130°$ to ${}^{I}\phi_E^Q = 142.5°$, making the "U"-shaped ionospheric LCS centered at ${}^{I}\phi_C^Q = 6.25°$.

Compared to the FTLE map shown in Figure 6.5, there are more structures in the modeled plasma drift as shown in Figure 6.6, because the $\vec{E} \times \vec{B}$ drift velocity is larger than the neutral wind velocity at high latitudes.

Table 6.5. Parameters of the equator-most thermospheric LCS and ionospheric LCS in the northern hemisphere for the geomagnetically quiet period on 16 March 2015. The IT flows are simulated by TIEGCM.

LCS	ϕ_W^Q	ϕ_E^Q	ϕ_C^Q
T-LCS-Q	-77.5°	165°	43.75°
I-LCS-Q	-130°	142.5°	6.25°

Table 6.5 shows the parameters of the thermospheric LCSs and the ionospheric LCSs, with the LCS types listed in the first column, the western-most and eastern-most points (ϕ_W and ϕ_E) listed in the second and third columns respectively, and the midpoint (ϕ_C) listed in the last column.

Since both the thermospheric LCS (T-LCS) and the ionospheric LCS (I-LCS) are horseshoe-like, to compare the T-LCS and the I-LCS, I use the angle between their midpoints to quantify the difference in their orientations.

The angle between the midpoints of the T-LCS and the I-LCS is computed by substituting the midpoints of the T-LCS and the I-LCS listed in the last column of Table 6.5 into Eq. 6.2. The longitudinal difference angle between the midpoints of the T-LCS and the I-LCS during the geomagnetically quiet period is $\Delta\phi_C^Q = -37.5°$, which indicates that the I-LCS is shifted westward 37.5° with respect to the T-LCS. The westward shift of the T-LCS with respect to the I-LCS matches the result discussed in Section 6.1.2, although the shift is not as great with TIEGCM as it is using the empirical models.

6.2.3 Comparison of the thermospheric LCSs and the ionospheric LCSs during the geomagnetically active period. Figure 6.7 shows the northern hemisphere FTLE map for neutral wind fields during the geomagnetically active period at t_0 = 12:00 UT on 17 March 2015 at 350 km. Local noon is fixed at the bottom of the plot. In this map the FTLE values are shown in pixel color ranging from 0 to $5 \times 10^{-4}\ s^{-1}$, and a yellow ridge is the repelling LCS.

As shown in Figure 6.7, there is a yellow ridge that runs east-west between $45°N$ and $75°N$ in the local noon sector. The LCS ridge is marked with red dots connected by a red line, shown in Figure 6.7. The horseshoe-like LCS runs east-west from ${}^T\phi_W^S = -102.5°$ to ${}^T\phi_E^S = 80°$. The LCS is centered at ${}^T\phi_C^S = -11.25°$. Compared to the thermospheric LCSs during the geomagnetically quiet period shown in Figure 6.5, the thermospheric LCSs shift sunward toward local noon. A comparison of LCSs during the geomagnetically quiet period (shown in Figure 6.5) and active period (shown in Figure 6.7) indicates that the thermospheric LCSs yielded from TIEGCM are sensitive to the geomagnetic conditions. The thermospheric LCSs respond to geomagnetic activity by shifting sunward and extending toward the equator.

Figure 6.8 is the north pole view of the FTLE map for plasma drift during the geomagnetically stormy period at 350 km with initial time t_0 = 12:00 UT on

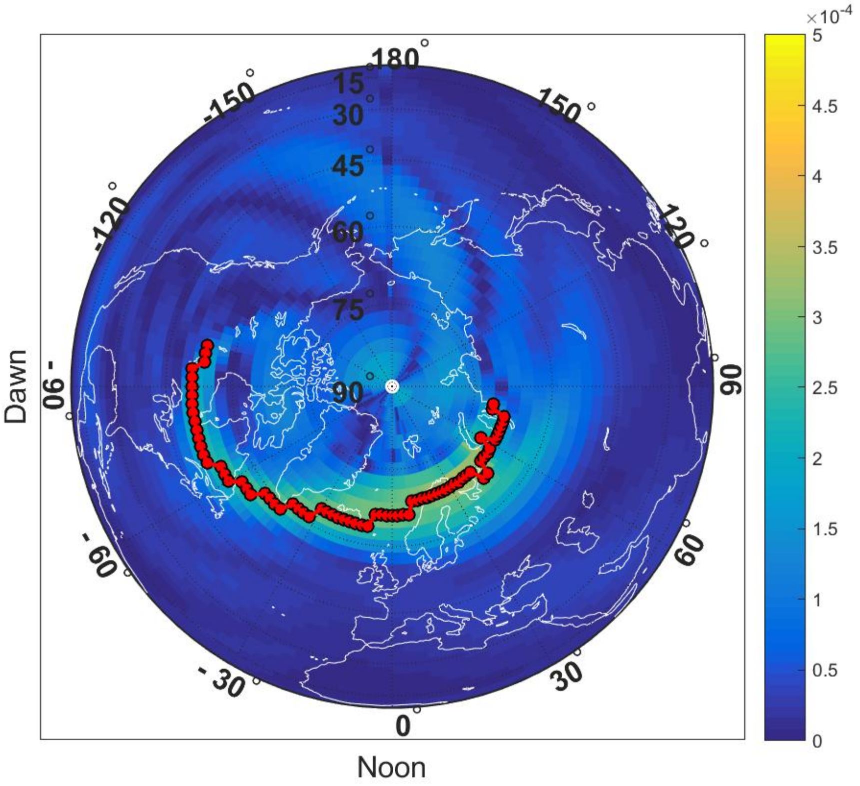

Figure 6.7. FTLE map for neutral winds at 350 km viewed from the geographic north pole on 17 March 2015 at $t_0 = $ 12:00 UT and an integration time $\tau = 3$ hours. Local noon is fixed at the bottom of the plot. The color scale represents the FTLE values varying from 0 to $5 \times 10^{-4}\ s^{-1}$; yellow ridges are the LCSs. The prominent LCS ridge is marked with red dots connected by a red line.

17 March 2015. In this map, there are more LCSs appearing at lower latitudes in the northern hemisphere compared to the FTLE map shown in Figure 6.7. There is a horseshoe-like repelling LCS that runs east-west in the day sector and curves poleward in the nightside.

The equator-most prominent LCS ridge, marked with red dots connected by a red line, lies in the latitude band of $45°N$ to $70°N$, running west to east from ${}^I\phi^S_W = -142.5°$ to ${}^I\phi^S_E = 110°$. The LCS is centered at ${}^I\phi^S_C = -16.25°$. With respect to the "U"-shaped ionospheric LCS during the geomagnetically quiet period shown in Figure 6.6, the horseshoe-like ionospheric LCS during the geomagnetically active

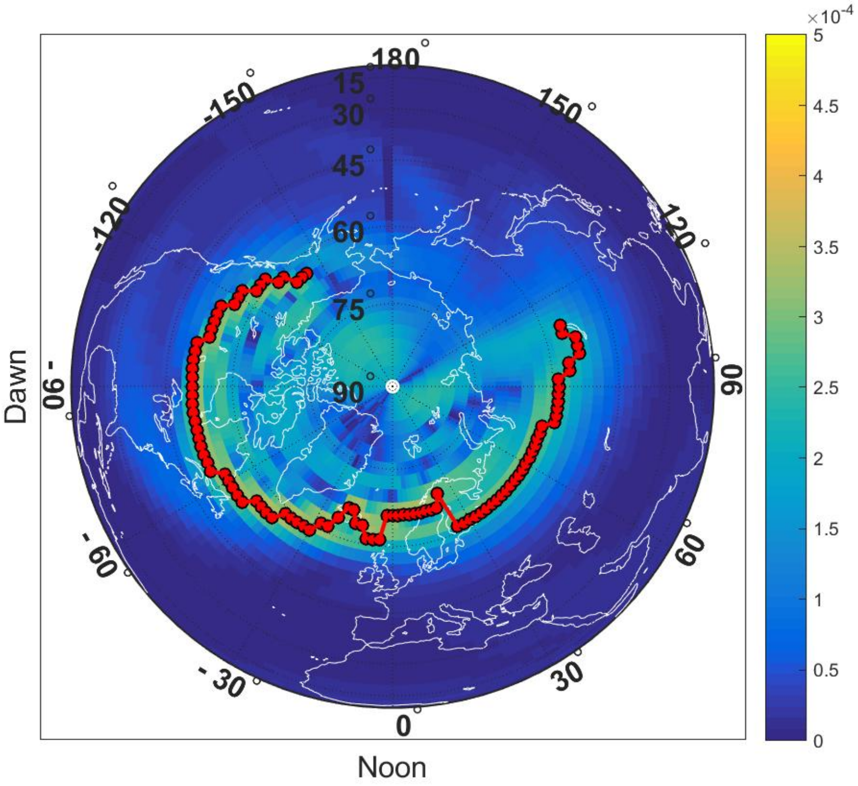

Figure 6.8. FTLE map for plasma drifts at 350 km viewed from the geographic north pole on 17 March 2015 at t_0 = 12:00 UT and an integration time τ = 3 hours. Local noon is fixed at the bottom of the plot. The color scale represents the FTLE values varying from 0 to 5×10^{-4} s^{-1}; yellow ridges are the LCSs. The prominent LCS ridge is marked with red dots connected by a red line.

period shifts to the morning sector, as the midpoint of the LCS has rotated westward by 22.5°.

Table 6.6. Parameters of the equator-most thermospheric LCS and ionospheric LCS in the northern hemisphere for the geomagnetically active period on 17 March 2015. The IT flows are simulated by TIEGCM.

LCS	ϕ_W^S	ϕ_E^S	ϕ_C^S
T-LCS-S	-102.5°	80°	-11.25°
I-LCS-S	-142.5°	110°	-16.25°

Since both the thermospheric LCS (T-LCS) and the ionospheric LCS (I-LCS) are horseshoe-like, to compare the shape of the T-LCS and the I-LCS, I use the angle between the center of those two "U"-shaped LCSs to quantify the shape difference. Table 6.6 shows the extent of the thermospheric LCS and the ionospheric LCS resulting from TIEGCM.

The angle between the midpoints of the T-LCS and the I-LCS is computed by substituting the midpoints of the T-LCS and the I-LCS listed in the last column of Table 6.6 into Eq. 6.2. The longitudinal difference angle between the midpoints of the T-LCS and the I-LCS during the geomagnetically active period is $\Delta\phi_C^S = -5°$, which indicates that the I-LCS has 5° westward shift with respect to the T-LCS. The westward shift of the T-LCS with respect to the I-LCS matches the result discussed in Section 6.1.3. During the geomagnetically active period, the orientation angle with TIEGCM is similar to that with empirical models.

6.3 Discussion

6.3.1 The dynamical analysis with IT flows from independent empirical models.

As shown in Sections 6.1.2 and 6.1.3, the delay angle during the geomagnetically quiet period is $\Delta\phi_C^Q = -53°$ and during the geomagnetically active period is $\Delta\phi_C^S = -7°$. The delay angle decreases as geomagnetic activity increases.

The thermosphere and ionosphere are coupled through the collision of neutral and charged particles. In the Earth's upper atmosphere (above 200 km), atomic oxygen dominates the composition of the thermosphere, and the ionosphere is dominated by the atomic oxygen ions ionized by the solar radiation. Hence the IT system's structure and dynamics are governed by the interactions of the O^+ ions and their parent gas [18]. Such parameters like the collision frequency of $O^+ - O$ can, at some stage, reflect the dynamical interaction in IT system.

The equation modeling O^+ neutral collision frequency ν_{O^+} shown below is reprinted from [54]:

$$\nu_{O^+} = aN_O(\frac{T_i + T_n}{2})^{0.5}[b - c\log_{10}(\frac{T_i + T_n}{2})]^2 + dN_{O_2} + eN_{N_2} \tag{6.3}$$

Where T_i and T_n are the temperatures of ions and neutral particles respectively, and N_O, N_{O_2}, and N_{N_2} stand for the density of atomic oxygen O, molecular oxygen O_2, and molecular nitrogen N_2 respectively. The constants $a - e$ can be found in Table 6.7.

Table 6.7. Constants and Their Values

Constant	Value	Units
a	4.45×10^{-11}	cm^3/s
b	1.04	-
c	0.0067	-
d	6.64×10^{-10}	cm^3/s
e	6.82×10^{-10}	cm^3/s

Eq. (6.3) shows that the collision frequency ν_{O^+} is a function of temperature, akin to a function of energy. During a geomagnetically active period, the energy of the IT system is increased due to the impact of solar wind and increases the collision frequency of $O^+ - O$ ν_{O^+} in the upper atmosphere. Since there are more collisions among charged particles and neutral particles during a geomagnetic storm, the neutral particles speed up rapidly compared to those moving during a geomagnetically quiet period.

For this reason, as the collision frequency ν_{O^+} increases under the geomagnetically active condition, the delay angle between the "U"-shaped LCSs in thermospheric flows and ionospheric flows decreases. The decrease in the I-LCS and the T-LCS midpoint angular difference during geomagnetically quiet and active periods appears to be the evidence of such a dynamical interaction in the IT system.

Note that this work is conducted using the neutral wind flows and plasma drifts modeled by two independent empirical models. Although the interactions of neutral particles and charged particles are not explicitly considered in these models, LCS analysis has the ability to show the dynamical connection of the flows simulated by the isolated models.

6.3.2 The dynamical analysis with IT flows modeled by TIEGCM.

As shown in Sections 6.2.2 and 6.2.3, the LCS orientation angle difference during the geomagnetically quiet period is $\Delta\phi_C^Q = -37.5°$ and during the geomagnetically active period is $\Delta\phi_C^S = -5°$. The orientation difference angle decreases as geomagnetic activity increases.

As described in Section 6.3.1, the thermosphere and ionosphere are coupled through the collision of neutral and charged particles, which is mainly dominated by the collisions between atomic oxygen ions O^+ and their neutral parent gas. The collision frequency of $O^+ - O$, ν_{O^+} is a function of temperature/energy. Under geomagnetically active conditions, the energy of the IT system increases, so the collision frequency increases as well. With more collisions among charged particles and neutral particles, the T-LCS and the I-LCS midlongitude difference decreases. The comparison of delay angle of the T-LCS with respect to the I-LCS during the geomagnetically quiet and active periods in a self-consistently coupled thermosphere-ionosphere model shows evidence of dynamical interaction in the IT system.

6.4 Summary

This chapter shows a way of analyzing dynamical interactions in the IT system via the LCS technique. The comparisons between the thermospheric LCSs and ionospheric LCSs during both geomagnetically quiet and active periods indicate that the dynamical interaction in the form of charge-neutral collisions can be visualized by the FTLE maps of the IT flows. During the active period, due to the high collision frequency, the difference angle between the LCSs in the neutral wind flows (T-LCSs) and the governing structures in the plasma drifts (I-LCSs) becomes smaller, and the T-LCSs and I-LCSs align more closely.

As with the LCSs yielded from the IT flows modeled by the empirical models described in Chapter 4 and Chapter 5, LCS ridges are predicted to exist in both neutral winds flows and plasma drifts modeled by TIEGCM. In the thermospheric flows, the LCSs are more prominent at higher latitudes and respond to geomagnetic activity. During a geomagnetic storm, the LCSs expand to lower latitudes. In the ionospheric flows, the strong repelling ridges are predominantly horseshoe-like structures centered in the day sector and curving back on themselves to form the opening of a "U" on the nightside. During a geomagnetic storm, LCSs appear at lower latitudes. Although TIEGCM models ionospheric drifts globally, including low-latitudes, no low-latitude drifts were investigated in this work. At low latitudes, the $\vec{E} \times \vec{B}$ drift are not in the horizontal plane, unlike the high-latitudes. To analyze and compare drifts with thermospheric winds, and globally, would require a 3-D analysis of LCSs.

The dynamical interaction in the IT region can be analyzed by applying LCS technique. By comparing the thermospheric LCSs are ionospheric LCSs, during both quiet and storm periods, the energy and momentum exchange between neutral particles and charged particles can be visualized as the T-LCS and I-LCS align more closely with the geomagnetic activity increasing.

CHAPTER 7

CONCLUSION

7.1 Overview

Lagrangian Coherent Structure (LCS) analysis has been widely applied to several fields, e.g. oceanography. However, prior to this work, LCS analysis had not been investigated in the upper atmosphere globally. The goal of this work was to identify the LCS in upper atmospheric flows for the first time, and to provide a novel way to reveal the dynamical interaction in the IT system. FTLE analysis of the modeled upper atmospheric flows provided insights into the following questions.

7.2 HOW to identify Lagrangian Coherent Structures at global scale

In Chapter 3, ITALCS, a 2-D algorithm for computing FTLE scalar field, was introduced. By testing with a canonical flow and comparing the result of FTLE maps with the outputs of FlowVC, a publicly available LCS numerical solver, ITALCS was validated.

To explore the structures in the upper atmospheric flows on a global scale, the domain was parameterized with longitude and latitude. In this case, the input velocity fields of ITALCS were described as angular rates. For the upper atmosphere, the spherical domain is periodic in both longitude and latitude. Additional logic in ITALCS keeps the particles within a longitudinal domain of $(\phi_{min}, \phi_{max}) = (-180^\circ, 180^\circ)$ and latitude domain of $(\lambda_{min}, \lambda_{max}) = (-90^\circ, 90^\circ)$. For particles flowing "beyond" the boundaries, the coordinates of those points will be wrapped around back into the domains.

ITALCS is an easily customized LCS numerical solver that can be applied to both periodic and aperiodic flows, both time-independent and time varying fields, both Euclidean and non-Euclidean domains, and can conduct FTLE computation both forward in time to get the repelling LCS and backward in time to get the attracting LCS. The outputs of ITALCS are both a FTLE scalar field of the domain and the positions and trajectories of the tracer particles. ITALCS offers an efficient and precise way to explore the LCSs in upper atmospheric flows.

7.3 WHERE are the LCSs in the thermospheric flows, and HOW can they bound material transport?

The innovation in Chapter 4 was the identification of the global scale LCSs in the thermospheric flows simulated by the empirical horizontal wind model HWM14.

A comparison among 150 km, 250 km, and 350 km height at 12:00 UT on 13 March 2015 indicated that thermospheric LCSs are more prominent at higher altitudes, due to the lower velocity caused by higher density and more collisions at lower altitudes. The structures are at $40° - 80°$ geographic latitudes in the morning sector during geomagnetic quiet period, while the LCSs have more complex topology and may extend into local afternoon due to active geomagnetic conditions. A test with water vapor observations revealed that the thermospheric LCSs can act as predictive transport barriers to bound material convection.

7.4 WHERE are the LCSs in the ionospheric flows, and HOW can they bound material transport?

In Chapter 5, ionospheric LCSs are predicted to exist based on the flows simulated by empirical model Weimer 2005 and IGRF-12.

The high latitude ionospheric LCSs are predominantly horseshoe-like structures centered in the day sector and curving poleward on the night side. The "U" shape structure rotates with respect to the Earth to keep the closed side of the "U" fixed to local noon. During a geomagnetic storm, LCSs have more complex topology and extend equatorward. Due to the vanishing potential at lower latitudes, the study in this chapter made no claims about the repelling structures at low latitudes.

A simulation of polar cap patch formation and propagation indicated that the storm enhanced density must exist poleward of the ionospheric LCS ridge in the plasma drift flows in order for the polar cap patch to be able to form.

7.5 WHAT are the dynamical interaction of LCSs in the IT system?

In Chapter 6, a comparison using the separate empirical models used in Chapter 4 and 5 was conducted, followed by the use of a self-consistent physical model TIEGCM to generate the modeled thermospheric flows and ionospheric flows. For both the empirical models and the coupled physics models, the flows yield LCSs, and the LCSs respond to geomagnetic activity. In the IT system, the dynamical interaction was analyzed by comparing the thermospheric LCSs and ionospheric LCSs. The increased alignment of LCSs in thermosphere and ionosphere during storm time reveals the enhanced energy and momentum exchange in the IT region.

7.6 Looking forward

7.6.1 ITALCS. In the future ITALCS can be updated to be a 3-D algorithm. This is simply an extension of the equations given in this work to a third dimension. Also the algorithm needs a routine implemented for computing the FTLE over a local area. For the local FTLE computation, the boundary problem can be solved by applying the finite domain FTLE method introduced by Tang et al., [65].

7.6.2 Thermospheric Lagrangian Coherent Structures. In the future, an analysis of the 3-D thermospheric flows via the updated 3-D ITALCS will give an insight of the vertical transport in the thermosphere using TIEGCM. The water vapor detection analysis could be extended to multiple days as more data sets similar to the space shuttle launch event on 8 July 2011 are documented in [62]. Also the LCSs analysis could compare with all the space shuttle exhaust events listed in [63]. Thermospheric LCSs might be usable as a proxy indicator of charge-neutral collision rate or nitrogen oxides (NO_x) or oxygen transport.

7.6.3 Ionospheric Lagrangian Coherent Structures. Since the gyration of the charged particles occurs about the magnetic field lines, 2-D ionospheric LCSs in the polar area acting as material transport barriers might be mapped out into the equatorial zone of the magnetosphere to act as the transport barrier in the magnetopause. At lower latitudes, the plasma drift convection has a vertical component. For that reason, a simulation including both low- and high-latitude electrodynamics will require a full 3-D integration in ITALCS.

7.6.4 The dynamical interaction in IT system via LCS analysis. In the future, applying image processing methods e.g. single value decomposition (SVD), to improve the resolution of the FTLE map with coarse grid will help in locating a well-defined LCS in both thermospheric flows and ionospheric flows modeled by TIEGCM. Switching to a high resolution physical model is another way to identify more well-defined structures in IT system. When analyzing the structures in the IT system, more parameters such as the particles' density and temperature, as well as the species of the particles can be considered.

APPENDIX A

FTLE MAPS FOR THE TIME-VARYING DOUBLE-GYRE

The time-varying double-gyre consists two vortices that alternately expand and contract with time as described in Section 3.1.2. The FTLE maps of double-gyre flow for different initial times over the interval $t_0 = [0\text{ s}, 0.98\text{ s}]$ and the integration time $\tau = 1$ s are shown in this appendix. For all the maps, each pixel color represents the FTLE value varying from 0 (blue) to 5 s^{-1} (yellow).

The FTLE values quantify the degree of separation, and the LCS is located at the locally maximum FTLE values (i.e., the bright yellow curve).

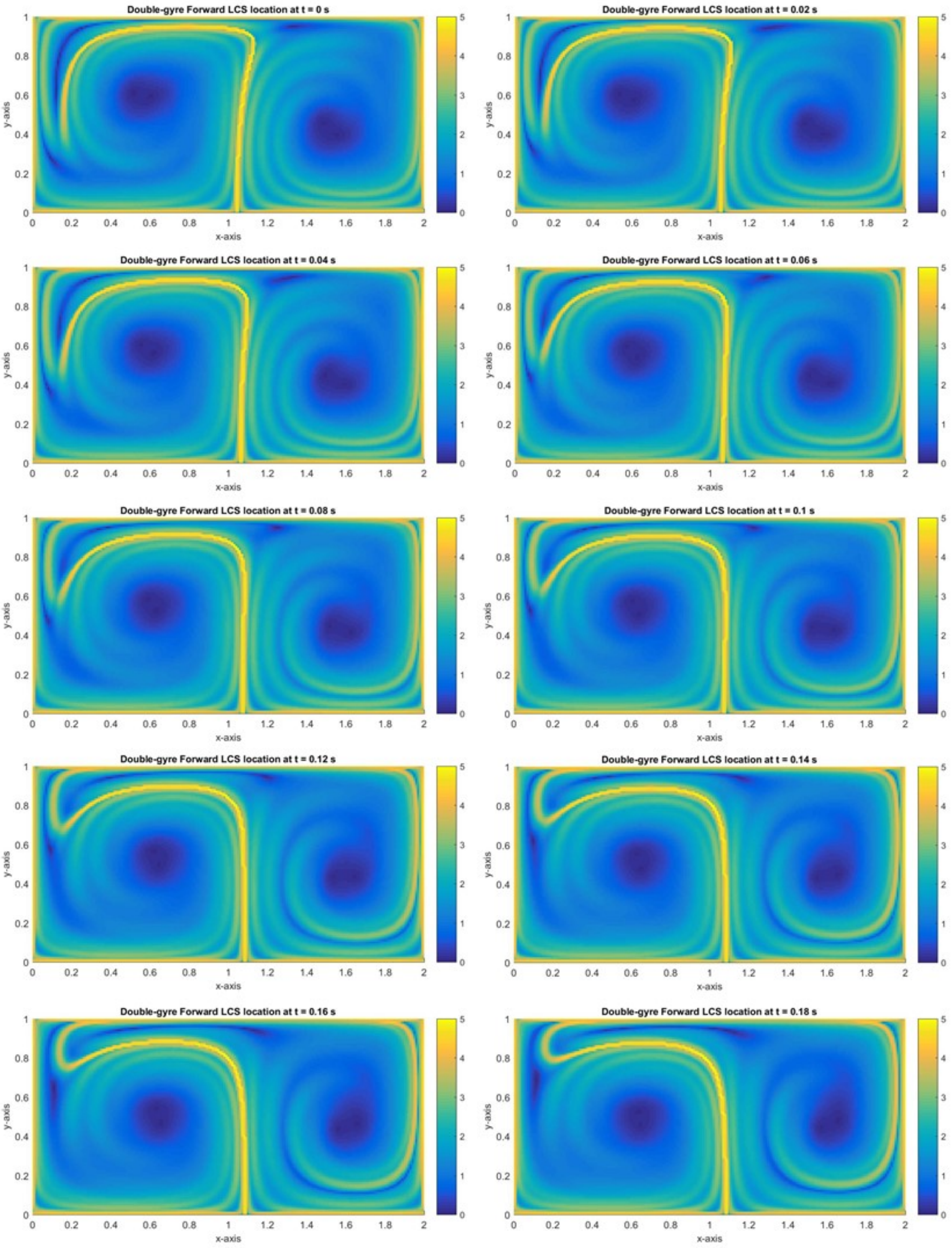

Double-gyre Forward LCS location at t = 0 s

Double-gyre Forward LCS location at t = 0.02 s

Double-gyre Forward LCS location at t = 0.04 s

Double-gyre Forward LCS location at t = 0.06 s

Double-gyre Forward LCS location at t = 0.08 s

Double-gyre Forward LCS location at t = 0.1 s

Double-gyre Forward LCS location at t = 0.12 s

Double-gyre Forward LCS location at t = 0.14 s

Double-gyre Forward LCS location at t = 0.16 s

Double-gyre Forward LCS location at t = 0.18 s

Figure A.1. FTLE maps for double-gyre field at $t_0 = 0$ s – 0.18 s

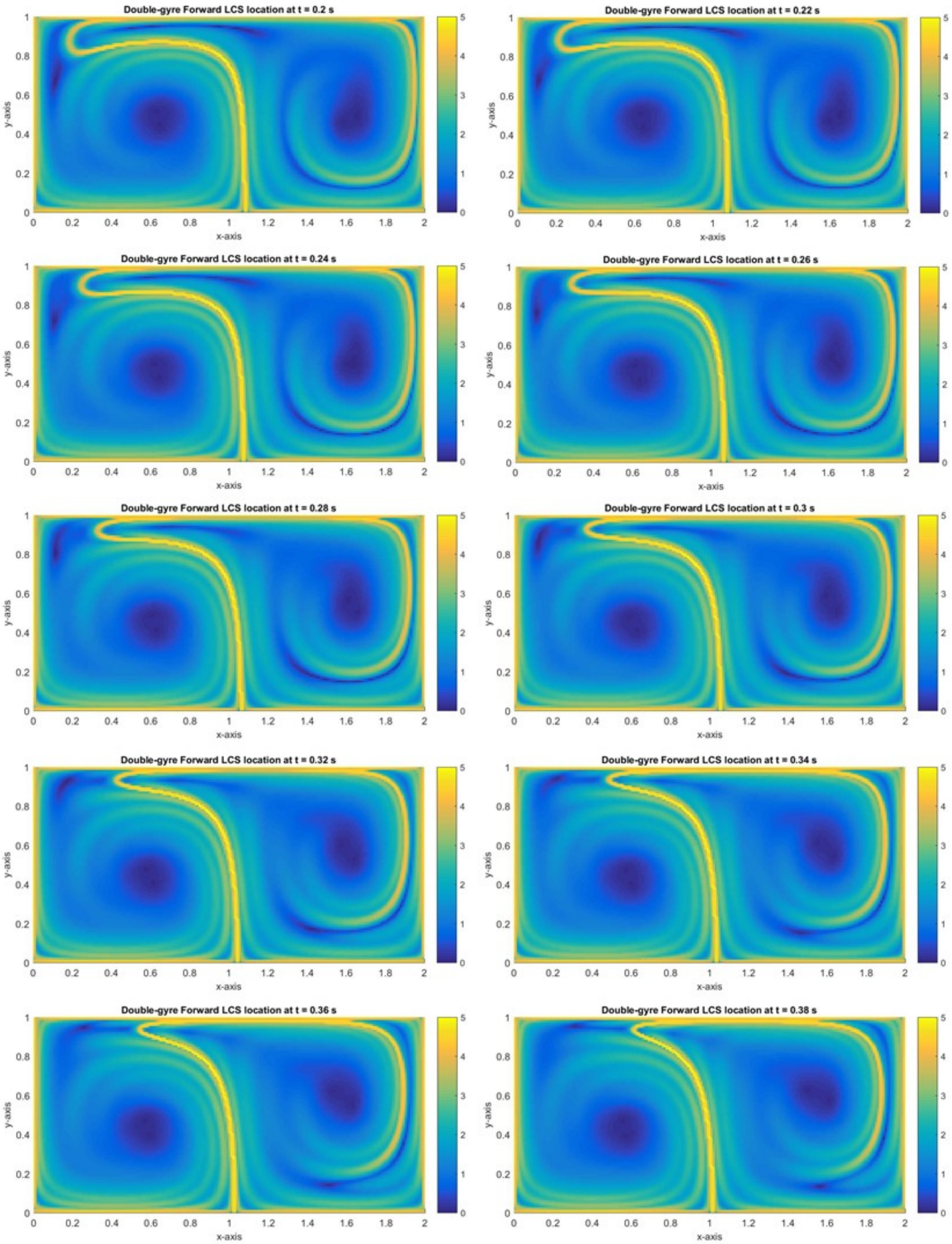

Figure A.2. FTLE maps for double-gyre field at $t_0 = 0.20$ s – 0.38 s

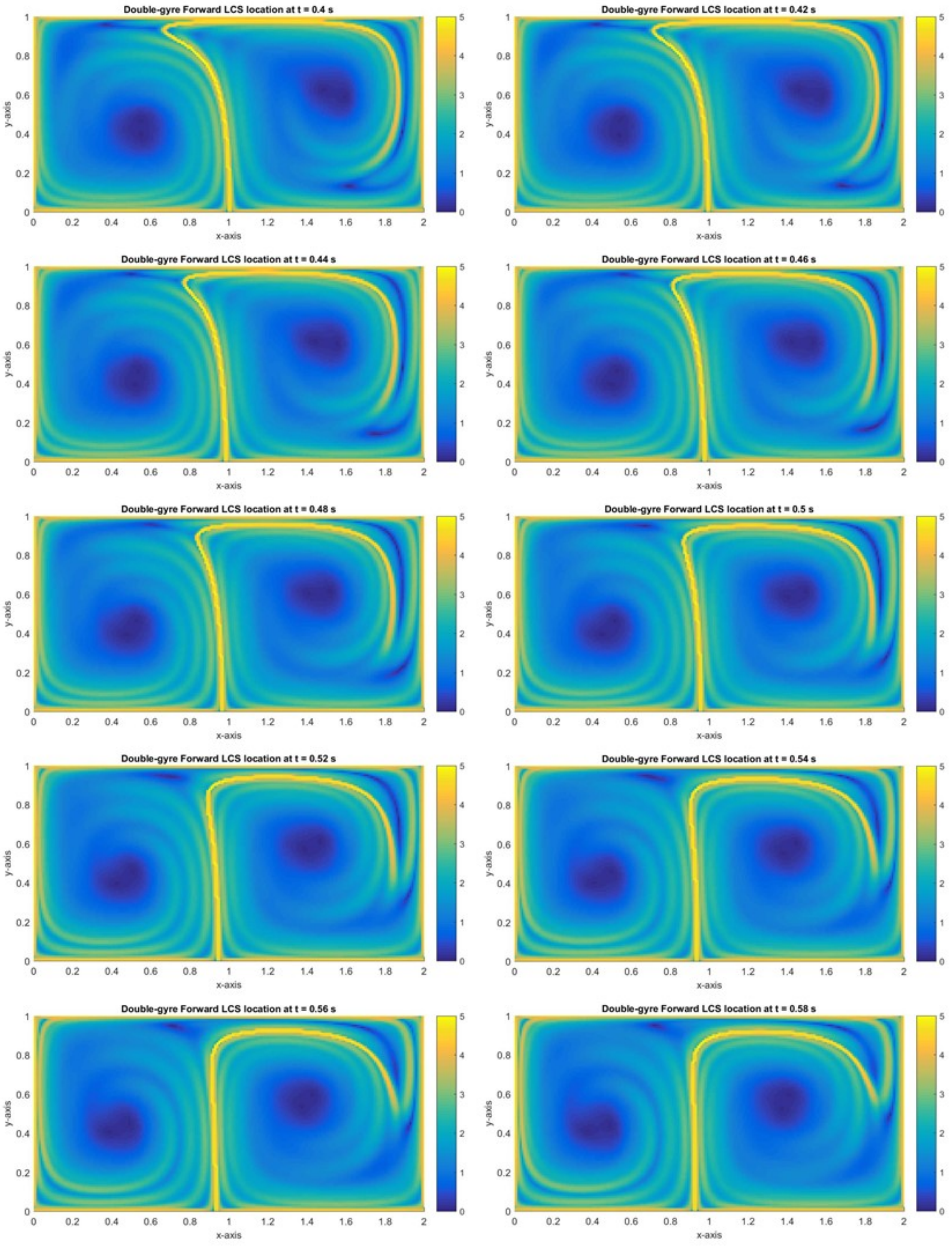

Figure A.3. FTLE maps for double-gyre field at $t_0 = 0.40$ s – 0.58 s

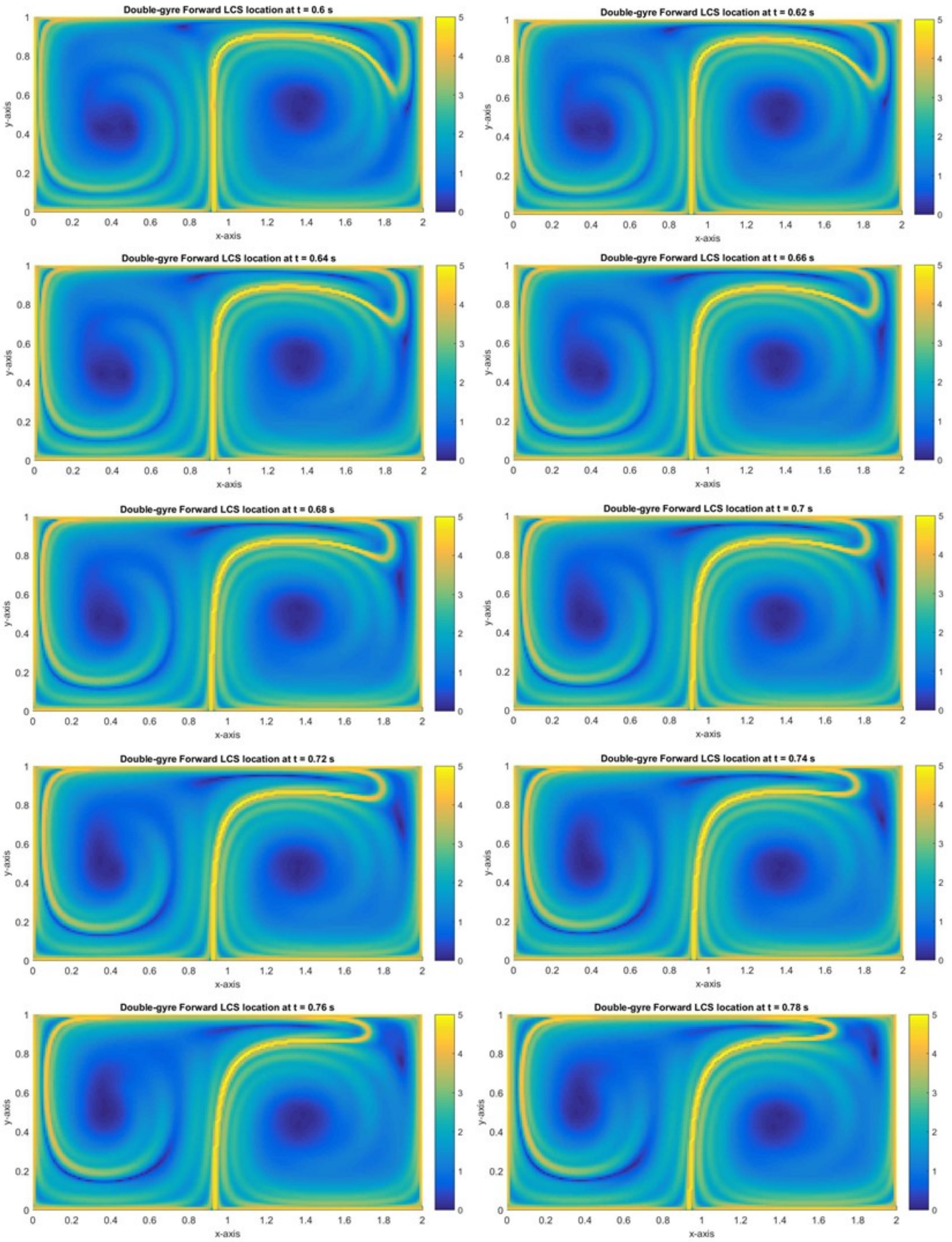

Figure A.4. FTLE maps for double-gyre field at $t_0 = 0.60$ s – 0.78 s

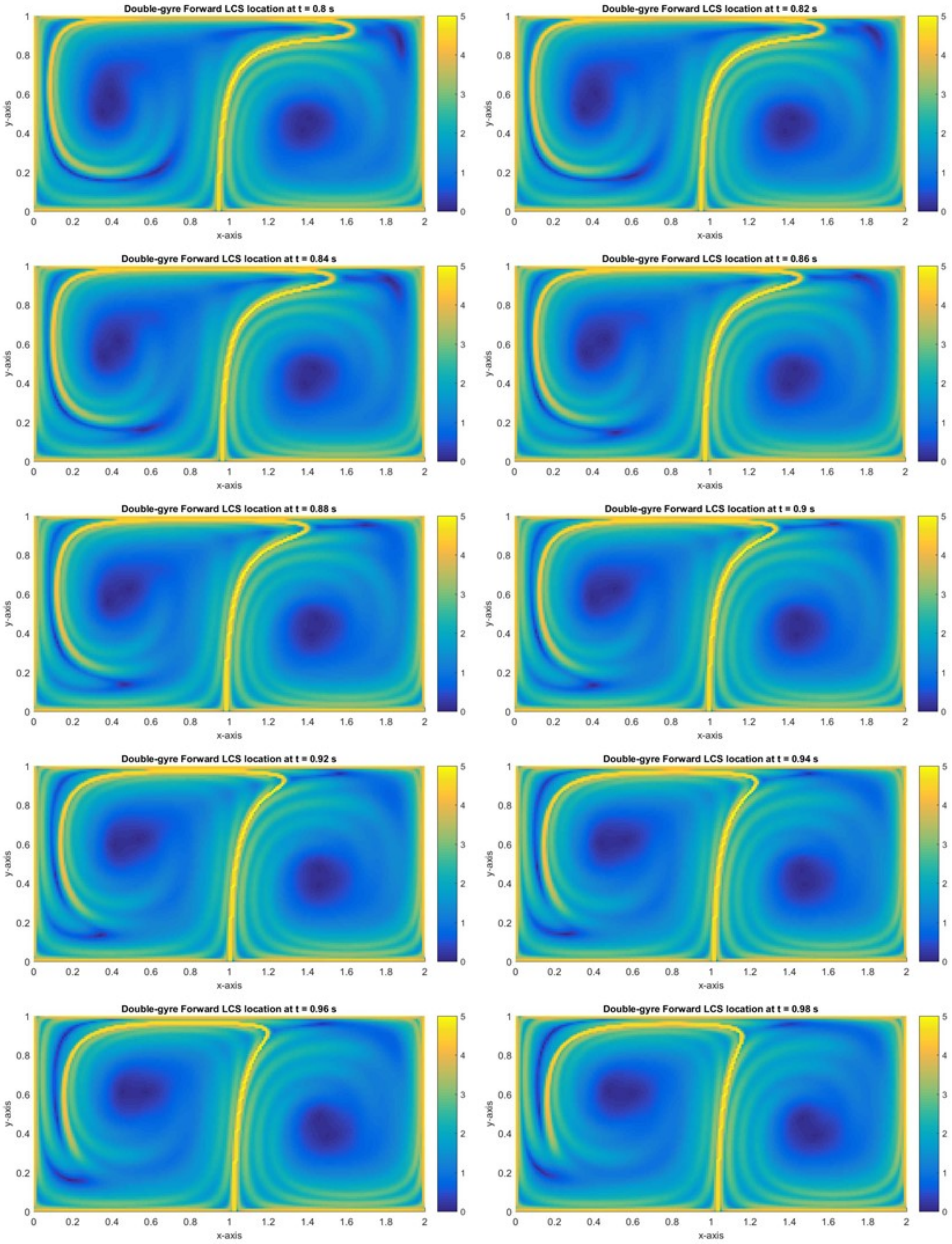

Figure A.5. FTLE maps for double-gyre field at $t_0 = 0.80$ s – 0.98 s

APPENDIX B

FTLE MAPS FOR NEUTRAL WINDS

B.1 Neutral winds FTLE maps during the geomagnetically quiet period.

The FTLE maps of neutral wind fields modeled by HWM14 during the geomagnetically quiet period on 13 March 2015 at 250 km height for different initial times over the interval $t_0 = [0{:}00 \text{ UT}, 23{:}00 \text{ UT}]$ and the integration time $\tau = 2$ days are shown in this section. For all the maps, each pixel color represents the FTLE value varying from 0 (blue) to 3×10^{-5} s^{-1} (yellow).

The FTLE values quantify the degree of separation, and the LCS is located at the locally maximum FTLE values (i.e., the bright yellow curve).

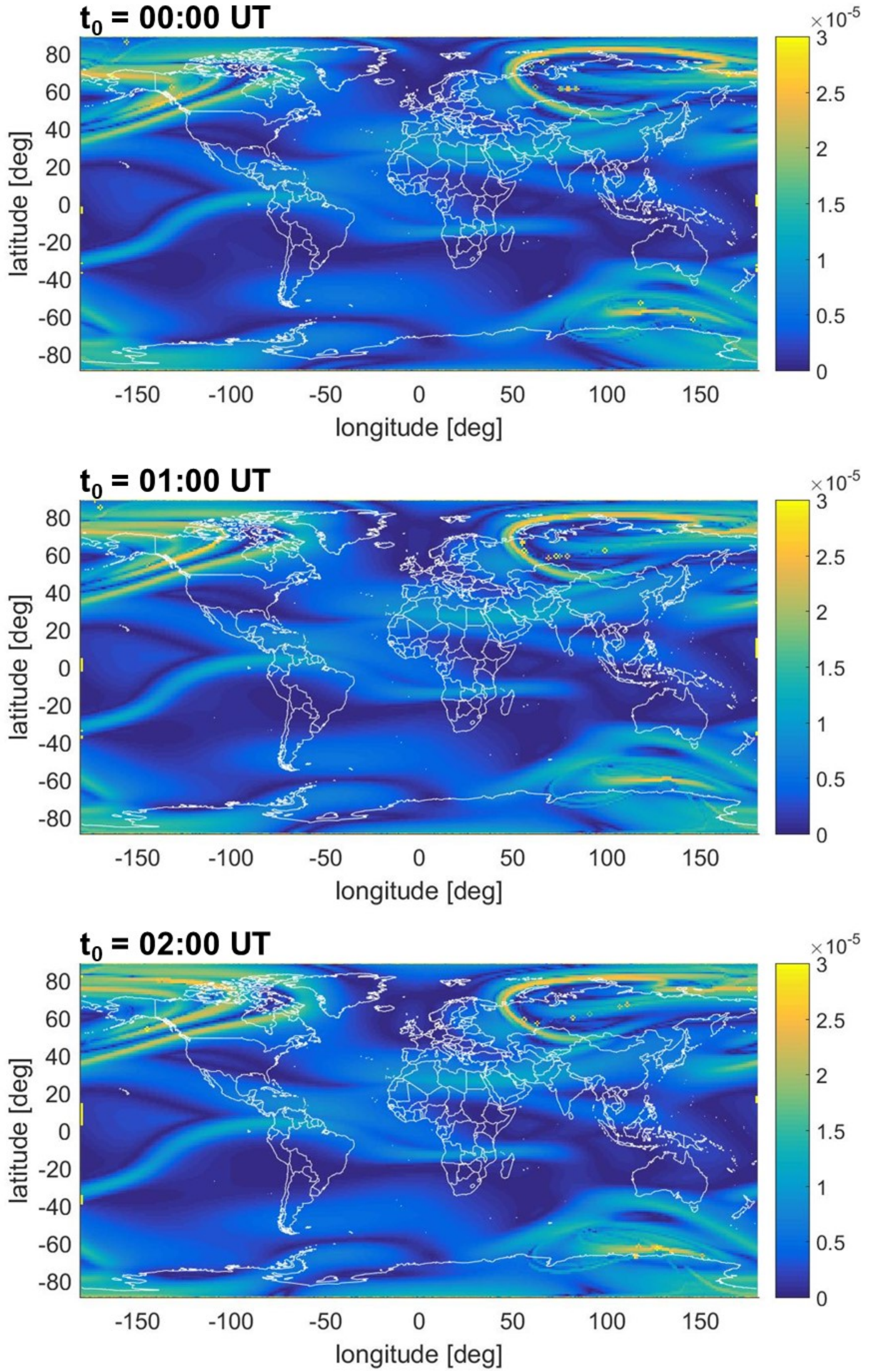

Figure B.1. FTLE maps for neutral winds during the geomagnetically quiet period on 13 March 2015 at t_0 = 00:00 UT – 02:00 UT

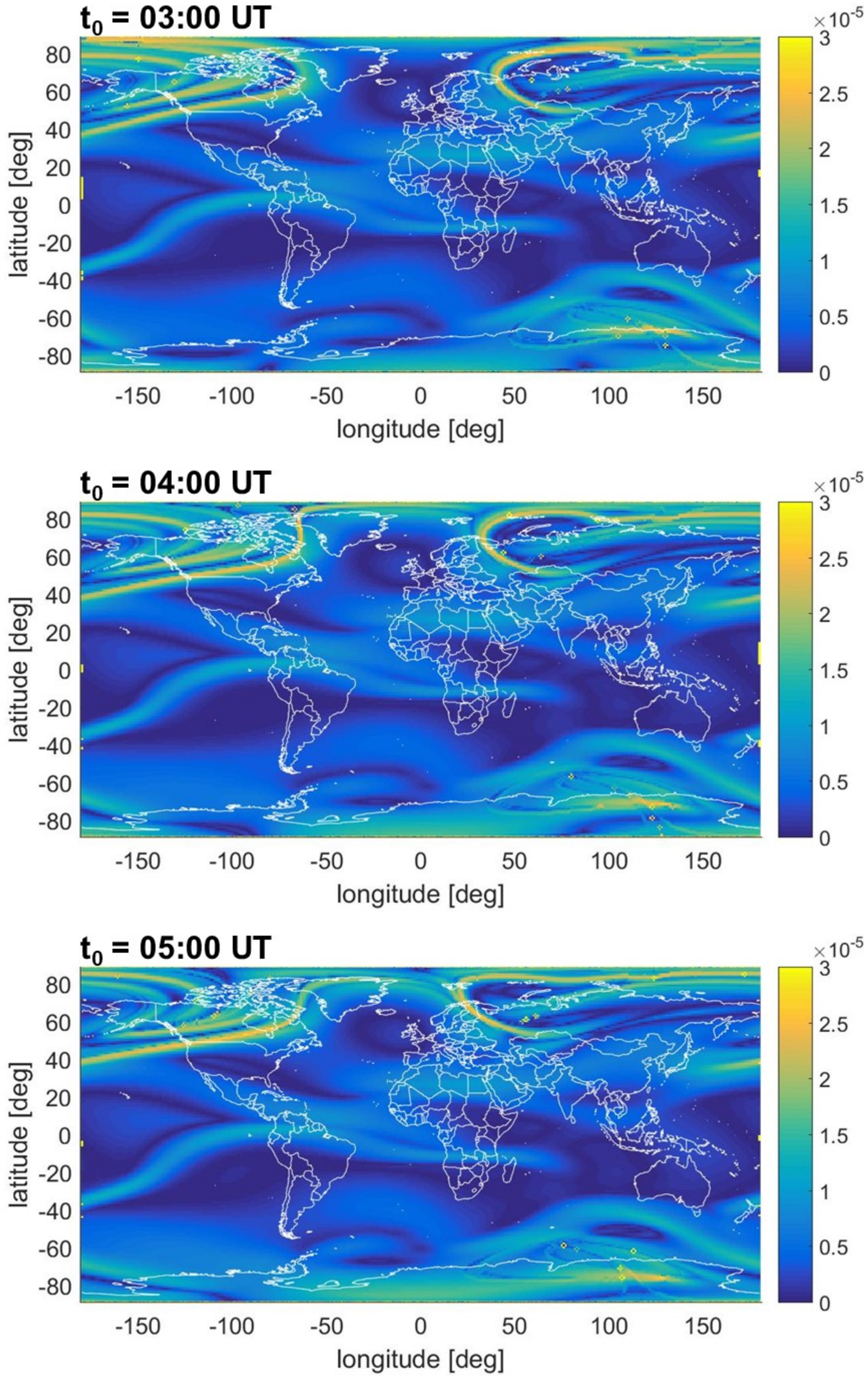

Figure B.2. FTLE maps for neutral winds during the geomagnetically quiet period on 13 March 2015 at t_0 = 03:00 UT – 05:00 UT

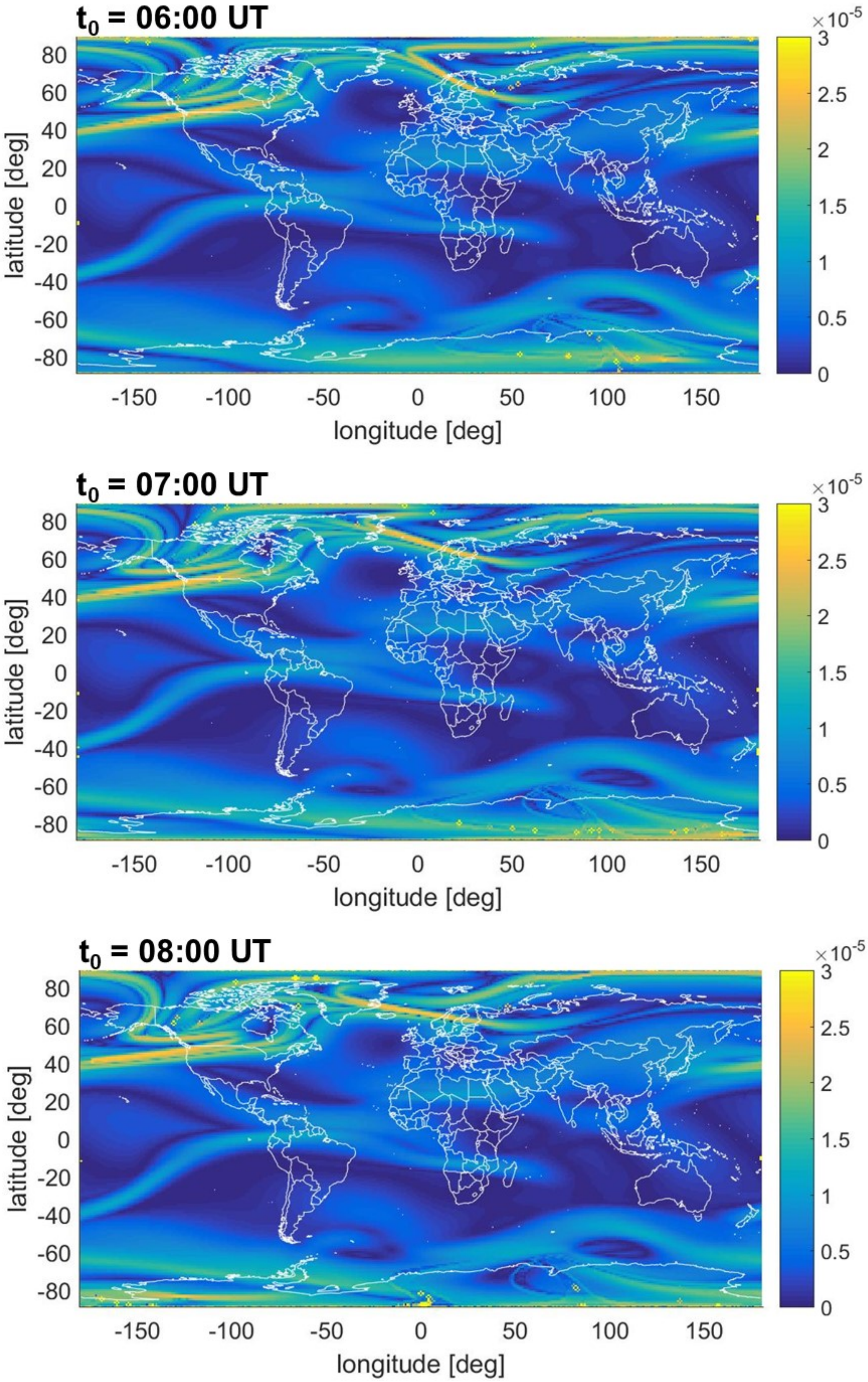

Figure B.3. FTLE maps for neutral winds during the geomagnetically quiet period on 13 March 2015 at t_0 = 06:00 UT – 08:00 UT

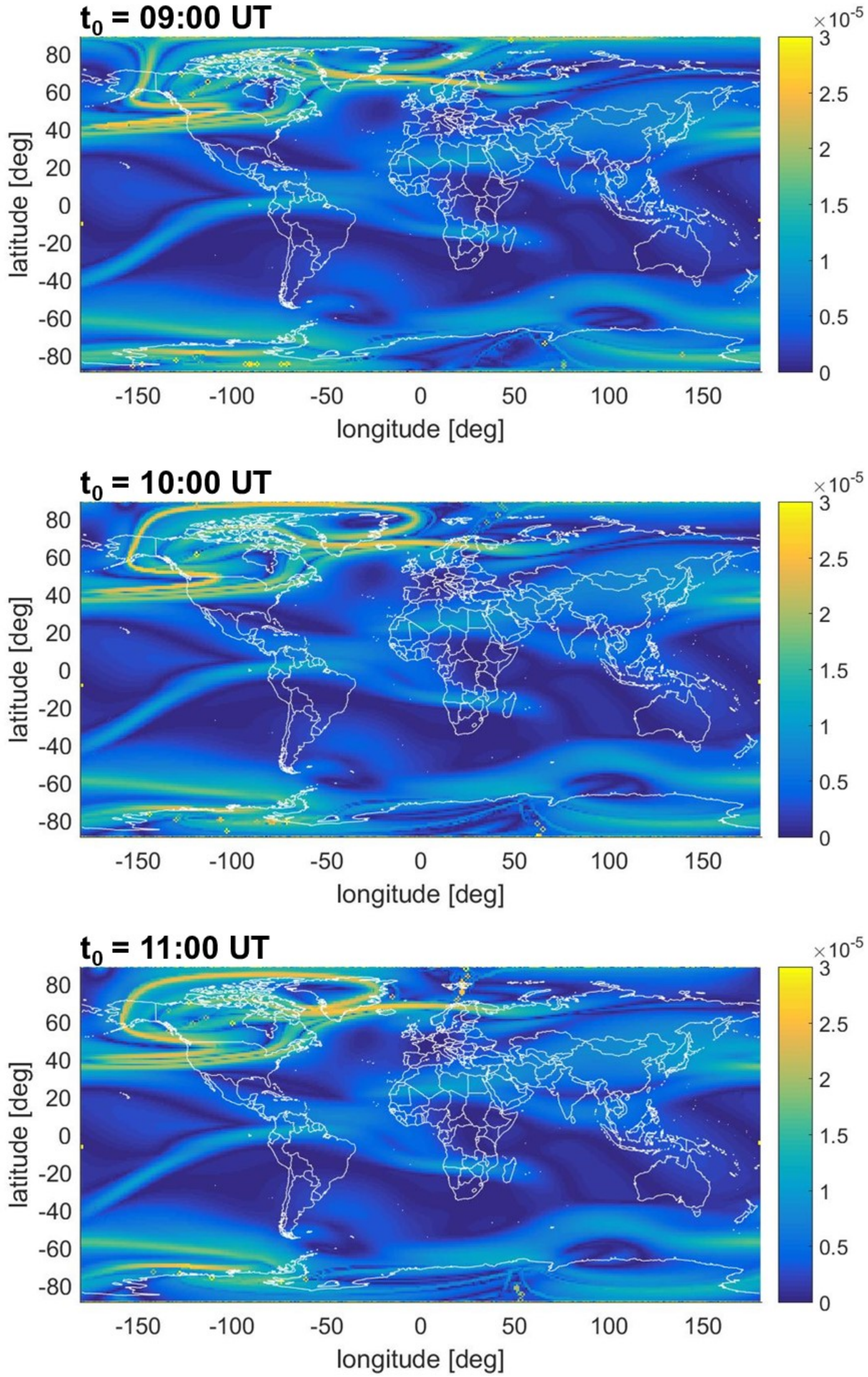

Figure B.4. FTLE maps for neutral winds during the geomagnetically quiet period on 13 March 2015 at $t_0 = $ 09:00 UT – 11:00 UT

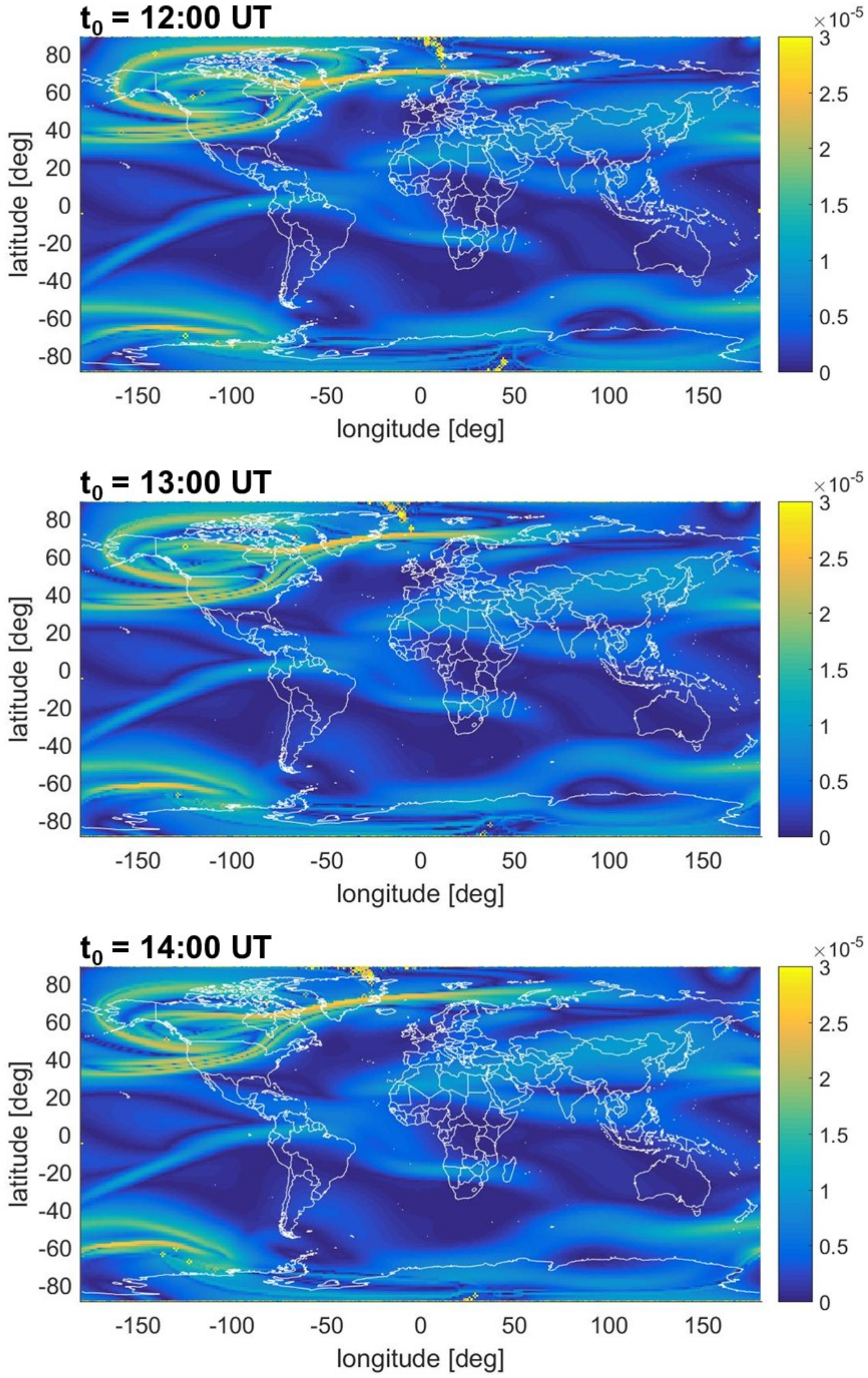

Figure B.5. FTLE maps for neutral winds during the geomagnetically quiet period on 13 March 2015 at t_0 = 12:00 UT – 14:00 UT

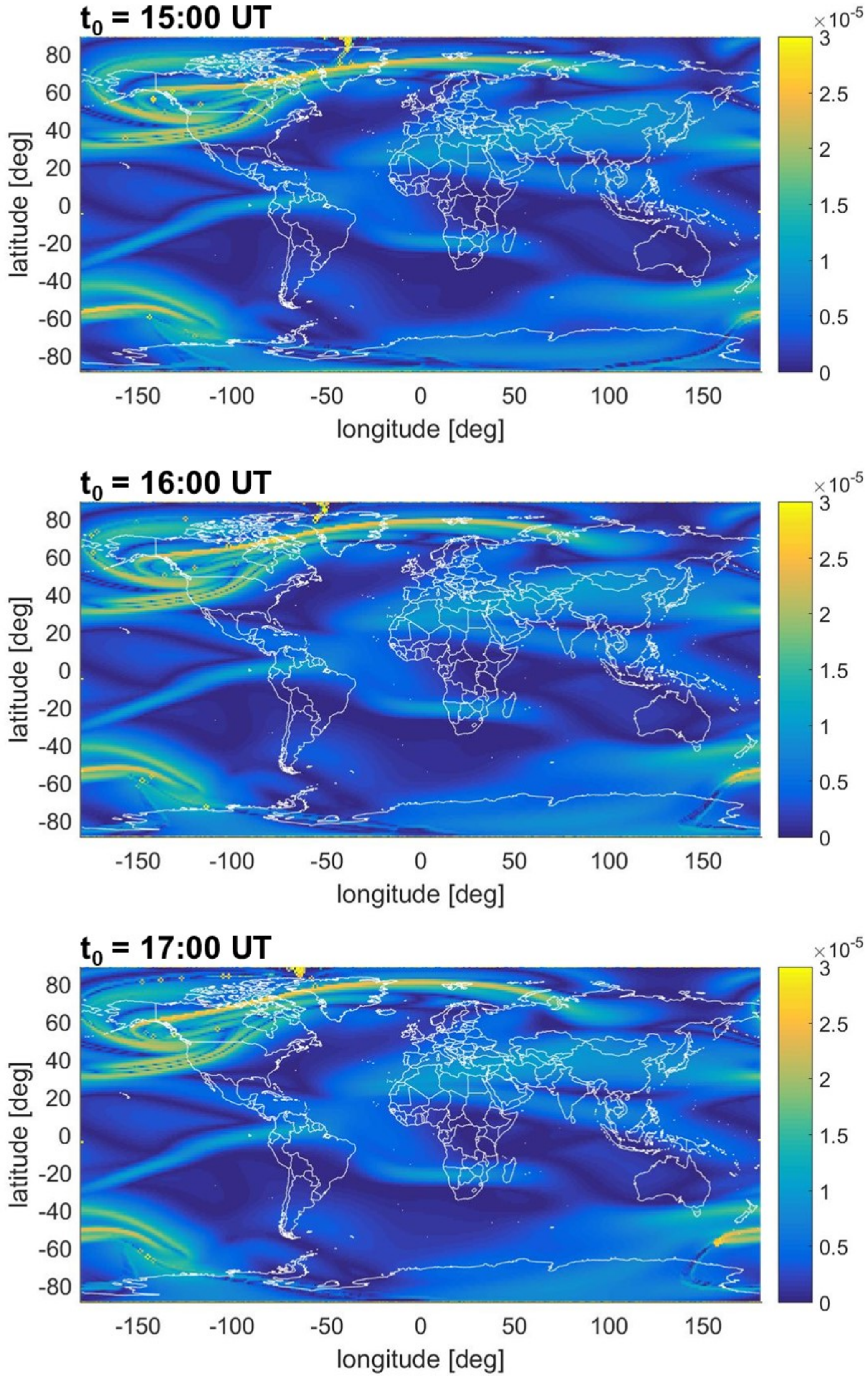

Figure B.6. FTLE maps for neutral winds during the geomagnetically quiet period on 13 March 2015 at t_0 = 15:00 UT – 17:00 UT

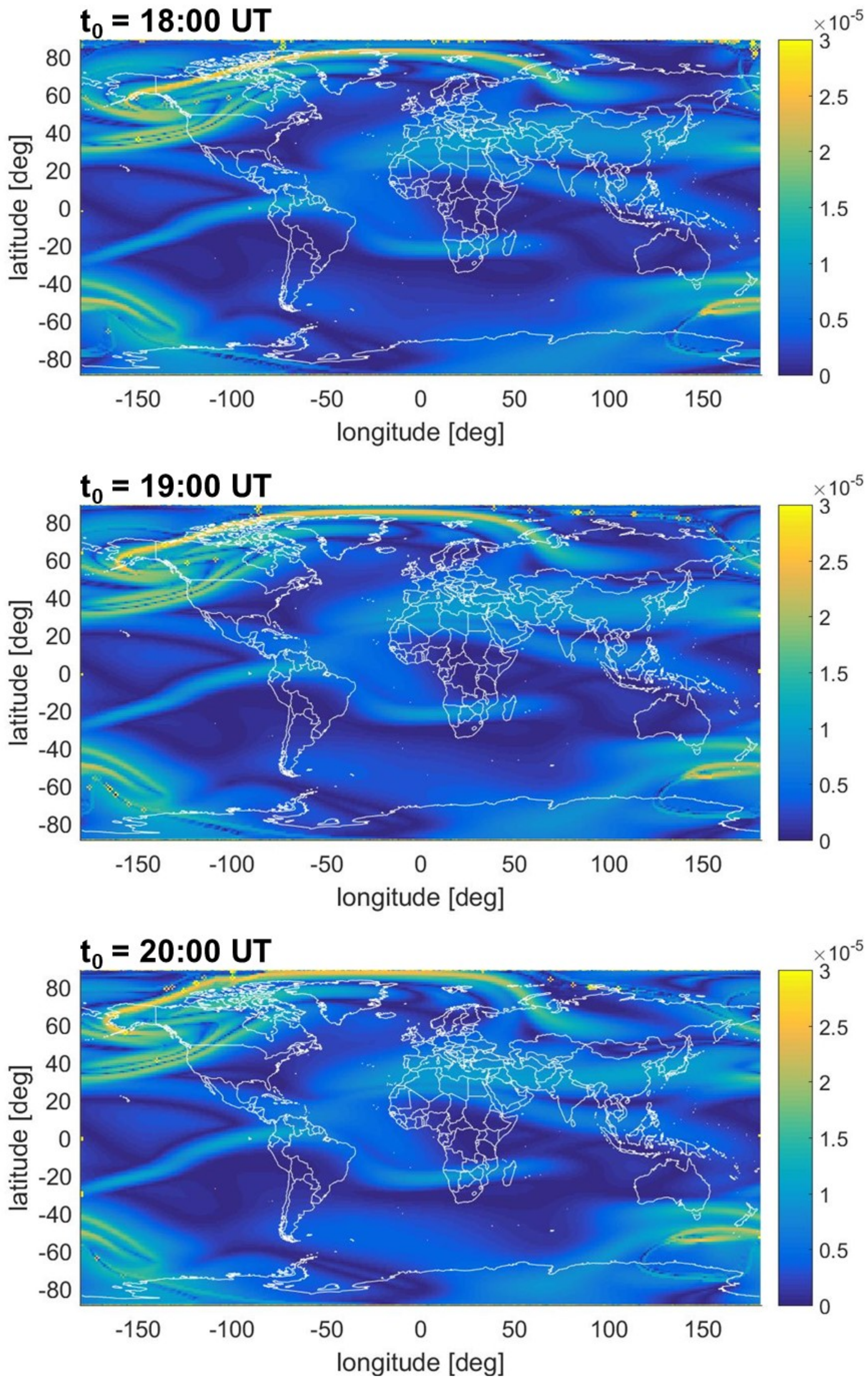

Figure B.7. FTLE maps for neutral winds during the geomagnetically quiet period on 13 March 2015 at t_0 = 18:00 UT – 20:00 UT

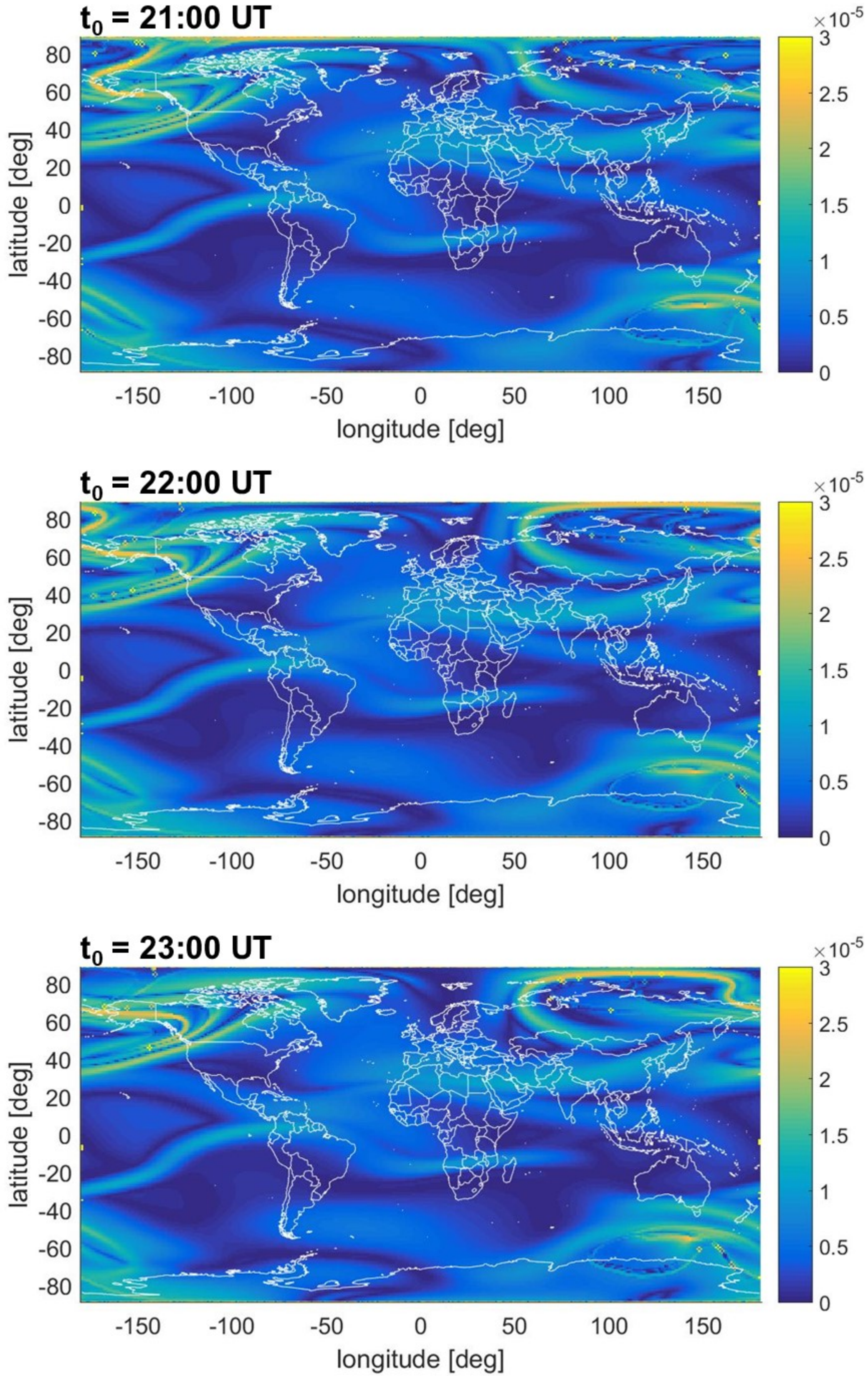

Figure B.8. FTLE maps for neutral winds during the geomagnetically quiet period on 13 March 2015 at t_0 = 21:00 UT – 23:00 UT

B.2 Neutral winds FTLE maps during the geomagnetically active period.

The FTLE maps of neutral wind fields modeled by HWM14 during the geomagnetically active period on 17 March 2015 at 250 km height for different initial times over the interval $t_0 = [0{:}00 \text{ UT}, 23{:}00 \text{ UT}]$ and the integration time $\tau = 2$ days are shown in this section. For all the maps, each pixel color represents the FTLE value varying from 0 (blue) to $3 \times 10^{-5}\ s^{-1}$ (yellow).

The FTLE values quantify the degree of separation, and the LCS is located at the locally maximum FTLE values (i.e., the bright yellow curve).

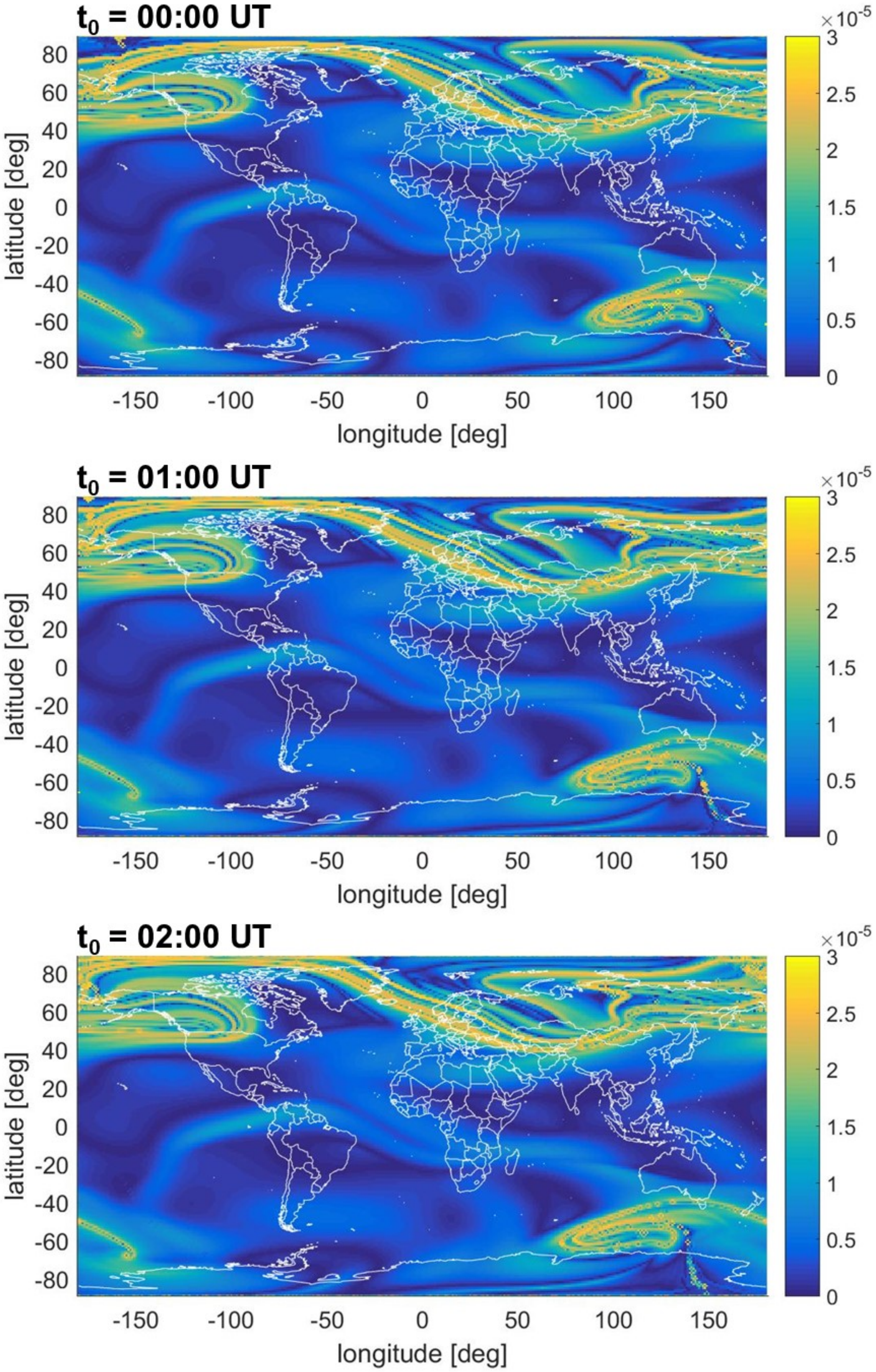

Figure B.9. FTLE maps for neutral winds during the geomagnetically active period on 17 March 2015 at t_0 = 00:00 UT – 02:00 UT

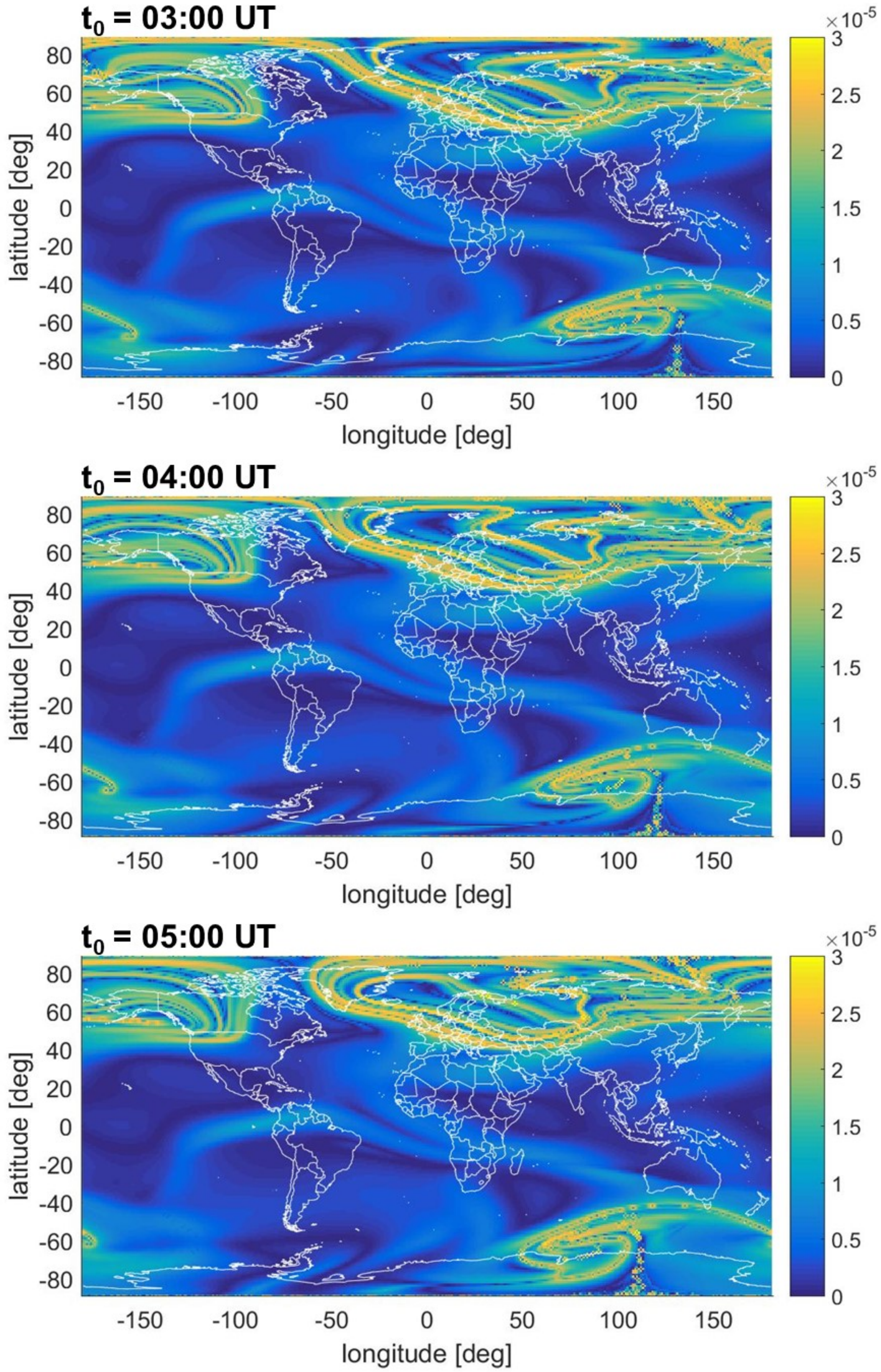

Figure B.10. FTLE maps for neutral winds during the geomagnetically active period on 17 March 2015 at t_0 = 03:00 UT – 05:00 UT

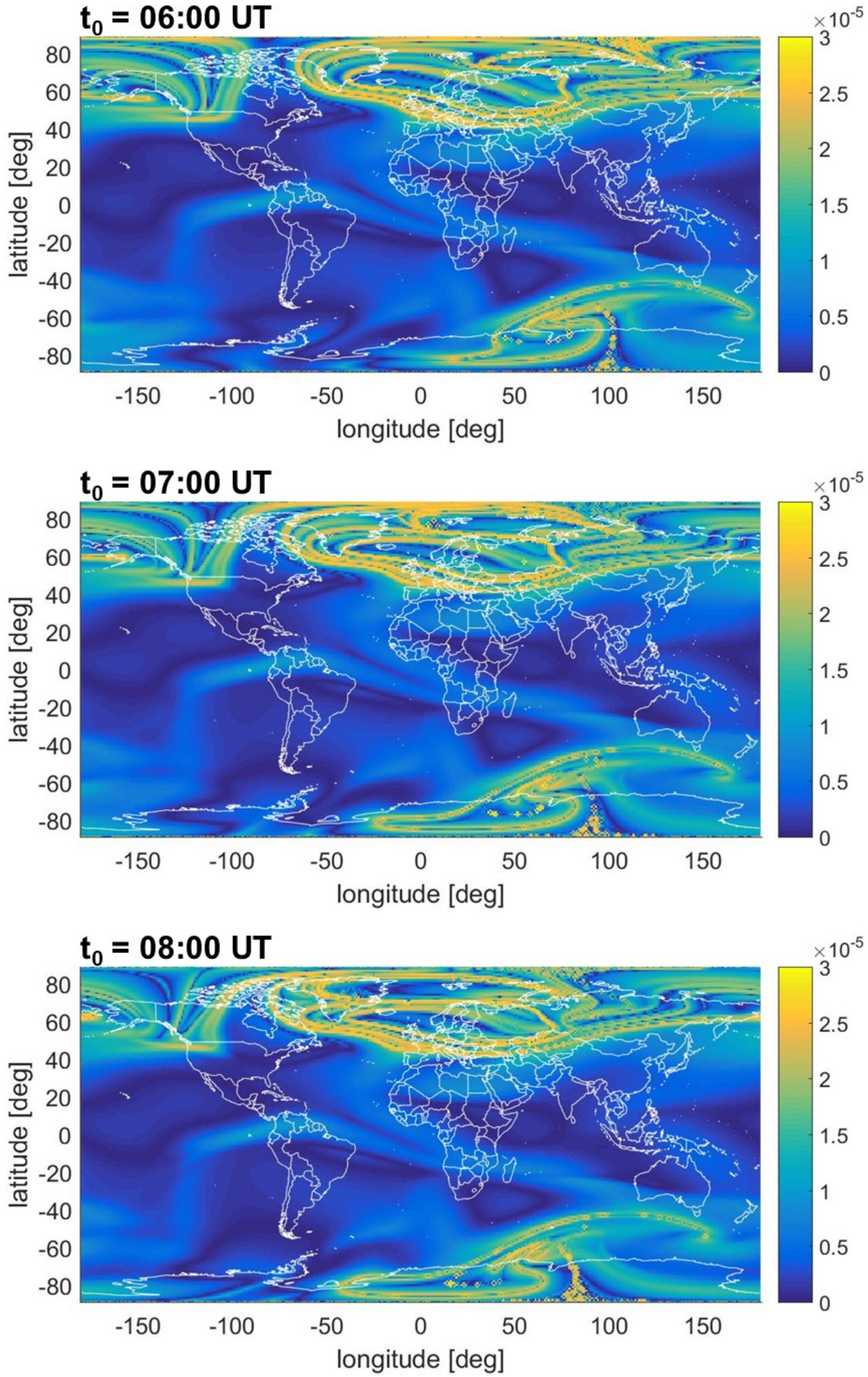

Figure B.11. FTLE maps for neutral winds during the geomagnetically active period on 17 March 2015 at $t_0 = 06{:}00$ UT – 08:00 UT

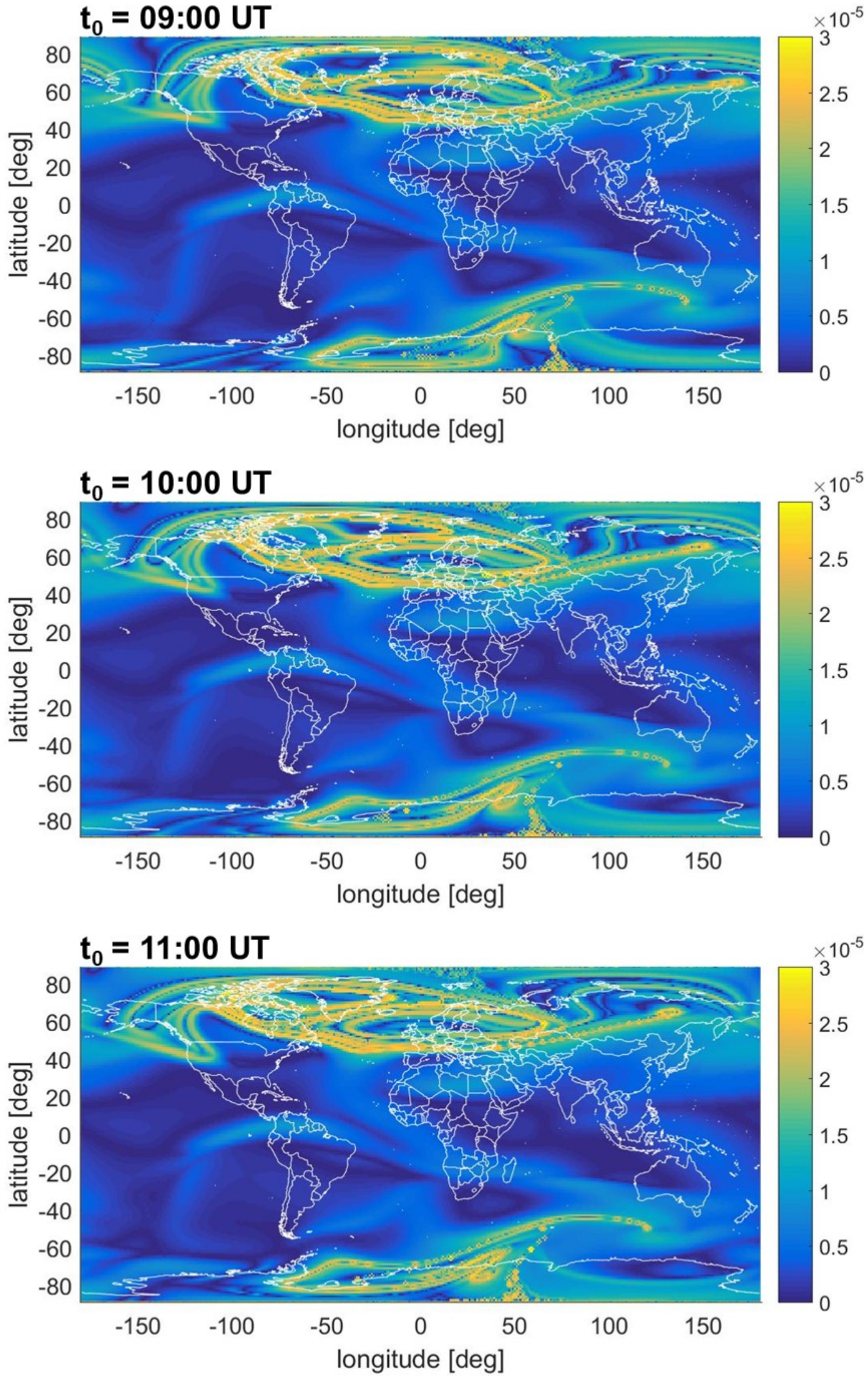

Figure B.12. FTLE maps for neutral winds during the geomagnetically active period on 17 March 2015 at $t_0 = 09{:}00$ UT – 11:00 UT

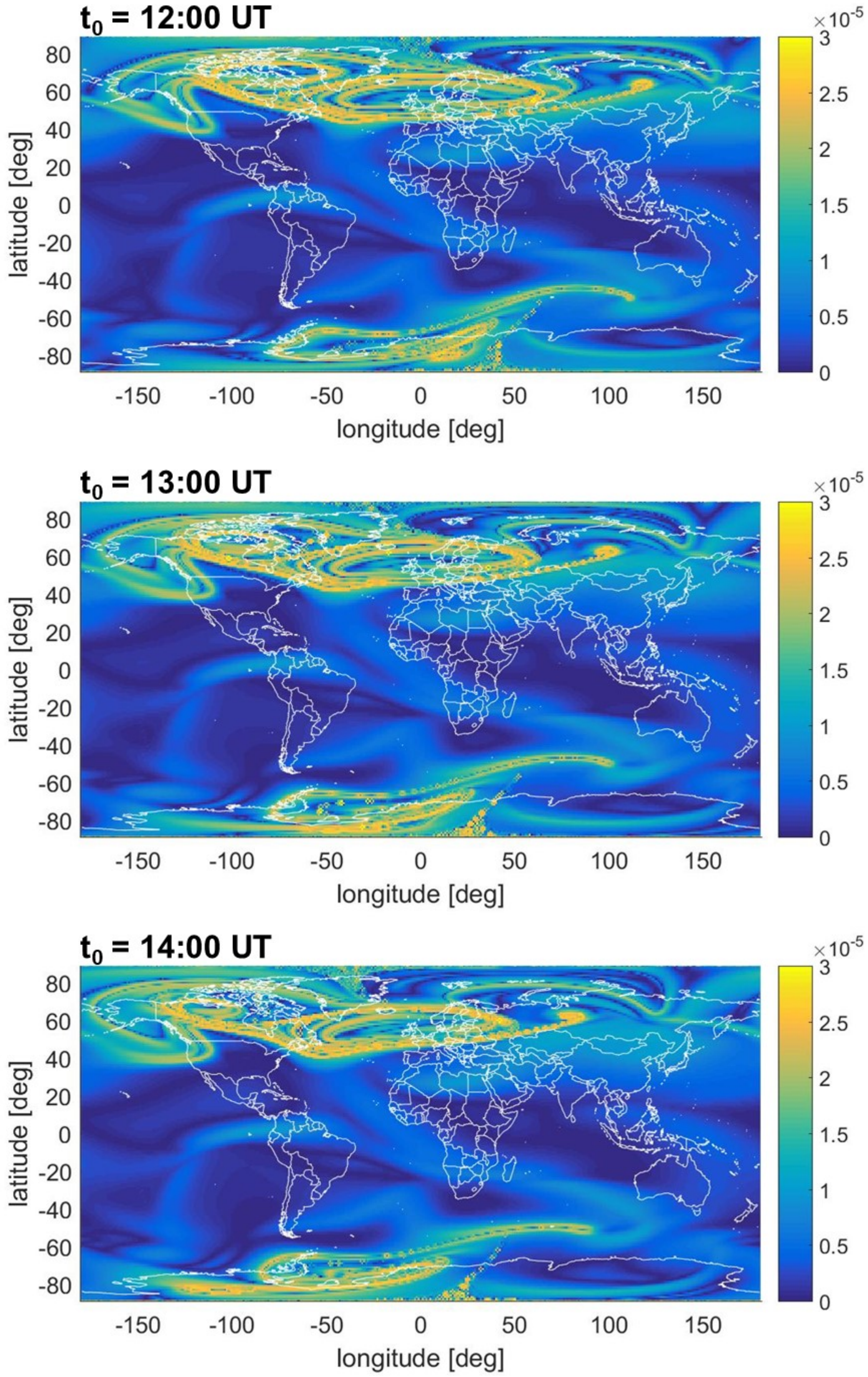

Figure B.13. FTLE maps for neutral winds during the geomagnetically active period on 17 March 2015 at t_0 = 12:00 UT – 14:00 UT

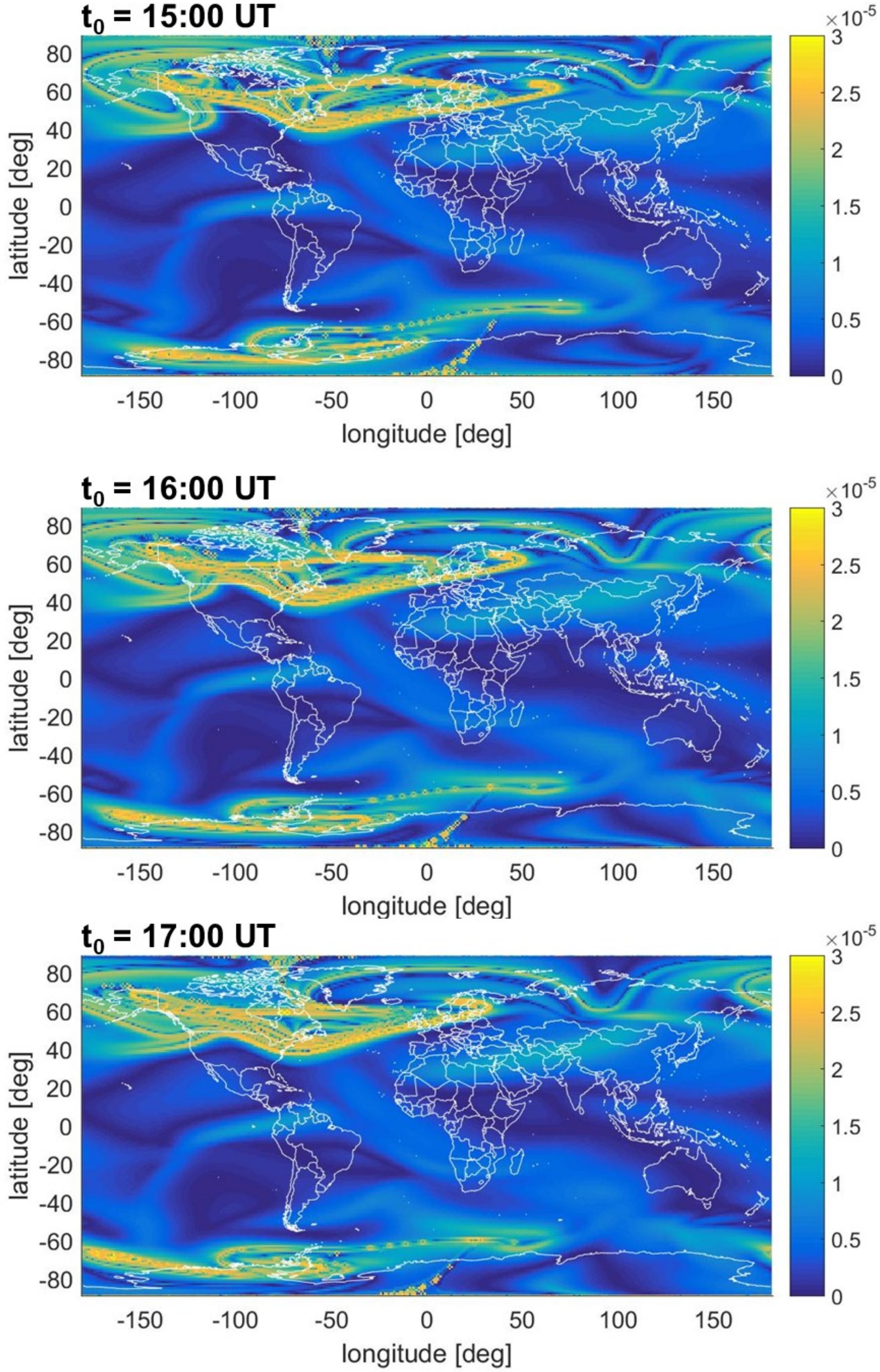

Figure B.14. FTLE maps for neutral winds during the geomagnetically active period on 17 March 2015 at t_0 = 15:00 UT – 17:00 UT

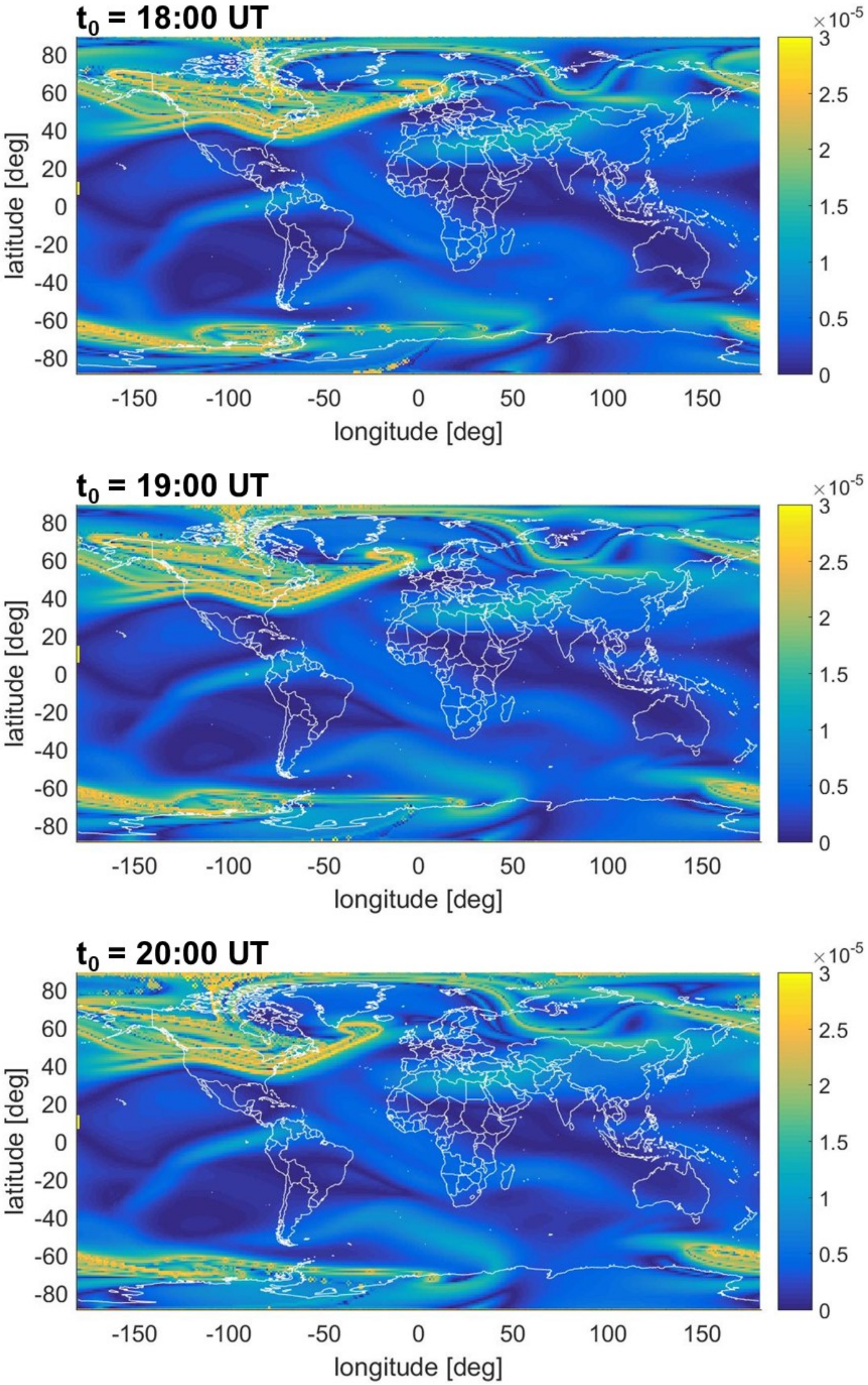

Figure B.15. FTLE maps for neutral winds during the geomagnetically active period on 17 March 2015 at t_0 = 18:00 UT – 20:00 UT

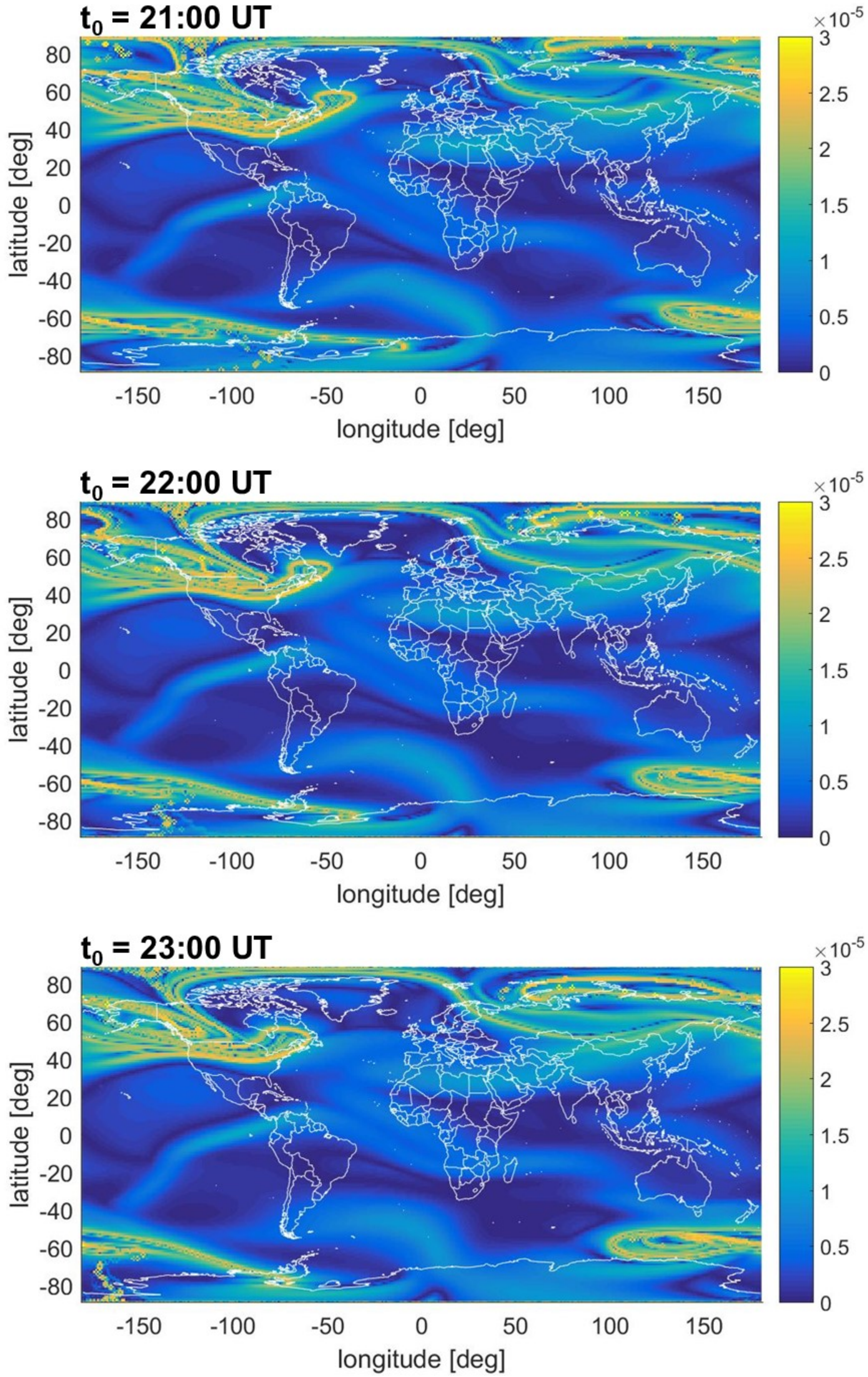

Figure B.16. FTLE maps for neutral winds during the geomagnetically active period on 17 March 2015 at t_0 = 21:00 UT – 23:00 UT

APPENDIX C

FTLE MAPS FOR PLASMA DRIFTS

C.1 FTLE maps for plasma drifts during the geomagnetically quiet period.

The FTLE maps of plasma drifts modeled by Weimer 2005 and IGRF-12 over the northern (left) and southern (right) hemispheres during the geomagnetically quiet period on 16 March 2015 at 350 km height for different initial times over the interval t_0 = [0:00 UT, 23:00 UT] and the integration time $\tau = 3$ hours are shown in this section. Local noon is fixed at the bottom of each figure. For all the maps, each pixel color represents the FTLE value varying from 0 (blue) to 5×10^{-4} s^{-1} (yellow). The blank area at low latitudes is due to the vanishing of the Weimer potential to 0.

The FTLE values quantify the degree of separation, and the LCS is located at the locally maximum FTLE values (i.e., the bright yellow curve).

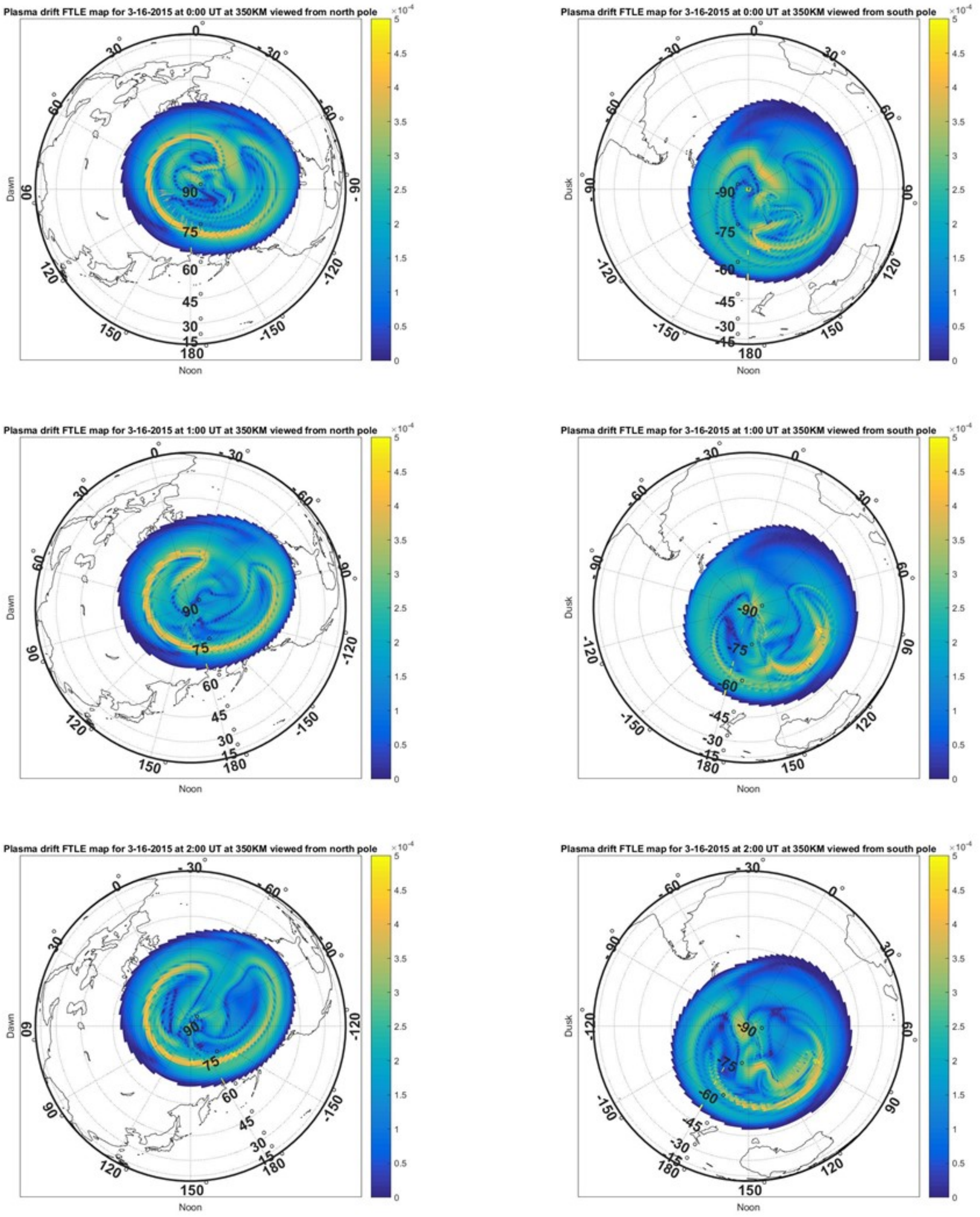

Plasma drift FTLE map for 3-16-2015 at 0:00 UT at 350KM viewed from north pole

Plasma drift FTLE map for 3-16-2015 at 0:00 UT at 350KM viewed from south pole

Plasma drift FTLE map for 3-16-2015 at 1:00 UT at 350KM viewed from north pole

Plasma drift FTLE map for 3-16-2015 at 1:00 UT at 350KM viewed from south pole

Plasma drift FTLE map for 3-16-2015 at 2:00 UT at 350KM viewed from north pole

Plasma drift FTLE map for 3-16-2015 at 2:00 UT at 350KM viewed from south pole

Figure C.1. FTLE maps for plasma drift during the geomagnetically quiet period on 16 March 2015 at $t_0 = $ 00:00 UT – 02:00 UT. (Left) north pole; (Right) south pole.

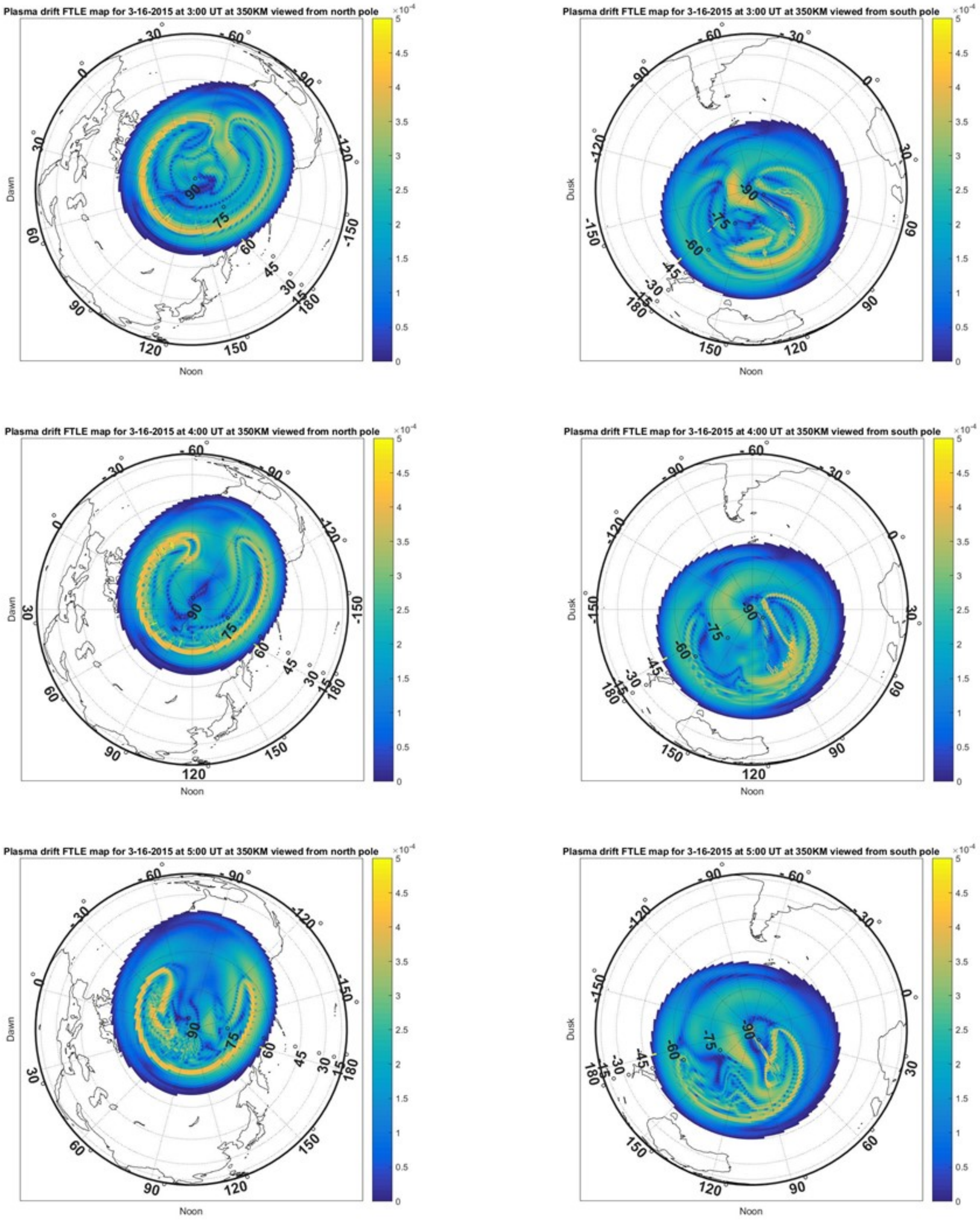

Figure C.2. FTLE maps for plasma drift during the geomagnetically quiet period on 16 March 2015 at $t_0 = $ 03:00 UT – 05:00 UT. (Left) north pole; (Right) south pole.

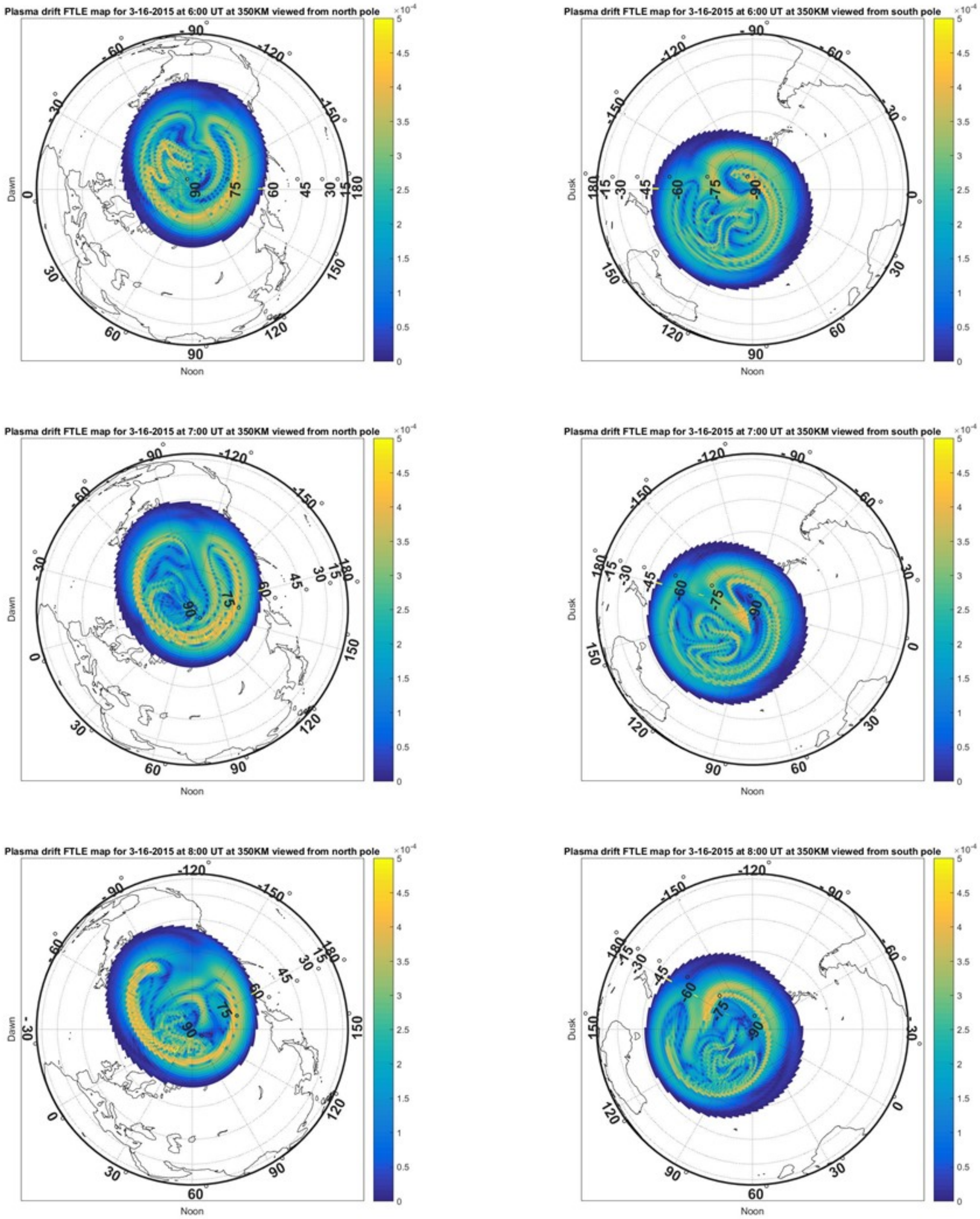

Figure C.3. FTLE maps for plasma drift during the geomagnetically quiet period on 16 March 2015 at $t_0 = $ 06:00 UT – 08:00 UT. (Left) north pole; (Right) south pole.

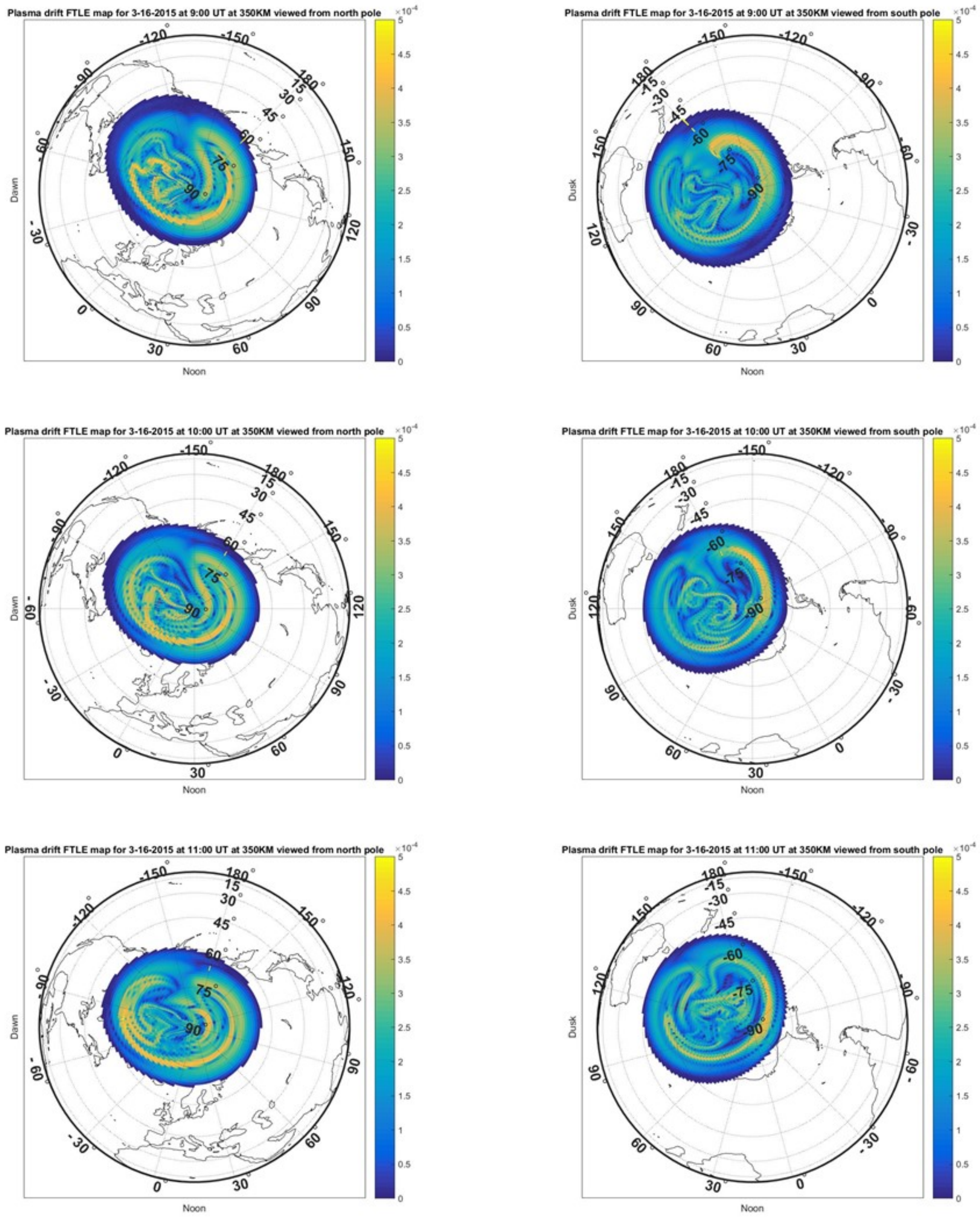

Plasma drift FTLE map for 3-16-2015 at 9:00 UT at 350KM viewed from north pole

Plasma drift FTLE map for 3-16-2015 at 9:00 UT at 350KM viewed from south pole

Plasma drift FTLE map for 3-16-2015 at 10:00 UT at 350KM viewed from north pole

Plasma drift FTLE map for 3-16-2015 at 10:00 UT at 350KM viewed from south pole

Plasma drift FTLE map for 3-16-2015 at 11:00 UT at 350KM viewed from north pole

Plasma drift FTLE map for 3-16-2015 at 11:00 UT at 350KM viewed from south pole

Figure C.4. FTLE maps for plasma drift during the geomagnetically quiet period on 16 March 2015 at $t_0 = $ 09:00 UT – 11:00 UT. (Left) north pole; (Right) south pole.

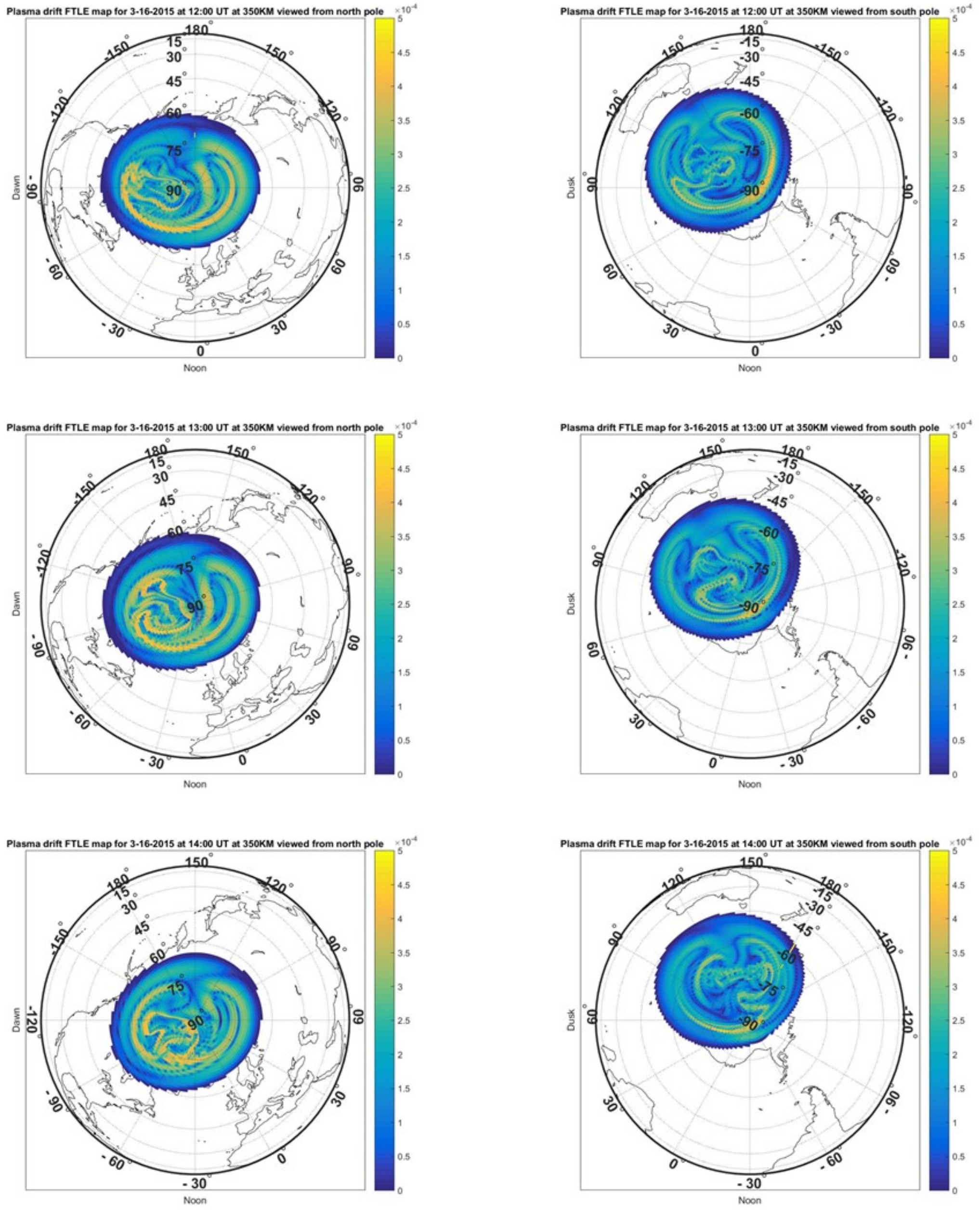

Plasma drift FTLE map for 3-16-2015 at 12:00 UT at 350KM viewed from north pole

Plasma drift FTLE map for 3-16-2015 at 12:00 UT at 350KM viewed from south pole

Plasma drift FTLE map for 3-16-2015 at 13:00 UT at 350KM viewed from north pole

Plasma drift FTLE map for 3-16-2015 at 13:00 UT at 350KM viewed from south pole

Plasma drift FTLE map for 3-16-2015 at 14:00 UT at 350KM viewed from north pole

Plasma drift FTLE map for 3-16-2015 at 14:00 UT at 350KM viewed from south pole

Figure C.5. FTLE maps for plasma drift during the geomagnetically quiet period on 16 March 2015 at $t_0 = $ 12:00 UT – 14:00 UT. (Left) north pole; (Right) south pole.

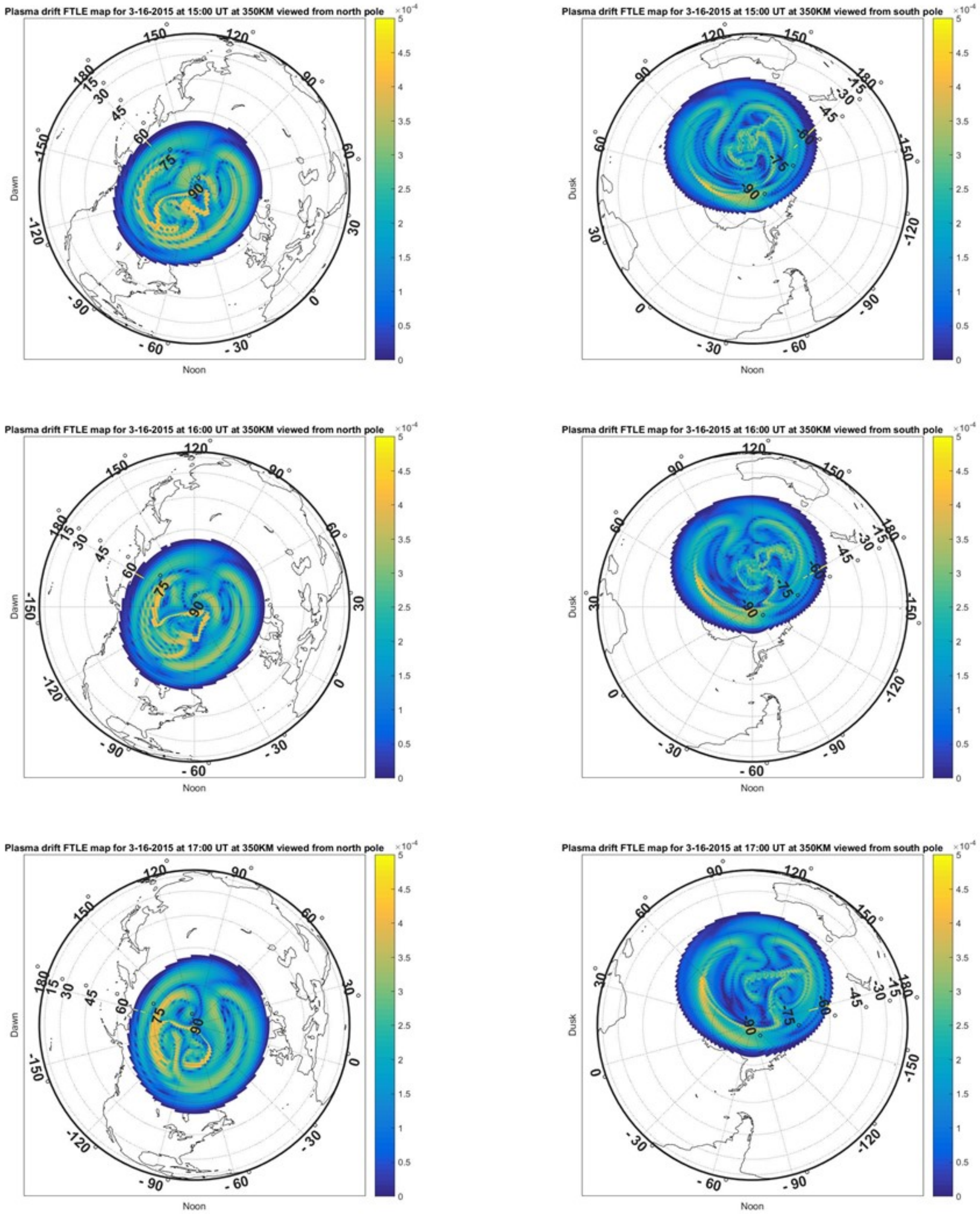
Plasma drift FTLE map for 3-16-2015 at 15:00 UT at 350KM viewed from north pole

Plasma drift FTLE map for 3-16-2015 at 15:00 UT at 350KM viewed from south pole

Plasma drift FTLE map for 3-16-2015 at 16:00 UT at 350KM viewed from north pole

Plasma drift FTLE map for 3-16-2015 at 16:00 UT at 350KM viewed from south pole

Plasma drift FTLE map for 3-16-2015 at 17:00 UT at 350KM viewed from north pole

Plasma drift FTLE map for 3-16-2015 at 17:00 UT at 350KM viewed from south pole

Figure C.6. FTLE maps for plasma drift during the geomagnetically quiet period on 16 March 2015 at $t_0 = 15{:}00$ UT – 17:00 UT. (Left) north pole; (Right) south pole.

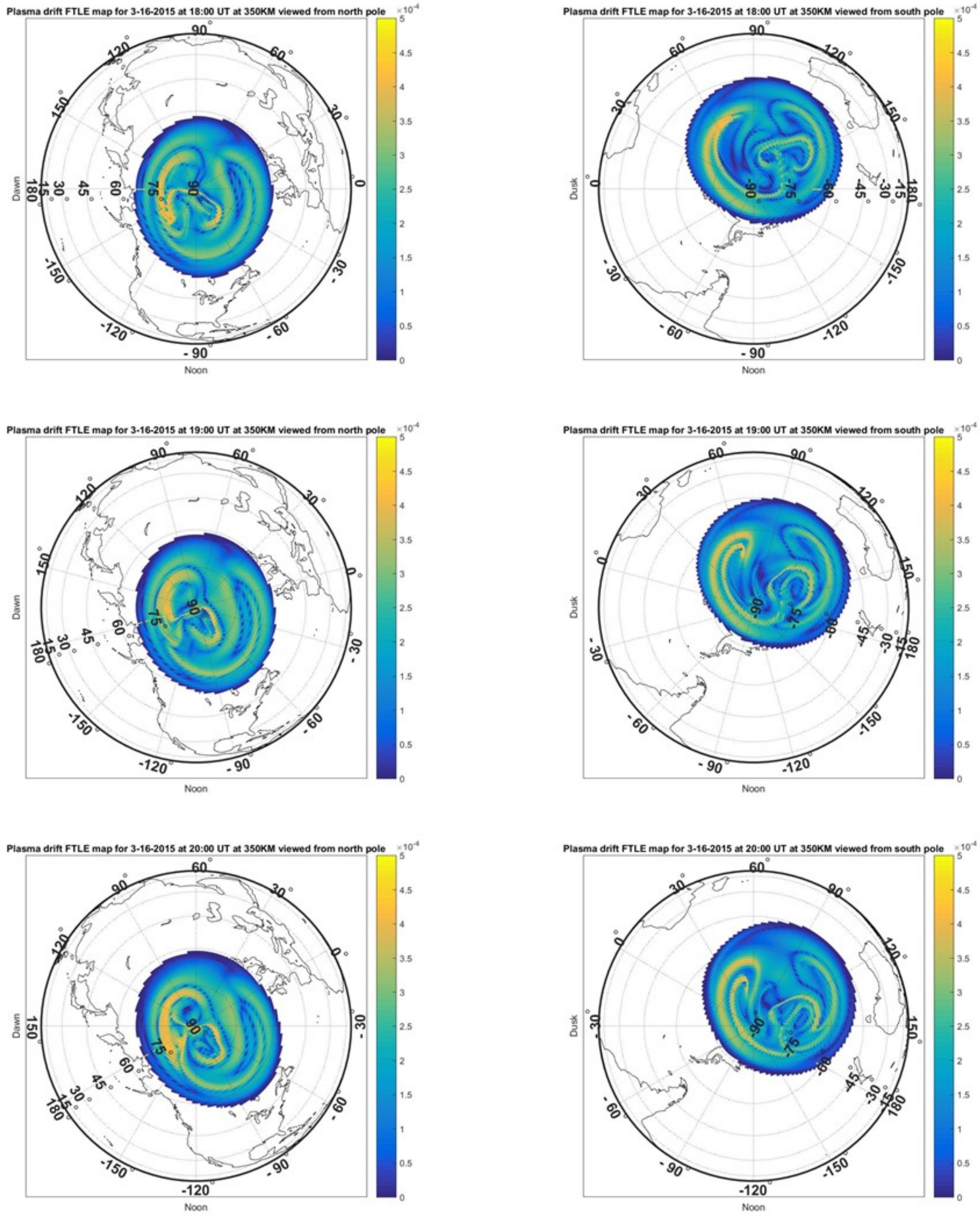
Plasma drift FTLE map for 3-16-2015 at 18:00 UT at 350KM viewed from north pole

Plasma drift FTLE map for 3-16-2015 at 18:00 UT at 350KM viewed from south pole

Plasma drift FTLE map for 3-16-2015 at 19:00 UT at 350KM viewed from north pole

Plasma drift FTLE map for 3-16-2015 at 19:00 UT at 350KM viewed from south pole

Plasma drift FTLE map for 3-16-2015 at 20:00 UT at 350KM viewed from north pole

Plasma drift FTLE map for 3-16-2015 at 20:00 UT at 350KM viewed from south pole

Figure C.7. FTLE maps for plasma drift during the geomagnetically quiet period on 16 March 2015 at $t_0 = $ 18:00 UT – 20:00 UT. (Left) north pole; (Right) south pole.

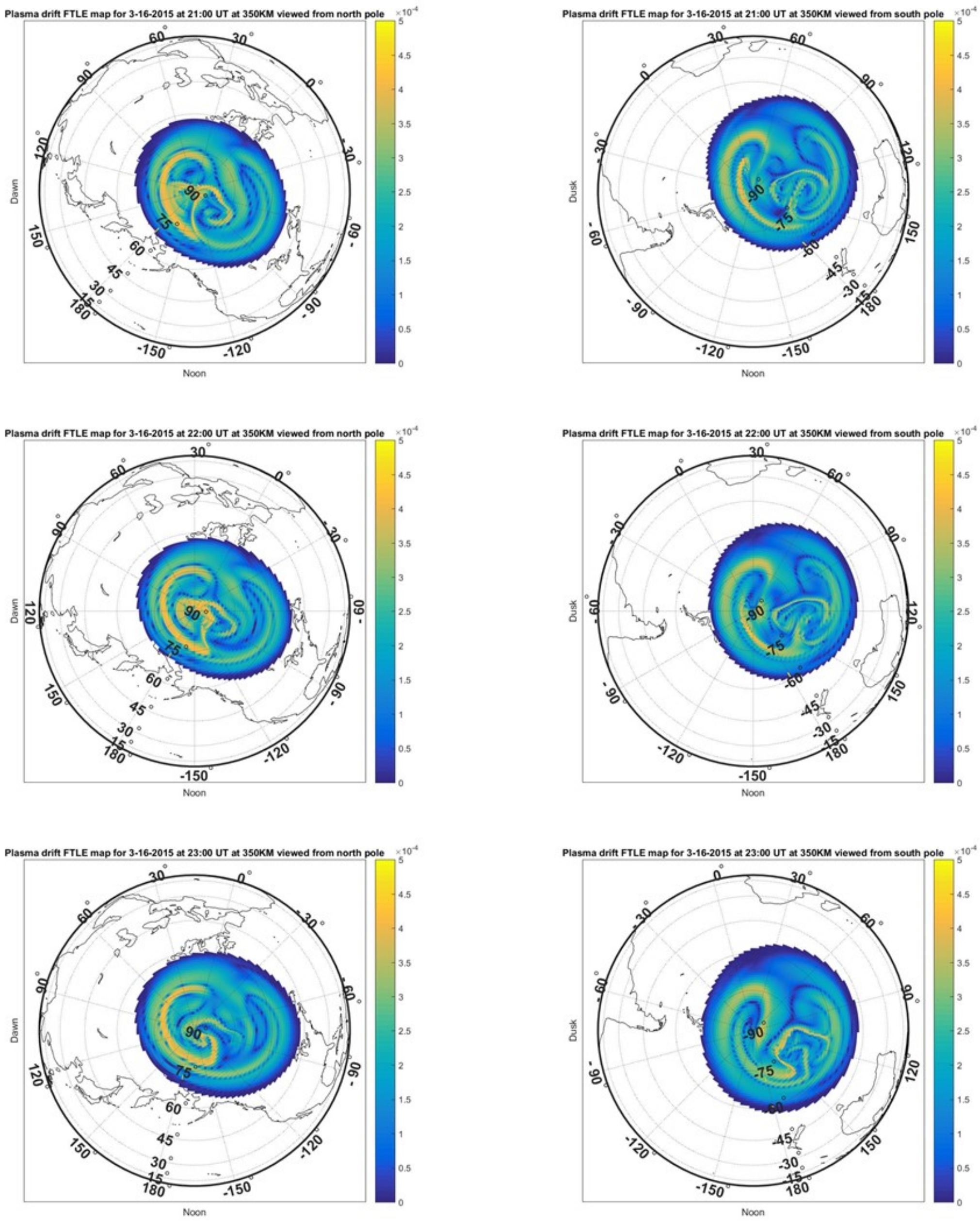
Plasma drift FTLE map for 3-16-2015 at 21:00 UT at 350KM viewed from north pole

Plasma drift FTLE map for 3-16-2015 at 21:00 UT at 350KM viewed from south pole

Plasma drift FTLE map for 3-16-2015 at 22:00 UT at 350KM viewed from north pole

Plasma drift FTLE map for 3-16-2015 at 22:00 UT at 350KM viewed from south pole

Plasma drift FTLE map for 3-16-2015 at 23:00 UT at 350KM viewed from north pole

Plasma drift FTLE map for 3-16-2015 at 23:00 UT at 350KM viewed from south pole

Figure C.8. FTLE maps for plasma drift during the geomagnetically quiet period on 16 March 2015 at $t_0 = $ 21:00 UT – 23:00 UT. (Left) north pole; (Right) south pole.

C.2 FTLE maps for plasma drifts during the geomagnetically active period.

The FTLE maps of plasma drifts modeled by Weimer 2005 and IGRF-12 over the northern (left) and southern (right) hemispheres during the geomagnetically active period on 17 March 2015 at 350 km height for different initial times over the interval $t_0 = [0{:}00 \text{ UT}, 22{:}00 \text{ UT}]$ and the integration time $\tau = 3$ hours are shown in this section. Local noon is fixed at the bottom of each figure. For all the maps, each pixel color represents the FTLE value varying from 0 (blue) to $5 \times 10^{-4}\ s^{-1}$ (yellow). The blank area at low latitudes is due to the vanishing of the Weimer potential to 0.

The FTLE values quantify the degree of separation, and the LCS is located at the locally maximum FTLE values (i.e., the bright yellow curve).

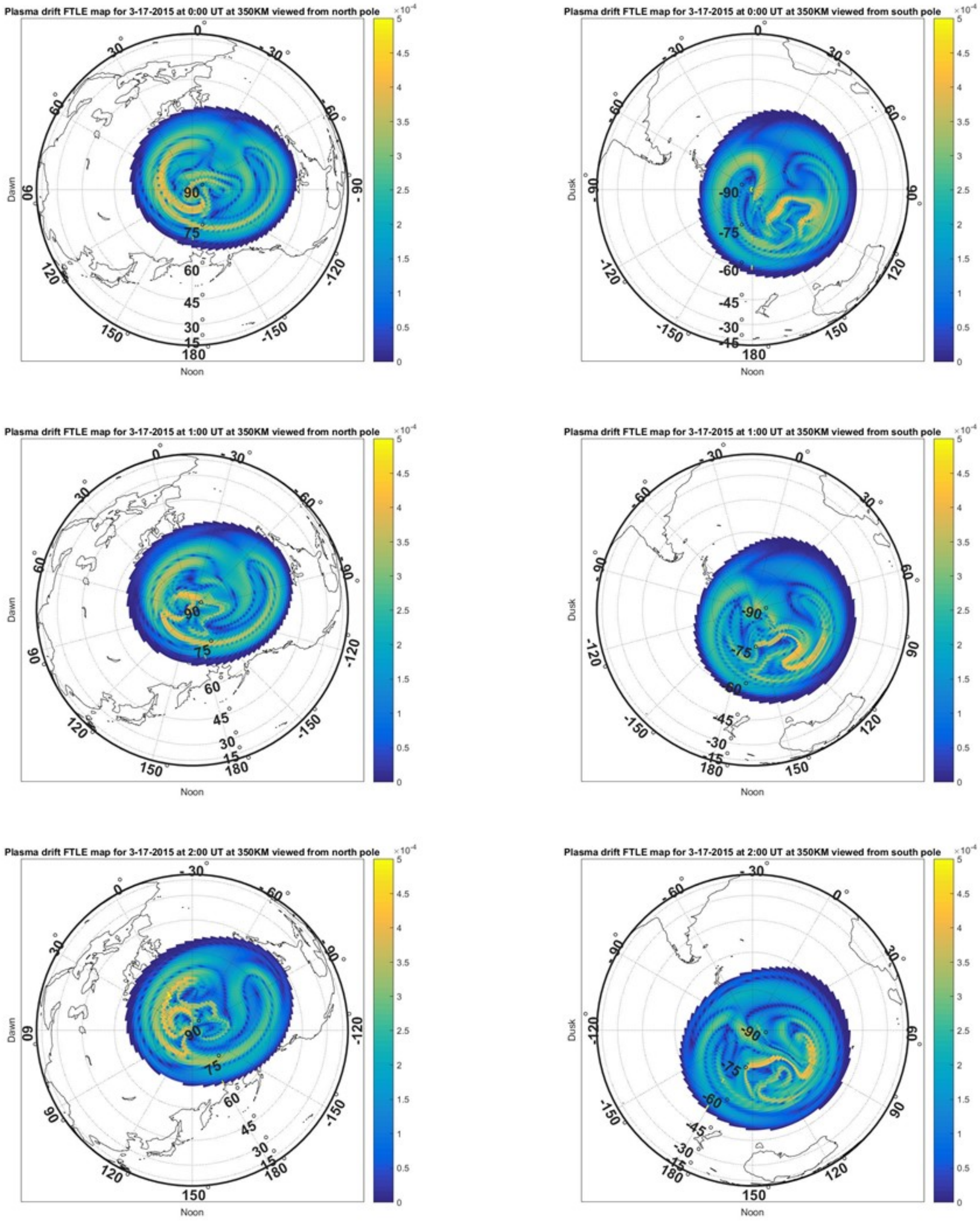
Plasma drift FTLE map for 3-17-2015 at 0:00 UT at 350KM viewed from north pole

Plasma drift FTLE map for 3-17-2015 at 0:00 UT at 350KM viewed from south pole

Plasma drift FTLE map for 3-17-2015 at 1:00 UT at 350KM viewed from north pole

Plasma drift FTLE map for 3-17-2015 at 1:00 UT at 350KM viewed from south pole

Plasma drift FTLE map for 3-17-2015 at 2:00 UT at 350KM viewed from north pole

Plasma drift FTLE map for 3-17-2015 at 2:00 UT at 350KM viewed from south pole

Figure C.9. FTLE maps for plasma drift during the geomagnetically active period on 17 March 2015 at $t_0 = $ 00:00 UT – 02:00 UT. (Left) north pole; (Right) south pole.

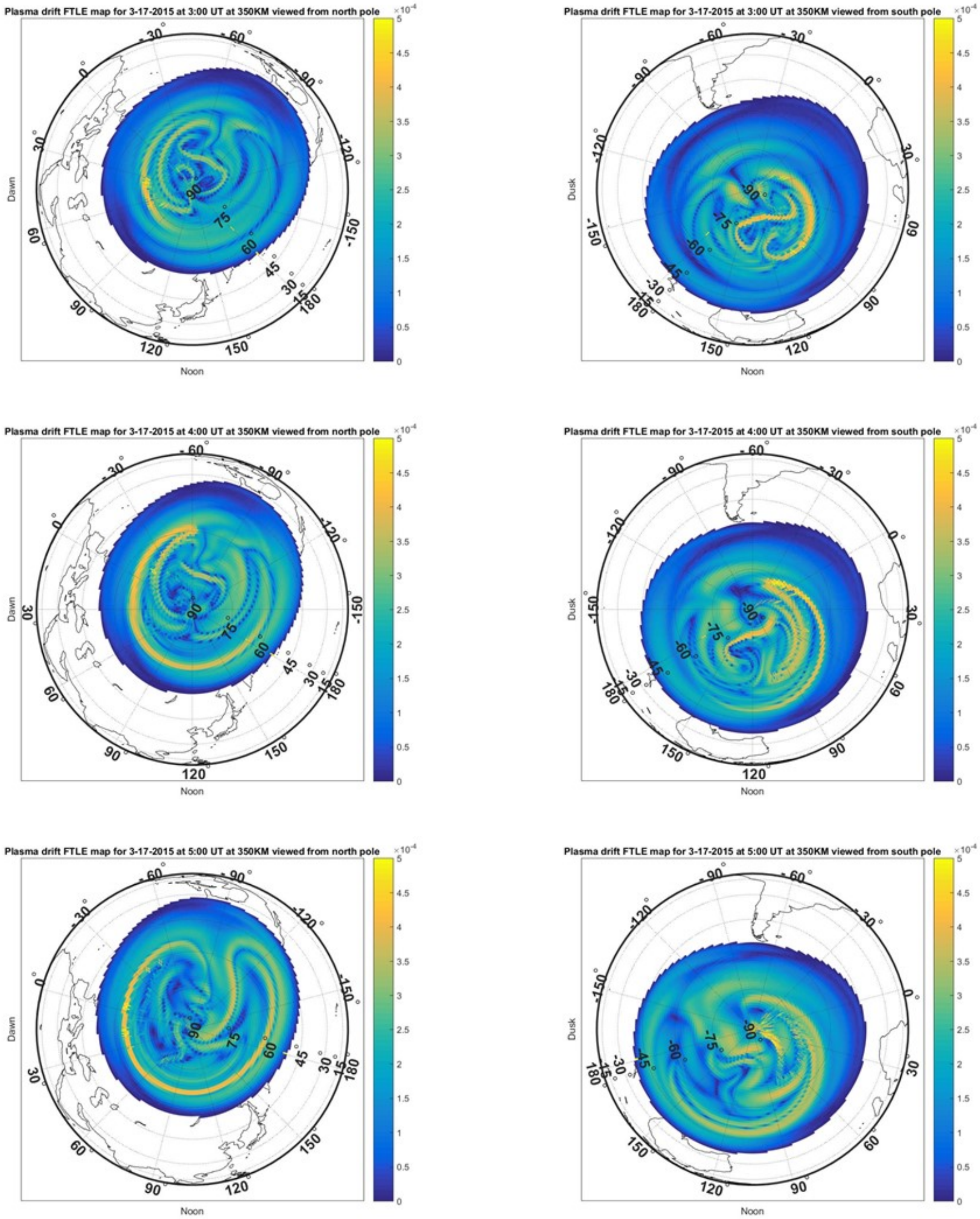
Plasma drift FTLE map for 3-17-2015 at 3:00 UT at 350KM viewed from north pole

Plasma drift FTLE map for 3-17-2015 at 3:00 UT at 350KM viewed from south pole

Plasma drift FTLE map for 3-17-2015 at 4:00 UT at 350KM viewed from north pole

Plasma drift FTLE map for 3-17-2015 at 4:00 UT at 350KM viewed from south pole

Plasma drift FTLE map for 3-17-2015 at 5:00 UT at 350KM viewed from north pole

Plasma drift FTLE map for 3-17-2015 at 5:00 UT at 350KM viewed from south pole

Figure C.10. FTLE maps for plasma drift during the geomagnetically active period on 17 March 2015 at $t_0 = $ 03:00 UT – 05:00 UT. (Left) north pole; (Right) south pole.

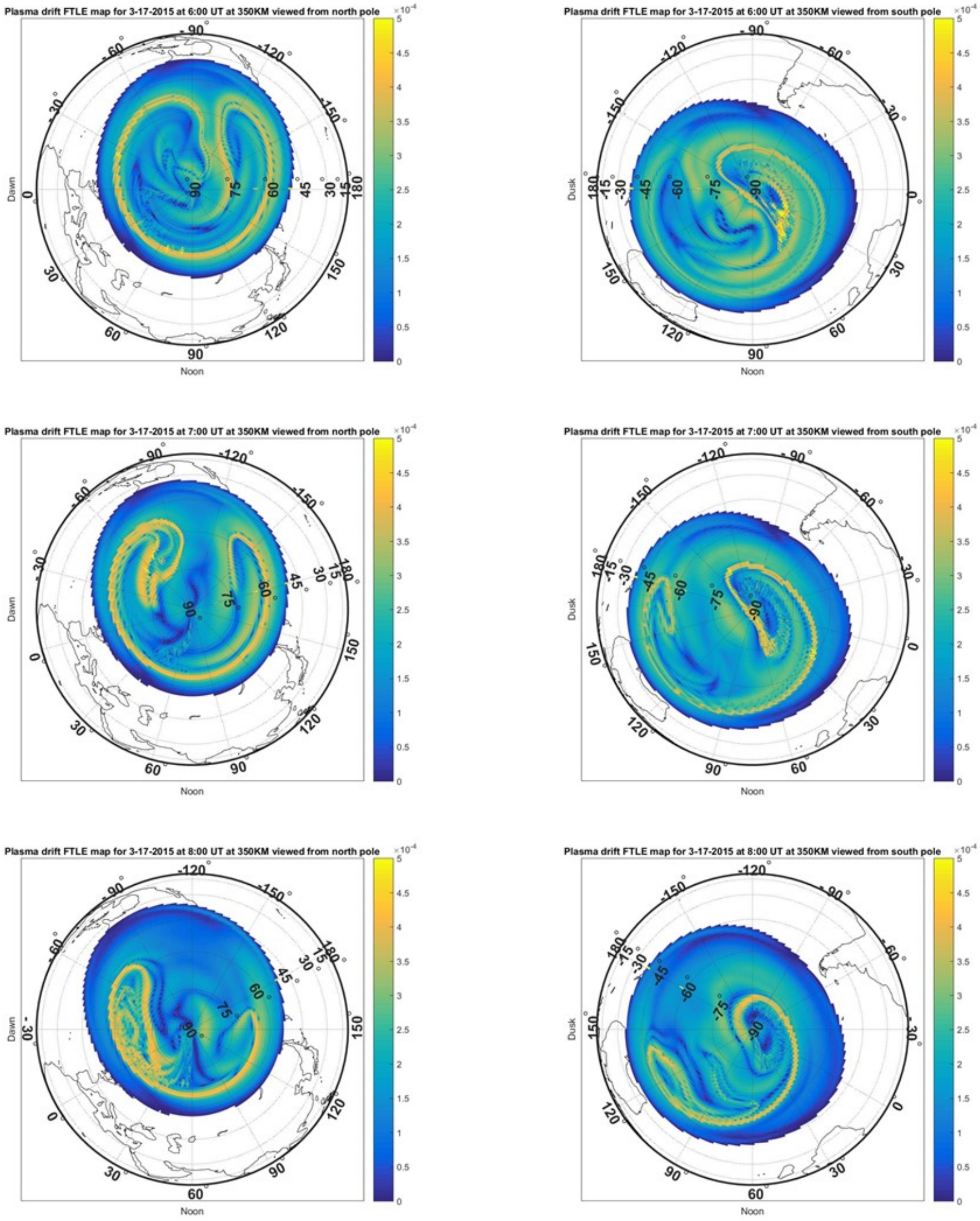

Plasma drift FTLE map for 3-17-2015 at 6:00 UT at 350KM viewed from north pole

Plasma drift FTLE map for 3-17-2015 at 6:00 UT at 350KM viewed from south pole

Plasma drift FTLE map for 3-17-2015 at 7:00 UT at 350KM viewed from north pole

Plasma drift FTLE map for 3-17-2015 at 7:00 UT at 350KM viewed from south pole

Plasma drift FTLE map for 3-17-2015 at 8:00 UT at 350KM viewed from north pole

Plasma drift FTLE map for 3-17-2015 at 8:00 UT at 350KM viewed from south pole

Figure C.11. FTLE maps for plasma drift during the geomagnetically active period on 17 March 2015 at t_0 = 06:00 UT – 08:00 UT. (Left) north pole; (Right) south pole.

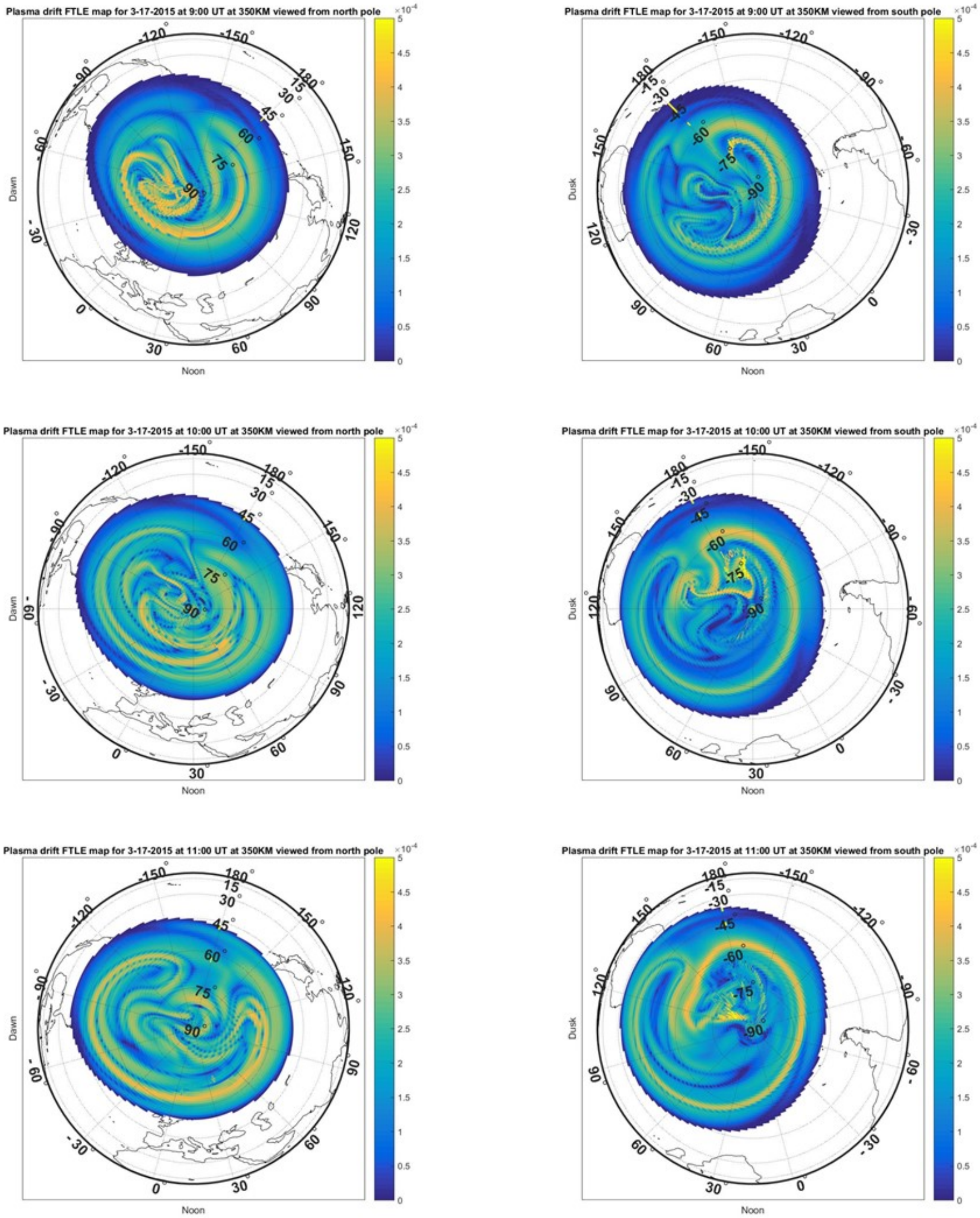

Figure C.12. FTLE maps for plasma drift during the geomagnetically active period on 17 March 2015 at $t_0 = $ 09:00 UT – 11:00 UT. (Left) north pole; (Right) south pole.

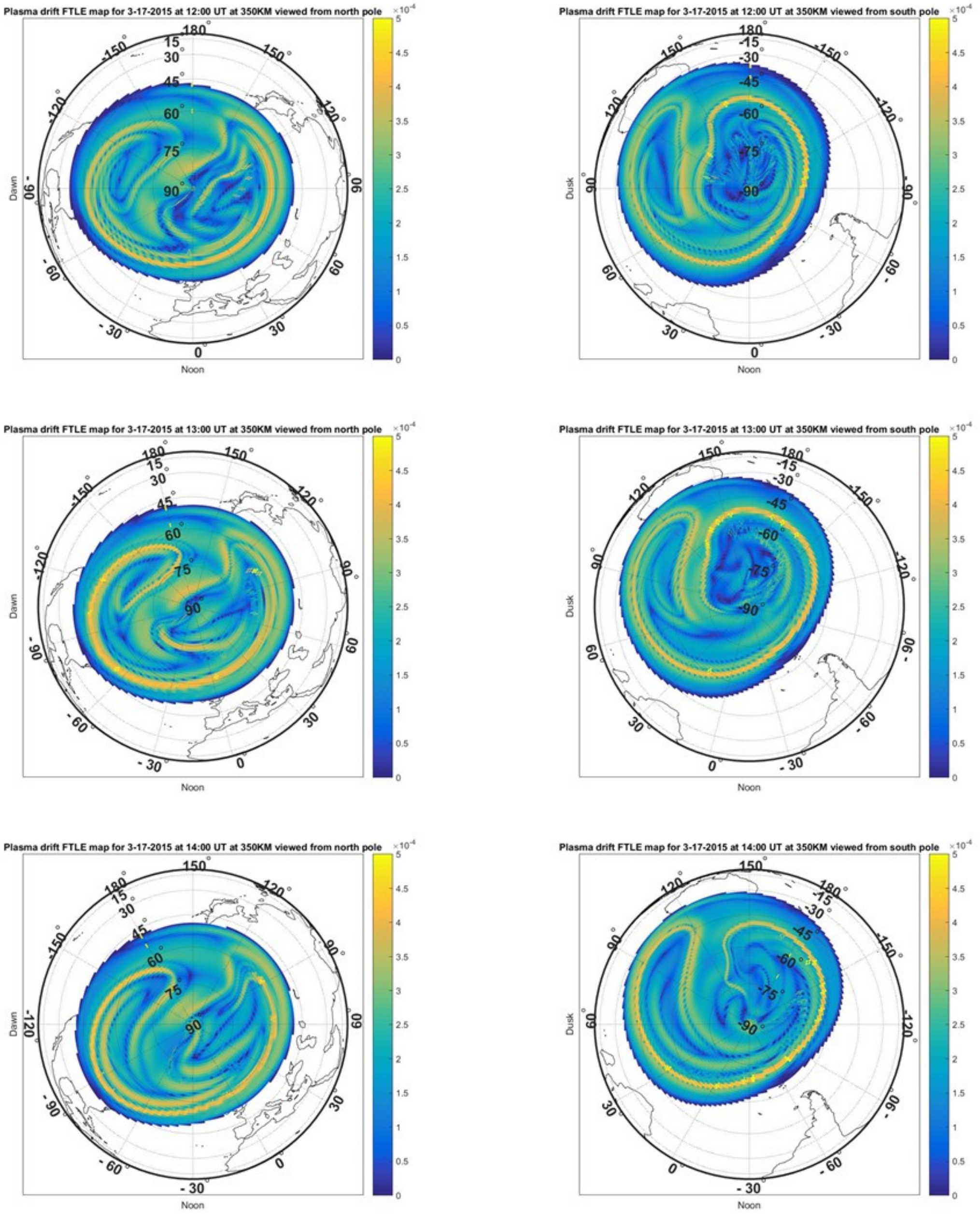

Figure C.13. FTLE maps for plasma drift during the geomagnetically active period on 17 March 2015 at t_0 = 12:00 UT – 14:00 UT. (Left) north pole; (Right) south pole.

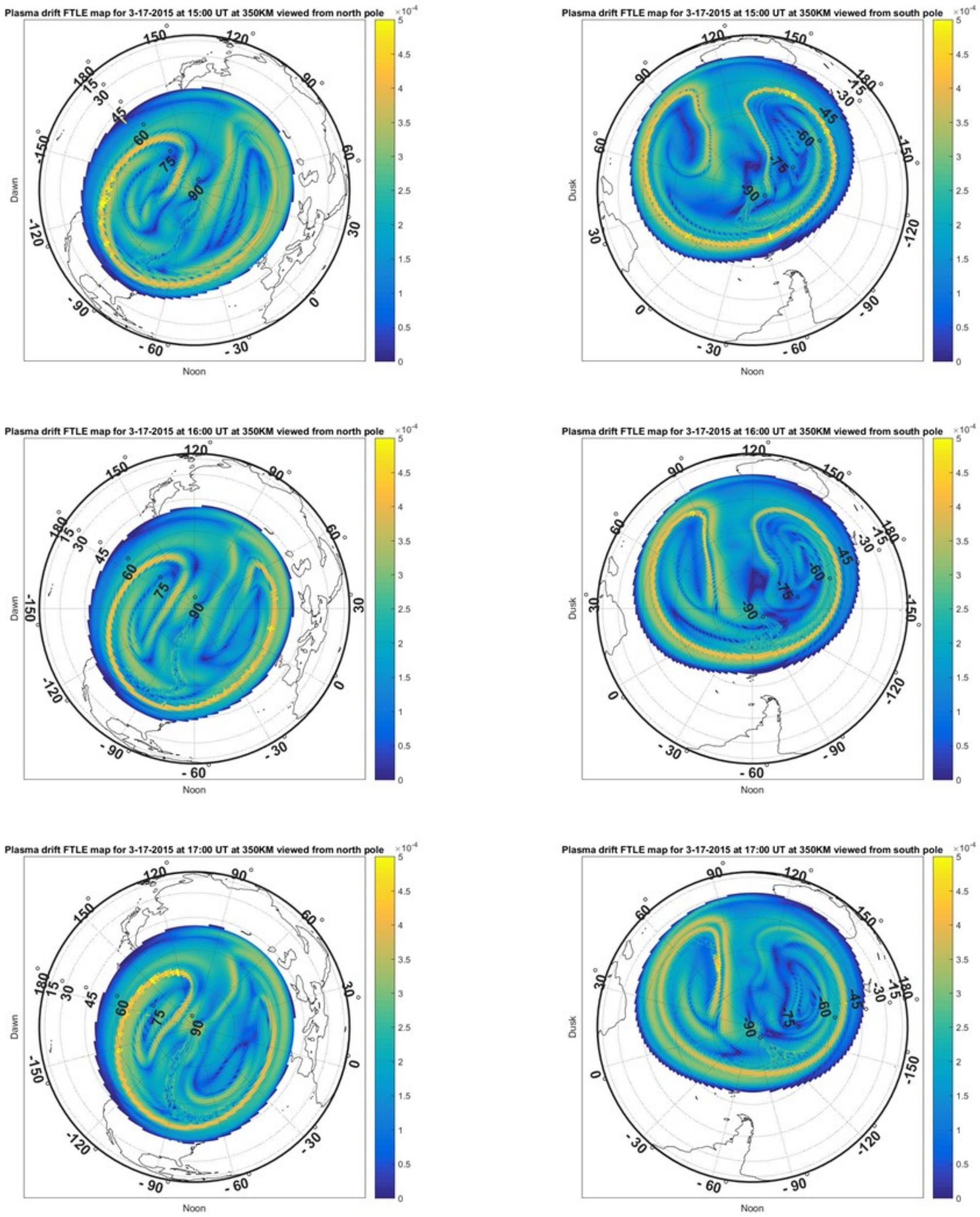

Figure C.14. FTLE maps for plasma drift during the geomagnetically active period on 17 March 2015 at t_0 = 15:00 UT – 17:00 UT. (Left) north pole; (Right) south pole.

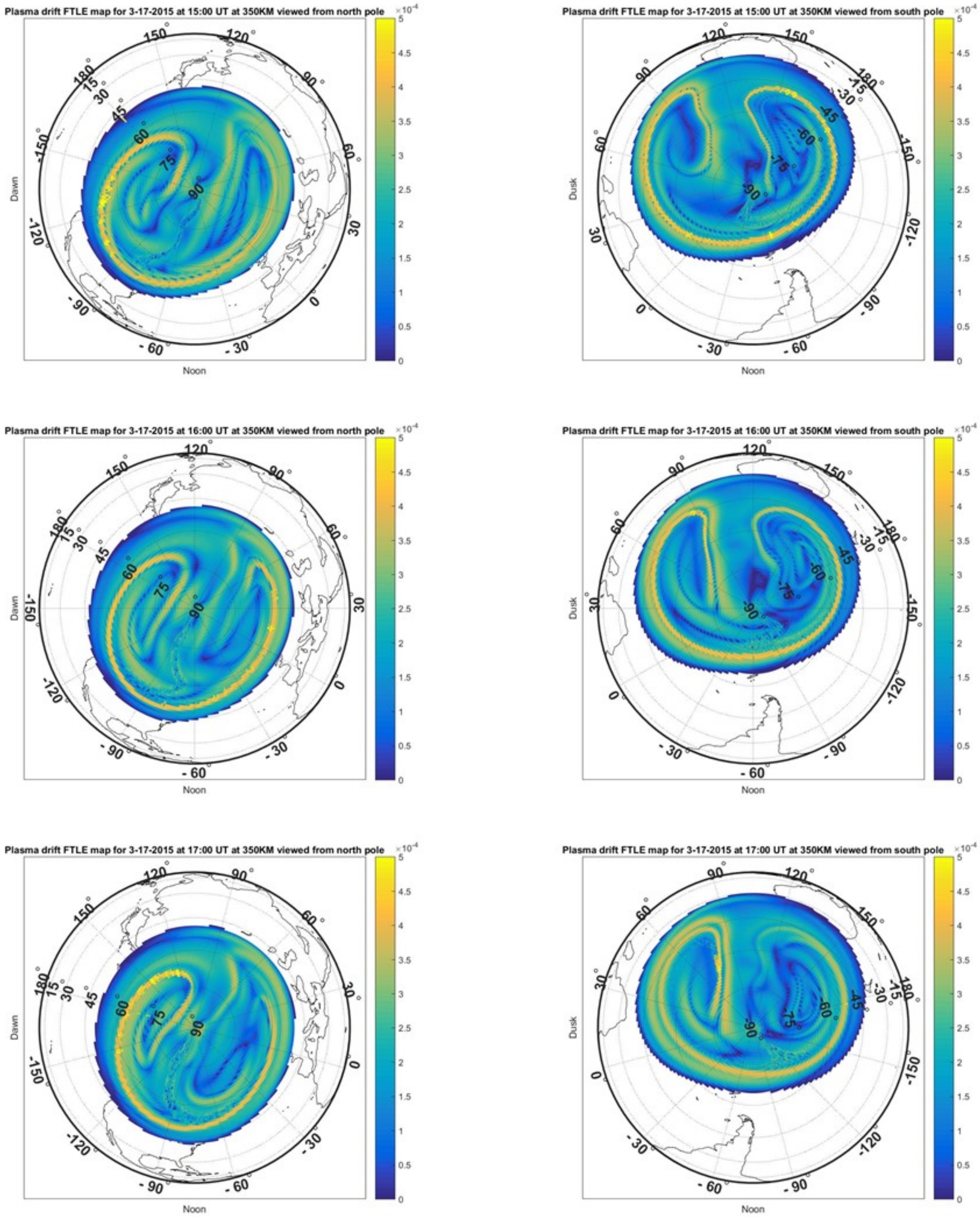

Plasma drift FTLE map for 3-17-2015 at 15:00 UT at 350KM viewed from north pole

Plasma drift FTLE map for 3-17-2015 at 15:00 UT at 350KM viewed from south pole

Plasma drift FTLE map for 3-17-2015 at 16:00 UT at 350KM viewed from north pole

Plasma drift FTLE map for 3-17-2015 at 16:00 UT at 350KM viewed from south pole

Plasma drift FTLE map for 3-17-2015 at 17:00 UT at 350KM viewed from north pole

Plasma drift FTLE map for 3-17-2015 at 17:00 UT at 350KM viewed from south pole

Figure C.15. FTLE maps for plasma drift during the geomagnetically active period on 17 March 2015 at t_0 = 18:00 UT – 20:00 UT. (Left) north pole; (Right) south pole.

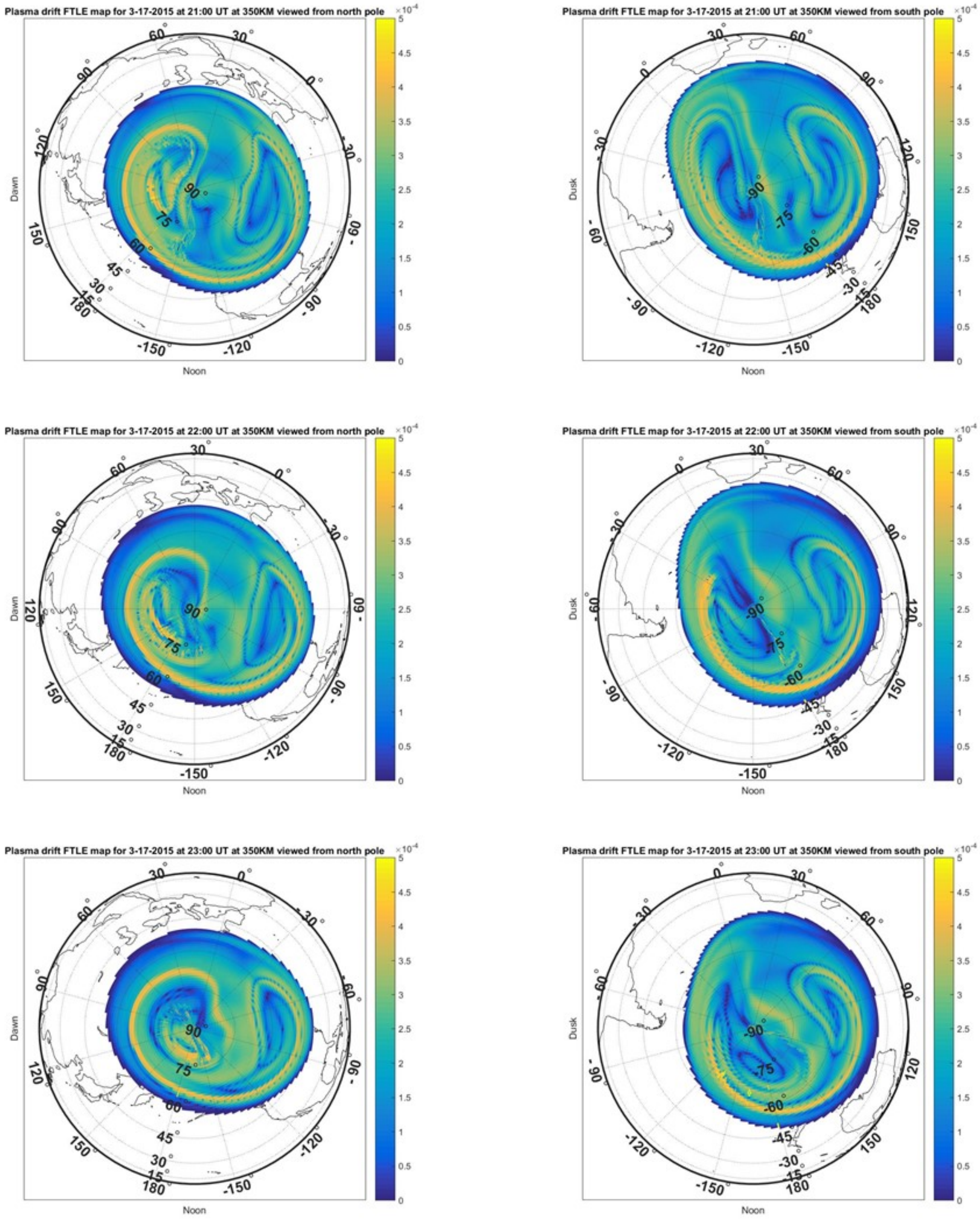

Plasma drift FTLE map for 3-17-2015 at 21:00 UT at 350KM viewed from north pole

Plasma drift FTLE map for 3-17-2015 at 21:00 UT at 350KM viewed from south pole

Plasma drift FTLE map for 3-17-2015 at 22:00 UT at 350KM viewed from north pole

Plasma drift FTLE map for 3-17-2015 at 22:00 UT at 350KM viewed from south pole

Plasma drift FTLE map for 3-17-2015 at 23:00 UT at 350KM viewed from north pole

Plasma drift FTLE map for 3-17-2015 at 23:00 UT at 350KM viewed from south pole

Figure C.16. FTLE maps for plasma drift during the geomagnetically active period on 17 March 2015 at t_0 = 21:00 UT – 23:00 UT. (Left) north pole; (Right) south pole.

BIBLIOGRAPHY

[1] D. N. Anderson, D. T. Decker, and C. E. Valladares. Global Theoretical Ionospheric Model (GTIM). In R. W. Schunk, editor, *Solar-Terrestrial Energy Program: Handbook Of Ionospheric Models*, pages 133–152. Logan UT : Center for Atmospheric and Space Sciences, 1996.

[2] David N. Anderson, Dwight T. Decker, and Cesar E. Valladares. Modeling boundary blobs using time varying convection. *Geophysical Research Letters*, 23(5):579–582, 1996.

[3] Jyoti K. Atul, Rameswar Singh, Sanjib Sarkar, Oleg V. Kravchenko, Sushil K. Singh, Prabal K. Chattopadhyaya, and P. K. Kaw. Magnetic shear damped polar convective fluid instabilities. *Journal of Geophysical Research: Space Physics*, 123(1):808–818, 2018.

[4] J. Bartels, N.H. Heck, and H.F. Johnston. The three-hour-range index measuring geomagnetic activity. *Terrestrial Magnetism and Atmospheric Electricity*, 44(4):411–454, 1939.

[5] J. A. Bittencourt. *Fundamentals of Plasma Physics (Third Edition)*. Springer Science & Business Media, 2013.

[6] Robert Burston, Cathryn Mitchell, and Ivan Astin. Polar cap plasma patch primary linear instability growth rates compared. *Journal of Geophysical Research: Space Physics*, 121(4):3439–3451, 2016.

[7] G. S. Bust and G. Crowley. Tracking of polar cap ionospheric patches using data assimilation. *Journal of Geophysical Research: Space Physics*, 112(5):1–17, 2007.

[8] Gary S. Bust and Cathryn N. Mitchell. History, current state, and future directions of ionospheric imaging. *Reviews of Geophysics*, 46(1), 2008.

[9] Herbert C. Carlson. Sharpening our thinking about polar cap ionospheric patch morphology, research, and mitigation techniques. *Radio Science*, 47(3):1–16, 2012.

[10] K. Chang. Spacex lauches rocket carrying space station cargo. *The New York Times*, 19, February 2017.

[11] Alex T. Chartier, Cathryn N. Mitchell, and David R. Jackson. A 12 year comparison of MIDAS and IRI 2007 ionospheric Total Electron Content. *Advances in Space Research*, 49(9):1348–1355, 2012.

[12] Thomas E. Cravens. *Physics of Solar System Plasmas*. Cambridge Atmospheric and Space Science Series. Cambridge University Press, 1997.

[13] G. Crowley. Critical review of ionospheric patches and blobs. *The Review of radio science, 1993-1996*, pages 619–648, 1996.

[14] S. Datta-Barua, Y. Su, K. Deshpande, D. Miladinovich, G. S. Bust, D. Hampton, and G. Crowley. First light from a kilometer-baseline Scintillation Auroral GPS Array. *Geophysical Research Letters*, 42(10):3639–3646, 2015.

[15] D. T. Decker, C. E. Valladares, R. Sheehan, Su Basu, D. N. Anderson, and R. A. Heelis. Modeling daytime F layer patches over Sondrestrom. *Radio Science*, 29(1):249–268, 1994.

[16] Douglas P. Drob, John T. Emmert, John W. Meriwether, Jonathan J. Makela, Eelco Doornbos, Mark Conde, Gonzalo Hernandez, John Noto, Katherine a. Zawdie, Sarah E. McDonald, Joe D. Huba, and Jeff H. Klenzing. An Update to the Horizontal Wind Model (HWM): The Quiet Time Thermosphere. *Earth and Space Science*, pages n/a–n/a, 2015.

[17] Philip C. du Toit and Jerrold E. Marsden. Horseshoes in hurricanes. *Journal of Fixed Point Theory and Applications*, 7(2):351–384, 2010.

[18] Salah Joseph E. Interim standard for the ion-neutral atomic oxygen collision frequency. *Geophysical Research Letters*, 20(15):1543–1546, 1993.

[19] J. T. Emmert, D. P. Drob, G. G. Shepherd, G. Hernandez, M. J. Jarvis, J. W. Meriwether, R. J. Niciejewski, D. P. Sipler, and C. A. Tepley. DWM07 global empirical model of upper thermospheric storm-induced disturbance winds. *Journal of Geophysical Research: Space Physics*, 113(11):1–16, 2008.

[20] J. C. Foster. Storm time plasma transport at middle and high latitudes. *Journal of Geophysical Research: Space Physics*, 98(A2):1675–1689, 1993.

[21] J. C. Foster, A. J. Coster, P. J. Erickson, J. M. Holt, F. D. Lind, W. Rideout, M. McCready, A. Van Eyken, R. J. Barnes, R. A. Greenwald, and F. J. Rich. Multiradar observations of the polar tongue of ionization. *Journal of Geophysical Research: Space Physics*, 110(A9):1–12, 2005.

[22] Roman O. Grigoriev. Transport and Mixing in Laminar Flows: From Microfluidics to Oceanic Currents. *Transport and Mixing in Laminar Flows: From Microfluidics to Oceanic Currents*, 2011.

[23] G. Haller. An objective definition of a vortex. *Journal of Fluid Mechanics*, 525:1–26, 2005.

[24] G. Haller. Lagrangian coherent structures. *Annual Review of Fluid Mechanics*, 47:137–162, 2015.

[25] K Hallgren. Climatology of middle atmospheric water vapour above the ALOMAR observatory in northern Norway. pages 31531–31560, 2012.

[26] J. K. Hargreaves. *The solar-terrestrial.* Cambridge Atmospheric and Space Science Series. Cambridge University Press, 2003.

[27] K. Hosokawa, J. P. St-Maurice, G. J. Sofko, K. Shiokawa, Y. Otsuka, and T. Ogawa. Reorganization of polar cap patches through shears in the background plasma convection. *Journal of Geophysical Research: Space Physics*, 115(1):1–10, 2010.

[28] K. Hosokawa, T. Tsugawa, K. Shiokawa, Y. Otsuka, N. Nishitani, T. Ogawa, and M. R. Hairston. Dynamic temporal evolution of polar cap tongue of ionization during magnetic storm. *Journal of Geophysical Research: Space Physics*, 115(12):1–33, 2010.

[29] K. Hosokawa, T. Tsugawa, K. Shiokawa, Y. Otsuka, T. Ogawa, and M. R. Hairston. Unusually elongated, bright airglow plume in the polar cap F region: Is it a tongue of ionization? *Geophysical Research Letters*, 36(7):1–5, 2009.

[30] R. D. Hunsucker and J. K. Hargreaves. *The high-latitude ionosphere and its effects on radio propagation*. Cambridge University Press, 2003.

[31] C. Jones and S. Winkler. Invariant manifolds and lagrangian dynamics in the ocean and atmosphere. *Handbook of dynamical systems*, 2:55–92, 2002.

[32] Y. Kamide and G. Rostoker. What is the physical meaning of the ae index? *Eos, Transactions American Geophysical Union*, 85(19):188–192, 2004.

[33] Daniel Karrasch and George Haller. Do finite-size lyapunov exponents detect coherent structures? *Chaos*, 23(4):1–22, 2013.

[34] M. C. Kelley, C. E. Seyler, and M. F. Larsen. Two-dimensional turbulence, space shuttle plume transport in the thermosphere, and a possible relation to the Great Siberian impact event. *Geophysical Research Letters*, 36(14):1–5, 2009.

[35] T L Killeen and R G Roble. An Analysis of the High-Latitude Thermospheric Wind Pattern Calculated by a Thermospheric General Circulation Model 2 . Neutral Parcel Transport. 91, 1986.

[36] T.L. Killeen, P.B. Hays, N.W. Spencer, and L.E. Wharton. Neutral winds in the polar thermosphere as measured from dynamics explorer. *Advances in Space Research*, 2(10):133–136, 1982.

[37] G. Kirchengast. The Graz Ionospheric Flux Tube Simulation Model. In R. W. Schunk, editor, *Solar-Terrestrial Energy Program: Handbook Of Ionospheric Models*, pages 73–94. Logan UT : Center for Atmospheric and Space Sciences, 1996.

[38] G. Le, H. Lhr, B. J. Anderson, R. J. Strangeway, C. T. Russell, H. Singer, J. A. Slavin, Y. Zhang, T. Huang, K. Bromund, P. J. Chi, G. Lu, D. Fischer, E. L. Kepko, H. K. Leinweber, W. Magnes, R. Nakamura, F. Plaschke, J. Park, J. Rauberg, C. Stolle, and R. B. Torbert. Magnetopause erosion during the 17 march 2015 magnetic storm: Combined field-aligned currents, auroral oval, and magnetopause observations. *Geophysical Research Letters*, 43(6):2396–2404, 2016.

[39] Francois Lekien. Time-Dependent Dynamical Systems and Geophysical Flows Thesis by. 2003, 2003.

[40] Qian Liying, Burns Alan G., Emery Barbara A., Foster Benjamin, Lu Gang, Maute Astrid, Richmond Arthur D., Roble Raymond G., Solomon Stanley C., and Wang Wenbin. The ncar tie-gcm. pages 73–83, 2014.

[41] M. Lockwood and H. C. Carlson. Production of polar cap electron density patches by transient magnetopause reconnection. *Geophysical Research Letters*, 19(17):1731–1734, 1992.

[42] M. Lockwood, J. A. Davies, J. Moen, A. P. van Eyken, K. Oksavik, I. W. McCrea, and M. Lester. Motion of the dayside polar cap boundary during substorm cycles: II. Generation of poleward-moving events and polar cap patches by pulses in the magnetopause reconnection rate. *Annales Geophysicae*, 23(11):3513–3532, 2005.

[43] S Lossow, J Urban, H Schmidt, D R Marsh, J Gumbel, and P Eriksson. Wintertime water vapor in the polar upper mesosphere and lower thermosphere : First satellite observations by Odin submillimeter radiometer. 114:1–13, 2009.

[44] John MacDougall and P. T. Jayachandran. Polar patches: Auroral zone precipitation effects. *Journal of Geophysical Research: Space Physics*, 112(5):1–16, 2007.

[45] Jonathan J Makela, Brian J Harding, John W Meriwether, Rafael Mesquita, Samuel Sanders, Aaron J Ridley, Michael W Castellez, Marco Ciocca, Gregory D Earle, Nathaniel A Frissell, Donald L Hampton, Andrew J Gerrard, John Noto, and Carlos R Martinis. Journal of Geophysical Research : Space Physics Storm time response of the midlatitude thermosphere : Observations from a network of Fabry-Perot interferometers. pages 6758–6773, 2014.

[46] R R Meier, John M C Plane, Michael H Stevens, L J Paxton, and A B Christensen. Can molecular diffusion explain Space Shuttle plume spreading? 37:1–5, 2010.

[47] Daniel S. Miladinovich, Seebany Datta-Barua, Gary S. Bust, and Jonathan J. Makela. Assimilation of thermospheric measurements for ionosphere-thermosphere state estimation. *Radio Science*, 51(12):1818–1837, 2016.

[48] Cathryn N. Mitchell and Paul S.J. Spencer. A three-dimensional time-dependent algorithm for ionospheric imaging using GPS. *Annals of Geophysics*, 46(4):687–696, 2003.

[49] J Moen, K Hosokawa, N Gulbrandsen, and L B N Clausen. On the symmetry of ionospheric polar cap patch exits around magnetic midnight. *Journal of Geophysical Research : Space Physics*, 2015.

[50] Jøran Moen, Kjellmar Oksavik, Lucilla Alfonsi, Yvonne Daabakk, Vineenzo Romano, and Luca Spogli. Space weather challenges of the polar cap ionosphere. *Journal of Space Weather and Space Climate*, 3:A02, 2013.

[51] K. Oksavik, V. L. Barth, J. Moen, and M. Lester. On the entry and transit of high-density plasma across the polar cap. *Journal of Geophysical Research: Space Physics*, 115(12):1–15, 2010.

[52] A Okubo. Horizontal dispersion of floatable particles in the vicnity of velocity singularies such as convergences. *Deep-sea Res.*, 17(445-454):445–454, 1970.

[53] T. Peacock and G. Haller. Lagrangian coherent structures: The hidden skeleton of fluid flows. *Physics today*, 66(2):41, 2013.

[54] Datta-Barua S., Bust G. S., Crowley G., and Curtis N. Neutral wind estimation from 4-d ionospheric electron density images. *Journal of Geophysical Research: Space Physics*, 114(A6), 2009.

[55] Shawn C. Shadden, Francois Lekien, and Jerrold E. Marsden. Definition and properties of Lagrangian coherent structures from finite-time Lyapunov exponents in two-dimensional aperiodic flows. *Physica D: Nonlinear Phenomena*, 212(3-4):271–304, 2005.

[56] Shadden, Shawn C. . FlowVC (Version 1) [Computer software], 2010.

[57] D E Siskind, M H Stevens, J T Emmert, D P Drob, A J Kochenash, J M Russell Iii, L L Gordley, and M G Mlynczak. Signatures of shuttle and rocket exhaust plumes in TIMED / SABER radiance data. 30(15):10–13, 2003.

[58] J J Sojka, M D Bowline, and R W Schunk. Patches in the polar ionosphere : UT and seasonal dependence magnetic. 99, 1994.

[59] J. J. Sojka, M. D. Bowline, R. W. Schunk, D. T. Decker, C. E. Valladares, R. Sheehan, D. N. Anderson, and R. A. Heelis. Modeling polar cap f-region patches using time varying convection. *Geophysical Research Letters*, 20(17):1783–1786, 1993.

[60] V. Sotnikov, T. Kim, J. Lundberg, I. Paraschiv, and T. A. Mehlhorn. Scattering of electromagnetic waves by vortex density structures associated with interchange instability: Analytical and large scale plasma simulation results. *Physics of Plasmas*, 21(5), 2014.

[61] Paul S J Spencer and Cathryn N. Mitchell. Imaging of fast moving electron-density structures in the polar cap. *Annals of Geophysics*, 50(3):427–434, 2007.

[62] Michael H. Stevens, Stefan Lossow, Jens Fiedler, Gerd Baumgarten, Franz Josef Lbken, Kristofer Hallgren, Paul Hartogh, Cora E. Randall, Jerry Lumpe, Scott M. Bailey, R. Niciejewski, R. R. Meier, John M C Plane, Andrew J. Kochenash, Donal P. Murtagh, and Christoph R. Englert. Bright polar mesospheric clouds formed by main engine exhaust from the space shuttle's final launch. *Journal of Geophysical Research Atmospheres*, 117(19):1–19, 2012.

[63] Michael H Stevens, Stefan Lossow, David E Siskind, R R Meier, Cora E Randall, James M Russell, Jo Urban, and Donal Murtagh. Journal of Atmospheric and Solar-Terrestrial Physics Space shuttle exhaust plumes in the lower thermosphere : Advective transport and diffusive spreading. *Journal of Atmospheric and Solar-Terrestrial Physics*, 108:50–60, 2014.

[64] Michael H. Stevens, R. R. Meier, Xinzhao Chu, Matthew T. DeLand, and John M C Plane. Antarctic mesospheric clouds formed from space shuttle exhaust. *Geophysical Research Letters*, 32(13):1–5, 2005.

[65] Wenbo Tang, Pak Wai Chan, and George Haller. Accurate extraction of Lagrangian coherent structures over finite domains with application to flight data analysis over Hong Kong International Airport. *Chaos*, 20(1):1–8, 2010.

[66] Wenbo Tang and Alex Mahalov. Stochastic Lagrangian dynamics for charged flows in the E-F regions of ionosphere. *Physics of Plasmas*, 20(3), 2013.

[67] T. Tascione. *Introduction to the Space Environment (Second Edition)*. Krieger Publishing Company, 2010.

[68] Erwan Thébault, Christopher C Finlay, Ciarán D Beggan, Patrick Alken, Julien Aubert, Olivier Barrois, Francois Bertrand, Tatiana Bondar, Axel Boness, Laura Brocco, Elisabeth Canet, Aude Chambodut, Arnaud Chulliat, Pierdavide Coïsson, François Civet, Aimin Du, Alexandre Fournier, Isabelle Fratter, Nicolas Gillet, Brian Hamilton, Mohamed Hamoudi, Gauthier Hulot, Thomas Jager, Monika Korte, Weijia Kuang, Xavier Lalanne, Benoit Langlais, Jean-michel Léger, Vincent Lesur, Frank J Lowes, Susan Macmillan, Mioara Mandea, Chandrasekharan Manoj, Stefan Maus, Nils Olsen, Valeriy Petrov, Victoria Ridley, Martin Rother, Terence J Sabaka, Diana Saturnino, Reyko Schachtschneider,

Olivier Sirol, Andrew Tangborn, Alan Thomson, Lars Tøffner-clausen, Pierre Vigneron, and Ingo Wardinski. International Geomagnetic Reference Field : the 12th generation. *Earth, Planets and Space*, 2015.

[69] Philip C Toit. Transport and Separatrices in Time-Dependent Flows Thesis by. 2010, 2010.

[70] B. T. Tsurutani, J. K. Arballo, G. S. Lakhina, C. M. Ho, J. Ajello, J. S. Pickett, D. A. Gurnett, R. P. Lepping, W. K. Peterson, G. Rostoker, Y. Kamide, and S. Kokubun. The January 10, 1997 auroral hot spot, horseshoe aurora and first substorm: A CME loop? *Geophys. Res. Lett.*, 25(15):3047–3050, 1998.

[71] J. G. Venditti, R. J. Hardy, M. Church, and J. L. Best. What is a coherent flow structure in geophysical flow? In J. G. Venditti, J. L. Best, M. Church, and R. J. Hardy, editors, *Coherent Flow Structures at Earth's Surface*, chapter 1. Wiley Blackwell, 2013.

[72] Ningchao Wang, Seebany Datta-Barua, Alex Chartier, Uriel Ramirez, and Cathryn N. Mitchell. Horseshoes in the high-latitude ionosphere. *Journal of Geophysical Research: Space Physics*, 0(ja), 2018.

[73] Ningchao Wang, Uriel Ramirez, Francisco Flores, and Seebany Datta-Barua. Lagrangian coherent structures in the thermosphere: Predictive transport barriers. *Geophys. Res. Lett.*, 44(2):4549–4557, 2017.

[74] W. Wang, A. G. Burns, M. Wiltberger, S. C. Solomon, and T. L. Killeen. Altitude variations of the horizontal thermospheric winds during geomagnetic storms. *Journal of Geophysical Research: Space Physics*, 113(2):1–17, 2008.

[75] E. J. Weber, J. Buchau, J. G. Moore, J. R. Sharber, R. C. Livingston, J. D. Winningham, and B. W. Reinisch. F layer ionization patches in the polar cap. *Journal of Geophysical Research: Space Physics*, 89(3):1683–1694, 1984.

[76] D R Weimer. Improved ionospheric electrodynamic models and application to calculating Joule heating rates. 110:1–21, 2005.

[77] D. R. Weimer. Predicting surface geomagnetic variations using ionospheric electrodynamic models. *Journal of Geophysical Research: Space Physics*, 110(A12):1–12, 2005.

[78] J Weiss. The dynamics of enstropy transfer in 2-dimensional hydrodynamics. *Physica D*, 48:273, 1991.

[79] World Data Center for Geomagnetism, Kyoto. Provisional Dst index, July 2018.

[80] Q. H. Zhang, B. C. Zhang, R. Y. Liu, M. W. Dunlop, M. Lockwood, J. Moen, H. G. Yang, H. Q. Hu, Z. J. Hu, S. L. Liu, I. W. McCrea, and M. Lester. On the importance of interplanetary magnetic field By on polar cap patch formation. *Journal of Geophysical Research: Space Physics*, 116(5):1–13, 2011.

[81] Q.-H. Zhang, B.-C. Zhang, M. Lockwood, H.-Q. Hu, J. Moen, J. M. Ruohoniemi, E. G. Thomas, S.-R. Zhang, H.-G. Yang, R.-Y. Liu, K. A. McWilliams, and J. B. H. Baker. Direct Observations of the Evolution of Polar Cap Ionization Patches. *Science*, 339(6127):1597–1600, 2013.

[82] Q. H. Zhang, B. C. Zhang, J. Moen, M. Lockwood, I. W. McCrea, H. G. Yang, H. Q. Hu, R. Y. Liu, S. R. Zhang, and M. Lester. Polar cap patch segmentation of the tongue of ionization in the morning convection cell. *Geophysical Research Letters*, 40(12):2918–2922, 2013.

[83] Shasha Zou, Mark B. Moldwin, Aaron J. Ridley, Michael J. Nicolls, Anthea J. Coster, Evan G. Thomas, and J. Michael Ruohoniemi. On the generation/decay of the storm-enhanced density plumes: Role of the convection flow and field-aligned ion flow. *Journal of Geophysical Research: Space Physics*, 119(10):8543–8559, 2014.